Technische Universität München
TUM School of Natural Sciences

Industrially Relevant Electrochemical Reduction of CO_2 to C_{2+} Compounds

Baran Şahin

Vollständiger Abdruck der von der TUM School of Natural Sciences der Technischen Universität München zur Erlangung eines

Doktors der Ingenieurwissenschaften (Dr.-Ing.)

genehmigten Dissertation.

Vorsitz: apl. Prof. Dr. Wolfgang Eisenreich

Prüfende der Dissertation:

1. Prof. Dr.-Ing. Kai-Olaf Hinrichsen
2. Hon.-Prof. Dr. Maximilian Fleischer

Die Dissertation wurde am 22.04.2024 bei der Technischen Universität München eingereicht und durch TUM School of Natural Sciences am 29.05.2024 angenommen.

Acknowledgements

This period of my life, marked by challenges and triumphs, has been a transformative experience that I will forever cherish. Looking back, I am very glad to have made the decision to embark on this difficult yet rewarding journey, and I would like to express my gratitude to everyone who has accompanied me along the way:

I am immensely thankful to my supervisor from Siemens Energy, Dr. Elfriede Simon, for offering me the opportunity to pursue my PhD at Siemens Energy, her guidance and unwavering support. I deeply appreciated her open-door policy, always welcoming me whenever I needed to talk, discuss, or exchange ideas. Her curious scientific mind, coupled with constant encouragement for my innovative ideas, played a pivotal role in creating an environment that facilitated the implementation of my research.

Special thanks to Prof. Dr. Olaf Hinrichsen for agreeing to be my academic supervisor and allowing me the opportunity to be an “external” part of his team at Chair of Technical Chemistry I at Technical University of Munich. I express my gratitude for his remarkably positive approach to new ideas and research questions, his academic guidance, as well as his support in supervising the Master's students from the university side to bring those ideas to fruition.

I also would like to thank all the committee members for dedicating their valuable time to read and evaluate this thesis.

I find myself lucky to be part of the Siemens Energy team in Munich. I owe my sincere gratitude to Prof. Maximilian Fleischer for co-supervision, for extending his full support even in uncertain times, for his openness to innovation and for always sharing the latest news and insights from the scientific community. Special acknowledgement to our world-class team: Dr. Angelika Tawil, Dr. Erhard Magori, Dr. Remigiusz Pastusiak and Dr. Kerstin Wiesner-Fleischer. Without their support in the lab, valuable discussions, motivation, and sense of humor on good and bad

days, this work could not have been realized. I extend my sincere thanks to my students, Samantha Kimberly Raymond, Vinicius Facci Allegrini and Mark Krähling for their dedication and hard work in the lab. Additionally, I would like to acknowledge the rest of the Siemens Energy team, and the members of Chair of Technical Chemistry 1 for their questions and suggestions throughout this work. I express my gratitude for the support and in-depth discussions with colleagues from the Technical University of Berlin, Johnson Matthey, and the University of Oxford on the subject of CO_2 electrolysis. Special thanks to Prof. Dr. Wolfgang Eisenreich for his assistance with NMR analyses. I extend my heartfelt gratitude to Marcel Dossow for his substantial contribution to proofreading my articles and for engaging in insightful exchanges about our experiences throughout our PhD journeys.

A thousand thanks to my immediate family—Anne, Baba, and Bulut—for their unconditional love and support in every aspect and every phase of my life. I'm also grateful to my extended family, uncles, aunts, and cousins, even though we are 1900 km apart. Another thousand thanks to my big family in Munich (countless names to be mentioned here), we all came here from different parts of the world and made a new “Zuhause” all together. I am grateful to have such wonderful friends who are always there for me and can’t wait to celebrate this instance all together. I must mention two names from my Munich family who significantly impacted my PhD journey: In the first half, there's Jane, who went beyond the role of a colleague and became a cherished friend. I thank her for being there for me also in rocky times. Antonino, in the second half, I thank him for being a source of strength and tranquillity throughout this period.

I extend my gratitude to everyone who has been a part of my story, even those unmentioned, for your steadfast support. You all have made the completion of this document possible.

Abstract

In the pursuit of a carbon-neutral economy and the integration of renewable electricity, Siemens Energy initiated a research program exploring the transformation of CO_2 and renewable electricity into economically valuable products. This doctoral thesis aligns with the initiative, focusing on the experimental exploration of the electrochemical reduction of CO_2 to value-added C_{2+} compounds (e.g. ethylene, ethanol and *n*-propanol) under industrially relevant conditions. Ethylene, as an example among these C_{2+} compounds, is one of the most significant building blocks for the chemical industry, with global production at scale of hundreds-million-ton and global market size at scale of hundreds-billion USD scale. Current methods of ethylene production are however energy intensive and leave a considerable carbon footprint. Realizing ethylene production via more carbon-neutral means would therefore be a significant achievement.

Despite its potential to defossilize significant industrial processes, such as production of commodity chemicals and sustainable aviation fuel, CO_2 electroreduction to C_{2+} faces various challenges, including achievement of high selectivity towards desired C_{2+} products, assurance of long-term stability at industrially relevant conditions, and maximizing the energy efficiency. In the literature, the predominant focus is placed on the catalyst research including morphological structure engineering, local catalytic environment design, heteroatom doping, theoretical as well as kinetic studies of electrochemical reaction mechanisms. Catalyst is undoubtedly a critical variable in the complex matrix of CO_2 electroreduction, nevertheless, for a selective, stable and efficient electroreduction of CO_2 necessitates an integral consideration of catalyst, gas diffusion electrode (GDE) design, cell design, and boundary conditions present during the reaction (i.e. operation conditions).

This thesis aims to improve these performance factors of CO_2 electrolysis technology by addressing critical gaps in understanding operational conditions' influences and the interplay

between cell and electrode designs. Throughout the dissertation, the same electrocatalyst, namely CuO, is consistently employed to exclusively investigate operational and design aspects.

Initially, the effects of a significant operational parameter, back pressure (pressure difference between the gas and liquid sides of the GDE) application, on stability and selectivity were studied. The motivation for this study was to counter the well-described flooding phenomenon (incorporation of liquid electrolyte into the porous structure of GDE blocking the gas diffusion) by exerting overpressure on the gas side. Experimental results demonstrated that back pressure significantly prolonged stable operation, doubling it to 72 hours compared to the base case. Yet it was revealed by control experiments that the prolonged stability was achieved due to increased CO_2 surface coverage effects at higher CO_2 partial pressures instead of the original motivation of countering flooding phenomenon. Back pressure regulation provided control over selectivity, with higher back pressure steering selectivity towards oxygenate products (mainly ethanol and *n*-propanol) due to adsorbed CO_2 species coverage.

Secondly, the effects of another operational parameter, the accumulation of liquid byproducts in the electrolyte, on selectivity, stability, and cell potential were discovered. Addressing critical upper limits for liquid product concentration in the electrolyte was the main motivation of this study as these limits can dictate the outputs of downstream liquid product separation steps of a possible industrial CO_2 electrolyzer. Critically, alcohol-induced flooding degraded the hydrophobic electrode, as the contact angle measurements clearly verified, compromising selective and stable ethylene formation shown by electrochemical measurements conducted with various alcohol concentrations in the electrolyte. 1.89 M *n*-propanol concentration in electrolyte led to catalyst layer abrasion observed by SEM imaging. 5.12 M ethanol concentration in electrolyte caused structural alterations in the Nafion 117 membrane proven by ATR-FTIR spectroscopy, resulting in elevated cell potentials.

Finally, readily scalable cell and electrode designs and their optimum combinations were explored. This study was primarily motivated by the goal of developing a CO_2 electrolyzer based on a readily scalable cell design, coupled with a correspondingly tailored gas diffusion electrode in order to achieve long-term stability, high selectivity towards C_{2+} compounds, and low cell potentials within a single, optimized cell and electrode design combination. Two promising, readily scalable CO_2 electrolyzer cell architectures for industrial applications were identified based on experimental evidence, with the CEM-based zero-gap cell and the CEM-based one-gap cell being notable options. CEM-based zero-gap cell required electrode modifications for C_2H_4 selectivity and therefore innovative gas diffusion electrode layer (based on anion exchange ionomer and TiO_2) was incorporated in to enable C_2H_4 formation proven by electrochemical measurements. However, focus shifted to the CEM-based one-gap cell due to superior selectivity and stability. A breakthrough in month-long stability for the production of C_2H_4 was achieved through electrode modifications and the concurrent implementation of optimum operational conditions. Degradation mechanisms revealed salt formation at lower current densities and catalyst agglomeration at higher ones shown by SEM/EDX analyses.

Overall, this dissertation contributes to advancing CO_2 electrochemical reduction to C_{2+} compounds in industrial conditions by offering insights into the importance of controlling operational conditions and optimizing cell/electrode designs for more selective, stable, and efficient electrolyzers.

Zusammenfassung

Im Streben nach einer kohlenstoffneutralen Wirtschaft und der Integration erneuerbarer Elektrizität initiierte Siemens Energy ein Forschungsprogramm zur Erforschung der Umwandlung von CO_2 und erneuerbarer Elektrizität in wirtschaftlich wertvolle Produkte. Diese Doktorarbeit steht im Einklang mit dieser Initiative und konzentriert sich auf die experimentelle Erforschung der elektrochemischen Reduktion von CO_2 zu wertvollen C_{2+} Produkten (z.B. Ethylen, Ethanol und *n*-Propanol) unter industriell relevanten Bedingungen. Ethylen ist dabei ein Beispiel für diese C_{2+} Produkte und gilt als einer der wichtigsten Bausteine der chemischen Industrie mit einer weltweiten Produktion im Bereich von Hunderten Millionen Tonnen und einem globalen Markt von Hunderten Milliarden USD. Die derzeitigen Methoden zur Ethylenproduktion sind jedoch energieintensiv und hinterlassen einen erheblichen CO_2-Fußabdruck. Die Realisierung der Ethylenproduktion mittels kohlenstoffneutralerer Mittel wäre daher ein bedeutender Fortschritt.

Trotz ihres Potenzials zur Defossilisierung wichtiger industrieller Prozesse, wie der Produktion von Massenchemikalien und nachhaltigem Flugtreibstoff, steht die CO_2-Elektroreduktion zu C_{2+} vor verschiedenen Herausforderungen, darunter die Erreichung einer hohen Selektivität der gewünschten C_{2+} Produkten, die Gewährleistung langfristiger Stabilität unter industriell relevanten Bedingungen und die Maximierung der Energieeffizienz. In der Literatur liegt der Schwerpunkt hauptsächlich auf der Katalysatorforschung, einschließlich der strukturellen Gestaltung, dem Design des lokalen katalytischen Umfelds, der Dotierung mit Heteroatomen sowie theoretischen und kinetischen Studien der elektrochemischen Reaktionsmechanismen. Der Katalysator ist zweifellos eine kritische Variable in der komplexen Matrix der CO_2-Elektroreduktion. Für eine selektive, stabile und effiziente Elektroreduktion von CO_2 müssen jedoch Katalysator, Gasdiffusionselektroden- (GDE) Design, Zelldesign und die während der Reaktion herrschenden Randbedingungen (d.h. Betriebsbedingungen) ganzheitlich berücksichtigt werden.

Diese Dissertation zielt darauf ab, diese Leistungsfaktoren der CO_2-Elektrolyse-Technologie zu verbessern, indem sie kritische Lücken im Verständnis der Einflüsse der Betriebsbedingungen und des Zusammenspiels zwischen Zell- und Elektrodenkonstruktionen angeht. Im Verlauf der Dissertation wird derselbe Elektrokatalysator, nämlich CuO, um ausschließlich betriebliche und designrelevante Aspekte zu untersuchen.

Zunächst wurden die Auswirkungen eines wesentlichen Betriebsparameters, des Gegendrucks (Druckunterschied zwischen Gas- und Flüssigseiten des GDE), auf Stabilität und Selektivität untersucht. Die Motivation für diese Studie war die Bekämpfung des bekannten Flutungsphänomens (Einschluss von Flüssigelektrolyt in die poröse Struktur des GDE, was die Gasdiffusion blockiert), indem auf der Gasseite ein Überdruck erzeugt wurde. Die experimentellen Ergebnisse zeigten, dass der Gegendruck die stabile Betriebszeit signifikant verlängerte, und zwar um das Doppelte auf 72 Stunden im Vergleich zum Basisfall. Kontrollversuche zeigten jedoch, dass die verlängerte Stabilität aufgrund erhöhter CO_2-Oberflächenbedeckung bei höheren CO_2-Partialdrücken erreicht wurde, anstatt aufgrund der ursprünglichen Motivation, das Flutungsphänomen zu bekämpfen. Die Regulierung des Gegendrucks ermöglichte die Steuerung der Selektivität, wobei ein höherer Gegendruck die Selektivität in Richtung sauerstoffhaltigen Produkte (*en. Oxygenates*) (hauptsächlich Ethanol und *n*-Propanol) lenkte aufgrund der adsorbierten CO_2-Spezies-Bedeckung.

Zweitens wurden die Auswirkungen eines weiteren Betriebsparameters, der Ansammlung von flüssigen Nebenprodukten im Elektrolyten, auf Selektivität, Stabilität und Zellpotential untersucht. Die Hauptmotivation dieser Studie war die Angabe kritischer Obergrenzen für die Konzentration von flüssigen Produkten im Elektrolyten, da diese Grenzen die Ergebnisse der nachfolgenden Schritte zur Abtrennung flüssiger Nebenprodukte in einem möglichen industriellen CO_2-Elektrolyseur bestimmen können. Kritisch war, dass alkoholinduzierte Flutungen die hydrophobe Elektrode beeinträchtigten, wie die Kontaktwinkelmessungen deutlich bestätigten,

was die selektive und stabile Ethylenbildung beeinträchtigte, wie durch elektrochemische Messungen mit verschiedenen Alkoholkonzentrationen im Elektrolyten gezeigt wurde. Eine Konzentration von 1,89 M *n*-Propanol im Elektrolyten führte zu einem Abrieb der Katalysatorschicht, wie durch REM-Aufnahmen beobachtet. Eine Konzentration von 5,12 M Ethanol im Elektrolyten verursachte strukturelle Veränderungen in der Nafion 117-Membran, wie durch ATR-FTIR-Spektroskopie nachgewiesen, was zu erhöhten Zellpotentialen führte.

Schließlich wurden leicht skalierbare Zell- und Elektrodenkonstruktionen und ihre optimalen Kombinationen erforscht. Diese Studie wurde in erster Linie durch das Ziel motiviert, einen CO_2-Elektrolyseur auf der Basis eines leicht skalierbaren Zelldesigns zu entwickeln, gekoppelt mit einer entsprechend maßgeschneiderten Gasdiffusionselektrode, um langfristige Stabilität, hohe Selektivität für C_{2+} Produkten und niedrige Zellpotentiale innerhalb einer einzigen, optimierten Zell- und Elektrodenkonstruktionskombination zu erreichen. Zwei vielversprechende, leicht skalierbare CO_2-Elektrolyseur-Zellarchitekturen für industrielle Anwendungen wurden auf der Grundlage experimenteller Ergebnisse identifiziert, wobei die CEM-basierte Zero-Gap-Zelle und die CEM-basierte One-Gap-Zelle bemerkenswerte Optionen darstellten. Die CEM-basierte Zero-Gap-Zelle erforderte Elektrodenmodifikationen für C_2H_4-Selektivität, und daher wurde eine innovative Gasdiffusionselektrodenschicht (basierend auf einem Anionenaustausch-Ionomer und TiO_2) eingebaut, um die C_2H_4-Bildung durch elektrochemische Messungen nachzuweisen. Der Fokus lag jedoch auf die CEM-basierte One-Gap-Zelle aufgrund ihrer überlegenen Selektivität und Stabilität. Ein Durchbruch in der monatelangen Stabilität für die Produktion von C_2H_4 wurde durch Elektrodenmodifikationen und die gleichzeitige Umsetzung optimaler Betriebsbedingungen erreicht. Degradationsmechanismen zeigten Salzbildung bei niedrigeren Stromdichten und Katalysatoragglomeration bei höheren, wie durch REM/EDX-Analysen gezeigt.

Insgesamt trägt diese Dissertation dazu bei, die elektrochemische Reduktion von CO_2 zu C_{2+} Produkten unter industriellen Bedingungen voranzutreiben, indem sie Einblick in die

Bedeutung der Kontrolle von Betriebsbedingungen und die Optimierung von Zell-/Elektrodenkonstruktionen für selektivere, stabilere und effizientere Elektrolyseure bietet.

Contents

1. Introduction

The introductory chapter serves as a gateway to understanding the setting and framework wherein this dissertation is situated, as well as explains the focus areas of the dissertation and objectives it aims to address. Lastly, an outline is provided at the end of the chapter.

1.1. Research context

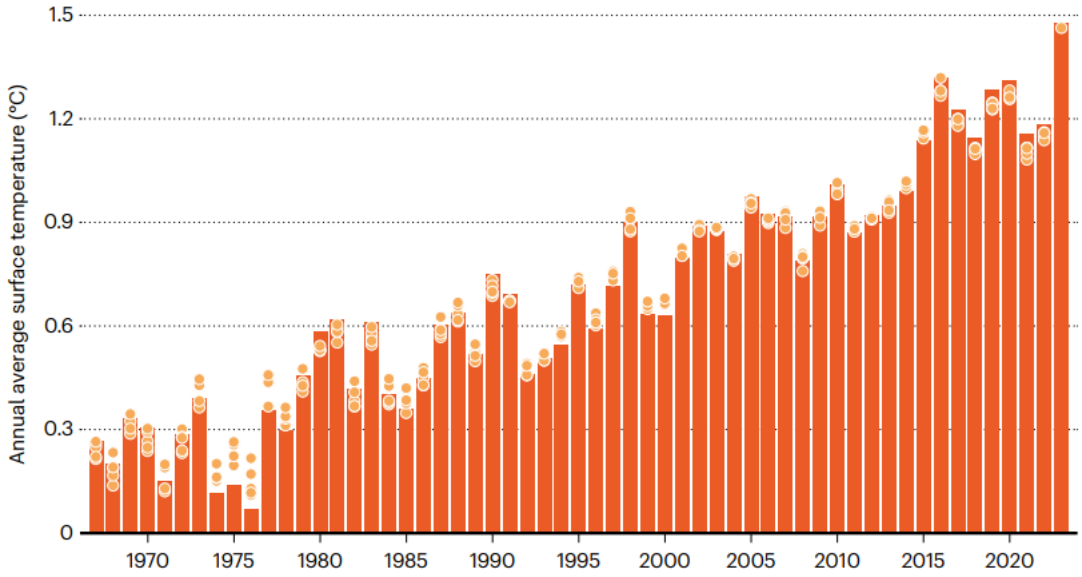

Figure 1. Annual global average surface temperature surpasses in compared to the pre-industrial period average (1850-1900). Reproduced from Witze [3] with permission from Springer Nature.

One of the most urgent and existential threat of our time is the issue of climate change due to greenhouse effects which were discovered in the second half of 1800s [1,2]. With each passing year, the growing concern on a rise in the global average temperature to well above 2ºC (compared to pre-industrial levels) becomes increasingly apparent. **Figure 1** points out that 2023 marked the hottest year ever recorded as the global average surface temperatures were reported to be 1.34 – 1.54 °C above the average global surface temperature in the pre-industrial period of 1850–1900 [3].

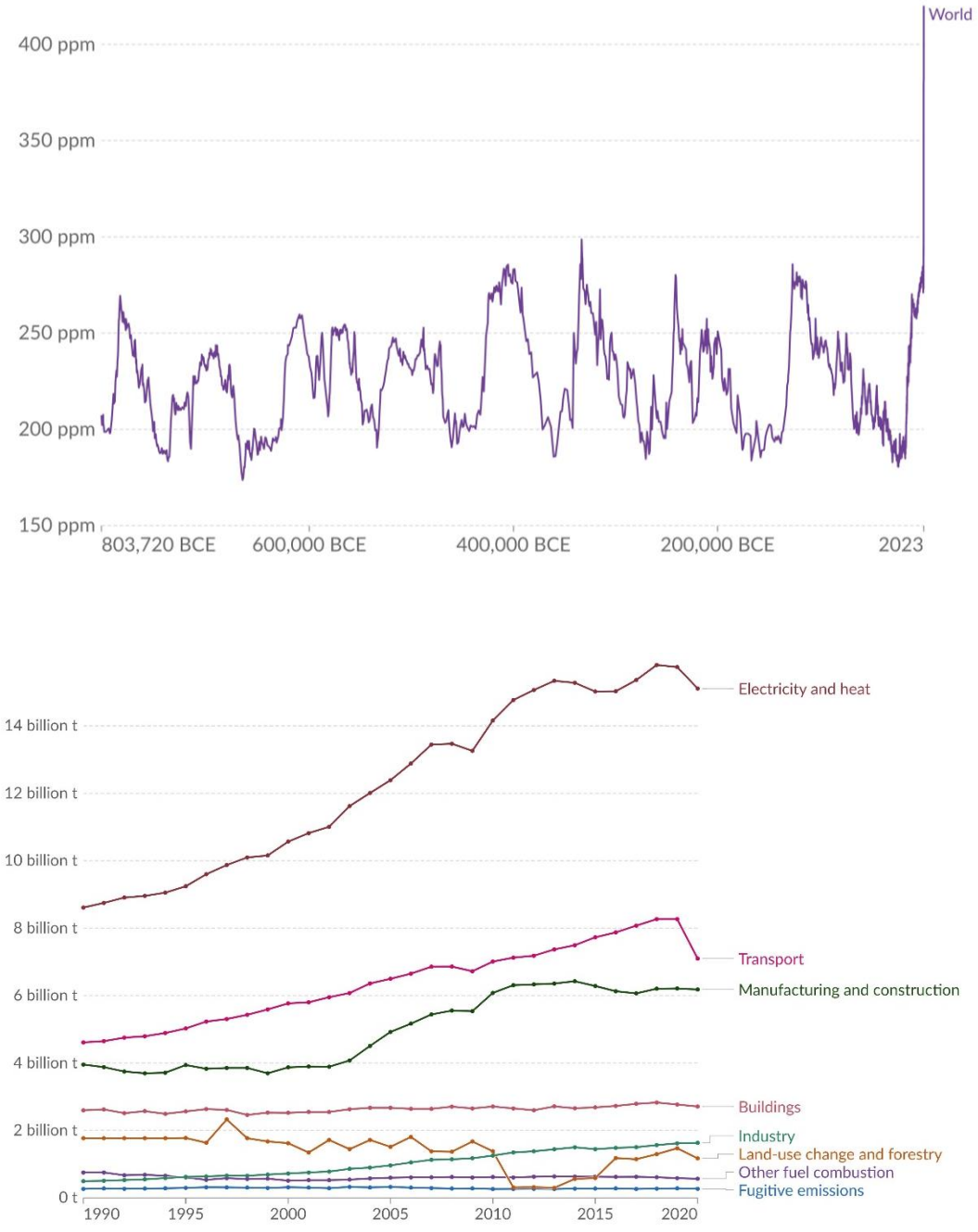

Figure 2. CO_2 concentration in the atmosphere in ppm units measured over 800,000 years until 2022. Past trends of atmospheric CO_2 concentration can be measured at high-resolution using air samples captured in ice cores **(Top image)**. Global CO_2 emissions by sectors between 1990 and 2020 measured in tonnes **(Bottom image)**. Both images were retrieved from Climate Watch (Ritchie et al.) [4].

Top image in **Figure 2** reveals a dynamic pattern of atmospheric CO_2 concentration oscillation over geological time scales. Scientific evidence, such as ice core data, suggests that

atmospheric CO_2 levels have fluctuated cyclically during this extended timeframe. Natural processes, including volcanic activity and changes in Earth's orbital parameters, have been identified as key drivers of these variations [5,6]. Notably, the graph illustrates a recent surge in CO_2 concentration, surpassing 400 ppm, a level unprecedented in the last several hundred thousand years. This rise is predominantly attributed to human activities, particularly the combustion of fossil fuels and deforestation [7]. The implications of this contemporary spike in CO_2 concentration are a subject of intense scientific scrutiny, with profound consequences for global climate and ecosystems.

An analysis of global CO_2 emissions spanning the period from last three decades reveals distinct trends among various sectors as shown in the bottom image in **Figure 2**. Notably, the sector of electricity and heat has exhibited a remarkable surge over the past three decades, culminating in an unprecedented increase that surpasses 14 billion tons of CO_2 emissions. This surge underscores the escalating demand for energy and the challenges associated with decarbonizing power generation as well as for heating and cooling in extreme weathers. Transport, occupying the second position, experienced a notable downturn in emissions during 2020, potentially attributed to the significant shifts in mobility patterns and economic activities in response to the global pandemic. The manufacturing and construction of buildings sector contributed substantially to overall emissions as well, emphasizing the need for targeted mitigation strategies linked with steel and cement production. Overall, the emission trends have been intricately dynamic and depended on many factors including economic growth, activities in each sector (e.g. declining construction activity, deployment of low-carbon vehicles, development of clean energy technologies), pandemic, political agendas, and armed conflicts [4,8].

Swiftly reducing carbon dioxide emissions may not be sufficient to prevent the adverse effects of rising temperatures. Therefore, it is crucial not only to cease CO_2 emissions but also to actively remove and address the excess carbon dioxide already present in the atmosphere [9,10].

To address these crucial objectives, scientists and engineers have focused on advancing technologies for carbon capture, utilization, and storage (CCUS). Carbon capture technologies include industrial CO_2 separation, post-combustion, pre-combustion, oxy-fuel combustion, chemical looping combustion and direct air capture, enabled by absorption, adsorption, membranes, cryogenic or biological CO_2 separation. The captured CO_2 can be utilized directly, e.g. as a feedstock for urea yield boosting or a solvent in enhanced oil recovery, or it can be converted to fuels, chemicals (olefins and polymers) or building materials (aggregates, cement and concrete). CO_2 can be stored, instead of being utilized, through storage through CO_2 enhanced oil recovery, storage in depleted oil and gas field, storage in saline formations, storage in basalt and ultramafic rock or in deep ocean [11].

While acknowledging the importance of carbon capture and storage, the focus of this thesis lies at utilizing CO_2 as a carbon feedstock, which is essential for achieving net-zero carbon emissions and transitioning to a post-fossil-fuel society. CO_2 conversion can be performed via thermochemical[12], biochemical[13], electrochemical[14], photochemical[15], and radiochemical[12,16] reactions. Among these conversion routes, the electrochemical conversion of CO_2, driven by clean energy, into high-value chemicals[17] and fuels[18,19], provides a promising avenue for carbon recycling and neutrality by storing renewable energy in chemical compounds, as illustrated in **Figure 3**.

CO_2 possesses the highest oxidization state of carbon atom, together with carbonates, having a formal oxidation state of +4. Cathodic CO_2 conversion involves the transfer of electrons to carbon, reducing its oxidation state. The set of reactions transforming CO_2 into chemically reduced products is commonly known as CO_2 reduction reactions (CO_2RR). These reactions are also frequently termed CO_2 hydrogenation for thermally driven processes involving the reaction with H_2 or CO_2 fixation in natural photosynthesis and bioinspired catalysis [20].

General form of CO_2RR can be written as the following:

$$xCO_2 + yH_2O + ze^- \rightarrow C_aH_bO_d^{-c} + eOH^- \quad (1)$$

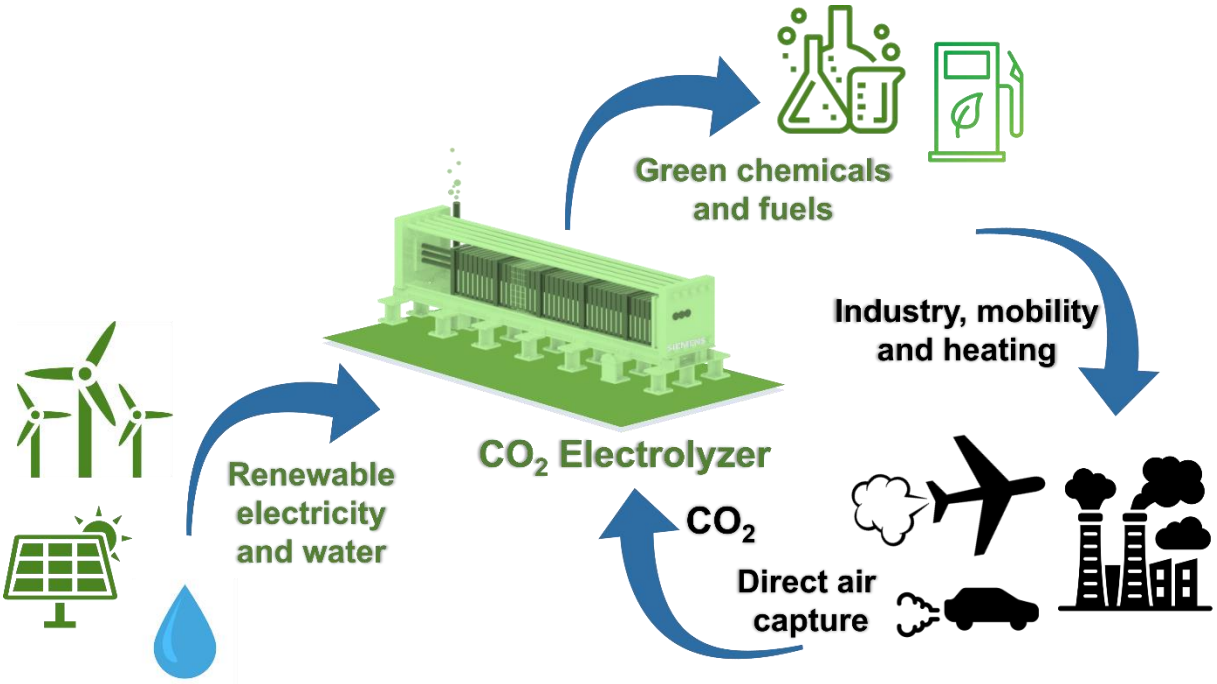

Figure 3. Schematic of the carbon-neutral cycle enabled by electrochemical CO_2 reduction.

Among the possible products, especially C_{2+} compounds such as ethylene, ethanol and *n*-propanol, are attracting particular attention due to their one-step conversion from CO_2. For instance, among the possible process chains for sustainable aviation fuel production, CO_2 electrolysis to ethylene route eliminates at least two process steps compared to alternative routes, as illustrated in **Figure 4**. The ethanol route employs starting with thermal reverse water gas shift (RWGS) reaction for syngas production and subsequent biocatalytic conversion of syngas to ethanol [21], followed by ethanol dehydration process to ethylene and subsequent olefine oligomerization and hydrogenation steps [22]. Fischer Tropsch (FT) routes require syngas input either from CO_2 to CO and H_2O to H_2 electrolyzers, or from RWGS reactor. Syngas output gas is fed then to FT unit producing long chained hydrocarbons, which is followed by hydrocracking and final hydrotreatment steps [23,24]. The methanol routes, either syngas being fed from CO_2 to CO and H_2O to H_2 electrolyzers or from RWGS reactor, include methanol synthesis, methanol-to-

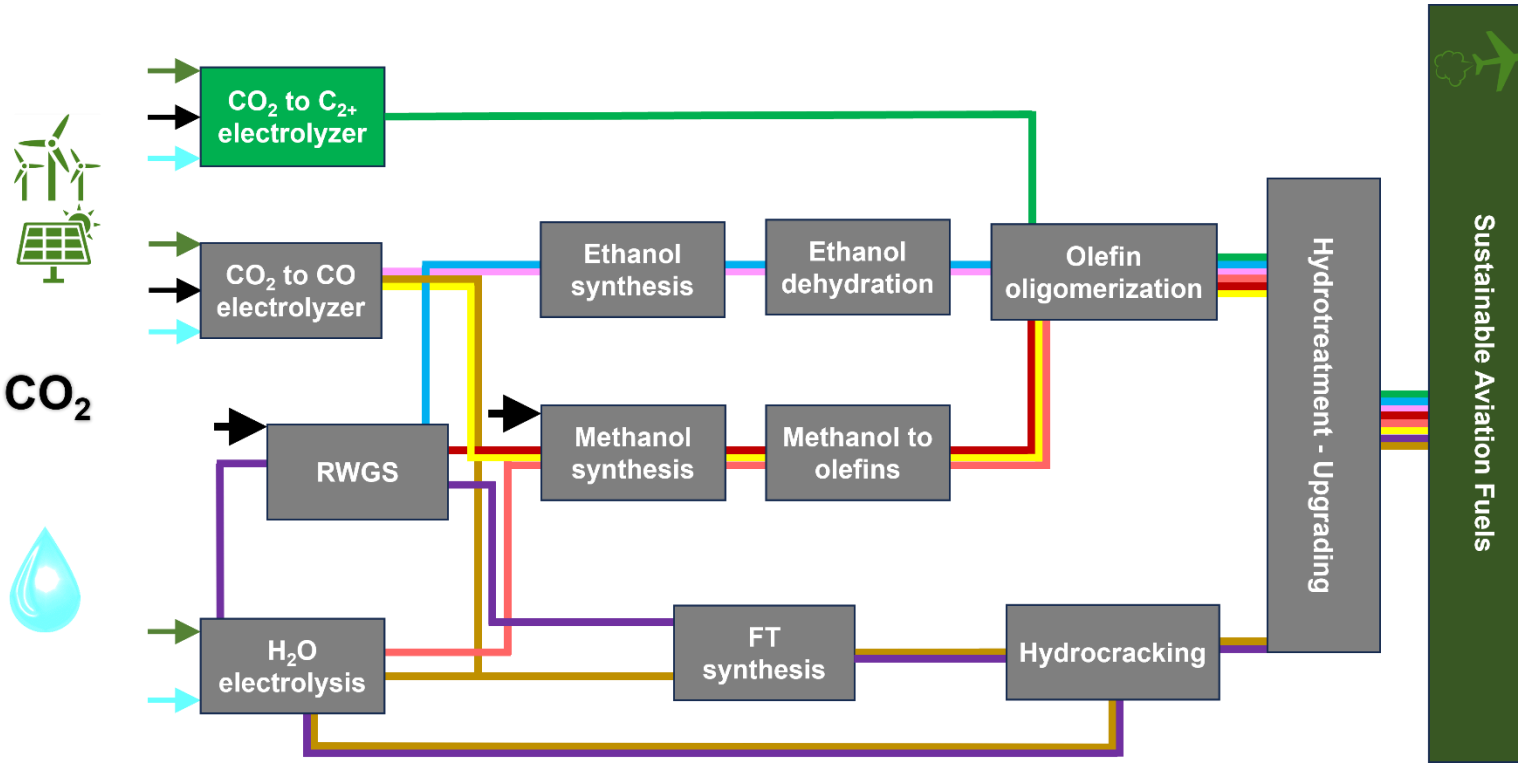

Figure 4. Most promising Power-to-Liquid pathways for sustainable aviation fuels (SAF) production, based on the literature[14–17]. The green line represents CO_2 electro conversion to ethylene route and its downstream to SAF via oligomerization. The dark yellow line represents FT route combined with CO_2 to CO and H_2O to H_2 electrolyzers, whereas the purple line represents the FT route combined with RWGS and H_2O to H_2 electrolyzer, both followed by downstream process to SAF via hydrocracking. The blue line represents the bioconversion of syngas obtained from RWGS to ethanol route, whereas the pink line represents CO_2 to CO electrolyzer as the syngas source, both with their downstream process to SAF via oligomerization. The dark red line represents methanol route combined with RWGS, whereas the light red line represents methanol route combined with H_2O to H_2 electrolyzer, and yellow line represents methanol route combined with CO_2 to CO electrolyzer; all three followed by downstream process via oligomerization.

olefins and olefin oligomerization, followed by hydrotreatment steps[24]. In recent years, there has been a focus on direct CO_2 + H_2 conversion for methanol[25] and FT[26] syntheses, moving away from traditional syngas feed approaches. While direct hydrogenation seems feasible for methanol, direct CO_2 to FT is still in early development phase[27]. In comparison to all, CO_2 to C_2H_4 electrolyzer offers an attractive short cut route with its direct olefin output followed by olefin oligomerization and hydrotreatment steps. It is nonetheless important that this one-step conversion occurs efficiently and selectively in order to be competitive to the alternative routes [28].

1.2. Scope and Outline

Striving for a carbon-neutral economy and the widespread integration of renewable electricity in the energy landscape have driven the development of innovative technologies aimed at converting electrical renewable energy into chemical energy. Siemens Energy, in line with these initiatives, initiated the development program to explore the fundamental feasibility of transforming CO_2 and renewable electricity into economically and energetically valuable products under Power-to-X field. In the context of this overarching program, this doctoral thesis focused on the experimental study of the electrochemical reduction of CO_2 to C_{2+} compounds, particularly at industrially relevant conditions.

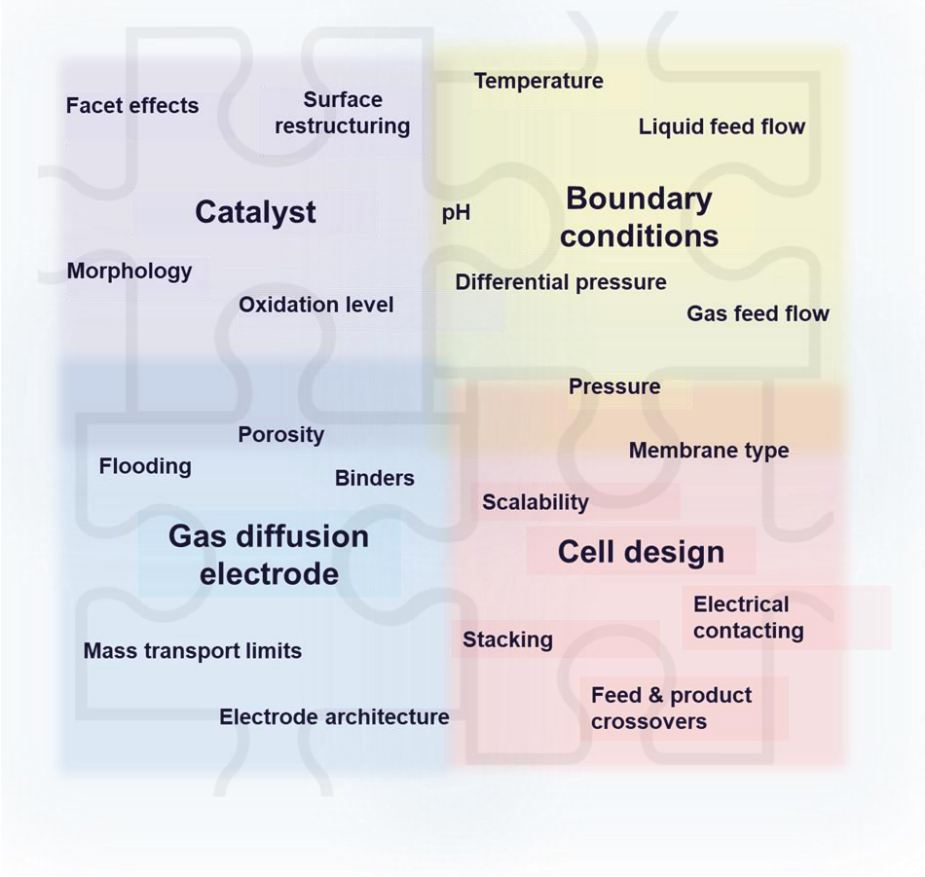

Figure 5. Key elements to achieve industrially relevant stable, selective, and efficient CO_2 to C_{2+} electrolysis.

Industrially relevant CO_2 to C_{2+} electrolysis requires a stable operation with selective conversion towards C_{2+} product(s) with high system efficiency. Conversely, CO_2 is a very stable molecule with its linear geometry and possess a low electron affinity, making it less prone to undergo spontaneous reactions. Hence, as summarized in **Figure 5**, achieving CO_2 reduction to C_{2+} compounds necessitates the synergistic integration of a highly selective catalyst, a stable gas diffusion electrode (GDE), an optimized cell design, and precisely tailored boundary conditions present during the operation. There has been great emphasis in the research community in the catalyst design in an effort to achieve the required selectivity. Nevertheless, critical research gaps persisted in understanding the operation conditions of CO_2RR, as well as the interactions between cell and electrode designs and their effects on product selectivity and stable operation. Throughout this dissertation, the same catalyst was consistently employed to exclusively

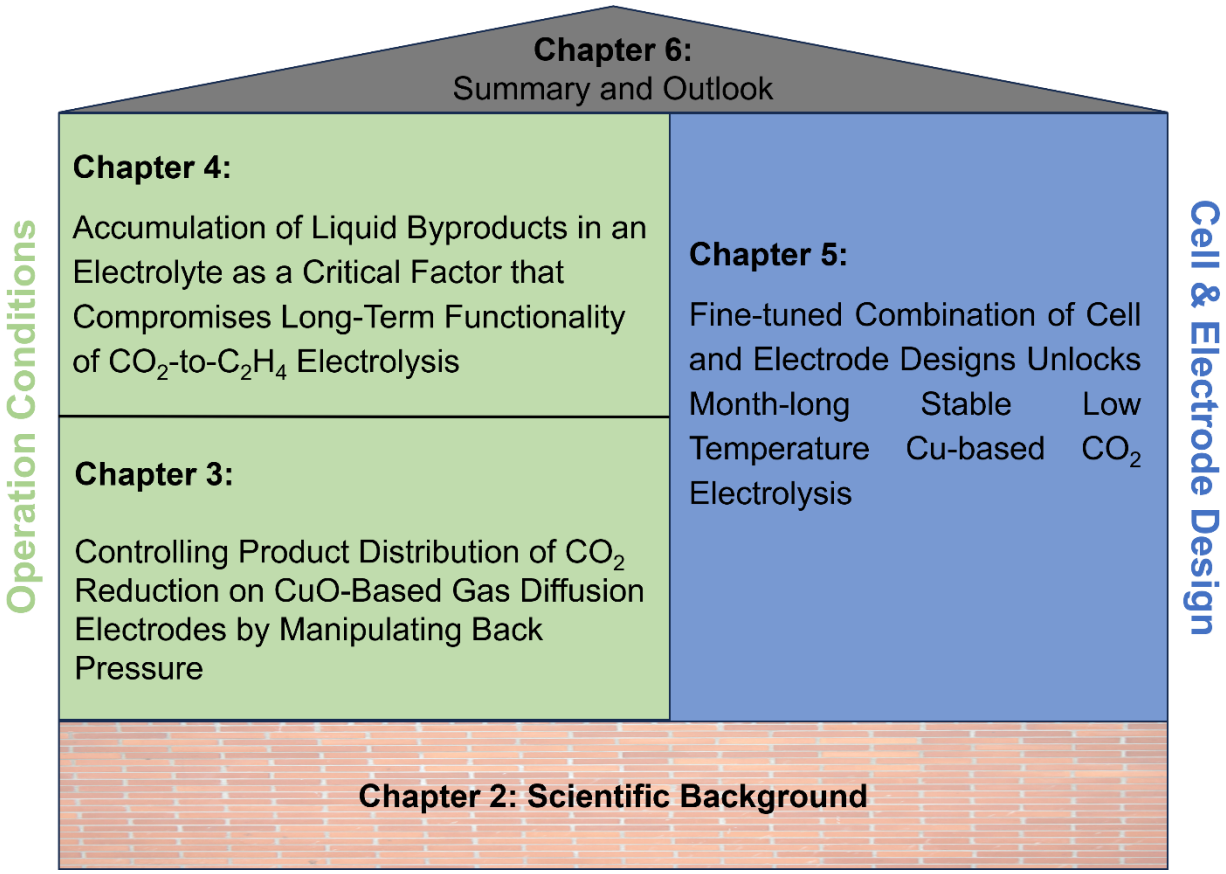

Figure 6. Schematic demonstration of the outline of the dissertation.

investigate, while purified from catalyst effects, the operation and design aspects that shaped the direction of this research.

As visualized in **Figure 6, Chapter 2** forms the cornerstone of the thesis and establishes a theoretical foundation of thermodynamics, kinetics, and reactor design for CO_2RR.

Chapters 3 - 4 delve into the operational conditions aspect, whereas **Chapter 5** covers the cell and electrode design. More specifically:

Chapter 3 explores the effects of employing back pressure on CO_2 electrolyzers. Experimental investigations on back pressure showing improved stability and controllable selectivity are presented. Additional control experiments are shown validating the corresponding hypotheses.

Chapter 4 focuses on the phenomena occurring with accumulation of liquid byproducts in the electrolyte with the effects on selectivity, stability, and cell potential. The root causes of the observed effects are identified by analytical methods and discussed.

Chapter 5, in the first part, various cell designs suitable for CO_2RR are compared based on cell potential, carbon crossover, and scalability criteria. The second part presents experimental investigations aimed at aligning electrode designs with the selected cell configurations. Leveraging insights gained from the operational conditions aspect, the study achieves long-term stability, and main degradation causes are identified through analytical methods and subsequently discussed.

Chapter 6 summarizes the key findings from the strategies employed to enhance the electrochemical reduction of CO_2, this section draws conclusions from the presented work. Furthermore, it provides an outlook by offering suggestions for further investigation, particularly building on insights from Chapters 3, 4, and 5.

2. Scientific Background

This chapter establishes the groundwork for understanding the intricacies of CO_2 electrolysis under industrially relevant conditions and provides a state-of-the-art overview for interpreting the research results to be introduced in the upcoming chapters. Commencing with an exploration of the relationship between thermodynamics and electrochemistry, the chapter delves into the fundamental principles that govern the electrochemical CO_2RR. It scrutinizes Cu metal as an electrocatalyst, elucidates the underlying mechanisms for CO_2RR products, and introduces the two main types of electrochemical cells employed typically in electrochemistry field.

2.1. Thermodynamics and Electrochemistry

In physical chemistry, thermodynamics plays a role akin to mathematics in physics. However, the connection between thermodynamics and electrochemistry is not immediately obvious. The chemical reaction taking place in both a flask and an electrochemical cell is identical. Therefore, the maximum potential work achievable under the same conditions (temperature, pressure, etc.) should also be identical. This forms the foundational basis that bridges classical thermodynamics and electrochemical thermodynamics [29].

The maximum non-volumetric work of a thermodynamical system in equilibrium at constant pressure and temperature is equivalent to the electrical work, w_E, for galvanic systems.

$$\mathrm{w_{max}} = \mathrm{w_E} = \Delta \mathrm{G^R} \qquad (2)$$

The thermodynamical equilibrium (${\Delta G_{eq}}^R = 0$) in electrochemistry is defined by the state of no current flow between the electrodes and therefore no chemical reaction occurring. The electrical work depends on the electrical potential difference between the electrodes (U) and can be calculated by its multiplication with total electric charge *Q* (Coulombs). Faraday law establishes the relationship between the total electrical charge and amount of material consumed

or produced. For a one-mole formula conversion, the Faraday law of electrolysis can be embedded into the electrical work equation under standard conditions, where z is the number of of electrons transferred in the reaction, F is the Faraday constant and E^0 is the thermodynamical equilibrium.

$$w_E = -Q \cdot U = -z \cdot F \cdot E^0 \tag{3}$$

The maximum non-volumetric work equation (Equation 2) and Faraday Law of electrolysis embedded electrical work equation (Equation 3) yields to the following equation for calculating the thermodynamical equilibrium potential:

$$\frac{\Delta G_{eq}{}^R}{z \cdot F} = -E^0 \tag{4}$$

It is noteworthy that E^0 remains constant irrespective of the stoichiometric coefficients' formulation in a cell reaction equation, as multiplying all coefficients by a factor increases $\Delta G_{eq}{}^R$ and *z* by the same factor, emphasizing that E^0 remains unchanged, while $\Delta G_{eq}{}^R$ varies with the quantity of substances. The minus sign in Equation 4 is a convention, i.e., for a spontaneous reaction, where $\Delta G_{eq}{}^R$ is negative, E^0 is positive. A reduction reaction with a more positive E^0 is thermodynamically more favorable according to the relationship.

Electrochemical cells with current flow can function as galvanic cells, where chemical reactions occur spontaneously, converting chemical energy into electrical energy. Alternatively, they can operate as electrolysis cells, where external electrical energy is transformed via otherwise non-spontaneous reactions into chemical energy. In both scenarios, a portion of the energy is converted into either positive or negative heat.[29]

In the realm of electrolysis, the applied cell potential (E_{cell}) and the thermodynamic cell potential (E^0) are fundamental parameters that play a pivotal role in governing the direction, reaction rate, and feasibility of electrochemical reactions. E_{cell} represents the actual electrical potential difference applied to the electrodes of an electrochemical cell from an external voltage source. This applied potential, which can be precisely controlled by the operator, is a critical driving force governing the electrochemical reaction within the cell. The direction of the electron flow is intrinsically linked to the polarity of the applied potential. In contrast, E^0, as explained above, is a thermodynamic parameter determined by the inherent properties of the reactants and products involved in a half-reaction at standard conditions. These standard conditions involve reactant concentrations of 1 M for solutions and 1 atm for gases. E^0 provides insights into the inherent thermodynamics of the half-reaction and offers valuable information regarding the feasibility of the process. The Nernst equation (Equation 5) serves as the bridge between E_{cell} and E^0. It quantifies how E_{cell} relates to E^0 and the activities (or concentrations) of the species involved in the electrochemical reaction. The relationship stems from the Gibbs energy dependency on the reaction components' composition combined with Equation 4, *Q* being the reaction quotient for the cell reaction [30].

$$\mathrm{E_{cell}} = \mathrm{E^0} - \frac{\mathrm{R \cdot T}}{\mathrm{z \cdot F}} \cdot \mathrm{lnQ} \tag{5}$$

2.2. Electrochemical CO_2 Reduction Reaction

Among various application areas of electrochemistry, low temperature CO_2 electrochemical reduction reaction (CO_2RR) attracts significant attention as mentioned in the previous chapter. The primary scientific challenge in CO_2RR field arise from the thermodynamic stability of CO_2 owing to its the linear molecule structure with a low electron affinity and a large energy gap (13.7 eV) between its lowest unoccupied molecular orbital and highest occupied molecular orbital. Direct CO_2 reduction reaction via single-electron transfer to form CO_2^{*-} (*

denotes an adsorption site on the catalyst surface) is energetically very demanding, making this process thermodynamically unfavourable[31]:

$$CO_2 + * + e^- \rightarrow CO_2^{*-} \qquad [E^0 = \text{-}1.9\ \text{V vs. SHE at pH}=7\ ] \quad (6)$$

2.2.1. Metal Catalysts for CO_2RR

The thermodynamic bottleneck of activating CO_2 (initiating the reduction reaction) via single-electron transfer, Equation 6, can be bypassed through a polar mechanism (e.g., nucleophilic attack of a metal center in a low oxidiation state at the carbon or oxygen atom), yet requiring a metal catalyst. In fact, proton-coupled multi-electron reactions yielding C_1, C_2 and C_3 molecules (**Table 1**) are thermodynamically more favourable than the direct CO_2 reduction reaction via single-electron transfer [32,33].

Research on electrocatalytic CO_2 reduction dates back to the second half of the 20th century. In 1985 and 1986, Yoshio Hori and colleagues conducted pioneering studies that quantified gaseous and liquid products of CO_2RR at different metal surfaces, achieving 100% of total Faradaic efficiency. These investigations categorized metal electrodes into four groups based on their primary products [34,35]:

1. Pb, Hg, Tl, In, Sn, Cd, and Bi primarily produce $HCOO^-$.
2. Au, Ag, Zn, Pd, and Ga mainly generate CO.
3. Ni, Fe, Pt, and Ti exhibit minimal CO_2 reduction, primarily reducing water to H_2.
4. Cu uniquely produces a variety of hydrocarbons, aldehydes, and alcohols, and stands out as the only metal capable of reducing CO_2 to products that require more than two electron transfers (referred to as ">2e^- products") with substantial Faradaic efficiencies.

Transition metals have free orbitals and active d-orbital electrons, which may facilitate bond creation between the metal and CO_2RR via *C or *O by injecting metal electrons into the antibonding orbital of the adsorbate [36–38]. Nature of this binding determined the product selectivity observed by Hori et al.: The product distributions can differ based on the strength of the binding between key intermediates, such as *CO, *COOH, and *CHO, to the catalytic active sites [39]. Bagger et al.[39] confirmed this grouping in their studies and visualized it (**Figure 7**) comparing CO* and H* binding strengths on different metals. Group 1 metals mainly yield HCOOH or $HCOO^-$ owing to weak adsorption of the intermediates. Group 2 metals, known for their selectivity towards CO, exhibit a weak binding of *CO (surface adsorbed CO). This weak binding enables the *CO

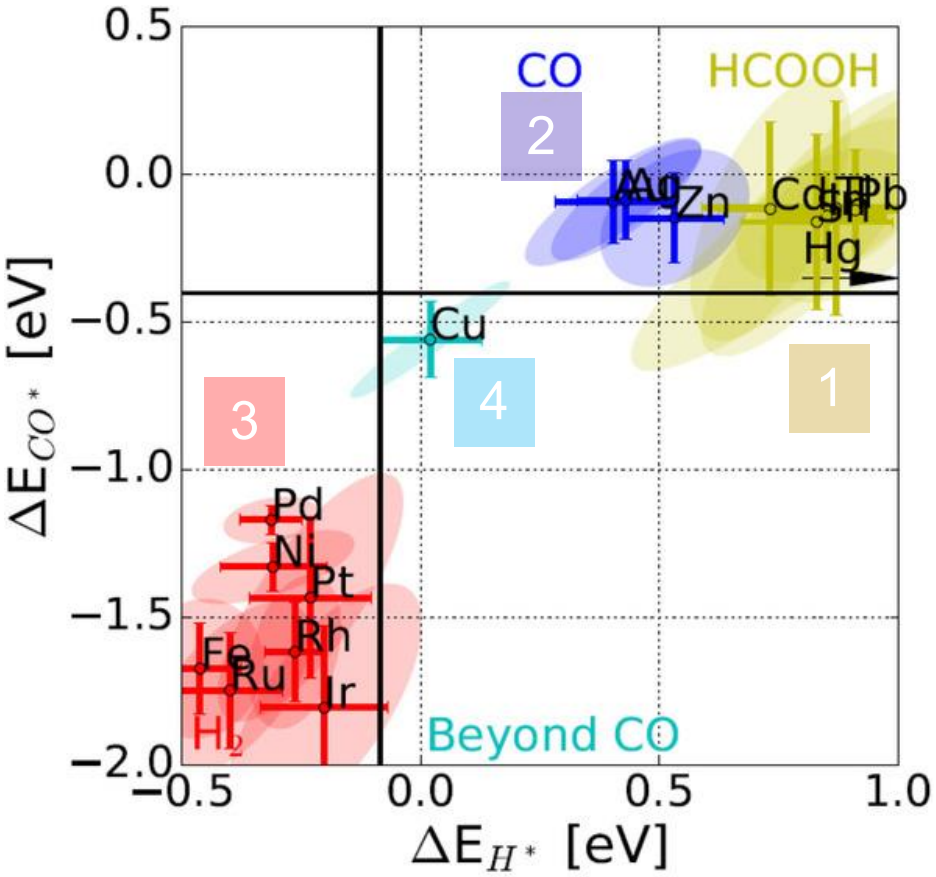

Figure 7. CO_2 reduction metal classification: The binding energies of the intermediates CO* and H* can be used to separate the Cu metal catalyst into its own group, and hence, explain the beyond CO* group. The black lines show the thermodynamics of adsorbed or none-adsorbed hydrogen (ΔG_{H^*} =0, for $H_2 + 2^* \leftrightarrow 2H^*$) or CO ($\Delta G_{CO^*}$ =0, for $CO + * \leftrightarrow CO^*$)). Reproduced with permission from Bagger et al.[1] Copyright 2023, John Wiley and Sons.

species to effortlessly desorb from the metallic surface in the form of gaseous CO. In contrast, Group 3 metals demonstrate a robust binding of *CO species, preventing their desorption (causing a poisoning effect) and suppressing the catalytic activity for CO_2RR. This, in turn, promotes the HER [40]. Being the sole transition metal of Group 4 with the ability to enable one or more C-C bonds (C_{2+} products), Cu exhibits a moderate binding when it forms a bond with *CO. This allows *CO species to undergo further reduction without CO* being desorbed (i.e., beyond CO).

2.2.2. Reaction Mechanism with Cu Electrodes

Commonly reported half-cell reactions occurring in a CO_2 electrolysis cell with Cu electrode in an aqueous electrolyte together are listed in **Table 1**. Cu is the only catalyst that can electrochemically reduce CO_2 into C_{2+} products such as ethylene, ethanol, acetate, acetaldehyde, *n*-propanol, propionate, and propionaldehyde, in addition to C_1 products such as carbon monoxide, formate, methane, and methanol, at substantial Faradaic efficiencies [41]. The multitude of potential products poses a significant challenge in comprehensively mapping the reaction pathways for each one. Nevertheless, over the past decade, the integration of density functional theory (DFT) with other computational modeling techniques, coupled with supporting experimental studies, has substantially enhanced our molecular-level understanding of the reaction mechanisms involved in CO_2 and CO reduction on copper surfaces.

Besides the CO_2RR, the competing Hydrogen Evolving Reaction (HER) is as well listed since it is inevitable in aqueous environments. The anode half-cell reaction typically involves the Oxygen Evolving Reaction (OER) given the advanced knowledge about the catalyst and electrode designs. However, Kenis et al. suggested an alternative by replacing OER with the oxidation of readily available chemicals like glycerol, a byproduct of biodiesel production, to formic acid. This substitution would allow for the formation of more valuable products than O_2 at the anode, at the same time substantially reducing the overall cell potential [42].

Table 1. Half-cell reactions for CO_2 electrolysis and their standard potentials.

Half-cell reactions	Standard potentials (V vs. SHE)
$2H_2O(l) \rightarrow O_2 + 4H^+ + 4e^-$	1.23
$CO_2(g) + H_2O(l) + 2e^- \rightarrow HCOO^-(aq) + OH^-(aq)$	-0.12
$CO_2(g) + H_2O(l) + 2e^- \rightarrow CO(g) + 2OH^-(aq)$	-0.10
$CO_2(g) + 6H_2O(l) + 8e^- \rightarrow CH_4(g) + 8OH^-(aq)$	0.17
$CO_2(g) + 5H_2O(l) + 6e^- \rightarrow CH_3OH(l) + 6OH^-(aq)$	0.03
$2CO_2(g) + 8H_2O(l) + 12e^- \rightarrow C_2H_4(g) + 12OH^-(aq)$	0.08
$2CO_2(g) + 5H_2O(l) + 8e^- \rightarrow C_2H_3O_2^-(l) + 7OH^-(aq)$	0.11
$2CO_2(g) + 9H_2O(l) + 12e^- \rightarrow C_2H_5OH(l) + 12OH^-(aq)$	0.09
$3CO_2(g) + 13H_2O(l) + 18e^- \rightarrow C_3H_7OH(l) + 18OH^-(aq)$	0.10
$2H^+ + 2e^- \rightarrow H_2(g)$	0.00

The calculated equilibrium potentials CO_2RR products closely align with HER. While theoretically suggesting similar potentials for driving both reactions, experimental measurements show significantly more negative potentials for CO_2RR after initiation. This discrepancy stems from the formation of multiple intermediates during the reaction pathway to a specific product, each with its unique activation barrier. These intermediates involve proton-electron coupled transfer steps, **Table 1** listing the necessary electron and proton numbers for each product. The need to overcome these barriers results in a higher overpotential requirement for driving CO_2 conversion compared to equilibrium potentials derived from thermodynamic data. Typically, approximately 1 V overpotential is necessary for effective CO_2RR. To minimize energy consumption, catalyst materials are crucial for reducing overpotential by lowering activation

barriers along the reaction pathways. These catalysts should not only address the energy aspect but also guide the reaction towards desired products [20].

2.2.2.1. CO_2 Activation on Cu

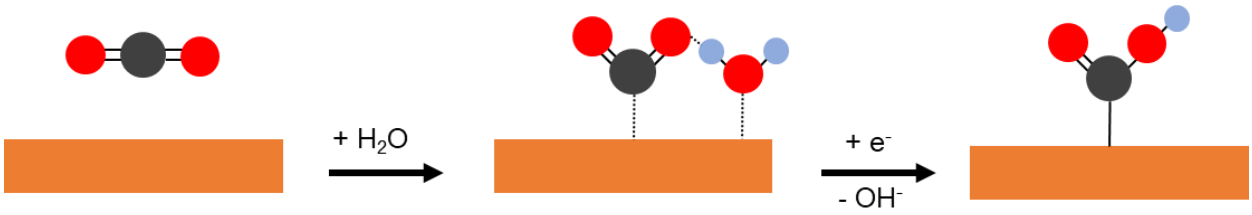

Figure 8. The mechanism for CO_2 activation on Cu electrodes through coupled proton-electron transfer (CPET), results in the formation of COOH* intermediate facilitating CO and C_{2+} product pathways. In the illustration, dark grey, red, and blue atoms signify carbon, oxygen, and hydrogen, respectively. The orange catalyst surface represents the Cu surface. The illustration is not to scale.

The initial stage in CO_2 reduction on copper, as well as other catalytically active metal surfaces for CO_2RR, involves activating the CO_2 molecule. Currently, two widely accepted mechanisms describe how this crucial initial step may occur: CO_2 bonding to Cu surface via C atom forming COOH* intermediate yielding to CO and C_{2+} products or CO_2 bonding to Cu surface via oxygen atoms forming OCHO* intermediate yielding to $HCOO^-$ product. Yet there are ongoing discussions about the exact mechanism of OCHO* intermediate formation including claims about protonation step via surface hydrogen or a carboxyl anion formation[43,44]. On the other hand, COOH* formation is discussed to follow CPET mechanism transforming the CO_2 geometry from linear to bent via hydrogen bond [45–47], as pictured in **Figure 8**. The proton donor to the surface intermediates in the CPET mechanism is most likely the water molecule. Proton donation from water molecules result in OH- generation, hence the pH adjacent to the electrode becomes higher than that of the bulk solution [48,49].

The external negative electric field is a must for the shift from physisorption to chemisorption of CO_2 on Cu surfaces. The application of the electric field results in increased adsorption energies, partial charges, and C−O bond elongations in CO_2. Rougher surfaces show enhanced responsiveness to the electric field, attributed to locally stronger fields and less-

coordinated surface atoms compared to flat surfaces. Controlling surface roughness and electric field strength can be effective parameters to optimize the CO_2 activation process on Cu surfaces [47].

Alkali cations in the electrical double layer are supposed to play a vital role in the activation of CO_2 on Cu surfaces. CO_2 bond angle decreases from 180° to 140° in the presence of a neighboring cation. Furthermore, the interfacial electric field substantially strengthens the adsorption of *COOH and coordination of partially dehydrated cations to negatively charged CO_2RR intermediates may also contribute to the surface species stabilization [50,51].

The formation of wide range of C_1, C_2 and C_3 products from the activated CO_2 molecules can be explained by the hypothesis that specific surface sites have the potential to catalyze the synthesis of various C_1 surface species, which become thermodynamically attainable at elevated overpotentials. These diverse C_1 species can interconnect to produce all the observed products. The broad spectrum of C_{2+} products observed could be elucidated if the C–C coupling step among the numerous conceivable C_1 intermediates is kinetically feasible [20]. Extensive research efforts have been dedicated to unraveling the reaction mechanisms leading to each specific product, as will be detailed below. It is crucial to highlight that the selectivity among end-products arises from a highly intricate multidimensional matrix. This matrix encompasses various factors, including, but perhaps not limited to, crystal structure, oxidation state, morphology, electrode potential, local pH and electrolyte composition.

2.2.2.2. Formation of C_1 Products

C_1 products primarily undergo two pathways, resulting in formate and carbon monoxide which is the main intermediate for the rest of the CO_2RR products. Early mechanistic studies proposed that the pathway leading to formic acid is distinct. The bonding of the first surface intermediate to the catalyst was identified as a crucial factor distinguishing between the $HCOO^-$

and CO pathways [48]. Based on the electronic configuration of the catalyst's surface, two distinct initial binding modes of the first intermediate can be identified. As depicted in **Figure 9**, the carboxyl (*COOH) intermediate yields to CO* when the bond to the catalyst's surface occurs through the carbon atom, while the formate (*OCHO) undergoes CPET to form formic acid when the bond to the catalyst's surface is established via oxygen atoms [52,53]. CO* is either desorbed to form CO product (2 e^-) or undergoes further CPETs to form CH_4 (8 e^-). Although the formation of formic acid has been demonstrated to be an electrochemical endpoint, representing a compound that cannot undergo further reduction, the generation of CO is considered a significant intermediate in CO_2 reduction reactions and a pivotal branching point.

According to Hori et al.[48], Akhade et al.[54], Dewulf et al.[55], and Rahaman et al.[56]; CH_4 pathway might involve an irreversible chemisorption of *C surface species leading to deactivation

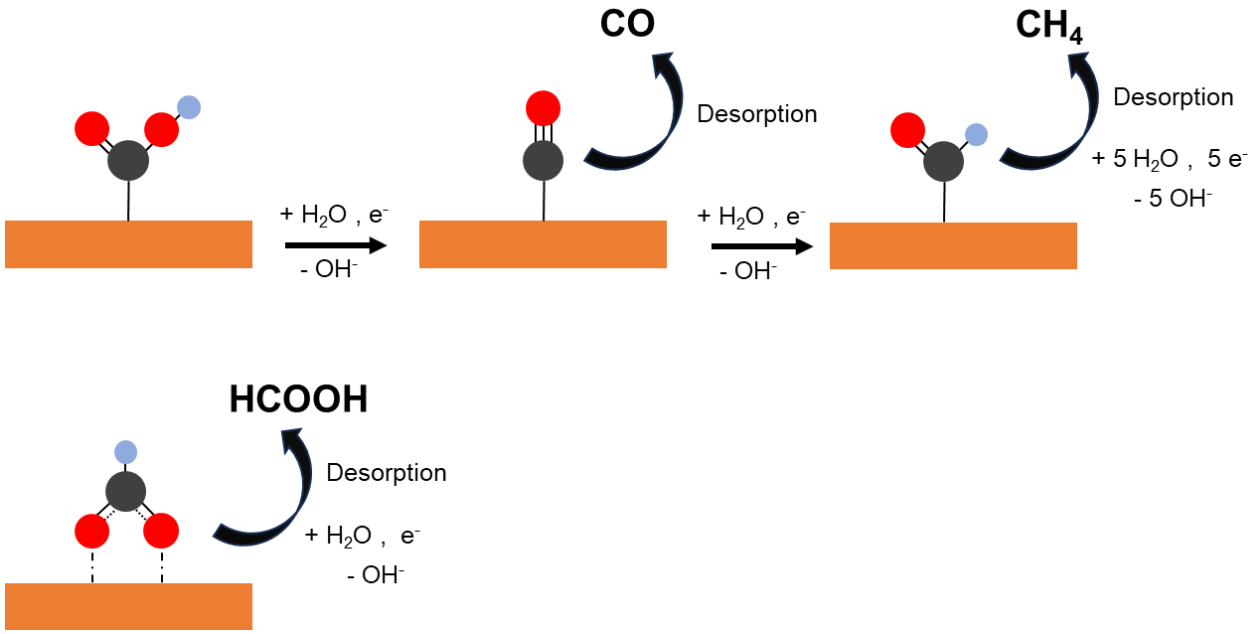

Figure 9. Formation mechanisms of C_1 products on Cu electrodes: COOH* intermediate is reduced via CPETs to CO or CH_4 requiring in total of 2 or 8 e^- to be formed from CO_2 reactant. OCHO* intermediate is reduced to formic acid via CPET presenting the separate pathway for formic acid formation from CO_2 reactant with 2 e^-. In the illustration, dark grey, red, and blue atoms signify carbon, oxygen, and hydrogen, respectively. The orange catalyst surface represents the Cu surface. The illustration is not to scale.

of the catalyst formed after CHO* intermediate. On the other hand, there are other groups describing CH_4 formation via COH* surface species and subsequent methoxy formation without including C* surface species in the proposed mechanisms [57,58], as illustrated in **Figure 9**. Methanol, rarely reported minor product, possibly follows a similar pathway to methane [59].

2.2.2.3. Formation of C_{2+} Products

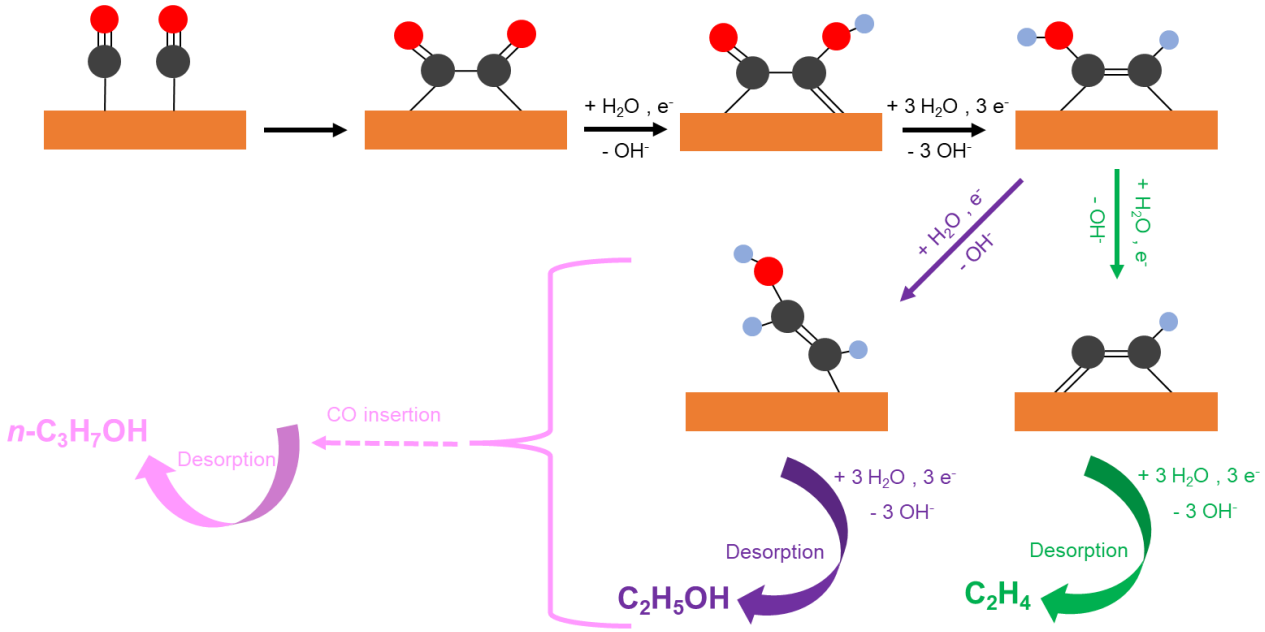

Figure 10. Formation mechanisms of main C_{2+} on Cu electrodes: *CO are dimerized without involvement of protons. *COCO is reduced to *COCOH and further to *CHCOH via subsequent PCETs. *CHCOH either leads to ethylene pathway through deoxidation of a hydroxyl or to oxygenate pathway through hydrogenation via PCETs. Oxygenate pathway includes ethanol formation. *N*-propanol formation occurs via a CO insertion mechanism to an uncertain intermediate in the oxygenate pathway. Ethylene and ethanol require in total of 12 e^- for their formation from CO_2, whereas *n*-propanol in total of 18 e-.

CO* adsorbed species is widely considered as the key intermediate for C_{2+} products, supported by investigations on the reduction of CO_2, CO as well as in situ measurements [55,60–68]. The formation of the C-C bond represents a critical reaction step that distinguishes the pathways for single and multicarbon products. The dimerization of two *CO species is widely recognized as

a pivotal step in the formation of C-C bonds, leading to the creation of bidentate *COCO intermediate species [41,61,66,69–71] .

Beyond *CO, a significant distinction between the C_1 and C_{2+} pathways lies in their sensitivity to pH. Ethylene formation is pH-independent on the SHE scale, contrasting with the pH-dependent nature of methane formation on the SHE scale [60,63]. This leads to the experimental observation of a lower onset potential (vs RHE) for C_{2+} products with increased pH. Consequently, the limiting step in C_1 formation is believed to involve CO protonation through a *COH or *CHO intermediate [58,63,72,73]. In contrast, the limiting step in C_{2+} formation is generally considered to be CO dimerization, without involvement of protonation [59,70,74,75]. CO dimerization is widely claimed to be a non-electrochemical step, supported by a combination of energy computations, controlled measurements, and in situ spectroscopy studies [58,76–79].

Following the initial C-C bond formation, the subsequent crucial step for ethylene and ethanol involves the hydrogenation of the initial C-C intermediate (*OCCO). This hydrogenation step can occur through the generation of *COCOH intermediate [66,74,80–82]. *COCOH may be further reduced to *CHCOH which is a critical intermediate determining the selectivity between ethylene and oxygenates[66,74,81], as shown in **Figure 10**. In this proposed mechanism, oxygenate and ethylene pathways differ, where hydrogenation of *CHCOH leads to the former and deoxidation of a hydroxyl group in *CHCOH to the latter. Some other research groups suggested instead that the critical intermediate for ethylene / oxygenate selectivity is $*CH_2CHO$, a surface species bound to Cu via O atom [80,82] . Acetaldehyde is proposed as an intermediate species in the mechanism for ethanol formation [60,83–85]. However, the formation mechanism of another C_{2+} product, acetate, remains another subject of discussion in the literature. One possibility may be via homogeneous chemical reactions in the alkaline conditions, such as Cannizzaro-type disproportionation: Acetate is likely formed from attack of OH^- on a surface-bound ketene or other carbonyl-containing intermediate after C–C bond formation has occurred [60,86,87].

N-propanol formation mechanism reportedly involves a selective C-C coupling of $*C_1$ and $*C_2$ intermediates, leading to the initial formation of propionaldehyde. This is followed by a rapid hydrogenation process, resulting in the production of *n*-propanol [56,63,85,88]. Chang et al. [89] determined a methyl carbonyl surface species as the most likely intermediate where a distinction between C_2 oxygenate and C_3 oxygenate occurs via a *CO insertion. Nevertheless, CO* insertion to a C_2* surface species was suggested also for other species than methyl carbonyl [20,90], which marks another disagreement in the literature about C_{2+} reaction mechanism.

Apart from the above discussed reaction pathways, numerous alternative reaction pathways have been proposed for multicarbon formation. These pathways mostly diverge from each other after the hydrogenation of the initial C-C intermediate. A comprehensive discussion of all proposed mechanisms for C_{2+} product formation exceeds the scope of this chapter.

2.3. CO_2RR Reactors: Electrochemical cells

Reactors for CO_2RR, named as electrochemical cells in electrochemistry field, serve as the core of the process, providing controlled environments for the conversion of carbon dioxide into valuable products. Among the diverse array of cell designs, H-cells and flow cells stand out for their distinctive characteristics.

H-cells typically operate with an aqueous-fed configuration, where reactant gases such as CO_2 are transported to the catalyst layer through CO_2 dissolution in the liquid electrolyte. CO_2 saturation of the liquid electrolyte via CO_2 gas supply ensures the reactant availability in cathode vicinity. Its H-like form with the anode and cathode compartments filled with liquid electrolyte also gave the name to the cell. The catalysts are typically deposited on glassy carbon or carbon paper. H-cells, despite being widely used for catalyst design studies, suffer from CO_2 mass transport limitations due to low CO_2 solubility and rapid carbonation with alkaline electrolytes, restricting their feasibility for industrial-scale CO_2RR processes [91,92].

Flow cells can operate with an aqueous-fed or a gas-fed configuration, where reactant gases are introduced to the catalyst layer through a gas diffusion layer (GDL). Such electrodes

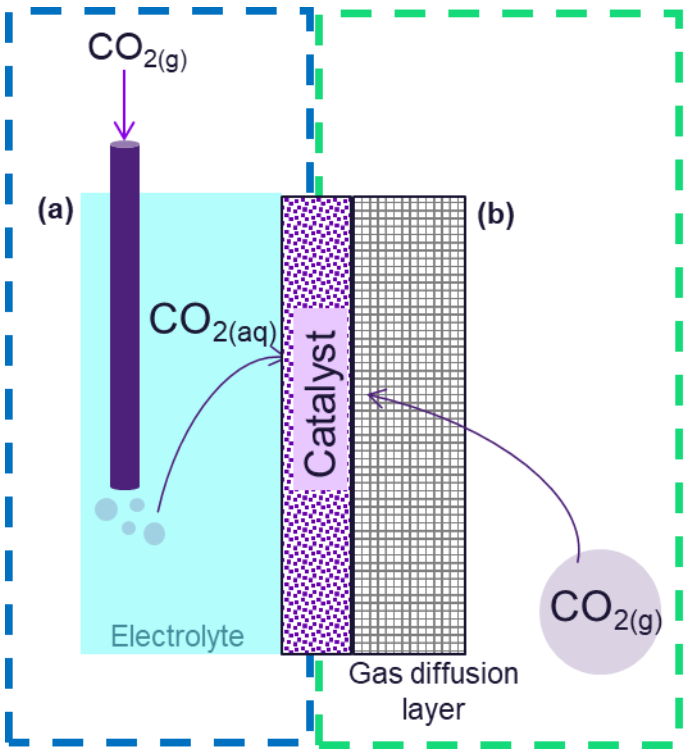

Figure 11. Illustration of CO_2 supply in a) aqueous-fed systems such as H-cells, b) gas-fed systems such as flow cells with gas diffusion electrodes.

consisting of gas diffusion layers are called gas diffusion electrodes - GDE. **Figure 11** illustrates aqueous-fed (marked with blue dashes) and gas-fed (marked with green dashes) CO_2 supply.

The utilization of GDEs in CO_2RR has addressed limitations associated with the low solubility of CO_2 in aqueous electrolyte solutions. Early studies in the late 1980s introduced a breakthrough by feeding CO_2 as a gas stream into GDEs, overcoming diffusion limitations encountered when CO_2 is dissolved in water. Gas-fed cells demonstrated a significant increase in partial current density compared to aqueous-fed electrolysers, making them a promising solution for achieving higher current densities and sparking industrial interest. Gas-fed cells employing GDLs offer distinct advantages over traditional H-cells, providing a larger

electrochemical surface area, enhanced CO_2 access, and shorter diffusion pathways. With porous structures facilitating the formation of a three-phase system of CO_2, electrolyte, and catalyst, GDLs prove superior for efficient and stable CO_2 reduction. Particularly in studies focusing on catalyst design, H-type cells are prevalent but face limitations in mass-transport and solubility. Their low solubility restricts them from operating with alkaline electrolytes, known to enhance CO_2RR activity. As a result, alternative setups, such as flow cells or gas-phase electrolysers, are recommended for testing and optimizing catalysts under industry relevant conditions, including current densities exceeding 200 mA/cm^2, stability tests of at least 24 hours, and continuous supply and cycling of gas and electrolyte streams [91–94]. Taking everything into account, H-cells offer a static approach, allowing precise investigation of electrochemical reactions, while flow cells, with their dynamic nature, facilitate continuous operation, addressing scalability and real-world applicability.

Figure 12 shows a representative illustration of a flow cell for CO_2RR. It characteristically consists of a gas supply chamber, cathode gas diffusion electrode, catholyte, separator, anolyte and anode electrode. There are various cell designs where the electrolyte chambers are omitted,

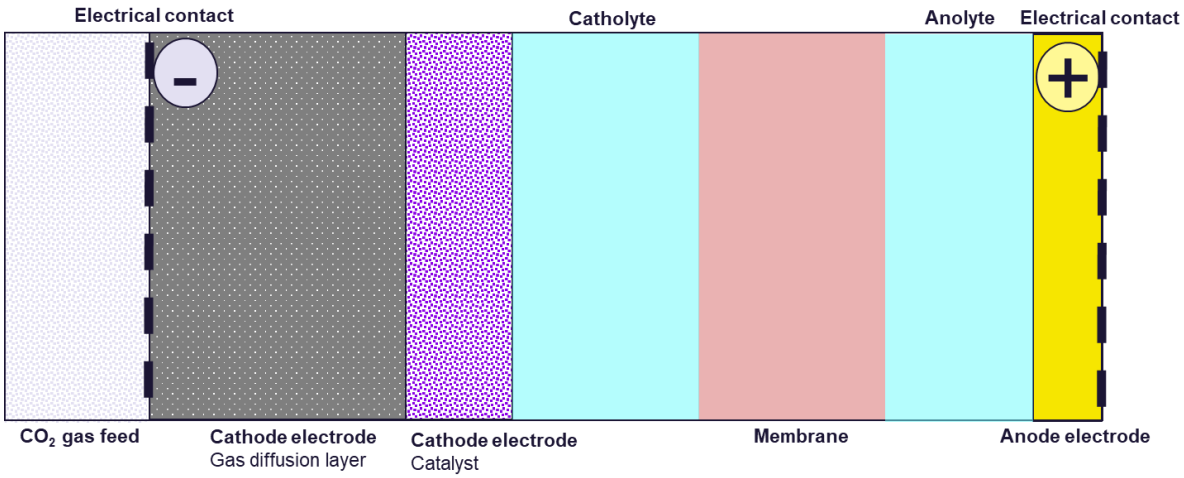

Figure 12. Representative illustration of a flow cell for CO_2 electro conversion at low temperatures. The cell consists of gas supply chamber, cathode gas diffusion electrode with gas diffusion layer and catalyst, catholyte, membrane or another separator, anolyte, anode electrode and electrical contacting points in the cathode and anode.

or different separator types are used, or a different electrical contacting method is employed. Various cell and electrode designs are discussed in detail in **Chapter 5.**

3. Controlling Product Distribution of CO_2 Reduction on CuO-Based Gas Diffusion Electrodes by Manipulating Back Pressure

In the past decade, there has been a growing focus in electrochemistry research on understanding the electrochemical reduction of CO_2 on Cu electrodes. Investigations have delved into various aspects such as reaction mechanisms, kinetics, catalyst and electrode design, electrolyte-catalyst interactions, and membrane-catalyst interactions. However, the effects of operational parameters, such as back pressure, have received less attention, despite their crucial role in scaling up CO_2 electrolyzers for industrial use. This research gap is addressed in this chapter.

The initial concept of manipulating back pressure aimed to counteract electrode degradation caused by the flooding phenomenon. As discussed extensively in the dissertation, flooding disrupts gas-liquid-solid interfaces by filling the pores with liquids, creating only liquid-solid interfaces. In such conditions, the competing reaction, HER, dominates as the main cathode reaction since the copper catalyst reduces the only available reducible species, H^+, in the absence of CO_2. Manipulating back pressure, defined as the pressure difference between the gas and liquid sides of the gas diffusion electrode, was envisioned to maintain gas-liquid-solid interfaces and prevent liquid effusion from the liquid side to the gas side, thus avoiding pore blockage.

Surprisingly, the manipulation of back pressures yielded an unexpected benefit: control over product selectivity. By increasing the availability of CO_2 at the electrode surface through back pressure, a specific group of CO_2 electroreduction products, namely oxygenates, were obtained in significantly higher quantities. This was attributed to the dependency of preferred reaction mechanisms on the surface coverage of intermediate species. Notably, longer stable formation of C_2H_4 was achieved by employing back pressures. However, control experiments with back

pressures using a diluted CO_2/N_2 gas mixture revealed that the extended stability resulted from higher CO_2 surface coverage due to elevated CO_2 partial pressures, rather than the prevention of liquid effusion as initially intended.

The findings from the back pressure study not only offered insights into the impact of back pressure on selectivity and stability but also paved the way for the practical implementation of this approach in industrial CO_2 electrolyzers.

This chapter is based on the following publication [95]:

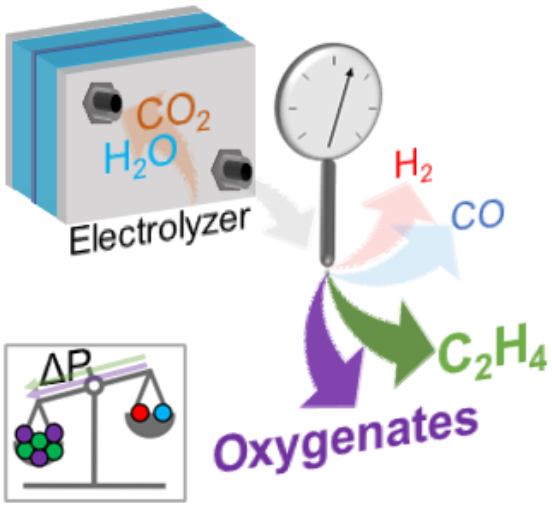

Sahin, B., Leung, J.J., Magori, E., Laumen, S., Tawil, A., Simon, E. and Hinrichsen, O. (2022), Controlling Product Distribution of CO_2 Reduction on CuO-Based Gas Diffusion Electrodes by Manipulating Back Pressure. Energy Technol., 10: 2200972. https://doi.org/10.1002/ente.202200972.

The contributions of the authors are summarized as follows:

- Baran Sahin: Conceptualization, methodology, experimental investigation, validation, data evaluation, manuscript preparation and visualization.

- Jane J. Leung: Experimental investigation, validation, data evaluation and manuscript editing.
- Erhard Magori: Conceptualization and methodology.
- Steffen Laumen: Data evaluation and manuscript editing.
- Angelika Tawil: Methodology and experimental investigation.
- Elfriede Simon: Supervision, project administration, funding acquisition and manuscript editing.
- Olaf Hinrichsen: Supervision and manuscript editing.

3.1. Abstract

The electrochemical reduction reaction of CO_2 (CO_2RR) is a promising avenue toward the renewable energy-driven transformation of a greenhouse gas toward fuels and value-added chemicals. While copper uniquely can catalyze this reaction to longer carbon chains, Cu-based electrodes continue to face numerous challenges, including low selectivity toward desired products and poor stability. To unlock its potential for large-scale industrial implementation, great interest is shown in tackling these challenges, primarily focusing on catalyst and electrode modifications and thereby leaving a research gap in the effects of operation conditions. Herein, back pressure application is introduced in CO_2 electrolyzers at industrially relevant current densities (200 mA cm^{-2}) in order to steer selectivity toward C_{2+} products. The back pressure adjusts CO_2 availability at the electrode surface, with a high CO_2 surface coverage achieved at ΔP = 130 mbar suppressing the competing hydrogen evolving reaction for 72 h and doubling of stable ethylene production duration. Faradaic efficiency of 60% for C_{2+} products and overall C_{2+} conversion efficiency of 19.8% are achieved with the easily implementable back pressure operation mode presented in this study. It is proven to be a promising tool for product selectivity control in future upscaled Cu-based CO_2 electrolysis cells.

3.2. Introduction

The products of CO_2RR, such as C_{2+} hydrocarbons and alcohols, attract significant global demand. Hori et al.[35] discovered in 1985 that Cu is the only metal that can electrochemically reduce and CO into significant amounts of hydrocarbons, and since then researchers working in the field of CO_2 electrochemical reduction have to this day continued to focus their efforts on Cu due to its unique ability to convert CO_2 into molecules that require more than two reduction electrons per CO_2 molecule (>2e^- products)[41,48,60,61,96]. This special capability of Cu stems from its

optimal binding energy for CO_2RR and hydrogen evolving reaction (HER) intermediates: a negative adsorption energy for CO*, indicating thermodynamically favorable interaction between components, and a positive adsorption energy for H*, indicating the opposite[20,39,61].

Despite these characteristics, electrochemical CO_2RR on Cu-based electrodes continues to face numerous challenges to its scalability, including product selectivity and stability[41,62,97]. Industrially relevant stable operation times (>10 000 h) and high selectivity toward specific value-added products (e.g., ethanol, propanol, or ethylene) at lower potentials are essential for future industrial applications but remain to be achieved. The parasitic HER constitutes one of the main issues, as it over time diverts selectivity toward undesired H_2, eroding away at stable CO_2RR operation. Scientists work on different aspects of the CO_2RR system to overcome these problems: modification of the catalyst structure (morphology[98–100], oxidation state[87,94,101], facets[69,97,102], grain boundaries[87]), application of multiatom catalysts (bimetallic systems[96], tandem catalysts[62,103,104], or dopants[105,106] as well as design of electrode structure[107–110] .

Engineering of the electrode structure is a broader aspect that answers to multitudinous facets of the CO_2RR challenges. In typical aqueous-fed CO_2 electrolyzers (liquid-phase reactors), electrodes suffer from CO_2 mass transport limitations, as CO availability is limited by its solubility in the electrolyte. In gas-fed CO_2 electrolyzers with gas diffusion (GDEs), the CO_2 solubility problem is eliminated as CO transported by gas diffusion to the three-phase boundary where electrolyte, catalyst, and CO_2 coexist. Yet, in cathodes of the GDE type, feed diffusion to the catalyst layer remains the mass transport limiting step. In addition to mass transport, electron and ion transport phenomena are also governed by GDEs. Various parameters can be manipulated to fabricate the optimum GDE, including porosity of diffusion layer, hydrophobicity, thickness of electrode and of catalyst layer, catalyst–diffusion layer interactions, ionomer or binder properties, catalyst– ionomer interactions etc [20,107,109].

The mechanism of CO_2RR on Cu is a highly debated topic in the literature with various postulated mechanisms for each product[41,48,62,63,70,76]. The product spectrum includes C_1–C_3 hydrocarbons and oxygenates: carbon monoxide ($2e^-$), formate ($2e^-$), methanol ($6e^-$), methane ($8e^-$), acetate ($8e^-$), acetaldehyde ($10e^-$), ethylene ($12e^-$), ethanol ($12e^-$), propionaldehyde ($16e^-$), allyl alcohol ($16e^-$), and *n*-propanol ($18e^-$)[41].

Formate and carbon monoxide, C_1 products requiring only $2e^-$ electrons for reduction, are typically the first products to be observed at lower (more positive) overpotentials, signaling that their formation demands the lowest kinetic barriers for their formation[20]. Adsorbed CO species have been identified in numerous studies as the key intermediate in the reduction of CO_2 to $>2e^-$ products[55,60–68]. Formate is the only product that does not involve a CO* species as intermediate[20,62]. Selectivity between the CO or $HCOO^-$ pathways is determined by the Cu-C and Cu-O bond strengths. Intermediate species, which are bound either by C or O atom(s) to the catalyst surface, lead to CO and $HCOO^-$ formation, respectively[20]. The other common C_1 product, methane, is formed from CO* with a series of electron–proton transfers, requiring $8e^-$ for its reduction from CO_2[20,41,111].

C_{2+} product mechanisms must include C–C coupling step(s), necessitating two adjacent C-containing adsorbates. Ethylene is formed via dimerization of two CO adsorbed species and its further reduction to the alkene form[41,61,66,69–71]. Ethanol and ethylene pathways differentiate from one another, where hydrogenation of *CHCOH leads to the former and deoxidation of a hydroxyl group in *CHCOH to the latter[66,81]. Acetaldehyde is suggested as an intermediate species in the ethanol formation mechanism[60,63,83–85]. Another C_{2+} product, acetate's formation mechanism, is not yet agreed upon in the literature. There are studies claiming that homogeneous chemical reactions in alkaline electrolytes resulting from OH^- attack on a surface-bound ketene or other carbonyl-containing intermediate (Cannizzaro-type disproportionation) after C–C coupling leads to acetate formation[86,87]. C_3 alcohol is possibly formed with a selective C–C coupling of $*C_1$ and

*C_2 intermediates that result in propionaldehyde formation and it is followed by rapid hydrogenation to C_3 alcohol[56,63,85,88].

The presence of various possible surface species and their coverage as defined by the applied potential makes C–C coupling a potential-dependent phenomenon[41]. Higher cathodic potentials are required to permit C–C coupling reactions[56,67,112]. In concordance with this requirement, it is proposed that C_2 pathways necessitate a lowered activation energy of CO–CO dimerization[66], which is the rate-determining step for C_2 pathways according to the literature[59,70,74,75]. The rate of C_{2+} formation is therefore determined by the rate of conversion of adsorbed CO* species to the C_{2+} product, assuming sufficient coverage of the key intermediate CO*[71]. The selectivity toward oxygenated products is higher at more positive onset potentials due to the weaker driving force for polarizing C–O-containing intermediates. As a result, the C-O bond remains, and it leads to oxygenate products[60].

Among Cu-based CO_2RR catalysts, oxide-derived Cu draws special attention owing to its better selectivity, stability and energy efficiency. Oxide-derived Cu compared to metallic Cu possesses more porous surfaces[20] with undercoordinated sites formed by special grain boundary terminations[20,56,103,113], enabling high selectivity towards oxygenates at relatively low overpotentials[60,84,87,103,114–116]. In-situ reduction of Cu oxides in the cathode under electrolysis conditions alter the crystal morphology, which has been shown to change the catalyst's selectivity and stability[60,94,99,111].

Cu-based electrodes' activity towards CO_2RR notoriously decay over time, posing the greatest obstacle for its commercialization. There are various hypotheses about the origin of this. Hori et al.[117] suggested deposition of metallic impurities as the cause of catalyst poisoning, whereas more recent studies claim impurity poisoning occurs only with very small electrode sizes[20,111] or result from C* surface species that can be formed as a reaction intermediate in the C_1 pathway[54–56,64,72,118–120]. CO_2RR instability is also attributed to surface reconstruction by both

sintering and declustering happening at different time periods of the electrolysis[121]. In addition to catalyst-related phenomena, limitation of CO_2 availability (e.g., by electrode flooding) on the electrode surface can compromise CO_2RR stability. Several studies suggest that flooding of GDEs is the key way in which electrolytes create CO_2-depleted zones, leading to the dominance of HER[122–124].

Among other operational parameters, pressure has a unique role in CO_2RR as it has a three-fold effect: capillary effects on the electrode flooding, mechanical effects providing better contact between electrolysis cell components, and increase in CO_2 concentration in the gas phase and therefore the CO_2^* surface coverage on the catalyst. By means other than manipulating pressure, researchers have controlled CO_x^* coverage on the electrode surface by manipulating CO_2 or CO feed concentration. Lie et al.[74] diluted the CO feed and Tan et al.[125] the CO_2 feed with N_2 to study their coverage effects. Applying an impulse current is another technique to control local CO_2 concentration by enabling transient conditions of high local CO_2 concentration[126,127] .

In this work, we have employed a different approach, by varying the back pressure of the gas side in the electrolyzer to manipulate CO_2^* coverage on the electrode surface and minimize flooding effects. We show that back pressure as an operation parameter in CO_2RR can be manipulated to control product selectivity and improve stability of the electrodes. With applied back pressure of 0–130 mbar between the gas side of the electrochemical cell and catholyte chamber, we demonstrate that the Faradaic efficiency (FE) for desired C_{2+} products is improved up to 60% at 200 mA/cm^2 and that stable operation of CO_2RR is maintained for more than 72 h, during which HER is successfully suppressed to below 25% FE (at 130 mbar). C_{2+} conversion efficiency for CO_2RR products reaches up to 19.8%. Our results prove that back pressure may be manipulated in future upscaled CO_2RR systems with CuO-based GDEs to control the product selectivity and improve the CO_2RR stability.

3.3. Experimental Section

3.3.1. Electrode Preparation

CuO powder particles delivered by Johnson Matthey were used for the preparation of Cu-based GDEs. A CuO ink was prepared with 40 mg of CuO powder, 160 mg of 5 wt% Sustanion XA-9 anionic ionomer in ethanol solution, and 4 mL of isopropanol (99.9%, Sigma Aldrich). The ink was sonicated in an ultrasonic water bath for 30 min and immediately drop cast onto a 10 cm x 5.5 cm carbon-based gas diffusion layer (GDL) from Freudenberg (H23C2), which consisted of two layers: a carbon-based microporous layer containing hydrophobic PTFE binder and a macroporous layer consisting of carbon fibers. Together with the drop-cast catalyst layer, the GDE therefore had three layers. Later, the electrode was dried overnight at room temperature under a N_2 atmosphere with a flow of 50 sccm. The dried electrode batch was cut into two pieces with a 48 mm x 44 mm cutting template. The active area that took part in the electrolysis was 10 cm^2. The catalyst loading was 0.73 mg/cm^2.

3.3.2. Electrode Surface Analysis

A Bruker D2 PHASER diffractometer (Cu K radiation, scan rate of 0.02° s^{-1}) was used to perform ex situ X-ray diffraction (XRD) analysis on electrodes pre- and post-electrolysis. Scanning electron micrographs (SEM) of the GDEs pre- and post-electrolysis were taken at different magnifications with a high-resolution field-emission scanning electron microscope (JSM-7500F, JEOL). Both XRD and SEM results are given in the Supporting Information.

3.3.3. Experimental Set-Up

An internally designed flow cell was used in all experiments (**Figure 27** in Supporting Information). The cell consisted of three compartments where gas, catholyte, and anolyte flow in and out, respectively. PTFE and PEEK materials were used to determine the fluid flow patterns, to ensure cell tightness and provide better mechanical stability for the GDE and membrane. An

IrOx-coated electrode with a 10 cm^2 active area (Electrocell) was used as the anode and the CuO GDE described above as the cathode. Anode and cathode chambers were separated from one another by a cation exchange membrane (CEM) (Nafion 117, Ion Power). 250 mL of 1 M $KHCO_3$ (+99.7% in dry basis, Alfa Aesar) was circulated in the system as electrolyte between the gaps of cathode–membrane (catholyte) and anode–membrane (anolyte). The electrolyte flows circulating in both anode and cathode gaps were mixed in an electrolyte chamber external to the cell and pumped continuously through the system with microdiaphragm liquid pumps (NFB 25 KPDCB-4A, KNF) operated at a constant flow of 100 mL/min. The gas chamber was fed with CO_2 (+99.998%, Linde) which was humidified by a custom-made water bubbler at room temperature. Gas flow rates in the system were controlled with mass flow controllers (SFC5400 Sensirion). In contrast to the electrolyte, the gas head spaces of catholyte and anolyte were kept separate. The gas outlet from the cell was mixed with catholyte head space. The setup and cell details are shown in the Supporting Information.

3.3.4. Electrochemical Measurements

Chronopotentiometric electrochemical measurements were performed at 200 mA/cm^2 (2 A) using a Bio-Logic VSP 3e potentiostat, controlled by the EC-Lab software. Ag/AgCl (3 M NaCl) was used as the reference electrode (RE). Control experiments (Base case at $\Delta P = 0$) were conducted without a back pressure valve, whereas back pressure was applied, as shown in **Figure 13**, for the back pressure experiments. Feed flow rate variation was based on the λ value, and simply the ratio of actual CO_2 flow rate to the CO_2 flow rate theoretically required for full utilization of electrons to ethylene formation, formulated in Equation 7, where $\dot{V}$ is the flow rate, F is the Faraday constant, I is the applied current, z is the number of electrons required for the reduction, t is the electrolysis time, R is the ideal gas constant, T is the temperature and P is the gas pressure:

$$\lambda = \frac{\dot{V}_{CO_2,actual}}{\dot{V}_{CO_2,theoretical}} = \frac{\dot{V}_{CO_2,actual}}{2 \times \frac{I \times t}{z \times F} \times \frac{R \times T}{P}} \quad (7)$$

C_{2+} conversion efficiency is defined as the ratio of the molar sum of the converted CO_2 into C_{2+} products to the CO_2 feed into the electrolyzer in moles, as expressed in Equation 8, where ϑ_i is the number of carbons in the product *i*, $\dot{n}_i$ is the produced amount of product *i* in moles and $\dot{n}_{CO_2,\,feed}$ is the molar amount of fed CO_2.

$$C_{2+}\ \text{conversion} = \frac{\sum \vartheta_i \times \dot{n}_i}{\dot{n}_{CO_2,feed}} \quad (8)$$

Electrochemical impedance spectroscopy (EIS) measurements were performed to determine cell resistance. Cell resistance, R, was used in the calculation of iR in order to correct the working electrode potential. High-frequency resistance obtained from EIS measurements corresponded to cell resistance and accounted for 0.34 Ω. iR-corrected working electrode potential corresponded to -0.79 V versus RHE. The potentials, recorded versus the RE, were converted to the reversible hydrogen electrode (RHE) scale according to the Nernst equation.

$$V\ \text{vs. RHE} = V_{measured}\ \text{vs.}\ Ag/AgCl + 0.209 + 0.059 \times pH \quad (9)$$

3.3.5. Product Analysis

The catholyte gas head space was connected to a gas chromatograph (GC) for quantitative product analysis (7890B Agilent, Santa Clara, USA). N_2 was mixed with the product stream before the GC inlet as an internal standard for quantification. He was the carrier gas

enabling the detection of H_2 as a negative peak. A thermal conductivity detector (TCD) and three serially connected columns were used: a HayeSeP Q-column, a Porapak Q-column for the separation of CH_4, CO_2 and C_2H_4, and a molecular sieve 5 Å-column to separate N_2, O_2, and CO. 1 mL of the gas product stream was automatically injected every 20 min from the cell to the gas chromatograph during the course of the electrolysis.

^{1}H nuclear magnetic resonance (NMR) was used for quantification of liquid products. Electrolyte circulated constantly in a separated closed system between reservoir and cell was sampled from a septum. The NMR measurements were performed in a 500 MHz Bruker (Bruker Bio-Spin, Karlsruhe, Germany) following the method described by Cuellar et al.[112]. The water peak was suppressed by a pre-saturation sequence. An aliquot of the $KHCO_3$ electrolyte containing liquid products (300 µL) was mixed with sodium fumarate as an internal standard (50 µL) in D_2O (250 µL) for the quantification.

FEs corresponding to gas and liquid products were calculated using the following equation, where n is the amount of product in moles:

$$FE = \frac{n \times z \times F}{I \times t} \tag{10}$$

3.4. Results and Discussion

The setups for CO_2RR with back pressure operation and experimental results are explained in three main categories: cell setup, stability under back pressure, product selectivities under different back pressure values, and flow rates. The characterization of the electrodes is presented in Supporting Information.

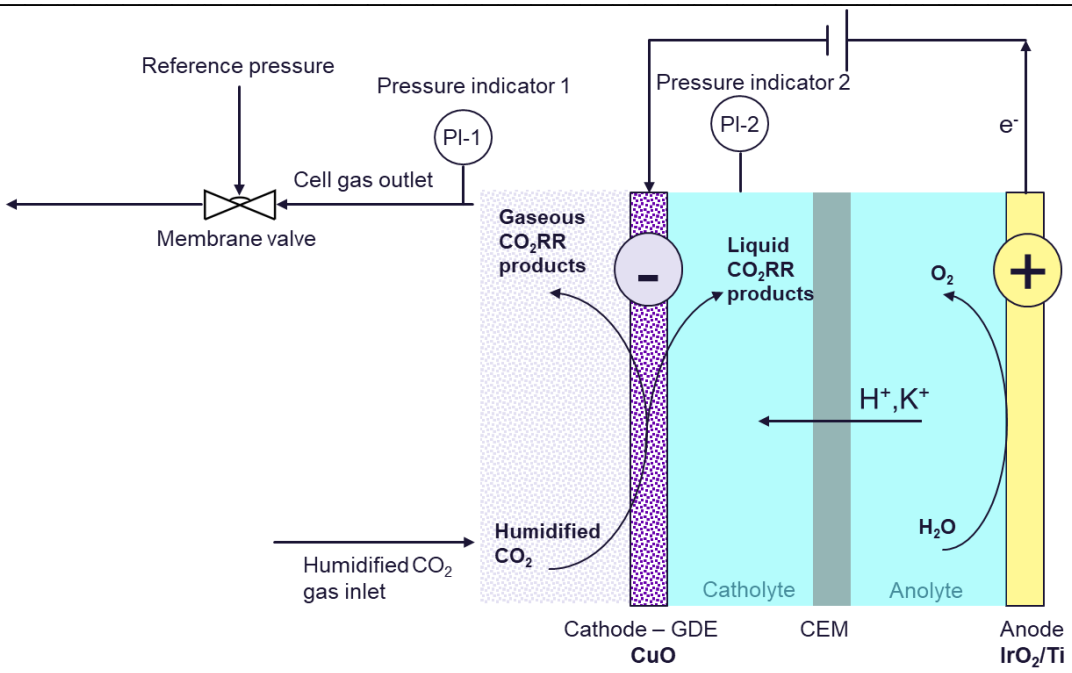

Figure 13. Experimental setup for CO2RR in flow cell architecture with back pressure application at the gas side.

3.4.1. Cell Setup and Application of Back Pressure

Back pressure experiments were performed on carbon-based GDEs embedded with a commercial CuO catalyst, positioned in a two-gap flow cell architecture. The cells consist of two electrodes separated by a CEM and two gaps that accommodate electrolyte flow (1 M $KHCO_3$, flow rate = 100 mL/min; **Figure 13**). The third compartment, namely, the gas chamber where humidified CO_2 (atmospheric gas inlet pressure) flows, comes into contact only with the cathode and therefore does not reside between the two conductive electrodes. A membrane valve is positioned at the gas outlet stream that carries mainly unconverted CO_2, H_2, and CO_2RR gas products. The absolute pressure in the gas compartment is increased and controlled by the membrane valve.

Pressures in the gas compartment and in the catholyte chamber were monitored with pressure sensors. The back pressure (ΔP) applied on the GDE is defined as the difference

between P1 (gas) and P2 (catholyte). This was set to 70 and 130 mbar at high gas flow rates and 40 mbar in low-gas flow rate experiments. It must be noted that higher back pressures can lead to so-called “flow-through” operation, where the pressure difference enables the gas to be pushed through the porous electrode to the catholyte chamber on the other side. For this reason, back pressure must be set to a value that maintains the desired “fllow-by” operation. This threshold value for flow-by strongly depends on the electrode architecture and properties, employed flow rate, catholyte properties, and cell design and size. We stress that optimum back pressure values can vary in differing cell systems and should therefore be optimized accordingly.

3.4.2. HER Suppression Under Back Pressure

The stability of the CuO electrodes was tested at an applied current density of 200 mA/cm^2 in two series of experiments: base case without back pressure and with ΔP = 130 mbar. In **Figure 14** , the FE for H_2 and C_2H_4 is depicted vs. time for both cases. HER as the competing reaction to CO_2RR is a good indicator for a decrease in CO_2RR catalytic activity. $FE_{C_2H_4}$ is chosen as an indicator of CO_2RR stability, as it is one of the more valuable CO_2RR products. At a back pressure of 130 mbar, FE_{H_2} is suppressed below 25% for 72 h, in comparison to the base case where H_2 selectivity is clearly higher already from the outset at 25-40% for the first 48 h and only becomes more dominant over time (FE_{HER} > 50%). Two separate phenomena are observed here:

1. Back pressure significantly decreased the selectivity for H_2. At 24 h, FE_{HER} was 15.1 (± 1.0) % under ΔP = 130 mbar, whereas in the base case it was almost doubled at 30.7 (± 5.6) %.

2. Back pressure provides longer stable CO_2RR operation. $FE_{C_2H_4}$ remained above 20% for only 36 h in the base case, while back pressure of 130 mbar prolonged its stability to 72 h, corresponding to a stability increase by a factor of two when 20% is assumed as the stability threshold.

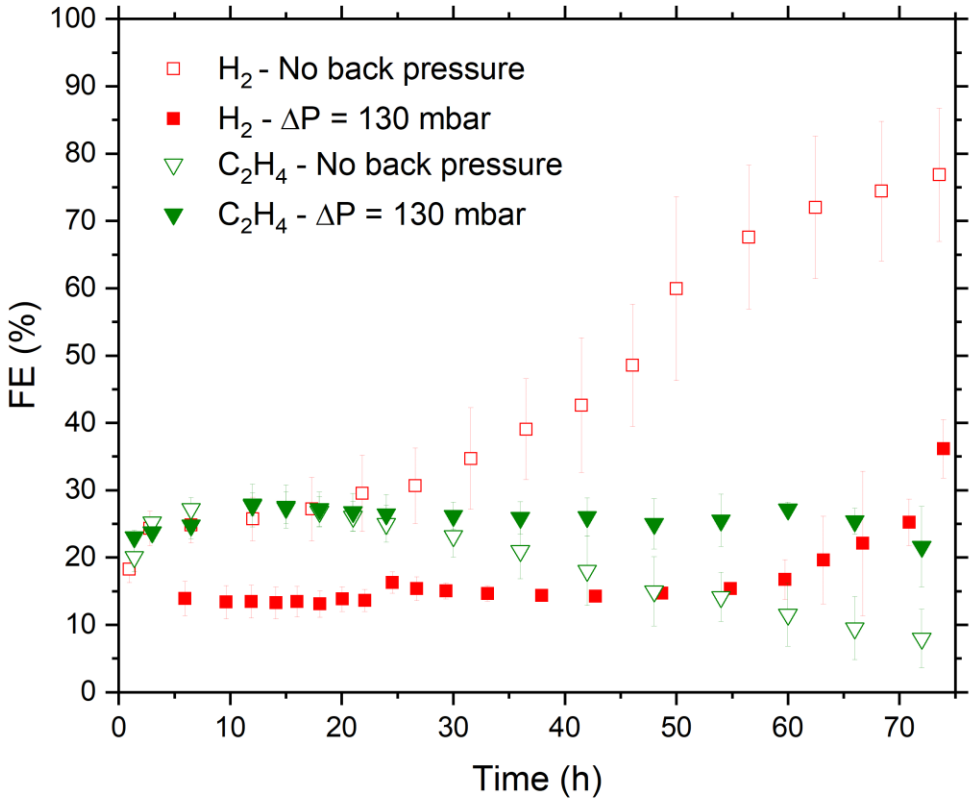

Figure 14. Stability of the CO_2 electrolysis system expressed in terms of hydrogen and ethylene faradaic efficiencies.

The two above phenomena must be regarded separately. Regarding the first, it has been suggested that abundant CO* coverage on Cu suppresses HER due to site-blocking effects and/or changes in H* binding energy, leading to higher FEs for CO_xRR [54,56,61,64,87,128,129]. The surface coverage of CO_2 on the catalyst is dependent on the local concentration of CO_2, as per

Equation 11 where θ is the coverage of vacant surface sites, E is the CO_2 adsorption energy on the surface, R is the ideal gas constant, and T is the temperature.

$$\theta_{CO_2} = \theta^* \times [CO_2] \times e^{\frac{-E}{RT}} \quad (11)$$

According to the adsorption equilibrium equation, adsorbed CO_2 species coverage (CO_2) increases with increasing CO_2 concentration in the gas phase, assuming that CO_2 adsorption is molecular and first order [74,125]. **Figure 15** schematically illustrates the increasing surface coverage of CO_2 with increasing partial pressure of CO_2 provided by application of back pressure. As of catalyst surface coverage of CO_2* and H* species under back pressure.

CO_2 adsorption ($CO_2 \rightarrow CO_2^*$) is the rate-determining step of CO_2 reduction to <2e$^-$ products

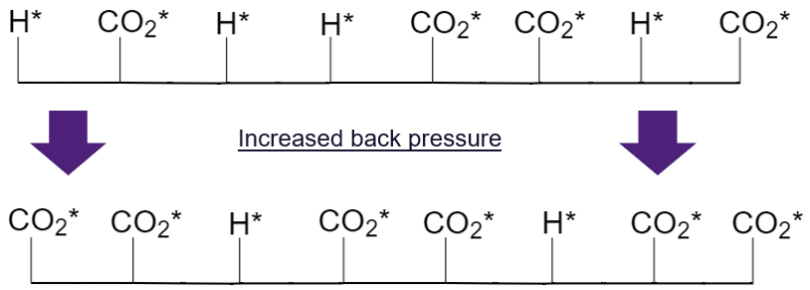

Figure 15. Simplified illustration of catalyst surface coverage of CO_2* and H* species under back pressure.

and the reaction from CO_2 to CO* is faster, a higher CO_2 partial pressure would accordingly translate into an abundant CO* surface coverage [20]. Based on our results, it can be assumed that increased back pressure leads to higher CO* coverage and therefore HER suppression.

On the second phenomenon, two explanations for longer stability under back pressure are possible. As mentioned, catalysts producing more C_{2+} relative to C_1 products may be more stable due to a possible graphitic intermediate in the C_1 route [68,75,111,121–125]. In mechanistic studies conducted by Rahaman et al.[56] and Akhade et al.,[54] the poisoning C* species is postulated to be formed via reduction of COH*, which is an intermediate of CO*-to-CH_4 reduction. As discussed in

the following subsections, abundant CO* coverage provided by back pressure suppresses C_1 hydrocarbon production (CH_4) and promotes C_{2+} selectivity. This may have resulted in the observed longer stability by avoiding poisonous C* intermediate formation, as this route is not preferred under high CO* coverage. Another possibility is that back pressure keeps the capillary pressure (local pressure difference between wetting and nonwetting media) at a sufficiently high value that minimizes the flooding of the catalyst and GDLs, an otherwise highly likely cause of deactivation[122–124]. When flooding is minimized, the salts present in the aqueous electrolyte do not crystallize in the pores of the electrode and do not increase its hydrophilicity. We hypothesize that flooding occurs to a smaller degree or can be delayed under back pressure. Mass transport limitation on CO_2 availability therefore remains low and can be avoided for a longer period.

3.4.3. C_1 Product Formation under Back Pressure

FEs of three main C_1 products, CO, COOH, and CH_4, obtained under CO_2RR conditions at an applied current density of 200 mA/cm^2 and at three different back pressure conditions are shown in **Figure 16**. Methanol was detected only in trace amounts and has not been included in the results.

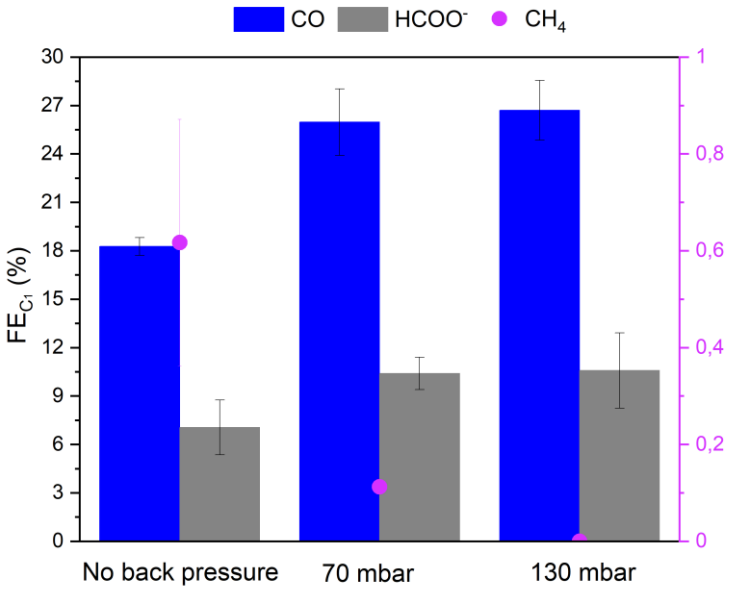

Figure 16. C_1 product distribution dependency on back pressure at t = 3 h.

The key intermediate CO was produced in significantly larger amounts when back pressure was applied, indicating that CO* desorbed before being reduced further to >2e$^-$ products. FE_{CO} = 18.3 (± 0.6) % in the base case compared with 26.0 (± 2.1) % under 70 mbar and 26.7 (± 1.8) % under 130 mbar back pressure. Therefore, a correlation between increasing back pressure and CO desorption may be established. A similar trend of increased CO production at higher pressures was described in the literature, the cause of which was given as the increased CO* surface coverage under higher pressures[56,111,125]. It has also been claimed that abundant CO_2 coverage reduces the CO* binding energy to the catalyst surface via adsorbate–adsorbate repulsion, which, in turn, causes CO to bond weakly and therefore its desorption [130]. Additionally, we hypothesize that shorter residence times due to a stronger driving force for diffusion through the catalyst layer at higher back pressures deprive CO_2 of sufficient residence time to react to >2e$^-$ products.

The production of formate, the only product that is formed exclusively from CO_2* and not through CO*, was also slightly greater under back pressure, enhanced by the higher CO_2* surface

coverage under such conditions. Notably, this increase in FE_{COOH} was not as high as that of CO. This might suggest that the proportion of CO_2 molecules bound to the Cu surface via the C atom (leading to CO pathways) became significantly higher under back pressure, whereas the number of CO_2 molecules bound to Cu surface by O atom(s) (leading to $HCOO^-$ pathway) did not increase as much.

FE for CH_4 was observed to decrease from 0.6% in the base case, to 0.1% at 70 mbar back pressure and to 0% at 130 mbar back pressure. The lower selectivity toward CH_4 in the base case could be attributed to the intrinsic catalytic behavior of CuO. Oxide-derived Cu catalysts are known to demonstrate low selectivities for CH_4 [56,131] and the presence of several Cu_2O facets was proven to diminish methane formation[56]. The gradual decrease of FE_{CH_4} with increasing back pressure and the complete suppression of CH_4 at 130 mbar may be correlated to abundant CO_2 coverage, which prohibited H* surface coverage and therefore protonation of CO* intermediates required for CH_4 formation.

3.4.4. C_{2+} Product Formation under Back Pressure

C_{2+} products from CO_2RR on Cu surfaces typically possess either 2 or 3 carbon atoms. It was logical to divide >2e- CO_2RR products into two groups as hydrocarbons and oxygenates as they follow distinct potential dependencies, mechanistic pathways, and surface coverage dependencies. Ethylene and methane constituted the hydrocarbons group whereas methanol, ethanol, *n*-propanol, allyl alcohol, acetaldehyde, propionaldehyde, and acetate constitute the oxygenates group. Ethylene was categorized separately from the others as it was the only C_{2+} hydrocarbon molecule, the rest being oxygenates. Acetaldehyde, propionaldehyde, and propionate were detected only in trace amounts and have not been included in the results, while allyl alcohol and acetate were observed in very small amounts and have been included within the C_{2+} and oxygenate groups.

$FE_{C_2H_4}$ did not change significantly at different back pressure levels and accounts for ≈23–25% in all cases (**Figure 17a**). FE for total C_{2+} products was however enhanced from 36.9% in the base case to 43.0% at ΔP = 70 mbar and 43.9% at ΔP = 130 mbar, and clearly stemmed not from ethylene but rather from oxygenate formation (**Figure 17b**). The ratio of >2e⁻ oxygenates to hydrocarbons could be tuned between 0.53 and 0.85 at 0 <ΔP < 130 mbar. An enhancement of $FE_{oxygenates}$ from 13% to 20% (accounting for an improvement of 54% in oxygenate selectivity) was driven mainly by ethanol and *n*-propanol formation and could be achieved simply by varying the back pressure.

The observed correlation between back pressure and C_{2+} selectivity could be explained with the predicted second-order kinetic dependency of CO* coverage for C–C coupling,[71] leading to accelerated C_{2+} production kinetics with higher CO* coverage. Nevertheless, we do not exclude the effect of possible changes in local pH when local CO_2 concentrations were higher due to back pressure. The selectivity between ethylene and oxygenates may be explained by the effects of high CO* coverage on the reaction mechanism, as Li et al. discussed with both density functional theory calculations and experimentation:[74] *CHCOH intermediates tendentially deoxidize to *CCH under lower CO* coverage, leading to the ethylene reaction pathway versus tending to hydrogenate to *CHCHOH under higher CO* coverage and hence the oxygenate pathway. Our experimental results confirmed this. Oxygenate selectivity improvements (and correspondingly

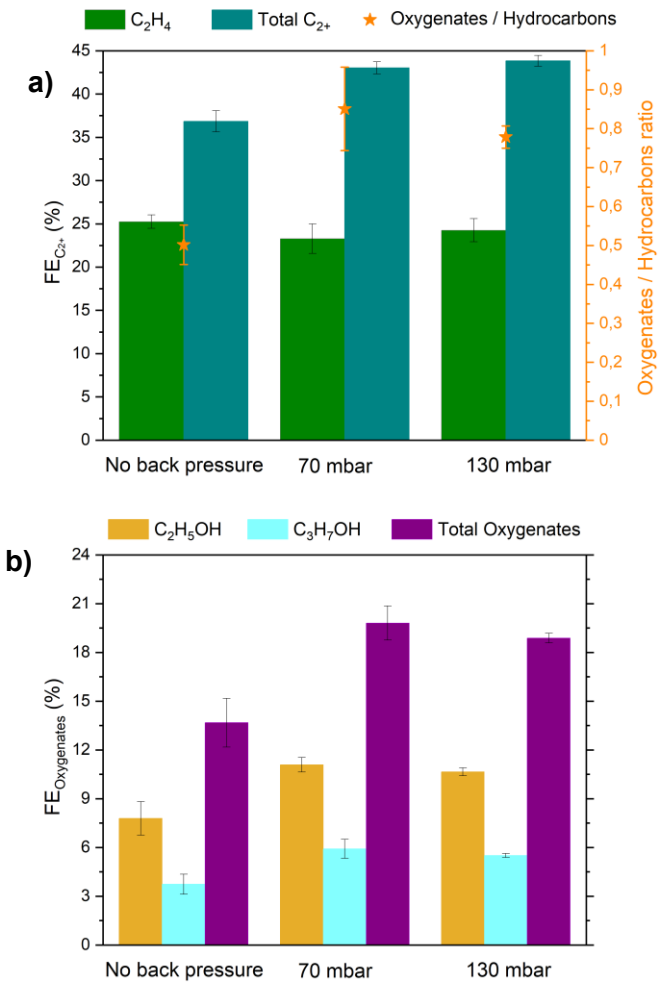

Figure 17. a) C_2H_4 and C_{2+} production under back pressure expressed in terms of FE and the ratio of FE sums of oxygenates to hydrocarbons at t = 3 h. **b)** FEs of oxygenate products at t = 3 h.

improved C_{2+} selectivity) achieved with higher CO_2 or CO feed [60,87,115] concentrations have similarly been reported by others. We therefore demonstrated that such trends may also be influenced by applying a back pressure.

In parallel with the aforementioned stability of C_2H_4 formation, FE_{C2+} dropped only minimally from 43.9% to 40.5% between the 3rd and 48th h of electrolysis when under ΔP = 130 mbar. In stark contrast to this, FE_{C2+} diminished drastically from 36.9 to 22.8% within same period when no back pressure was applied. A detailed breakdown of product selectivities over time is given in **Table 4**.

3.4.5. Deconvolution of Back Pressure Effects on Stability and Selectivity

Control of CO_2* coverage over catalyst surface and capillary pressure control circumventing the electrode flooding have been mentioned as the possible underlying reasons of the stability and selectivity effects of back pressure application. To decouple these two phenomena from each other, two various experiment series both with ΔP = 130 mbar (P_{abs} = 1.13 bar) back pressure application at different two different feed compositions were performed: 100% CO_2 feed (P_{CO_2} = 1.13 bar) and CO_2: N_2 feed in volumetric ratio of 88.5:11.5 (P_{CO_2} = 1.00 bar). The diluted feed experiments with ΔP = 130 mbar had the same CO_2 partial pressure of 1.00 bar as the control experiments with no back pressure in the base case (P_{abs} = 1 bar, P_{CO_2} = 1 bar).

C_2H_4 and H_2 FEs over time were shown as the stability indicators in **Figure 18**. N_2-diluted CO_2-fed experiments at ΔP = 130 mbar exhibited C_2H_4 stability for 48 h, almost identically to the base case with no back pressure. It was significantly inferior to the 72 h stability of pure CO_2-fed experiments at ΔP = 130 mbar. H_2 was not as suppressed with P_{CO_2} = 1.00 bar as it was with P_{CO_2} = 1.13 bar, its FE was on constant rise after 48 h, similar to the base case with no back pressure. In the light of these results, back pressure could provide H_2 suppression and stable C_2H_4 formation primarily by means of increased CO_2 coverage and not necessarily through capillary pressure preventing electrolyte incorporation into the catalyst layer, as the same ΔP = 130 mbar with diluted CO_2 feed could not maintain stable C_2H_4 formation and H_2 suppression.

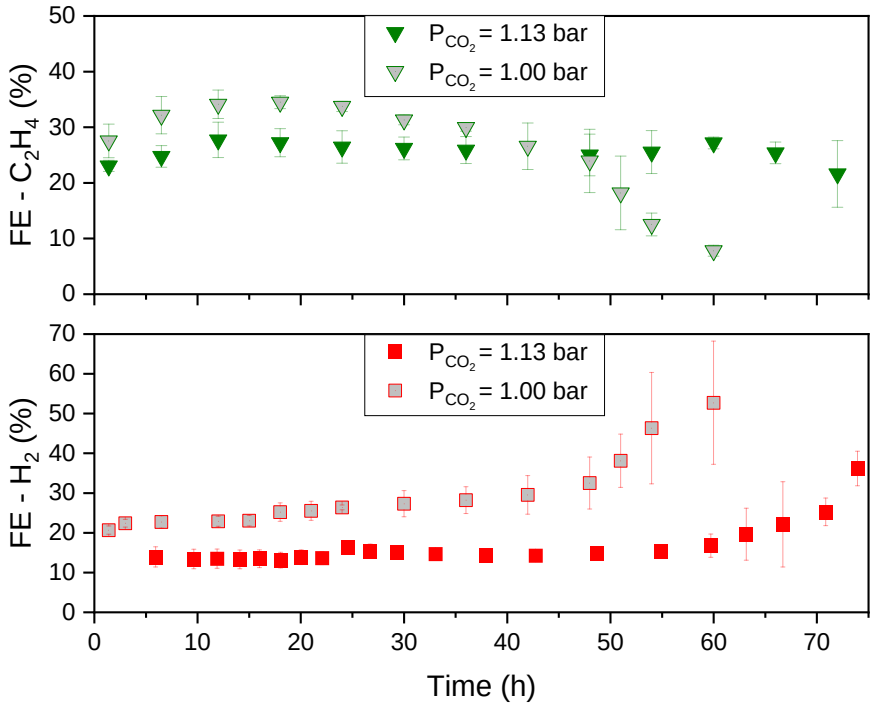

Figure 18. Faradaic efficiencies of C_2H_4 and H_2 over time with 1.13 and 1.00 bar of CO_2 partial pressures under ΔP = 130 mbar back pressure applications.

Figure 19 sets out the effects of P_{CO_2} on product distribution under the same back pressure of ΔP = 130 mbar. CO selectivity did not differ significantly and failure of H_2 suppression at P_{CO_2} = 1.00 bar was discussed thoroughly above. $FE_{C_2H_4}$ was greater at P_{CO_2} = 1.00 bar with diluted CO_2 feed (29.6%) compared to the P_{CO_2} = 1.13 bar case (24.3%). COOH was formed substantially in smaller amounts at lower P_{CO_2}. Oxygenate selectivity was significantly improved at higher P_{CO_2}. In line with the previous findings, we confirm that high CO_2 coverage at P_{CO_2} = 1.13 bar promotes COOH and oxygenate selectivities. P_{CO_2} = 1.00 bar condition with diluted CO_2 feed (88.5 vol.%) possibly enabled a milder CO_2, shifting the oxygenate–hydrocarbon (C_2H_4) selectivity toward the hydrocarbon.

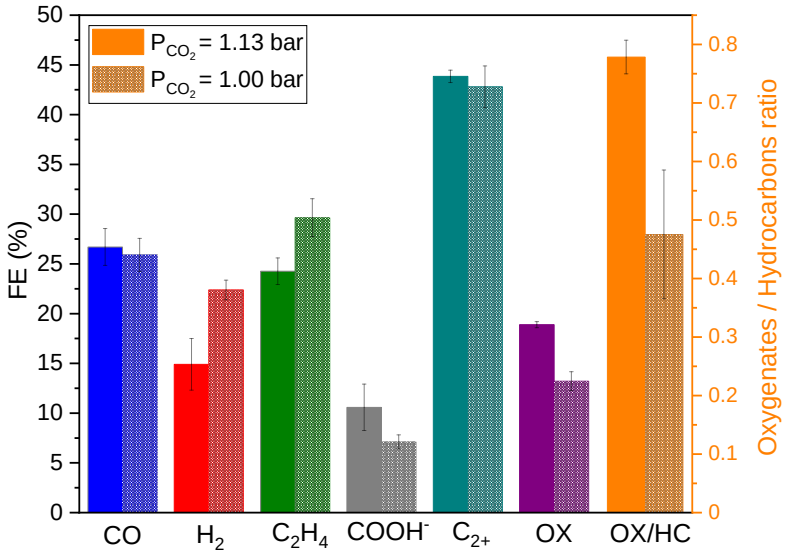

Figure 19. Product distributions with 1.13 and 1.00 bar of CO_2 partial pressures under ΔP = 130 mbar back pressure applications at t = 3 h.

Base case experiments (P_{abs} = 1 bar) and dilute CO_2 feed experiments at ΔP = 130 mbar back pressure (P_{abs} = 1.13 bar), both employing P_{CO_2} = 1 bar, showed similar product distribution (**Figure 29** in Supporting Information). The slight differences favoring CO and C_2H_4 over H_2 in the dilute CO_2 feed at ΔP = 130 mbar may be attributed to the prevention of electrolyte incorporation to the catalyst layer by the presence of back pressure.

3.4.6. Combined Effect of Back Pressure and Low Flow Rates

Despite the improvements obtained in terms of stability and selectivity toward C_{2+} oxygenates through back pressure applications, the increase observed in CO production remained (**Figure 16**) and limited the overall selectivity for C_{2+} that could be achieved as it implied lost opportunity for CO further reduction. Additionally, improved C_2H_4 selectivity has not been achieved despite abundant surface coverage of CO_2 provided by back pressure.

Shorter residence times at the catalyst-coated surface of the was is a possible reason for the above observations. A series of experiments at a lower CO_2 feed flow rate were conducted to

investigate whether a further reduction of CO* may be achieved by a longer residence time and a more optimum surface coverage for C_2H_4. Feed flow rates were expressed in terms of λ, which is the ratio of actual CO_2 flow rate to the CO_2 flow rate theoretically required for full utilization of electrons for ethylene formation ($FE_{C_2H_4}$ = 100%; see in Equation 7 in the Experimental Section). A CO_2 feed of 50 sccm, equivalent to λ = 10.78, was supplied for high flow rate experiments and 14 sccm CO_2, equivalent to λ = 3.01, was fed to the electrolyzer for low flow rate experiments. CO_2RR was conducted under four different conditions: high flow rate experiments under ΔP = 130 and 0 mbar back pressure and low flow rate experiments under ΔP = 40 and 0 mbar back pressure. The back pressures applied in each of these flow rate conditions corresponded to the maximum achievable back pressure if a flow-by operation were to be maintained; a pressure difference exceeding these values for the two cases caused flow-through operation. It is worth noting that the maximum achievable back pressure for flow-by operation strongly depended on electrode characteristics, cell design, catholyte wetting properties and gas flow rate, and the values reported here were therefore highly specific to the experimental materials and design employed.

It is important to emphasize that CO_2 availability in the catalyst layer of the electrode changes fundamentally under low flow rate conditions. The bulk CO_2 gas concentration was reduced from 81.9 to 33.3 mol%, when CO_2 was fed into the electrolyzer cell inlet at 50 and 14 sccm, respectively (see **Table 2** in Supporting Information). The local CO_2 gas concentration at the catalyst was predicted to be even lower in the low λ case, as a thicker gas boundary layer

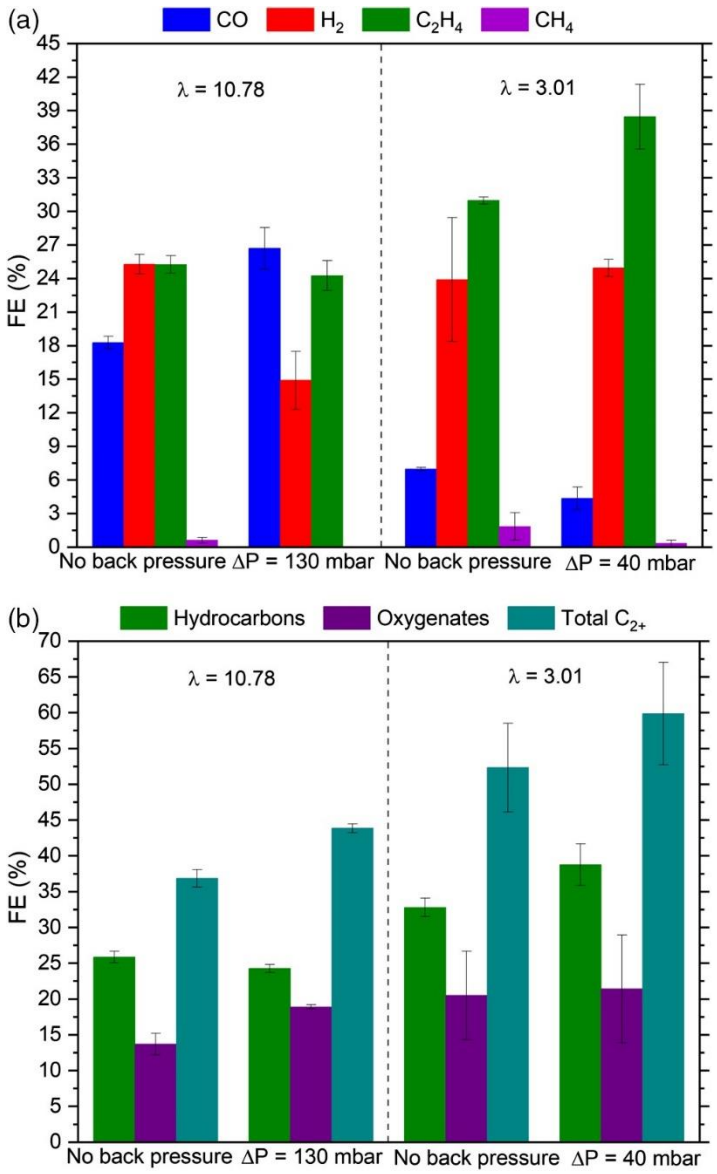

Figure 20. a) FEs of CO, H_2, C_2H_4 and CH_4 with various back pressure and flow rates at t = 3 h. b) Selectivities of oxygenate, hydrocarbon and C_{2+} products with various back pressure and flow rates at t = 3 h.

with higher mass transfer resistance can be expected. Therefore, the difference between the bulk and locally available CO_2 gas concentrations is predicted to be greater at lower flow rates. Tan et al.[125] discussed the same trend for CO_2 local availability in CO_2RR environments at low flow rates.

As shown in **Figure 20a**, FE_{CO} declines from 18.3% to 7.0% when the CO_2 flow rate was reduced from λ = 10.78 to 3.01. Interestingly, an even lower FE for CO was observed under combined back pressure and low λ conditions (from 26.7% to 4.4%). Back pressure enhanced CO production at higher λ, whereas it appeared to facilitate the opposite at lower λ. This suggests that the surface coverage at combined back pressure and low flow rates offers an environment where CO* does not desorb but further reacts to C_{2+} products. Lower λ conditions showed H_2 FEs similar to that of high λ, at the 25% range, independent of back pressure. HER was not suppressed at combined low λ and back pressure (FE_{H2} = 25.0%) as much when compared with high λ and back pressure case (FE_{H2} =14.9%). The interpretations from CO and H_2 production signal that CO_2 surface coverage reaches a smaller extent under lower flow rates, leading to lower CO* coverage and more abundant H*. FE_{CH4} going up to 1.83% at low λ confirms that H* availability is higher at lower flow rates.

Most interestingly, a lower CO*/H* coverage ratio and shorter residence time obtained by combined back pressure and low λ boosted C_2H_4 production. $FE_{C_2H_4}$ was increased from 24.3% to 38.5% when a low flow rate was used in combination with back pressure. A smaller improvement to the base case, to $FE_{C_2H_4}$ of 31.0%, was observed at low flow rates without back pressure, this would suggest that back pressure contributed significantly to overall improvement and that the combined effects of optimum CO*/H* coverage and longer residence time in the catalyst layer favored C_2H_4 formation. Together with boosted C_2H_4 production, FE_{C_2} = 60% was

achieved by combining back pressure and low flow rates, which was significantly greater than the 37% achieved in the base case (**Figure 20b**).

Finally, **Figure 21** shows how C_{2+} conversion efficiency depended on feed flow rate and back pressure. A combination of low feed flow rate and back pressure delivered the highest C_{2+} conversion efficiency at 19.8%, compared to 3.5% in the base case. Significantly lower levels of unconverted CO_2 at low feed flow rates and higher selectivity towards C_{2+} with back pressure and

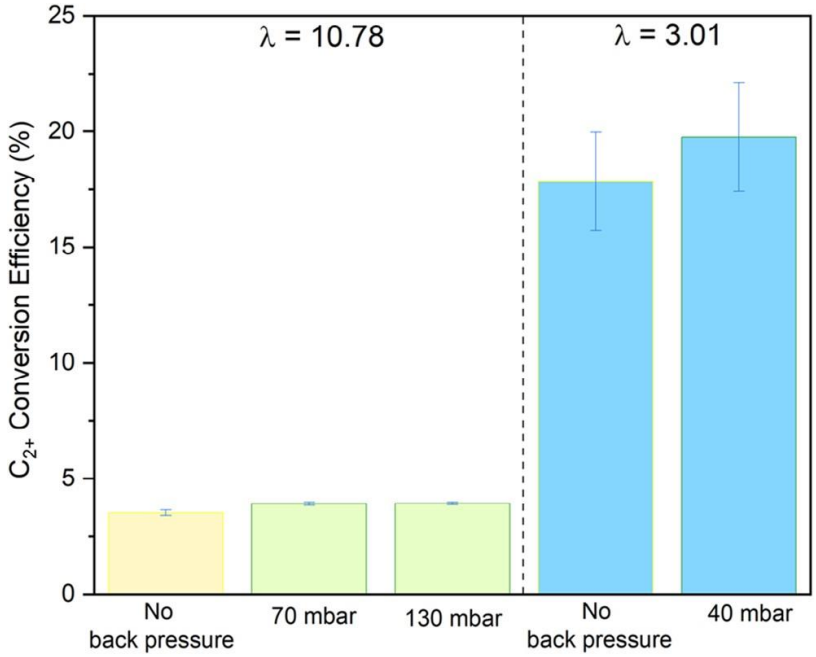

Figure 21. C_{2+} conversion efficiencies at different feed flow rates and back pressures at t = 3 h.

low flow rate enabled this remarkable improvement in the conversion efficiency. C_{2+} conversion efficiency was defined in the Equation 9 in the Experimental section.

3.5. Conclusions

CO_2RR on CuO gas diffusion cathode electrodes were investigated in a flow cell environment at an applied current density of 200 mA/cm^2 under various back pressures and feed flow rates. Applying back pressure of 130 mbar was shown to prolong the stable operation time

to 72 h (FE_{H_2} < 50%, $FE_{C_2H_4}$ > 20%), doubling the duration observed from the base case. A high CO* coverage due to abundant CO_2 provided by back pressure suppressed HER by possibly blocking the active sites and/or changing the H* binding energy. Suppressing HER increased the selectivity toward CO_2RR products in addition to prolonging CO_2RR stability. By differing the partial pressure of CO_2 at ΔP = 130 mbar, the primary reason for stability increase with back pressure application was shown to be abundant CO_2 coverage rather than decrease in the degree of electrode flooding.

Back pressure at ΔP = 130 mbar not only lowered H_2 production, but also enabled higher production of CO and oxygenates. The ratio of oxygenates to hydrocarbons could be tuned from 0.53 to 0.85 at ΔP = 0–130 mbar range. This enhancement in oxygenate production stemmed from higher selectivity toward ethanol and propanol and was suggested to be driven by the formation of *CHCHOH intermediates under higher CO* coverage. While boosting stability and oxygenate selectivity, back pressure also resulted in a loss of CO* by desorption and therefore high CO production, possibly due to high CO_2 coverage and short residence times in the electrode. For this reason, back pressure and low flow rates were combined to ensure a longer residence time and a more optimum CO_2 coverage for C_2H_4 formation. This enabled a significant reduction of CO in favor of C_{2+} products, mainly ethylene. FEs of 38.5% for ethylene and 60% for C_{2+} and CO_2 conversion efficiency to C_{2+} of 19.8% were reached. Mild CO*/H* coverage and long residence time in the catalyst layer were shown to be optimal for C_2H_4 production.

In summary, we demonstrate that the method of controlling back pressure is an easily implementable option in industrial applications toward manipulating the product selectivity in upscaled Cu-based CO_2 electrolysis cells. Further research must be done to achieve the optimum electrode and cell design that enables a more stable operation for a possible future commercialization.

Acknowledgements

The authors thank Luke Luisman and Iain Malone from Johnson Matthey Public Limited Company for supplying the CuO cathode catalyst. B.S. would like to express his gratitude to Katia Rodewald from Technical University of Munich for her support with scanning electron micrograph characterization of the electrodes, to Professor Dr. Wolfgang Eisenreich from Technical University of Munich for his support with NMR measurements, to Nemanja Martic for conducting XRD measurements, and to Dr. Remigiusz Pastusiak and Dr. Kerstin Wiesner-Fleischer for the valuable discussions and support in the laboratory. B.S. and S.L. acknowledge support from the TUM Graduate School. This research did not receive any specific grant from funding agencies in the public, commercial, or not-for-profit sectors.

3.6. Supporting Information

3.6.1. Ex-situ characterization of gas diffusion electrode

3.6.1.1. XRD analysis of pristine and post-mortem CuO-based GDE

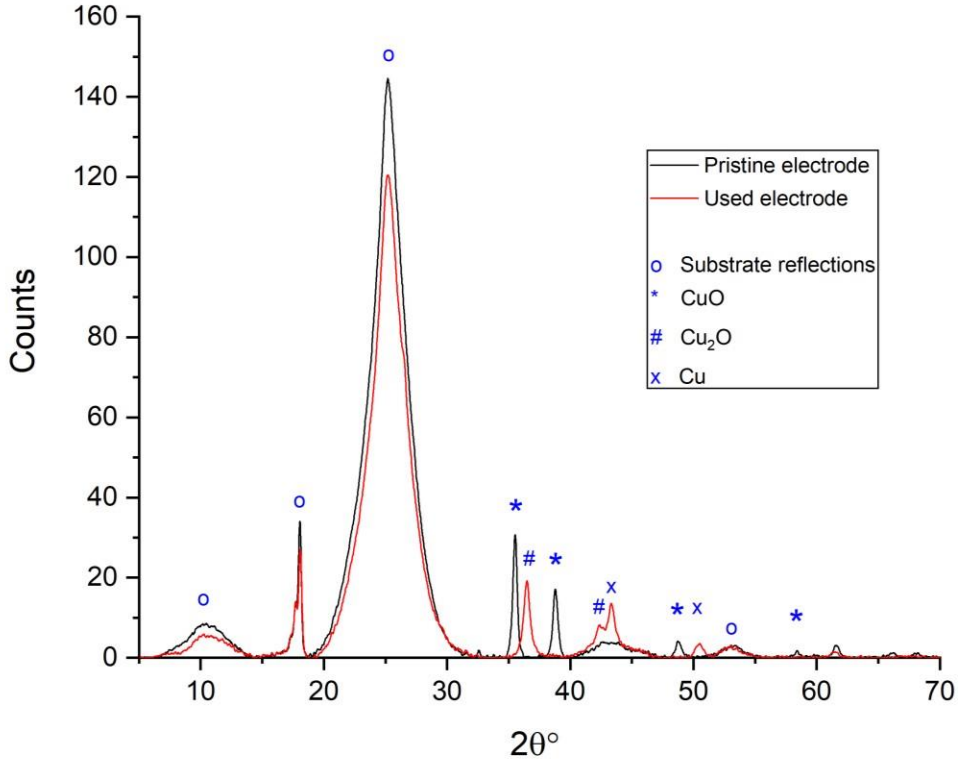

Figure 22. XRD patterns of pristine and post-electrolysis CuO gas diffusion electrodes.

The catalyst layer of the GDE was prepared by layer-by-layer drop casting of the catalyst ink (see Experimental Section). CuO was used in the catalyst ink and was expected to be reduced to Cu under the cathodic conditions of -1.5 V vs. RHE (iR drop compensated) employed in the experiments. The Pourbaix diagram for Cu in aqueous systems at 25 °C shows that Cu-oxide

derived catalysts exist in Cu(I) or Cu(0) form under cathodic conditions at slightly alkaline conditions (pH = 8.5). The XRD spectrum of the pristine electrode in **Figure 22** indicates that the only Cu phase present on the pristine catalyst layer was CuO. The peaks resulting from the gas diffusion electrode substrate itself (including carbon fibers and chemical binders) were also marked. The XRD spectrum of post-electrolysis electrodes clearly shows that Cu no longer existed in the Cu(II) oxidation state. Rather, Cu_2O and Cu peaks were visible. The nature of ex-situ measurements rendered it impossible to exclude the possibility of re-oxidation of Cu species following electrolysis. For this reason, based solely on these ex-situ measurements, the presence of both Cu(0) and Cu(I) during the CO_2RR could not be ruled out. The effect of the presence of Cu_2O on the product selectivity was discussed in the context of the C_1 product distribution.

3.6.1.2. SEM images of the CuO-based gas diffusion electrodes

Top-down SEM images were taken for both control experiments and back pressure experiments before and after the electrochemical measurements in order to detect the possible changes occurring on the electrode surface as a result of back pressure operation. For each case, four various magnitudes and corresponding spatial resolutions were chosen: x5000, x10000, x20000 and x50000.

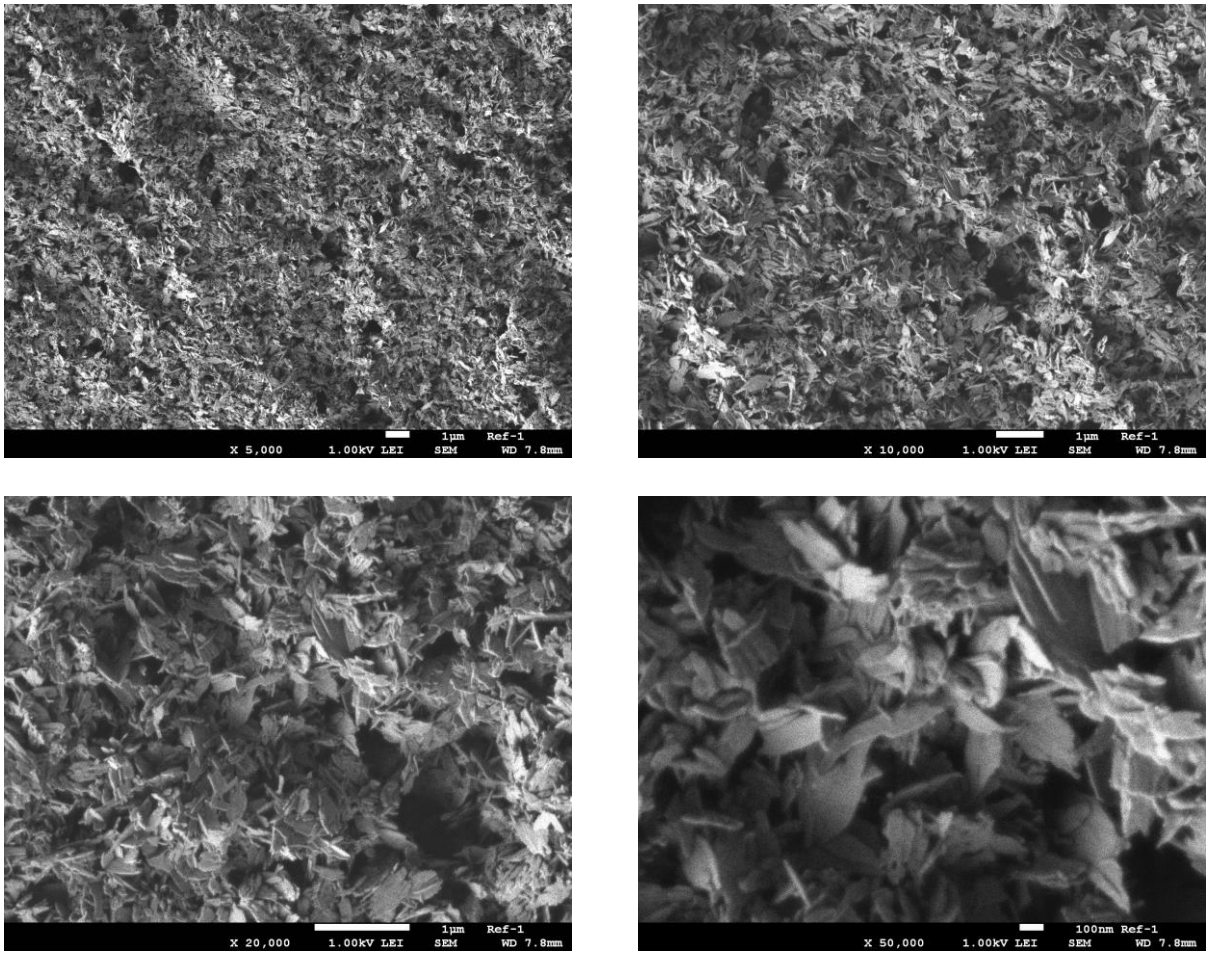

Figure 23. Top-down SEM images of pristine electrodes.

Figure 23 shows the SEM images of pristine CuO-based electrodes. The metallic bright areas depicted a dense coverage with flaky CuO particles.

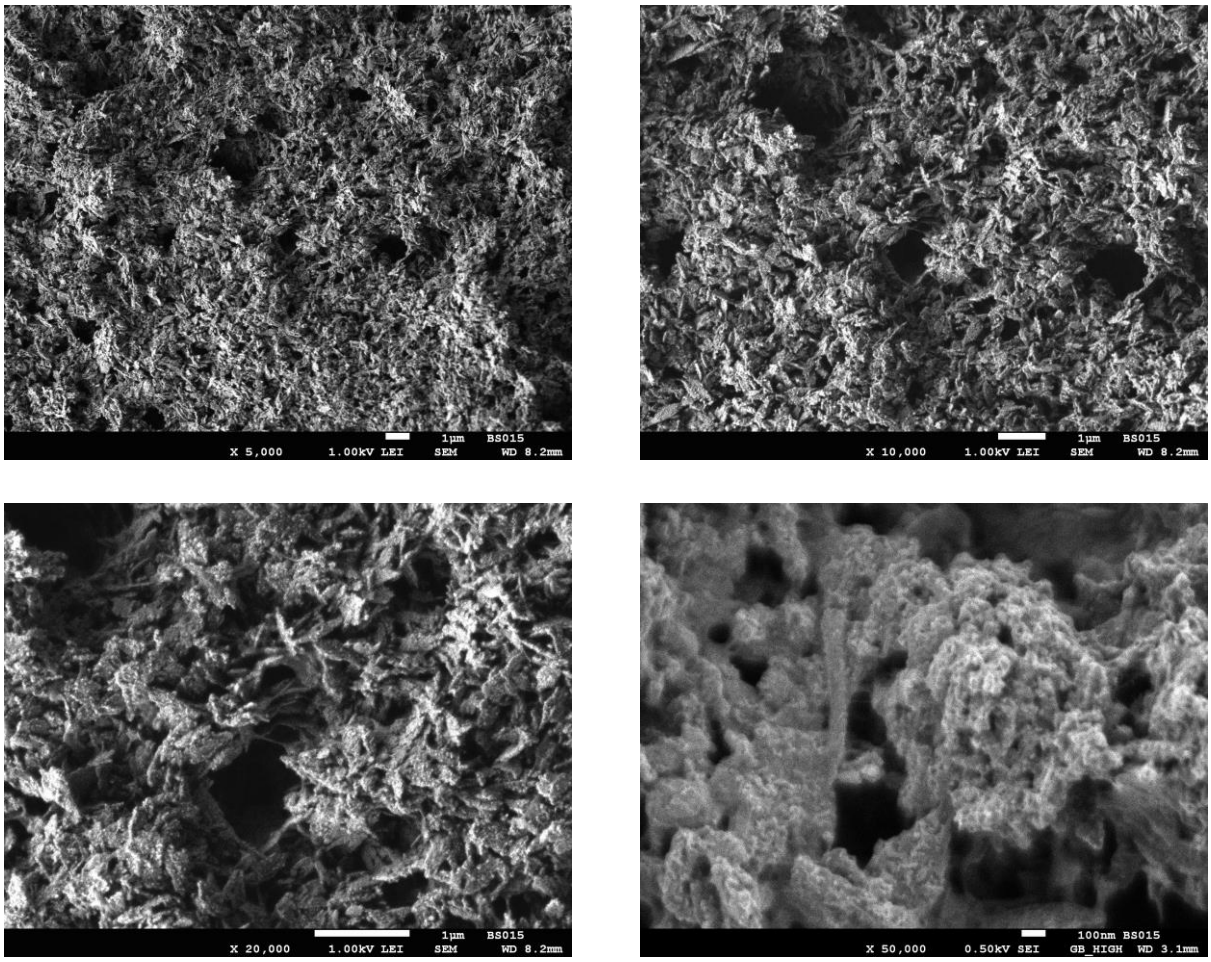

Figure 24. Top-down SEM images of post-electrolysis electrodes in a control experiment.

Figure 24 shows the SEM images of post-mortem CuO-based electrodes after a control experiment. The bright metallic blotches depicted flaky particles with small globular nanoparticle clusters at their tips. Within the coppery islands many, larger, globular nanoparticle clusters were present.

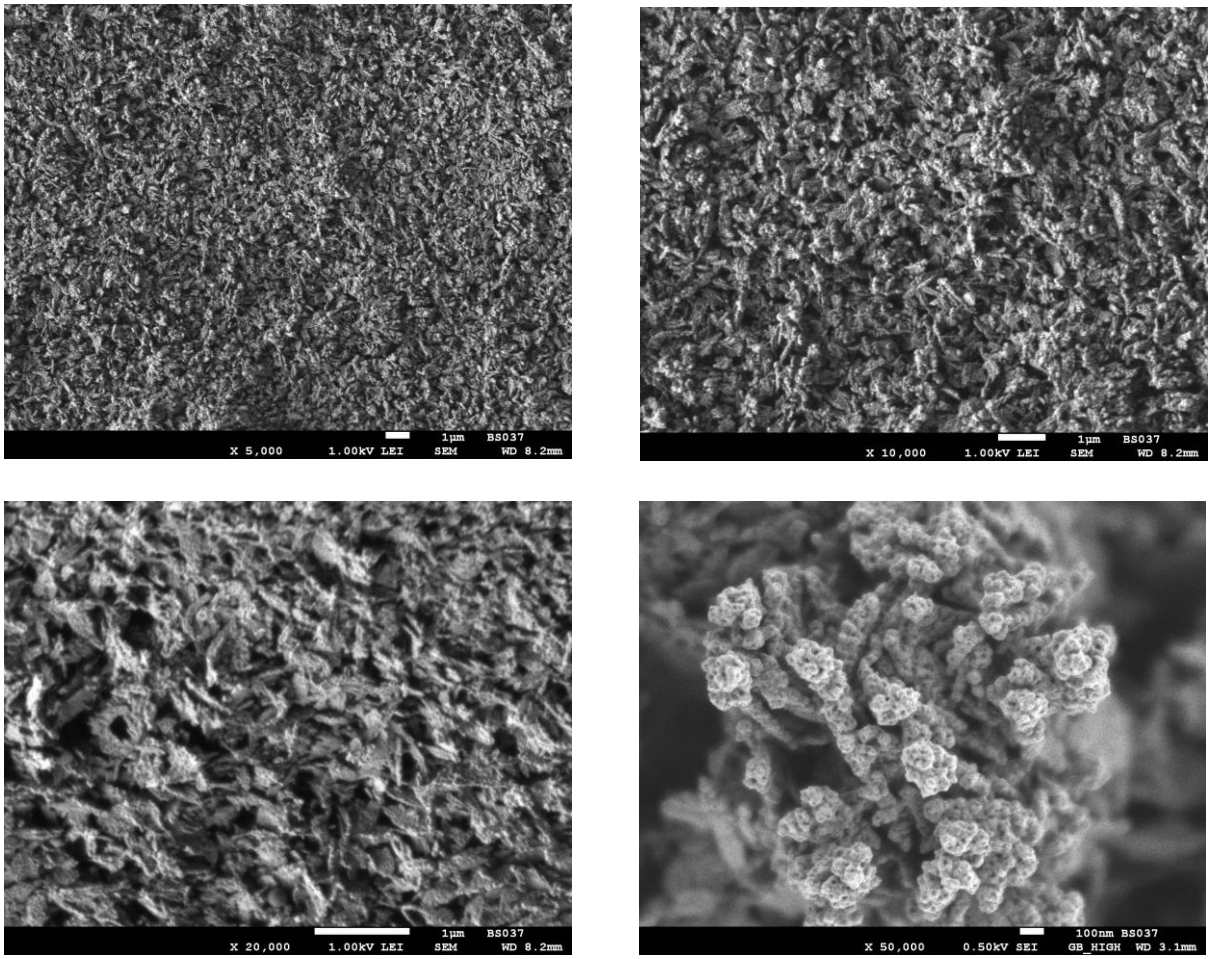

Figure 25. Top-down SEM images of post-electrolysis electrodes used in back pressure experiment.

Figure 25 shows the SEM images of post-mortem CuO-based electrodes after a back pressure experiment. Similar to control experiment, the bright metallic blotches depicted flaky particles with small globular nanoparticle clusters at their tips. Within the coppery islands many, larger, globular nanoparticle clusters were present. Therefore, no significant surface variation on the electrode was detected between control and back pressure experiments.

3.6.2. Experimental Setup for Back Pressure Experiments

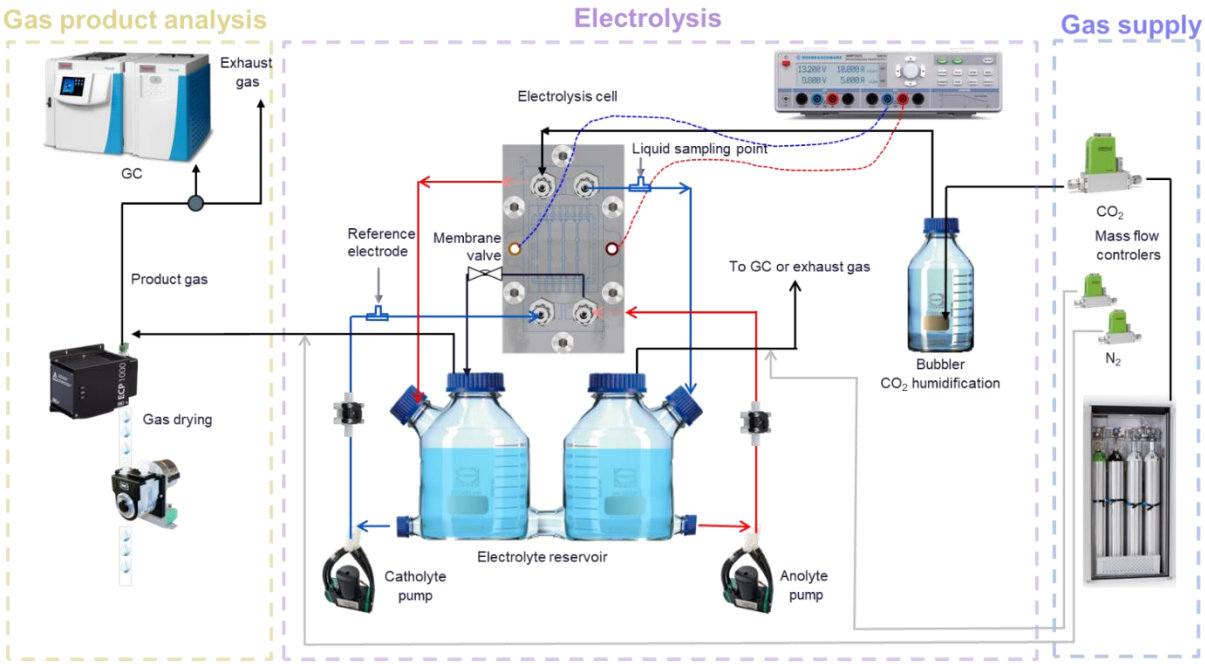

Figure 26. Detailed schematic illustration of the test stand.

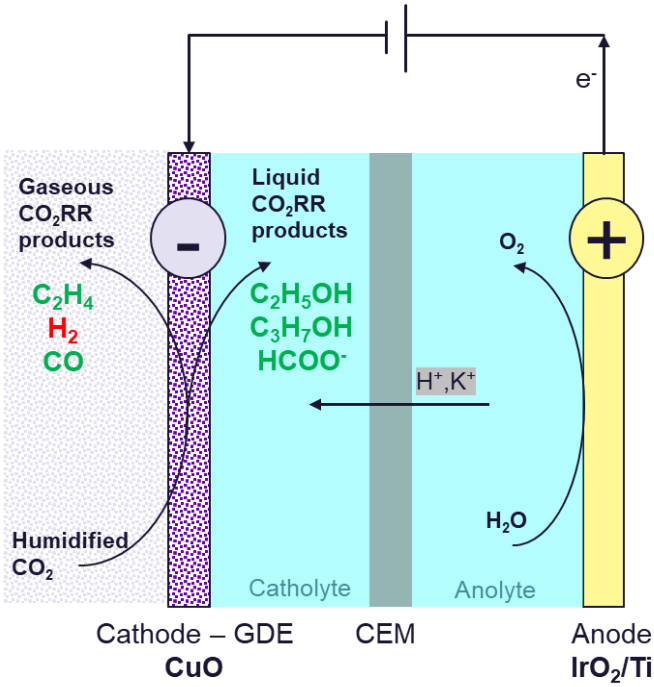

Figure 27. Two-gap flow cell environment for CO_2 electrolysis to hydrocarbons on CuO-based electrode.

3.6.3. Gas Phase Composition under Different Back Pressures and Flow Rates

Normalized cathode gas head space concentrations are given below. Normalization was necessary for scientific reporting as N_2 as the internal standard for quantification was also present in the product gas stream. The amount of N_2 was subtracted from the total product gas stream and the sum of the remaining products was normalized to 100%. The averaged values and their ranges were derived from normalized results of repeated experiments as well as the components' timely change during the first 16 hours of the electrochemical reaction.

Table 2. Normalized bulk gas concentrations in the cathode head space.

Feed flow rate (sccm)	Averaged CO_2 concentration (mol.%)	Averaged C_2H_4 concentration (mol.%)	Averaged CO concentration (mol.%)	Averaged H_2 concentration (mol.%)
14	28.91 ±2.03	10.91 ±2.94	5.88±1.69	51.26 ±11.76
50	81.93 ±2.06	1.83 ±0.14	6.06 ±1.99	10.16 ±2.03

3.6.4. Quantitative Product Analysis

The precision of quantitative product determination was ensured via a number of ways. Potential sources of error were minimized by adding internal standards. Frequent calibration of the measurement instruments was also performed.

3.6.4.1. Liquid products

^{1}H NMR was used for quantification of liquid products. The NMR measurements are performed following the method described by Cuellar et al.[112] in a 500 MHz Bruker (Bruker Bio-Spin, Karlsruhe, Germany). The water peak was suppressed by a pre-saturation sequence. An aliquot of the $KHCO_3$ electrolyte containing liquid products (300 µL) was mixed with 0.1 M sodium fumarate internal standard (50 µL) in D_2O (250 µL) and this mixture analysed by NMR. **Figure 28** illustrates an example of a product spectrum, taken of a liquid sample from a control experiment

and evaluated with MestReNova software. Peaks resulting from the protons of CO_2 liquid products were identified by the help of Chatterjee et al.'s recent study on use of NMR for product analysis in CO_2RR research[132]. **Table 3** lists the liquid products detected in our samples with their chemical shifts and peak properties.

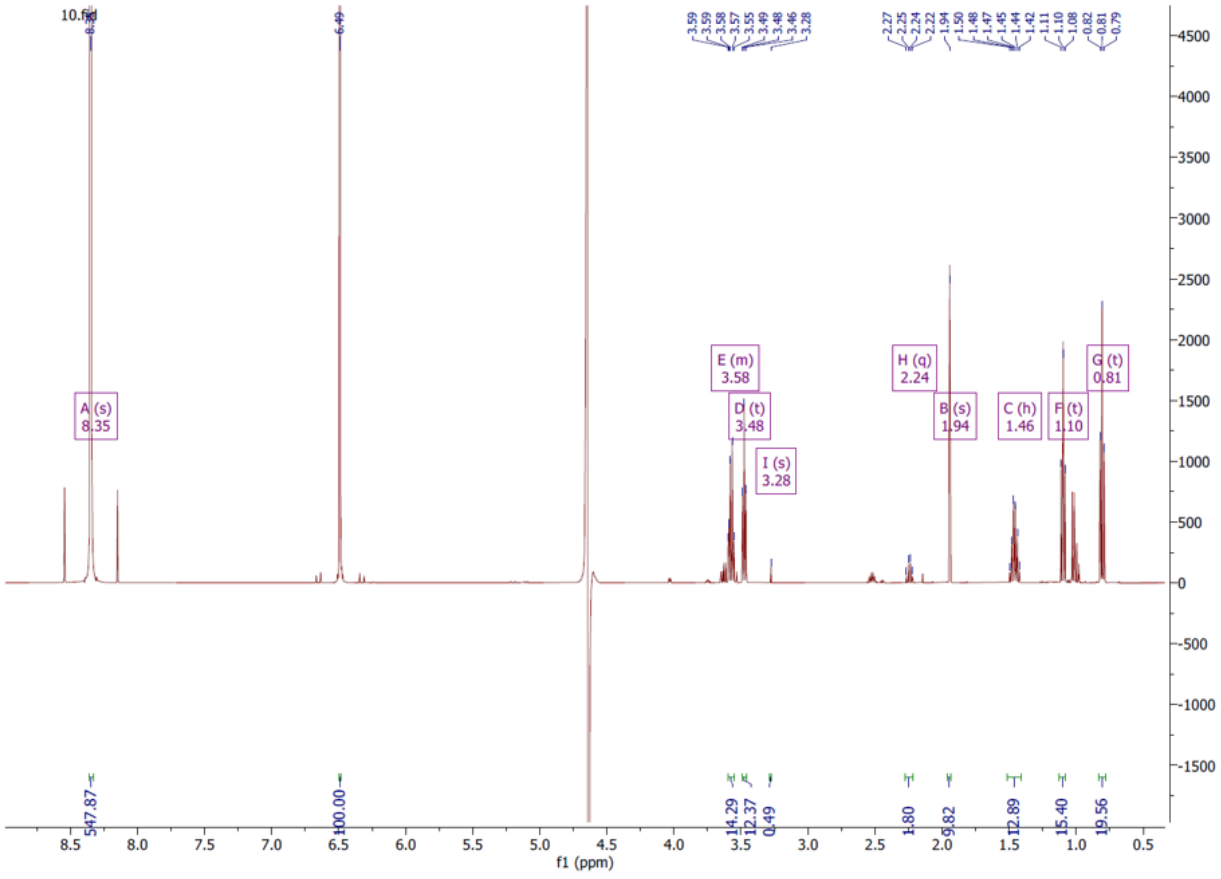

Figure 28. NMR spectrum of a liquid sample of a control experiment.

$$n_{product} = \frac{I_p}{I_{IS}} \times \frac{N_{IS}}{N_p} \times \left(C_{IS} \times \frac{V_{IS}}{V_s} \right) \times V_{electrolyte} \quad (12)$$

Quantification of the liquid products was realized by using Equation 12 , where $n_{product}$ is the mole amount of the quantified product in the electrolyte, $\frac{I_p}{I_{IS}}$ is the ratio of peak integrals of product to that of the internal standard, $\frac{N_{IS}}{N_p}$ is the ratio of number of protons of internal standard to that of the product, C_{IS} is the concentration of stock internal standard solution, $\frac{V_{IS}}{V_s}$ is the ratio of volume of the internal standard solution in the tube to that of the liquid sample taken from the electrolyte, and $V_{electrolyte}$ is the total volume of electrolyte in the experiment. With the calculated molar amounts of each product, the faradaic efficiencies of these products were calculated with the Equation 13**,** where F is the Faraday constant, I is the current in A , e is the number of electrons transferred, t is the electrolysis time in seconds and n is the amount of product in moles.

$$FE = \frac{n \times z \times F}{I \times t} \quad (13)$$

Table 3. NMR chemical shifts of liquid products.

Chemical shift (ppm)	**Compound**	**Splitting**	**Relative area**
0.77-0.90	Propanol	Triplet	3
0.92-1.03	Propionaldehyde	Triplet	3
1.06-1.15	Ethanol	Triplet	3
1.2-1.3	Acetaldehyde	Doublet	3
1.42-1.57	Propanol	Sextet	2
1.47	Propionaldehyde	Doublet of triplets	2
1.87	Acetate	Singlet	3
2.12	Acetaldehyde	Doublet	3
2.44-2.49	Propionaldehyde	Quadruplet	2
3.23-3.33	Methanol	Singlet	3
3.44-3.57	Propanol	Triplet	2
3.53-3.63	Ethanol	Quadruplet	2
3.54	Ethylene glycol	Singlet	4
3.99-4.07	Allyl alcohol	Doublet of triplets	2

4.85-4.95	Propionaldehyde	Triplet	1
4.94-5.03	Glycoaldehyde	Triplet	1
5.07	Allyl alcohol	Doublet	2 in total across both peaks (same protons)
5.17	Allyl alcohol	Doublet	
5.9	Allyl alcohol	Multiplet	1
6.49	Fumarate standard	Singlet	2
8.33	Formate	Singlet	1
9.55-9.65	Acetaldehyde	Quadruplet	1
9.57-9.67	Propionaldehyde	Singlet	1

3.6.4.2. Gas products

As seen in **Figure 26** catholyte gas head space was mixed with internal standard N_2 before being fed to the GC. The N_2 flow rate was set to the same value as that of the CO_2 flow rate. 7890B Agilent (Santa Clara, USA) was used as GC. He was the carrier gas enabling the detection of H_2 as a negative peak. A thermal conductivity detector (TCD) and three serially connected columns were used: a HayeSeP Q-column, a Porapak Q-column for the separation of CH_4, CO_2 and C_2H_4, and a molecular sieve 5 Å-column to separate N_2, O_2, and CO. 1 mL of the gas product was automatically injected every 20 min from the cell to the gas chromatograph during the electrolysis. GC software evaluated the results automatically and reports the gas product composition of the injected sample.

$$\dot{V}_{product} = \frac{n_{p\text{-}GC}}{n_{IS\text{-}GC}} \times \dot{V}_{IS} \qquad (14)$$

Quantification of the gas products was performed with the Equation 14, where $\dot{V}_{product}$ is the volumetric flow rate of the quantified gas product, $\frac{n_{p\text{-}GC}}{n_{IS\text{-}GC}}$ is the ratio of concentration of product concentration to that of internal standard, and $\dot{V}_{IS}$ is the volumetric flow rate of the internal standard. Once the gas product amounts are quantified, faradaic efficiencies of gas products are calculated with the identical equation above.

The above-described quantification method was validated with control experiments. The electrochemical cells were built and tested in the same way as schematically illustrated in **Figure 26** and **Figure 27**. The gas flows (50 sccm for CO_2 gas inlet and 50 sccm N_2 as internal standard, identical to the experiment conditions) and electrolyte liquid loop were initiated. In order to validate the 1:1 ratio of CO_2: N_2, the product stream was measured at GC without applying any electrical potentials to the cells. The results obtained at the 7890B Agilent GC instrument were verified with another GC instrument (Thermofischer 1310). 49.93 ± 0.97 vol. % of CO_2 and 50.05 ± 1.06 vol.% of N_2 were detected in the GC instruments, validating our quantification method.

3.6.5. Product Distributions

Table 4. Product distributions at different flow rates and back pressures in terms of faradaic efficiencies.

λ	ΔP (mbar)	t (h)	CO	H_2	C_2H_4	CH_4	$HCOO^-$	CH_3COO^-	C_2H_5OH	C_3H_7OH	C_3H_5OH
10.78	0	3	18.3 ± 0.6	25.3 ± 0.9	25.2 ± 0.8	0.6 ± 0.3	7.1 ± 1.7	0.8 ± 0.3	7.8 ± 1.0	3.7 ± 0.6	0.5 ± 0.1
10.78	70	3	26.0 ± 2.1	15.9 ± 1.8	23.3 ± 1.7	0.1 ± 0.0	10.4 ± 1.0	1.0 ± 0.1	11.1 ± 0.4	5.9 ± 0.6	0.4 ± 0.0
10.78	130	3	26.7 ± 1.8	14.9 ± 2.6	24.3 ± 1.3	0.0 ± 0.0	10.6 ± 2.3	1.0 ± 0.2	10.7 ± 0.2	5.5 ± 0.1	0.5 ± 0.1
3.01	40	3	4.4 ± 1.0	24.9 ± 0.8	38.5 ± 2.9	0.3 ± 0.3	6.6 ± 3.0	0.9 ± 0.0	13.8 ± 6.4	5.8 ± 1.1	0.3 ± 0.1
3.01	0	3	7.0 ± 0.1	23.9 ± 5.5	31.0 ± 0.3	1.8 ± 1.2	11.0 ± 2.0	3.1 ± 1.0	12.9 ± 6.1	4.6 ± 0.2	0.9 ± 0.1
10.78	0	24	9.4 ± 0.6	34.9 ± 3.6	24.6 ± 2.2	0.7 ± 0.2	3.6 ± 3.0	1.3 ± 0.7	6.8 ± 0.7	3.5 ± 0.6	0.2 ± 0.1
10.78	70	24	17.9 ± 2.7	16.4 ± 2.1	28.7 ± 2.1	0.1 ± 0.0	7.3 ± 2,7	1.1 ± 0.0	7.7 ± 0.7	5.3 ± 0.4	0.2 ± 0.0
10.78	130	24	22.0 ± 2.3	15.2 ± 2.0	25.3 ± 1.3	0.0 ± 0.0	8.3 ± 3.3	0.8 ± 0.1	7.7 ± 1.8	4.9 ± 0.3	0.2 ± 0.1
10.78	0	48	5.0 ± 1.0	58.3 ± 10.4	15.3 ± 5.3	0.4 ± 0.2	1.0 ± 0.5	1.6 ± 1.3	4.1 ± 1.0	1.8 ± 0.6	0.1 ± 0.0
10.78	70	48	13.5 ± 2.6	19.4 ± 3.4	26.5 ± 1.3	0.1 ± 0.1	5.2 ± 4.2	1.8 ± 0.4	7.4 ± 2.2	5.0 ± 1.1	0.1 ± 0.1
10.78	130	48	17.5 ±2.0	15.2 ± 1.0	26.0 ± 4.0	0.0 ± 0.0	10.0 ± 2.0	1.2 ± 0.2	5.4 ± 0.8	4.7 ± 0.1	0.1 ± 0.0

3.6.6. Deconvolution of Back Pressure Effects on Stability and Selectivity

Faradaic efficiencies of three experiment series with various absolute pressures assured by back pressure valves and various partial pressures of CO_2 obtained by N_2 dilution were presented below. The in-depth discussion about the observed trends can be found in the manuscript.

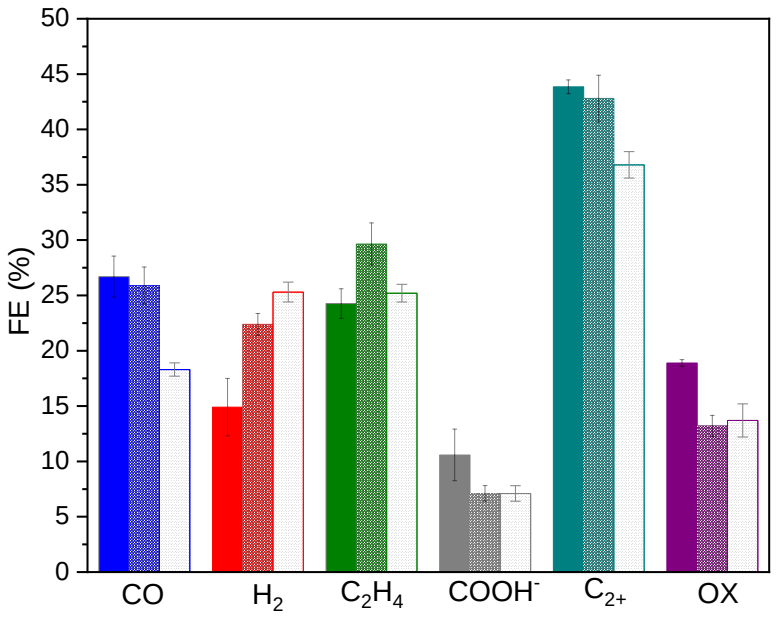

Figure 29. Product distributions of experiments at t = 3 h with P_{abs} = 1.13 bar, P_{CO2} = 1.13 represented with filled blocks; P_{abs} = 1.13 bar, P_{CO2} = 1.00 bar represented with checkered blocks; P_{abs} = 1.00 bar, P_{CO2} = 1.00 bar represented with dotted blocks.

4. Accumulation of Liquid Byproducts in an Electrolyte as a Critical Factor That Compromises Long-Term Functionality of CO_2-to-C_2H_4 Electrolysis

Similar to back pressure, the concentration of liquid product species in the electrolyte, as another operational parameter for CO_2 electrolyzers, has not been studied, creating a research gap. It was crucial to explore the negative effects of this operational parameter as it establishes critical upper limits for the concentration of liquid products in the electrolyte. The downstream process of an industrial CO_2 electrolyzer, including liquid product separation, must adhere to these concentration limits. Motivated by these considerations, we conducted a dedicated study to quantify the effects of liquid byproduct accumulation in the electrolyte, presented in this chapter.

The study revealed that high concentrations of alcohol products can adversely impact the stability and selectivity of the cathode GDE. Additionally, exposure to high alcohol concentrations led to catalyst layer abrasion and structural disfigurements, even with relatively short exposure times in lab-scale research compared to industrial-scale applications. This raises concerns about upscaling and prompts new scientific inquiries into the long-term effects of exposure to alcohols, even in low concentrations.

Importantly, all the aforementioned aspects also influence the economic feasibility of CO_2 electrolyzers. The need for electrolyzer maintenance resulting from long-term exposure to liquid byproducts must be considered in economic assessments. The study's findings highlight the necessity for researchers to be mindful of liquid byproduct concentrations in their experimental setups (e.g., avoiding very small electrolyte volumes to prevent concentrated liquid products) and in the interpretation of experimental results, especially in terms of long-term stability. Without necessary countermeasures, the accumulation of alcohols could eventually lead to degradation. From an industrial scaling perspective, this study can serve as a guideline for designing downstream processes of CO_2 electrolyzers, particularly in liquid product separation.

This chapter is based on the following publication [133]:

Sahin, B., Raymond, S. K., Ntourmas, F., Pastusiak, R., Wiesner-Fleischer, K., Fleischer, M., Simon, E., Hinrichsen, O. (2023), Accumulation of Liquid Byproducts in an Electrolyte as a Critical Factor That Compromises Long-Term Functionality of CO_2-to-C_2H_4 Electrolysis, ACS Appl. Mater. Interfaces. 15 (9), 45844-45854. DOI: 10.1021/acsami.3c08454.

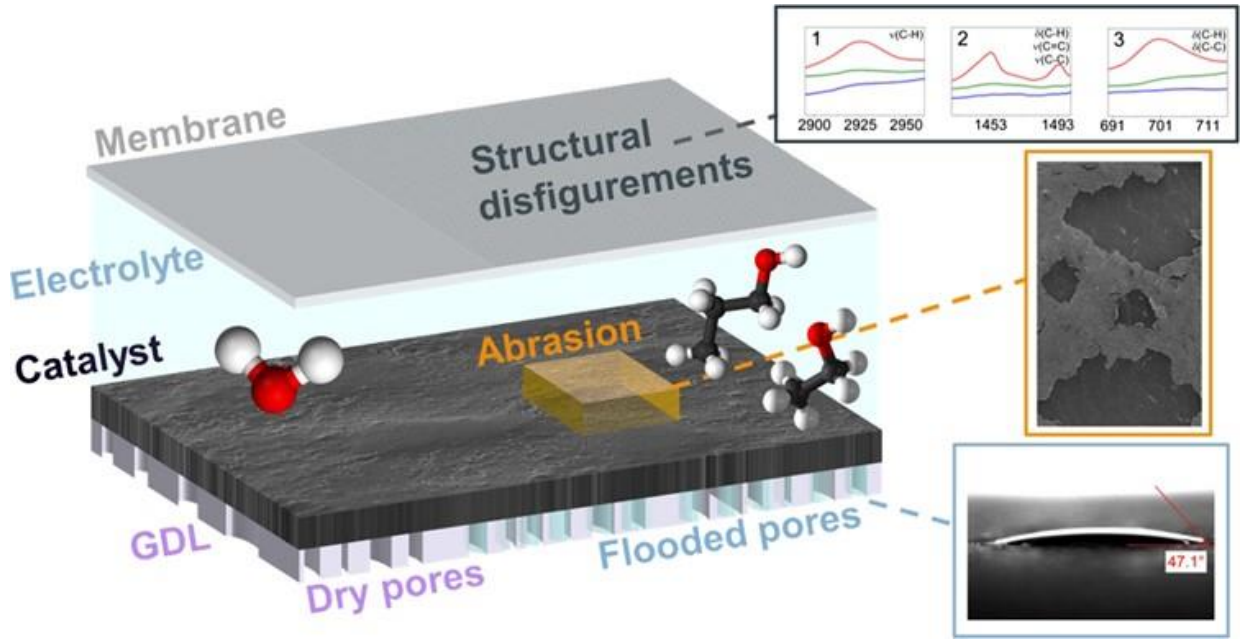

The contributions of the authors are summarized as follows:

- Baran Sahin: Conceptualization, methodology, experimental investigation, validation, data evaluation, manuscript preparation and visualization.
- Samantha K. Raymond: Experimental investigation, data evaluation and visualization.
- Felix Ntourmas: Experimental investigation and data evaluation.
- Remigiusz Pastusiak: Visualization and manuscript editing.
- Kerstin Wiesner-Fleischer: Project administration, funding acquisition and manuscript editing.
- Maximillian Fleischer: Funding acquisition and manuscript editing.
- Elfriede Simon: Conceptualization, methodology, supervision, funding acquisition and manuscript editing.
- Olaf Hinrichsen: Supervision and manuscript editing.

4.1. Abstract

Electrochemical conversion of CO_2 using Cu-based gas diffusion electrodes opens the way to green chemical production as an alternative to thermocatalytic processes and a storage solution for intermittent renewable electricity. However, diverse challenges, including short lifetimes, currently inhibit their industrial usage. Among well-studied determinants such as catalyst characteristics and electrode architecture, possible effects of byproduct accumulation in the electrolyte as an operational factor have not been elucidated. This work quantifies the influence of ethanol, *n*-propanol, and formate accumulation on selectivity, stability, and cell potential in a CO_2-to-C_2H_4 electrolyzer. Alcohols accelerated flooding by degrading the hydrophobic electrode characteristics, undermining selective and stable ethylene formation. Furthermore, high alcohol concentrations triggered the catalyst layer's abrasion and structural disfigurements in the Nafion 117 membrane, leading to high cell potentials. Therefore, continuous removal of alcohols from the electrolyte medium or substantial modifications in the cell components must be considered to ensure long-term performing CO_2-to-C_2H_4 electrolyzers.

4.2. Introduction

CO_2 electrolysis to multicarbon products receives great interest from academia and industry due to its potential contribution to the defossilization of the chemical industry by supplying green feedstock, replacing thermocatalytic processes, and being an alternative solution to the storage of intermittent renewable electricity supply [20,134]. Techno-economical assessment studies show that low-temperature CO_2 electrochemical conversion can be economically viable, particularly when the product price and its market size are attractive, as in the case for C_2H_4 [28,135]. The global market for C_2H_4 is expected to surpass 200 billion USD by 2028,[136] paving the way for the demand of upscale green ethylene production.

Cu is the only catalyst that can electrochemically reduce CO_2 into C_{2+} products such as ethylene, ethanol, acetate, acetaldehyde, *n*-propanol, propionate, and propionaldehyde, in addition to C_1 products such as carbon monoxide, formate, methane, and methanol [41]. Besides the CO_2 reduction reaction (CO_2RR), Cu also catalyzes the parasitic hydrogen evolving reaction (HER), reducing water to H_2 [48]. CO_2RR and HER have very similar thermodynamic requirements: CO_2RR between −0.1 and +0.1 V and HER at 0 V versus the pH-independent reversible hydrogen electrode [20]. CO_2RR, especially to C_{2+} products, necessitates much more complex kinetic mechanisms than HER and thus requires higher cathodic overpotentials [71]. Therefore, once the requirements enabling the CO_2RR over HER do not prevail, the faradic selectivity is driven to the uncomplicated HER.

These required properties for maintaining stability and selectivity are widely discussed in the literature. The following are postulated: Cu oxidation state [94,137–139], catalyst morphology [140–142], pH [71,129,143], CO_2 availability [95,107,125,144], the surface coverage of reaction intermediates [69,145,146], and electrode design [107,147–149]. Different phenomena, including the most discussed electrode flooding, can cause changes in the above-mentioned fine-tuned properties and result in the switch to HER.

The flooding phenomenon can be defined as the penetration of liquids into the pores of the gas diffusion layer, blocking the CO_2 diffusion pathway partially or entirely. CO_2-depleted zones in the catalyst layer create a mass transfer limitation for CO_2RR, and therefore the Cu electrode dominantly catalyzes HER to meet the faradic rule [20]. Causes of GDE flooding are well established in the literature and include electrowetting [144,150–152], salt formation in the GDE [124,144,153], pressure distributions inside the GDE [154,155], feed gas humidification [156,157], and polymerization of reaction intermediates on the catalyst layer [158]. These can occur concurrently, especially salt formation in the GDE is reported to amplify the flooding phenomenon [124,150,151,153,159] regardless of the root cause.

Future CO_2 electrolyzers must also be efficient besides being selective and stable. Wyndorps et al.[160] showed that CO_2 to C_2H_4 electrolyzers must have lower than 2.5 V cell potentials to compete with the alternative C_2H_4 production route (direct methanol production with H_2 from PEM electrolyzers and CO_2 from direct air capture and subsequent ethylene production via methanol-to-olefins) in terms of GHG reduction. As for economic feasibility, Sisler et al.[28] reported that CO_2 to C_2H_4 electrolyzers (both one-step direct electrolysis and two-step conversion including CO_2 to CO with a solid oxide fuel cell and a subsequent CO to C_2H_4 electrolyzer) in any case must have cell potentials lower than 2.5 V to come anywhere near to the reference ethylene price of 1000 $/ton. Hence, every cell resistance contributing to the total cell potential becomes vital to understanding and optimized.

CO_2RR systems at industrially relevant current densities run in the flow cell systems in which the liquid phase (electrolyte and liquid products) flow is maintained by pumps. Gas species (feed and products) flow continuously in and out of the system regulated by mass flow controllers in steady-state conditions. The liquid flow is circulated in a closed loop in lab-scale test rigs, which results in unsteady-state conditions for several parameters such as bulk phase pH and liquid product concentration. Catholyte pH increases and anolyte pH decreases in the course of the reaction unless catholyte and anolyte streams are mixed (**Figure 30A**) to compensate for the OH^- generation in the cathode with H^+ generation, stabilizing the pH overall (**Figure 40** in Supporting Information). The second unsteady-state condition, i.e., liquid product accumulation in the electrolyte, requires continuous separation of each liquid product from the aqueous electrolyte solution. It is a sophisticated engineering problem that is not the focus of electrochemical CO_2RR research in general. Nevertheless, electrochemical measurement results in **Figure 30B** suggest that increasing concentrations of the main liquid products coincide with decreasing $FE_{C_2H_4}$ and increasing FE_{H_2}.

A few researchers mentioned that liquid products such as alcohols might negatively affect the gas diffusion electrode and the membrane [144,161,162]. Leonard et al.[162] showed that the wettability of bare graphite and PTFE substrates increases as formic acid and alcohols are introduced as liquid droplets on them in ex situ experiments. Li et al. [144] discussed the desired wetting conditions of the electrode components for ideal CO_2RR performance in their review work and briefly mentioned the possible effects of alcohols. Gabardo et al. [161] reported that the

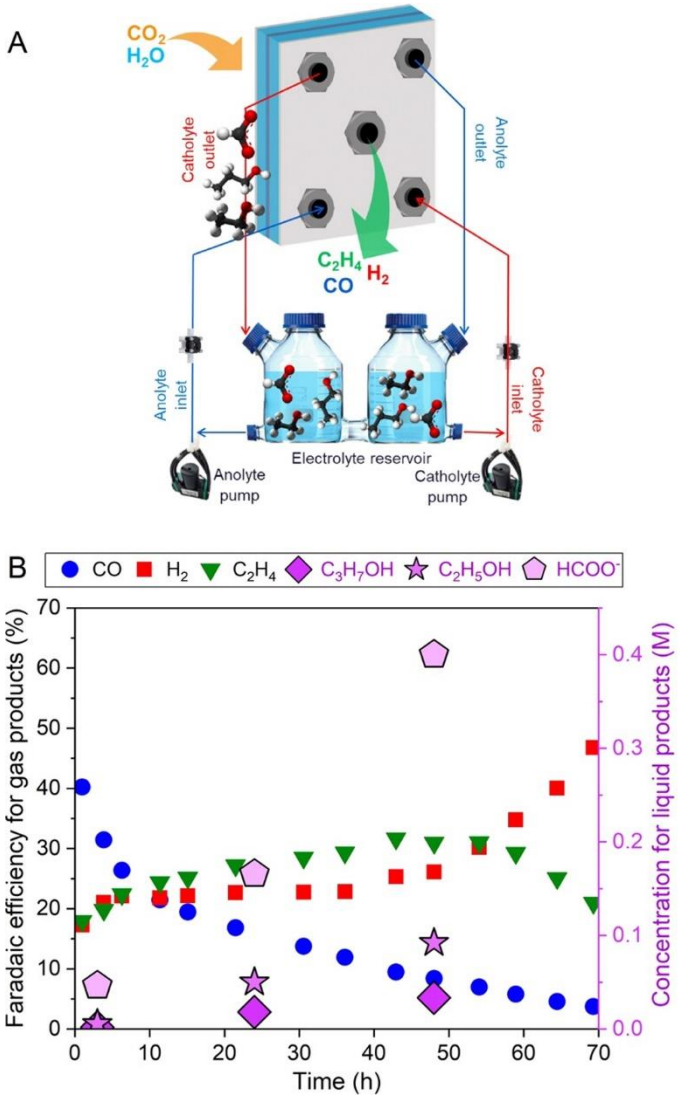

Figure 30. Schematic demonstration of the mixed-electrolyte flow cell system for CO_2 electrolysis in Cu electrodes (**A**). Formation of the CO_2RR gas and liquid products as well as parasitic HER product H_2 with a CuO-based electrode over time at 200 mA/cm^2 (**B**).

membrane used in CO_2RR experiments formed holes in the presence of concentrated alcohols in the electrolyte. Although various ideas and observations on wettability and flooding have been reported in the CO_2RR research, the all-around evaluation of the liquid product effects on CO_2 to C_2H_4 electrolyzers by systematic experiments is still an existing research gap in the field.

Herein, we report the effects of liquid product accumulation on the selectivity, stability, and cell potential of the CO_2RR with Cu electrodes. Selectivity toward the CO_2RR was significantly tilted to the HER in the presence of alcohols in the electrolyte. The electrochemical measurements at 200 mA/cm^2 proved that the cathode reaction was almost exclusively HER at high concentrations of ethanol (EtOH) and *n*-propanol (PrOH), 5.12 and 1.89 M, respectively. Mild concentrations of EtOH and PrOH, 1.54 and 0.57 M, respectively, triggered the formation of acetate and propionate. Stable ethylene formation declined severely from 50 h down until 1 h in the presence of EtOH and PrOH, depending on their concentration. Decreased surface tension between the electrode surface and the electrolyte due to alcohols was hypothesized to cause electrode flooding and the selectivity shift to H_2 together with shorter stability. Contact angle measurement results confirmed that EtOH and PrOH containment in the electrolyte obliterates the hydrophobic nature of the electrode surface (θ_{H_2O}= 141.3 ≥ 90°) and turned it into a hydrophilic surface ($\theta_{H_2O:EtOH} < 90°$ and $\theta_{H_2O:PrOH} < 90°$). SEM images revealed the alcohols to be disruptive to the electrode surface, possibly by defunctionalizing the ionomer binder, which glued the catalyst particles to each other and the gas diffusion layer. The significantly high cell potentials recorded in the tests with 5.12 M EtOH were proven to relate with irreversible structural changes in the membrane that may have resulted in the obstructed cation conductivity.

4.3. Experimental Section

Electrode preparation, experimental setup, and liquid product analysis methods, product quantification methods were identical to our previous work [95], elucidated in **Section 3.3**.

4.3.1. Gas product analysis

A gas chromatograph (GC) instrument (Thermo Scientific Trace 1410) equipped with two thermal conductivity detector channels (TCD) for H_2, CO_2, O_2, N_2, and CO, and a flame ionization detector channel (FID) for CH_4 and C_2H_4 was connected to the test stand for performing online analyses of the product gas composition. Further, 5 Å mol-sieve columns (Restek) and micropacked GC columns (HayeSeP Q, Restek) were used to separate the gas mixture with Ar and He carrier gases. One milliliter of the gas product was automatically injected to the GC sampler every 8 min. The product stream was mixed with internal standard N_2 before being fed to the GC. Chromeleon software was used for the automated measurements and data evaluation.

4.3.2. Estimation of Accumulating Product Concentrations

Amounts of formate, EtOH, and PrOH accumulated in the electrolyte after 24 h during the control experiments were determined using NMR quantitative analysis. Their average reaction rates (mol cm^{-1} h^{-1}) between t = 0 and t = 24 h were calculated. Assuming constant reaction rates throughout the operation, the hypothetical accumulation concentrations of EtOH and PrOH were calculated for the 10th, 30th, and 100th day. Accordingly, concentrations of 0.51 M EtOH and 0.19 M PrOH after 10 days, concentrations of 1.54 M EtOH and 0.57 M PrOH after 30 days, and concentrations of 5.12 M EtOH and 1.89 M PrOH after 100 days would be reached in the defined experimental setup under the defined experimental conditions with the Cu electrode described in this work. The calculated hypothetical amounts of alcohols were added to the electrolyte prior to the experiment to stimulate their accumulation effects in the electrolyte without having to wait for 10, 30, or 100 days. The details of the calculations are summarized in **Table 5**, **Table 6** and **Table 7** in Supporting Information.

4.3.3. Electrode Characterization

Characterizing the hydrophilicity of the electrode surface was achieved by contact angle measurements. A Kruess MSA (Kruess Scientific) instrument was used with its sessile drop method. A drop of a test liquid was dispensed onto the sample. A video image of the drop was analyzed, and the contact angle was measured as the angle between the contour of the drop and the line representing the surface (baseline). Test liquids were pure water (obtained by Milli-Q instrument, Merck), mixtures of pure water and EtOH, and mixtures of pure water and PrOH. The mixtures were prepared in the identical concentrations of the experimented 10th, 30th, and 100th day of EtOH and PrOH in water. Software Advance by Kruess did the automatic data evaluation of the experiments.

Scanning electron micrographs (SEM) of the postelectrolysis gas diffusion electrodes were taken at different magnifications with a highresolution field emission scanning electron microscope (JSM-7500F, JEOL).

4.3.4. Membrane Characterization

The chemical structure of the membrane was characterized by a Fourier transform infrared (FTIR) spectrometer (PerkinElmer Spectrum Two) equipped with a $LiTaO_3$ MIR detector and an optical system with KBr windows. A universal attenuated total reflection (UATR) accessory by the manufacturer with a diamond crystal was used to examine the membrane samples directly in their as-is state without further preparation. The spectra were obtained from 4000 to 450 cm^{-1} at a spectral resolution of 4 cm^{-1}. The number of scans was set to 16 after preliminary runs showed a sufficiently high signal-to-noise ratio. Before each measurement, the crystals were cleaned, dried, and checked for contamination by collecting and comparing a background spectrum. Contact pressure between the sample and the crystal's surface was achieved by using a force gauge-controlled pressure arm. After each measurement, a polynomial baseline correction was applied

to all spectra, and the measured transmittance was converted into absorbance ($A = -\log T$). The further evaluation of the spectra, especially the bands' interpretation, was carried out by using irAnalyze software.

4.4. Results and Discussion

The three main reaction products in the aqueous electrolyte phase are formate, ethanol, and *n*-propanol and their accumulation in the course of the reaction is the focus of this article. As formate is an ionic species, it was added to the system in two forms: formic acid ($pK_a = 3.7$) and potassium formate ($pK_b = 10.7$), introducing no foreign ions to the liquid phase with products and a 1 M $KHCO_3$ buffer solution. However, these species change the bulk pH of the electrolyte significantly, ruling out the deconvolution of the pH and formate accumulation effects from each other in this work. Interestingly, neutral conditions (pH = 7 with 0.83 M HCOOH-containing 1 M $KHCO_3$ electrolyte) enabled the most extended stable ethylene formation of 92 h among all experiments, as shown in **Figure 35**. This finding is in line with the latest opinions in the literature about the influence of alkalinity on poor electrode stability despite its kinetic promotion for C_{2+} formation [69,124,143,144,146,156]. This is comprehensively discussed in the Supporting Information (**Section 4.6**). The remaining main liquid products are alcohols, and their accumulation effects are considered from three perspectives: selectivity, stability, and cell potential.

4.4.1. Influences on Selectivity and Stability

Electrochemical control experiments at 200 mA/cm^2 resulted in the accumulation of 0.0128 mol EtOH and 0.0048 mol PrOH within 24 h of the reaction. The hypothetical accumulated amounts after 10, 30, and 100 days of CO_2RR in the same conditions were calculated based on the assumption of the constant reaction rate observed in the first 24 h of control experiments (a detailed explanation and corresponding calculations are presented in the Supporting Information). These amounts were added to a 1 M $KHCO_3$ electrolyte prior to the experiment to uncover their

accumulation effects without running the experiments for 10 days. It was estimated that the concentration of EtOH would be 0.51, 1.54, and 5.12 M after 10, 30, and 100 days, respectively, in 250 mL of a 1 M $KHCO_3$ electrolyte; likewise, the PrOH concentration would be 0.19, 0.57, and 1.89 M, respectively. The three concentration levels for each species corresponding to the hypothetical reaction durations will be referred to as the first, second, and third concentration levels for readability throughout the article.

Full product spectra obtained after 3 h of chronopotentiometric measurements at 200 mA/cm^2 with alcohol-containing electrolytes are shown in **Figure 31A**, **Figure 31B**. Important to note is that faradic efficiency for the added species in corresponding experiments was not calculated, for example, FE_{EtOH} was not calculated if ethanol was added to the electrolyte. First level concentrations for both EtOH and PrOH minimally affected the full product spectrum compared to the control experiments, except for acetate and propionate formation. A 0.51 M EtOH concentration in the electrolyte induced acetate formation significantly, increasing $FE_{CH_3COO^-}$ from 0.8 to 6.2%. A 0.19 M PrOH concentration induced propionate formation notably, increasing $FE_{C_2H_5COO^-}$ from 0.2 to 3.2%. Second level concentrations of both alcohols changed the product spectrum compared to the control experiments in an analogous manner: H_2 became the main produced species following the FE_{H_2} gains from 20.4% in control experiments to 31.9 and 45.3% in 1.54 M EtOH and 0.57 M PrOH-containing electrolyte media, respectively. FE_{CO} decreased from 29.9% in the control experiments to 14.9 and 6.9% with 1.54 M EtOH and 0.57 M PrOH concentrations in the electrolyte, respectively. The trend regarding acetate and propionate formation grew stronger with second level alcohol concentrations in the electrolyte: $FE_{CH_3COO^-}$ reached 8.6% and $FE_{C_2H_5COO^-}$ extended to 9.8% with EtOH and PrOH addition, respectively. Intriguingly, there was no notable change in the selectivity of other C_{2+} products including C_2H_4 with the first and second level concentrations. Third level concentrations (5.12 M EtOH and 1.89

M PrOH) suppressed the CO_2RR entirely and drove the selectivity to a single product, H_2. All of the other product species were detected only in trace amounts.

Even though the first and the second concentration levels of alcohols seemed not to affect C_{2+} and especially C_2H_4 selectivity at t = 3 h, the stability experiments unveiled that alcohol addition to the electrolyte reduced the duration of stable C_2H_4 formation, as presented in **Figure 31C**, **Figure 31D**. $FE_{C_2H_4}$ at t = 24 h differs depending on the alcohol content in the electrolyte and it follows: Control experiment > 0.51 M EtOH ≈ 0.19 M PrOH > 1.54 M EtOH > 0.57 M PrOH > 1.89 M PrOH ≈ 5.12 M PrOH. Third level concentrations of both species allowed C_2H_4 formation only in trace amounts, and 0.57 M PrOH also ppressed C_2H_4 formation almost completely at t = 24 h. Control experiments and experiments with first level concentrations exhibited stable C_2H_4 formation for over 50 h. The second level concentrations cut down the stability, not even qualifying a stable C_2H_4 formation of 12 h.

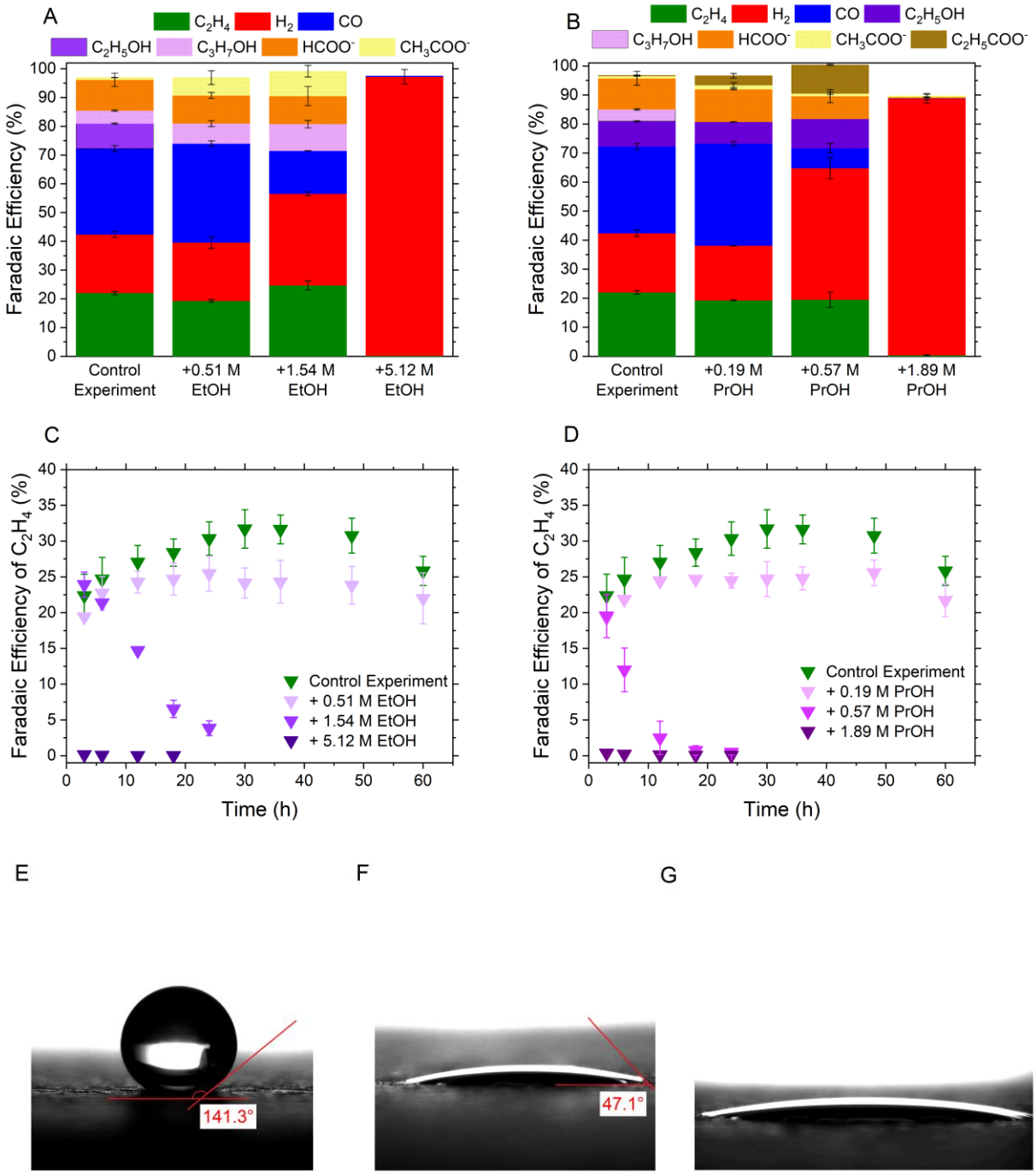

Figure 31. Product spectra at t = 3 h of electrochemical measurements at 200 mA/cm^2 with different initial ethanol concentrations (**A**). Product spectra at 3 h of electrochemical measurements at 200 mA/cm^2 with different initial *n*-propanol concentrations (**B**). Stability of C_2H_4 formation over time at 200 mA/cm^2 with different initial ethanol concentrations (**C**). Stability of C_2H_4 formation over time at 200 mA/cm^2 with different initial *n*-propanol concentrations (**D**). Contact angle measurement of a single H_2O droplet on the catalyst layer of the GDE (**E**). Contact angle measurement of a single droplet from a 0.51 M aqueous ethanol mixture on the catalyst layer of GDE (**F**). Contact angle measurement of a single droplet from a 0.19 M aqueous *n*-propanol mixture on the catalyst layer of GDE (**G**).

All experimental results coherently indicate that the accumulation of EtOH and PrOH worsens the selectivity for CO_2RR products as well as the C_2H_4 formation rate over time. This observation supports the hypothesis that the presence of alcohols turns the hydrophobic electrode into a hydrophile one and accelerates the flooding phenomenon. In order to characterize the wetting effects of alcohols, a series of contact angle measurements were performed on the pristine GDEs with pure water and alcohol:water mixtures. As the measured contact angle of 141.3 ± 1.0° between the pure water droplet and the catalyst side of the GDE suggested, the GDE is highly hydrophobic (θ_{H_2O}= 141.3 ≥ 90°, shown in **Figure 31E**). The wetting behaviors almost at the super hydrophobicity level were defined as $\theta_{H_2O} \geq 150°$ [163]. EtOH/H_2O and PrOH/H_2O mixtures were tested for wettability at the hypothetical first, second, and third level concentrations. Alcohol/water mixture droplets wetted the GDE very easily, and the surface exhibited hydrophilic behavior at every tested concentration. A contact angle of 47.1 ± 9.6° was measured between the 0.51 M EtOH/ H_2O droplet, and the catalyst side of the GDE **Figure 31F**) before the droplet was totally absorbed by the electrode surface within approximately 5 s. The 1.54 and 5.12 M EtOH/H_2O droplets did not form a circular shape and were rapidly absorbed by the electrode surface within approximately 3 and 4 s, respectively. Therefore, contact angle measurements were not possible for these concentrations of the EtOH/H_2O mixtures. For PrOH/H_2O mixtures, no contact angle measurements were possible at even the lowest concentration of 0.19 M, as the droplets were too quickly absorbed for proper measurements. **Figure 31G** is a capture from the microscope video camera, which could be taken before the 0.19 M PrOH/ H_2O droplet was absorbed within approximately 3 s. Postmortem electrode samples did not suit contact angle measurements, as they were already wet with a salt electrolyte medium after the electrochemical measurements. Procedures such as drying or washing were excluded, as they redefine hydrophilicity.

In light of these findings, it is possible to hypothesize that the accumulation of EtOH and PrOH can steer the selectivity to H_2 by escalating the wetting and subsequent flooding of the

electrode. This hypothesis corroborates the findings of a great deal of the previous modeling and experimental works on the wettability of aqueous alcohol mixtures on hydrophobic surfaces [164,165]. The hydrophobic electrode surface normally disrupts the hydrogen-bonded water network; therefore, the water molecules must pay a large entropic penalty to be next to the surface. EtOH and PrOH, which possess both hydrophobic and hydrophilic segments, may position close to the hydrophobic surface with their hydrophobic segments facing the surface. Their hydrophilic groups may build hydrogen networks with the water molecules, enabling the approach of water molecules to the surface without having to pay a large entropic penalty [165]. Consequently, alcohol existence can reduce the surface tension, leading to effortless wetting of the initially highly hydrophobic electrode. If the pores of the gas diffusion layer are fully occupied due to wetting, this circumvents the transport of CO_2 molecules in the gas form to the catalyst layer since they must be solved in the liquid phase. The CO_2 solubility thereby limits the CO_2 supply in the wetting medium, giving rise to the unfavorable mass diffusion limitations, often referred to as electrode flooding. **Figure 32** depicts alcohol molecules being able to concentrate in the immediate vicinity of the

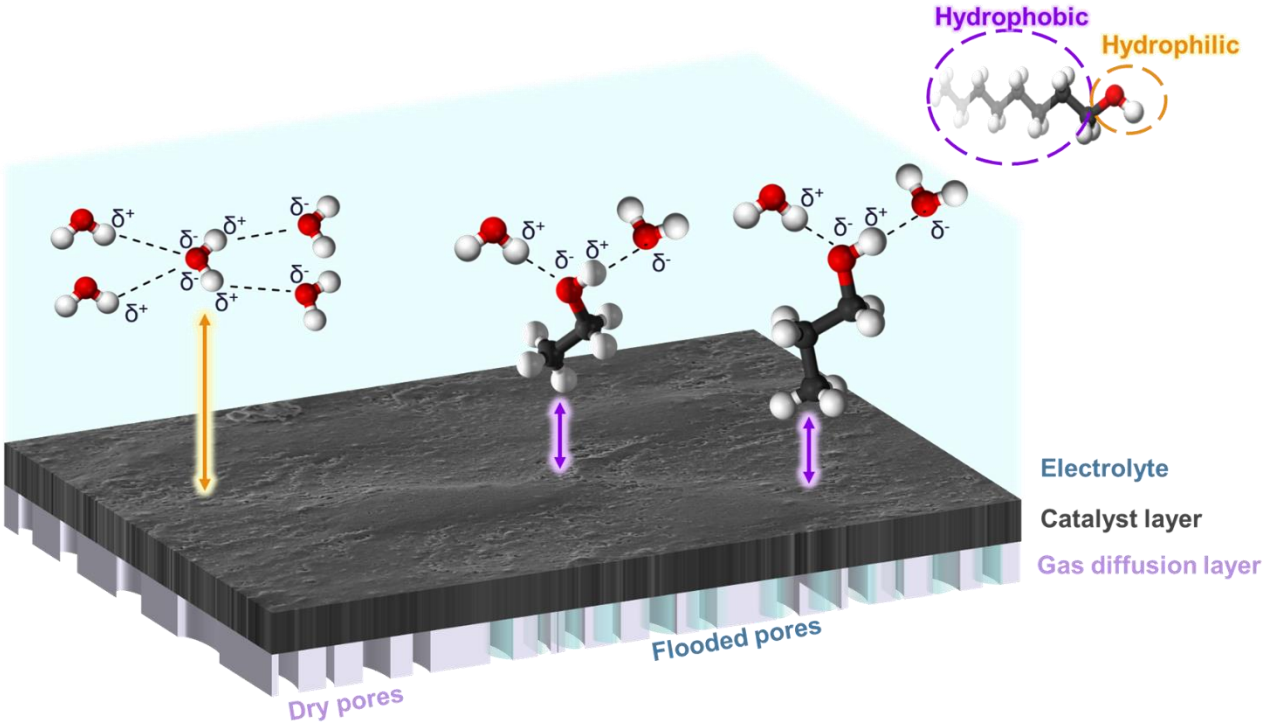

Figure 32. Illustration of the flooding phenomenon of the hydrophobic electrode surface with ethanol and *n*-propanol. Red, white, and black colored atoms correspond to oxygen, hydrogen, and carbon atoms, respectively. The orange arrow represents the distance of the hydrogen-bonded water network to the hydrophobic electrode surface. Purple arrows represent the distance of hydrogen networks of alcohol with water molecules to the hydrophobic electrode surface. Depiction is not to scale.

hydrophobic electrode and penetrating the liquid phase elements into the gas diffusion layer pores, whereas water molecules without alcohols form a hydrogen network only with each other.

Flooding does interfere with several crucial requirements for maintaining the CO_2RR, leading to an essential failure of the CO_2 electrolysis system, as proven in our results above. The primary failing requirement is the hydrophobic electrode design; consequently, the CO_2 availability and the surface coverage of the CO_2 reduction intermediates fail as well. The reason PrOH had more drastic effects on the CO_2RR failure at even lower concentrations compared to EtOH can be that PrOH has a higher wettability. In agreement with the literature [165,166], we argue that PrOH may be present close to the surface in higher interfacial concentrations lowering the polarity and, therefore, the dipole−dipole cohesive forces of the electrolyte. This results in a lower surface

tension and higher wettability with PrOH compared to EtOH. Another striking effect was discovered by the postmortem SEM imaging of the GDEs tested in the electrolytes containing 5.12 M EtOH and 1.89 M PrOH. **Figure 33** illustrates that the GDE tested in the control experiment stayed intact, whereas the GDEs tested in the third level alcohol concentrations showed distinct indications of catalyst layer abrasion. No such effects were observed in the rest of the experiments with lower alcohol contents. Visible dark gray spots/areas representing the bottom layer (carbon-based gas diffusion layer) signified that the light gray layer representing the top layer (CuO-based catalyst layer) was abraded. The anionic exchange ionomer binding the two layers together is

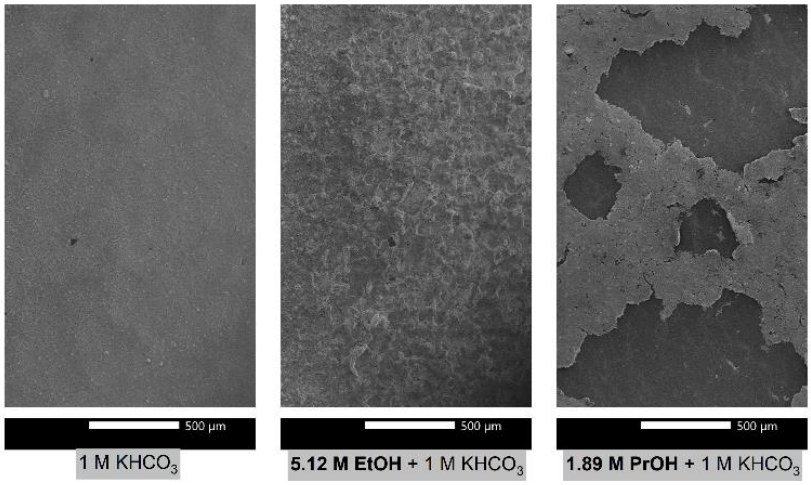

Figure 33. Post-mortem top view SEM images of copper oxide coated GDEs tested in different electrolyte media for 48 hours at 200 mA/cm^2. From left to right: GDE tested in 1 M $KHCO_3$ electrolyte, GDE tested in electrolyte containing 1 M $KHCO_3$ and 5.12 M ethanol, GDE tested in electrolyte containing 1 M $KHCO_3$ and 1.89 M *n*-propanol. The top layer is the CuO catalyst layer (light grey), and the bottom layer is the carbon-based gas diffusion layer (dark grey).

knowingly dispersible by the alcohols. This property of the used binder led to the abrasion of the catalyst layer in the presence of 5.12 M EtOH and 1.89 M PrOH, the latter being more potence in abrading. Beyond any doubt, the loss of the active catalyst particles for CO_2RR [150] and the consequential exposure to the HER-active carbon-based layer contributed to the observed HER dominance with the highest alcohol concentrations.

One unanticipated finding was the increased formation of acetate and propionate species triggered by the addition of EtOH and PrOH to the electrolyte. We presumed that alcohols might

have been oxidized to their acidic anions in the anode. However, additional control experiments with separate electrolyte reservoirs in which only the anolyte reservoir contained alcohols refuted this claim. The amounts of EtOH and PrOH in the anolyte reservoir were monitored by hourly NMR measurements and they did not decrease over time (**Figure 38** in Supporting Information). Besides, no acetate and propionate were detected in the anolyte, excluding alcohol oxidation in the anode under the tested conditions. Another possible explanation would be the lower buffer capacity of 1 M $KHCO_3$ near the electrode due to the higher interfacial concentration of alcohols at the surface. Alkaline conditions at the cathode may not have been buffered efficiently, causing conceivably high cathodic local pH. Li et al.[74] and Overa et al.[167] reported acetate and propionate formation in highly alkaline CO_2 reduction conditions. Nevertheless, further detailed mechanistic study is required to clarify the kinetics of acetate and propionate formation induced by alcohols.

4.4.2. Cell Potential

Experiments with and without the addition of alcohols differed significantly in cell potential. **Figure 34A** summarizes the recorded cell potentials at 24 h after the reaction start (light colored bulk), together with the calculated ohmic overpotential, i.e., *iR* drop, of the electrolyte media (dark colored bulk). Its calculation as well as the online potentiostat measurements of cell potentials can be found in the Supporting Information. The slight increases of the electrolyte overpotential from 1.28 to 2.42 V arose from the decreases in the electrolyte conductivity upon the alcohol addition, yet it did not justify the measured extraordinarily high cell potentials of 11.64 ± 2.03 and 16.79 ± 3.01 V, with 1.89 M PrOH and 5.12 M EtOH concentrations in the electrolyte, respectively. Cathode potential was recorded as the working electrode potential as the reference electrode was built in the system in the vicinity of the cathode in the catholyte inlet stream. Working electrode potentials were measured in the range of −2.1 ± 0.1 V vs Ag/AgCl at a fixed total current density of 200 mA/cm^2, independently of the alcohol concentrations. The high cell potential originated disproportionately from the counter electrode potential, which included all of the contributors to

the cell potential except the cathode. The optical changes observed in the Nafion 117 membrane after experiments in high alcohol concentrations rendered the membrane overpotential to stand out as the possible source of the increasing cell potentials amid various contributors to the counter electrode potential such as anode kinetic overpotentials, mass transport overpotentials, and the aforementioned electrolyte ohmic overpotential. Nafion 117 is a perfluorosulfonic acid (PFSA) polymer membrane consisting of a polytetrafluoroethylene backbone with perfluoroether pendant side chains terminated by sulfonic acid groups. The clear phase separation between the hydrophobic fluoropolymer matrix and the hydrophilic acidic side chains provides distinctive nanostructured morphology, which is the key determinant of the ionic conductive properties in PFSA membranes. According to the cluster-network model, the ionic sulfonic groups of the perfluorinated backbone are solvated by water and form spherically shaped ionic clusters confined within the fluoropolymer matrix. Ionic channel networks are established via narrow channels with diameters of 1 nm connecting the ionic clusters with radii of 2 nm, where the proton transport through the membrane is enabled [168–170]. **Figure 34B** schematically describes the ionic channel networks in PFSA membranes.

To elucidate the assumed alcohol accumulation effects on the membrane and the concomitant high cell potentials, the pristine and postmortem characterization of Nafion 117 membranes were performed with attenuated total reflectance Fourier transform infrared (ATR-FTIR) spectroscopy. A pristine (protonated yet not used in any CO_2 electrolysis) sample, a sample used in a control experiment with a 1 M $KHCO_3$ electrolyte, and another sample used in an experiment with 1 M $KHCO_3$ + 5.12 M EtOH as an electrolyte were chosen to be compared on the grounds of distinguished effects observed with 5.12 M EtOH addition. As shown in **Figure 34C**, the pristine sample and the control sample produced almost identical spectra characterizing diverse bonds within the main and side chains of PFSA, in alignment with the reported literature data [171,172]: OSO bending vibration around 510 cm^{-1}, CS stretching vibration at 632 cm^{-1}, stretching vibrations of

the COC ether linkages between 950 and 990 cm^{-1}, and symmetric SO stretching vibration at 1060 cm^{-1}. The membrane experimented with a 5.12 M EtOH-containing electrolyte unveiled additional weak absorption bands at the frequencies of 701, 1453, 1493, and 2925 cm^{-1}, which can possibly be attributed to the vibrations arising from newly formed CC and CH bonds [173,174]. The new additional bands (e.g., CC, CH) are characteristic for substitution and degradation processes that start with radical attacks of bonds in PFSA (e.g., −C−, −CF−, and $-CF_2-S-$), leading to new bonds and successive degradation of larger molecular structures of PFSA.

The findings suggest that EtOH-containing electrolytes initiated structural changes that were related to a possible degradation in the fluoropolymer matrix of the PFSA, whereas the sulfonic groups were preserved (510 and 1060 cm^{-1} bands were unaffected). Correlating these findings with the ion conductance principle of PFSA membranes might explain the observed high cell potentials: a clear separation between the fluoropolymer matrix and ionic clusters assures the formation of ionic cluster networks. While water molecules can solvate only the hydrophilic sulfonic groups, alcohols can both solvate sulfonic groups and fluoroether groups in the side chains of PFSAs [169,175]. Moreover, alcohol molecules can be absorbed in PFSAs to a large extent, leading to irreversible structural changes such as mechanical deformation by swelling as well as the plasticization of the fluorocarbon matrix [168,175]. Thus, swelling with alcohol affects the morphology of ionomer domains (increasing disorganization of the hydrophobic fluoropolymer matrix and the hydrated hydrophilic acidic side chains) and causes nonuniform distribution of alcohol and water, resulting in low ionic conductivity, as shown by Katzenberg et al. [168], with in-plane membrane conductivity measurements for alcohol-saturated membranes. Confirming their findings with our real-time measurements of cell potentials in CO_2 electrolysis cells, we show for

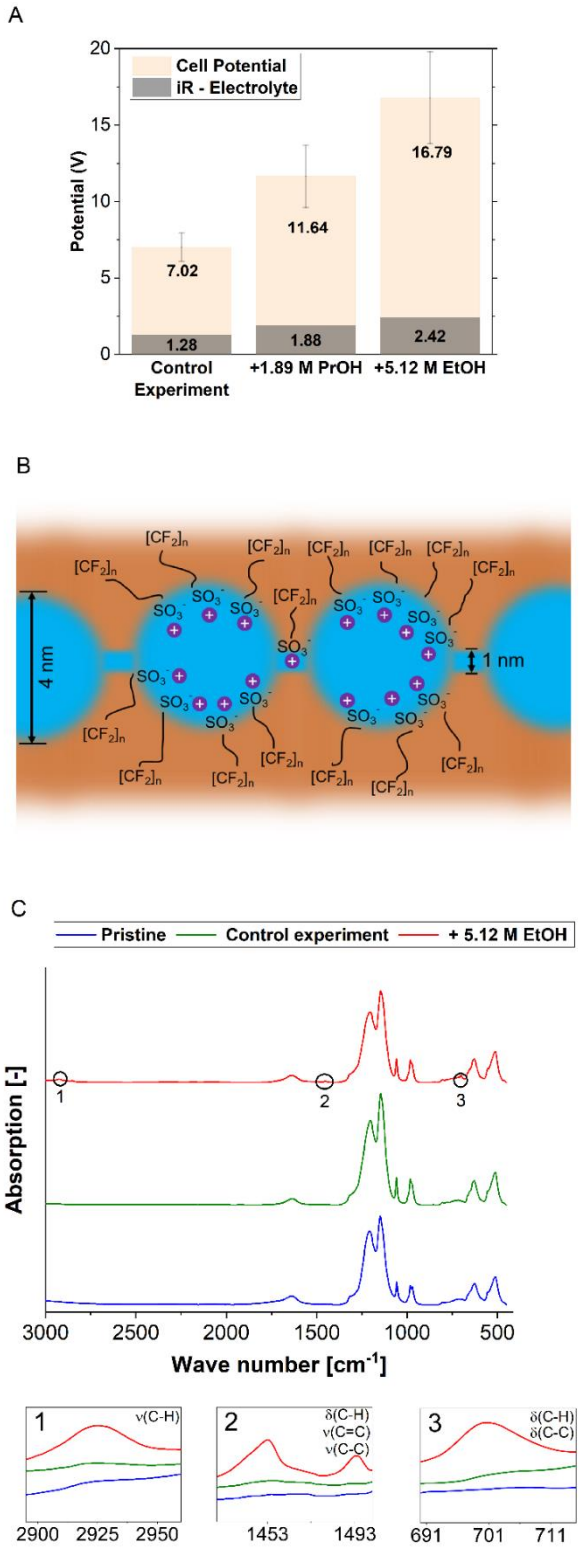

Figure 34. Recorded CO_2 electrolyzer cell potentials at t = 20−24 h in different electrolyte media with alcohol addition (**A**). Formation of an ion-cluster network in hydrated PFSA membranes enables cation transfer. The blue area denotes formed hydration clusters, and the orange area denotes the fluorocarbon matrix of the PFSA membrane. Not to scale. Reproduced based on the findings from Gierke et al. [111] (**B**). ATR-FTIR spectra of various Nafion 117 samples: the pristine protonated sample blue line, the sample used in a control experiment with 1 M $KHCO_3$ as an electrolyte green line, and the sample used in an experiment with 1 M $KHCO_3$ + 5.12 M ethanol as an electrolyte red line. (**C**).

the first time that the EtOH in high concentrations cause irreversible structural changes of the assembled PFSA membrane separator by inexpedient disfigurement of ion networks and thereupon lead to high cell potentials in CO_2 electrolyzers. A 1.89 M PrOH concentration hiked the cell potential significantly compared to the control experiment (from 7.02 ± 0.92 to 11.65 ± 2.03 V), as well as compared to the cell potential observed with the 1.54 M EtOH-containing electrolyte (8.94 ± 2.38 V). This was probably due to Nafion 117′s higher uptake ability for PrOH than EtOH [168,176].

4.5. Conclusions

In summary, we determined the possible effects of CO_2RRinduced liquid byproduct accumulation in the electrolyte on the product selectivity, stability of C_2H_4 formation, and cell potential. The effects regarding formate accumulation could not be deconvoluted from the prominent pH impacts, yet an interesting result of a 0.83 M HCOOH-containing electrolyte (pH = 7.0) prolonging the stability to 92 h compared to the control group (pH = 8.5) is noteworthy for future research. Electrochemical measurements at 200 mA/cm^2 with electrolyte media containing EtOH and PrOH showed that alcohols shift the faradic selectivity from CO_2RR products to H_2. At high concentrations (5.12 M for EtOH and 1.89 M for PrOH) in the electrolyte, the CO_2RR was completely inhibited by HER. Interestingly, mild concentrations (1.54 M EtOH and 0.57 M PrOH) led to increased formation of acetate and propionate, respectively. The duration of stable C_2H_4 formation significantly diminished from 50 h in the control experiments to 1 h at high alcohol concentrations and to less than 12 h at mild alcohol concentrations. Contact angle measurements with test liquids containing either pure water, pure water, and EtOH mixtures or pure water and PrOH mixtures evidently verified that the hydrophobic electrode surface turned into a hydrophile electrode (θ_{H_2O} = 141.3 ≥ 90 °) turned into a hydrophile electrode ($\theta_{H_2O:EtOH}$ < 90 ° and $\theta_{H_2O:PrOH}$ < 90 °) even at the low concentrations of alcohols (0.51 M EtOH and 0.19 M PrOH). This observation supported our hypothesis on the electrodes being flooded easily upon their

decreased surface tension caused by the alcohol presence. The flooded electrodes steered the selectivity toward H_2 and cut down the duration of stable C_2H_4 formation. The catalyst layers of the electrodes tested in electrolyte media with high alcohol concentrations were abraded, likely as a result of ionomer binder dispersion by alcohols. ATR-FTIR measurements of the used Nafion 117 membranes uncovered that the 5.12 M EtOH-containing electrolyte caused irreversible structural changes, assumedly by mechanical deforming due to swelling and plasticization of the polymer backbone. These effects were only observed in the highest tested alcohol concentrations, PrOH being detrimental at a lower concentration presumably by its higher sorption by the membrane material. The structural changes in the membrane may have disturbed the ionic channel networks obstructing the cation transfer and leading to the recorded high cell potentials.

This combination of findings stipulates that the alcohols should be removed from the electrolyte medium continuously to disallow their accumulation in the electrolyte. A further detailed process simulation study may be beneficial to integrating alcohol removal and electrolyte recycling steps. From catalyst perspective, ongoing efforts for selective Cu-based materials for C_2H_4 may obsolete the problematics of liquid byproduct accumulation in the long term. Future research may concentrate on the oleophobic surface coating of the electrodes, which may be useful to combat the decreasing surface tension of the electrode in the presence of alcohols. Apart from the electrode design, future studies should also look for alternatives to membranes (e.g., ZrO_2 diaphragm) and ionomer binders (e.g., conjugated conductive polymer binders used in Li ion battery research) that are unsusceptible to mechanical and chemical changes under long-term exposure to alcohols.

Acknowledgements

Research leading to these results has received funding from the European Union's Horizon 2020 Research and Innovation Program under grant agreement no. 101006701, EcoFuel. The authors thank all partners of the EcoFuel project and especially Toby Hodges and Dr. Elena C. Corbos from Johnson Matthey Public Limited Company, for supplying the CuO cathode catalyst. B.S. would like to express his gratitude to Dr. Hans Wilke from Siemens AG for his support with the SEM characterization of the electrodes and to Dr. Angelika Tawil and Dr. Erhard Magori for the valuable discussions and support in the laboratory. B.S. acknowledges support from the TUM Graduate School.

4.6. Supporting Information

4.6.1. Estimation of Product Concentrations in the Electrolyte at Certain Operation Times

Quantitative NMR analysis revealed that 0.0128 mols of ethanol (EtOH), 0.0048 mols of *n*-propanol (PrOH), and 0.0425 mols of formate were accumulated in the electrolyte during control experiments at 200 mA/cm^2 with 10 cm^2 electrodes in the accumulation of within 24 hours of reaction. Based on this quantification, the reaction rates of these reaction products were calculated. Yet, the reaction rates were representative only for the interval between reaction start and t = 24 h. Yet, we assumed that reaction rates would stay constant. The constant reaction rates were used to estimate the amount of the liquid product *i* at a specific operation time ($n_{Liq,i}(t)$). The hypothetical accumulation concentrations of EtOH and PrOH were calculated for the 10th, 30th and 100th days, given in **Table 5**. Those amounts of alcohols were added to the electrolyte ($V_{added,i}$) before the experiment to observe their accumulation effects in the electrolyte without waiting for 10, 30 or 100 days.15

Calculations were done with the equations below,

$$r_i = \frac{\Delta n_i}{A \cdot \Delta t} \quad (16)$$

$$N_{Liq,i}(t) = r_i \cdot t \cdot A \quad (17)$$

$$V_{added,i} = \frac{n_{liq,i} \cdot M_i}{\rho_i} \quad (18)$$

where r_i is the reaction rate of the product *i*, Δn_i is the increased mole amount quantified by NMR analysis of the product *i* in the electrolyte, A is the electrode area, Δt is the reaction time interval for the observed accumulation of the product *i*, M_i the molar mass of the product *i* and ρ_i is the density of the product *i*.

Formate is an anionic species, and this enabled two possible forms for adding formate to our system without introducing foreign ions to the $KHCO_3$ electrolyte: formic acid and potassium formate. Details of the estimation of formate concentration are given in **Table 6**. Detailed results of the experiments with formate addition are discussed in the next section.

Table 5. Calculation of estimated concentrations of EtOH and PrOH in the electrolyte after 10, 30 and 100 days based on NMR results of control experiments.

Product	Detected amounts in the electrolyte after 24 h in control experiments at 200 mA/cm^2 (mol)	Reaction rate (mol cm^{-2} h^{-1})	Estimated concentration of the product in 250 mL $KHCO_3$ after 10 days (mol L^{-1})	Estimated concentration of the product in 250 mL $KHCO_3$ after 30 days (mol L-1)	Estimated concentration of the product in 250 mL $KHCO_3$ after 100 days (mol L-1)
EtOH	0.0128	5.33 x 10^{-5}	0.51	1.54	5.12
PrOH	0.0048	2.00 x 10^{-5}	0.19	0.57	1.89

Table 6. Calculation of estimated concentrations of formate in the electrolyte after 10 days based on NMR results of control experiments.

Product	Detected amount in the electrolyte after 24 h in control experiments at 200 mA/cm^2 (mol)	Reaction rate (mol cm^{-2} h^{-1})	Estimated concentration of the product in 250 mL $KHCO_3$ after 10 days (mol L^{-1})
Formate	0.0425	1.77×10^{-4}	1.65

Table 7. Added amounts of products in the electrolyte prior to electrochemical experiment begin.

Product	Added amount of product (mL)	Molarity of product in the 250 mL KHCO3 solution (mol L-1)
Ethanol	7.47	0.51
Ethanol	22.41	1.54
Ethanol	74.71	5.12
PrOH	3.53	0.19
PrOH	10.59	0.57
PrOH	35.29	1.89
Formate (as formic acid)	7.78	0.83
Formate (as formic acid)	15.57	1.65
Formate (as potassium formate)	34.50*	1.65

*grams, not mL.

4.6.2. Investigation of Formate Accumulation Effects on Stability

Formate is a terminal product in the CO_2 reduction on Cu catalysts in the pH > 3.5 conditions [177–179]. It was one of the main liquid products observed in this work, as shown in the control experiment product spectrum in **Figure 31A** of the main manuscript. Therefore, this work focused on also formate accumulation in the electrolyte with time.

Yet adding isolated formate anion in the electrolyte is not possible as it always coexists with cations as salts or with H^+ as formic acid. Adding formate salts with different cations would introduce a new influence parameter to the system: cations' effect on the cathode reactions. The cations form hydrates and reside in the electrical double layer of the cathodes. They coordinate with dissolved CO_2, interact with the CO_2RR intermediates at the surface through an increased interfacial electrical field, hinder the mobility of H^+, and affect local pH. The effects of these phenomena on CO_2 reduction depend on their hydration shell sizes[50]. Such substantial changes

in the electrode microenvironment would complicate the investigation of formate accumulation effects. Thus, formate was added to the system only with its already existing counter ions in the system: H^+ and K^+.

1 M $KHCO_3$ electrolytes containing 1.65 M HCOOH, 0.83 M HCOOH, and 1.65 M HCOOK were tested under the same conditions with control experiments without any formate addition. HCOOH addition acidified the electrolyte as expected, leading to a pH of 4.0 with 1.65 M and 7.0 with 0.83 M in the electrolyte. 1.65 M potassium formate concentration led to an electrolyte pH of 10.0.

Figure 35 presents varying durations of stable C_2H_4 formation with changing formate concentration and bulk electrolyte pH. Interestingly, neutral conditions (pH = 7 with additional 0.83 M HCOOH in 1 M $KHCO_3$) enabled the longest stable reaction of 92 hours ($FE_{C_2H_4}$ > 20%) among all experiments. This finding is in line with the latest opinions in literature about the influence of alkalinity on poor electrode stability despite its kinetic promotion for C_{2+} formation.

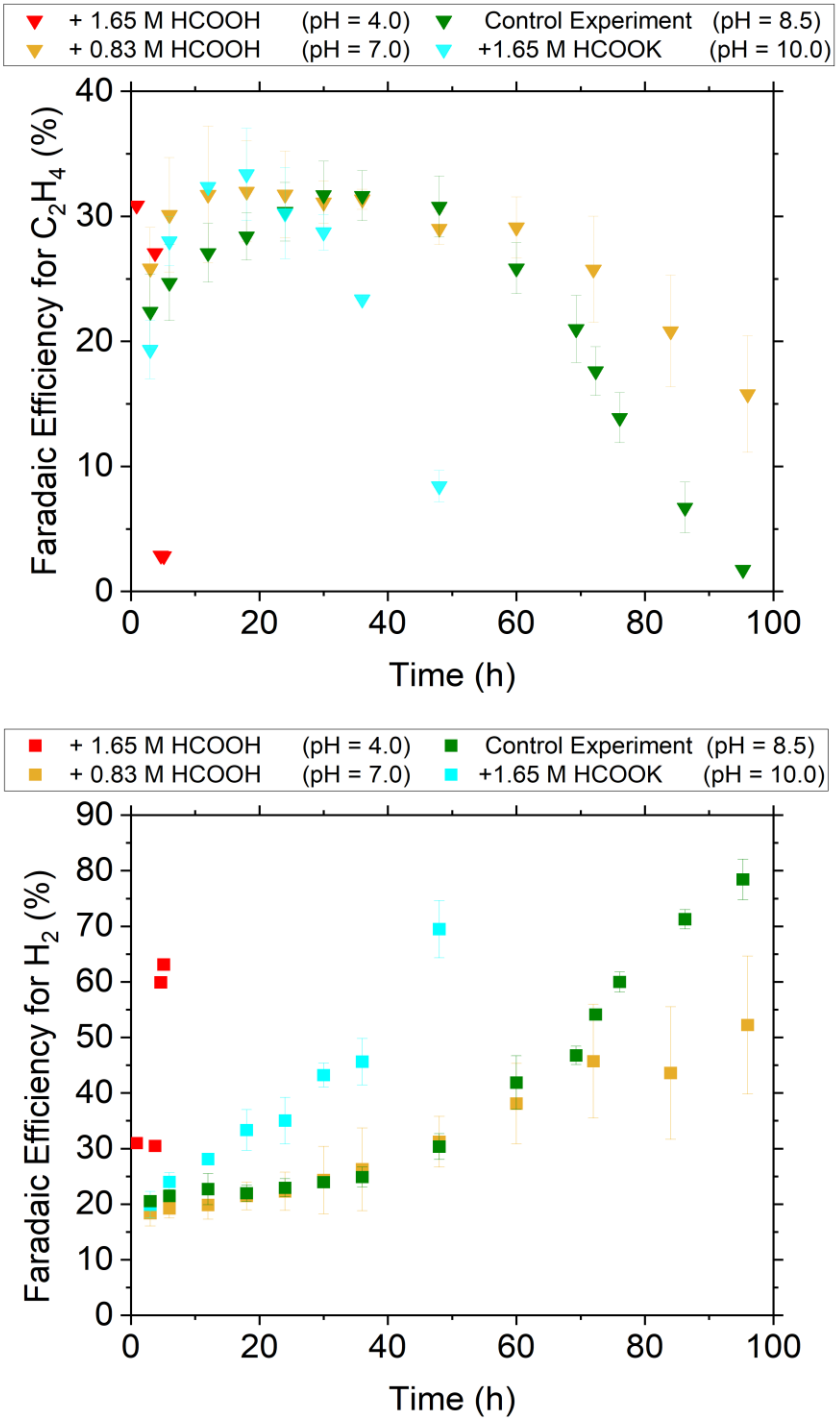

Figure 35. Combined effects of pH and formate concentration in electrolyte on the faradaic efficiency of ethylene over time at a current density of 200 mA/cm^2.

Adding formic acid (pK_a = 3.7) or potassium formate (pK_b = 10.7) significantly changes the electrolyte's pH. It is well known in the literature that pH can fundamentally regulate which reaction mechanisms occur on the Cu surface[71,129]. Local alkaline conditions are reported to enhance C-C coupling (C_{2+}) kinetics, thus promoting C_2H_4 formation. Nevertheless the salt formation problem is amplified in the alkaline cathodes hindering CO_2 availability[69,124,143,144,146,156]. Local acidic conditions steer the reaction mechanisms to C_1 formation and hydrogen evolving reaction[71,143,180,181].

In light of this discussion, the formate concentration effects could not be decoupled from the pH effects in this work. Future studies should consider this complication and work on the deconvolution of pH and formate accumulation effects without introducing foreign cations to the system.

4.6.3. Experiments with both Ethanol and *N*-propanol Addition in the Electrolyte

Apart from understanding the individual effects of the alcohols on the product spectrum, it was also interesting to analyze their coexistence as both EtOH and PrOH accumulate simultaneously in the actual conditions. Hypothetical amounts estimated for the 30th day of two species were added to 250 mL of 1 M $KHCO_3$ before the experiment and tested at identical conditions with the control experiments. **Figure 36** indicates the significant difference between the product spectra with and without alcohol addition. Hydrogen evolving reaction became the dominant reaction consuming most of the supplied electrons. C_2H_4 and CO formation was severely suppressed. Acetate and propionate formation was induced in the presence of 1.54 M EtOH and 0.57 M PrOH. The results obtained in the experiments with adding EtOH and PrOH in

the electrolyte were parallel to the discrete effects of EtOH and PrOH. Yet, their coexistence amplified the CO_2RR suppression and HER promotion.

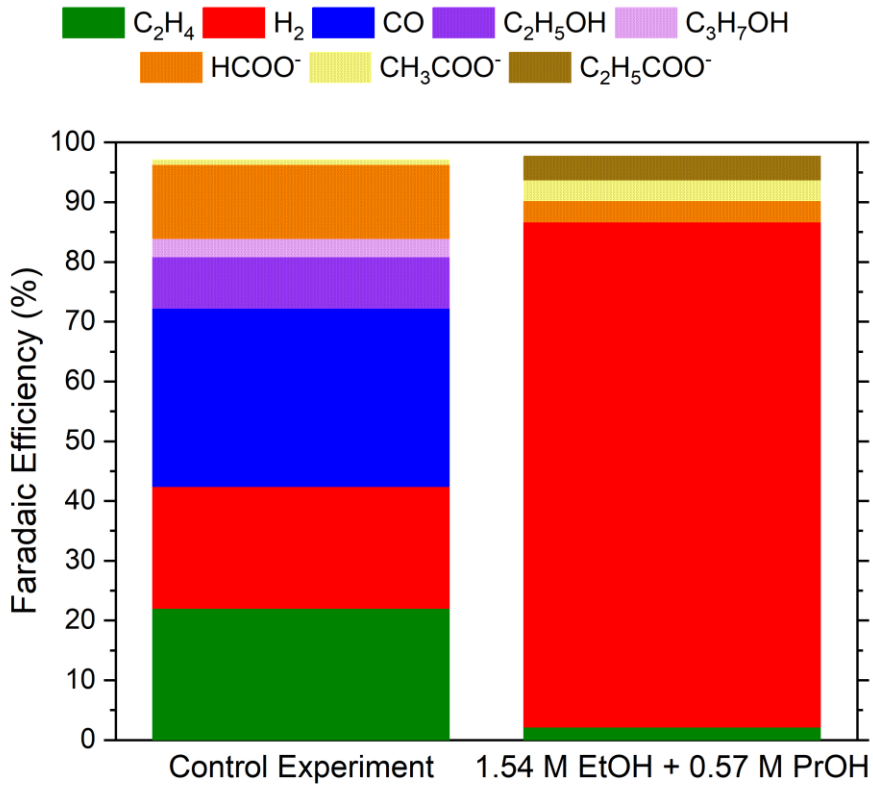

Figure 36. Product spectrum comparison at t = 3 h at 200 mA/cm^2 between the control experiments with 1 M $KHCO_3$ electrolyte and the experiments with 1 M $KHCO_3$ electrolyte containing 1.54 M of ethanol and 0.57 M of *n*-propanol.

Figure 37 shows the stability of ethylene formation over time with and without the addition of alcohols. The coexistence of EtOH and PrOH in their 30th day concentrations amplified the decrease in C_2H_4 formation compared to their discrete effects at 30th day concentrations (**Figure 31C and Figure 31D**).

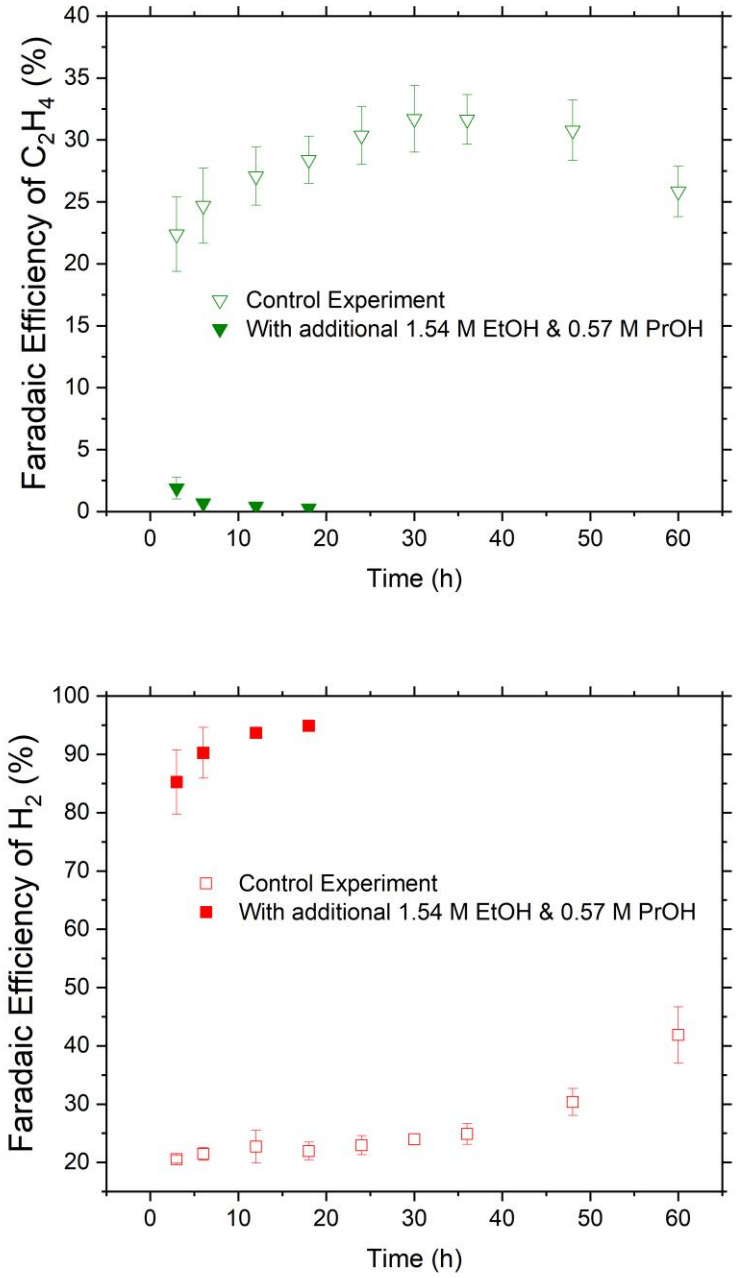

Figure 37. Faradaic efficiencies of ethylene and hydrogen over time for control experiments with 1 M $KHCO_3$ and the experiments 1 M $KHCO_3$ electrolyte containing 1.54 M of ethanol and 0.57 M of *n*-propanol.

4.6.4. Control Experiments on the Possible Alcohol Oxidation at the Anode

The increased formation of acetate and propionate species triggered by EtOH and PrOH addition to the electrolyte was initially linked with the possible oxidation of the alcohols at the anode. Several control experiments were performed to assess this possibility with a separated catholyte reservoir containing only 1 M $KHCO_3$ and anolyte reservoir containing 1 M $KHCO_3$ along with EtOH and PrOH. Such a setup allowed us to monitor the alcohol amount in the anolyte as opposed to the rest of the experiments, where a mixed electrolyte reservoir was used for the pH compensation. Except for separate electrolyte reservoirs for anolyte and catholyte, the rest of the cell and test stand details were kept identical to what is shown in **Section 4.6.6**.

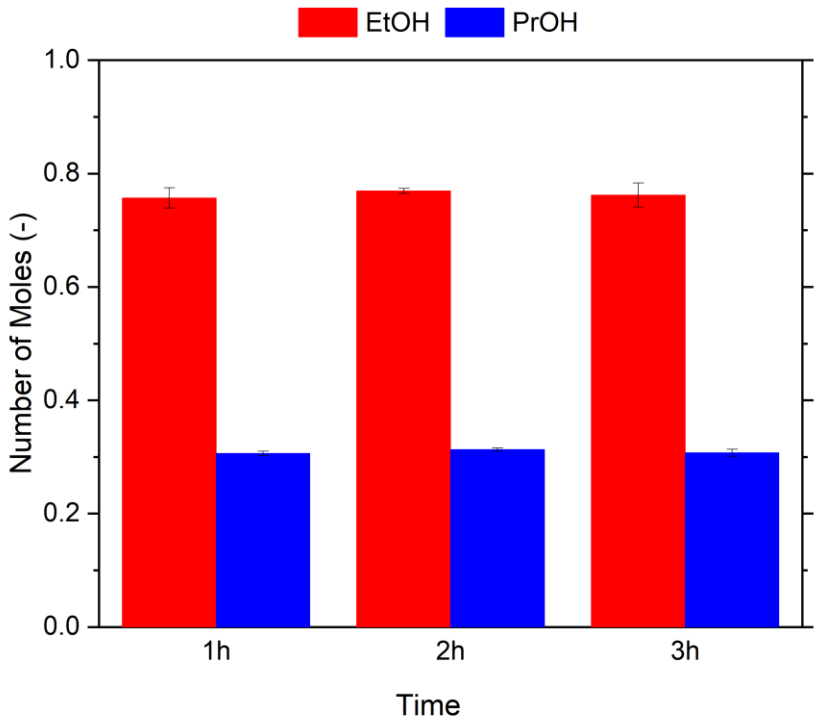

Figure 38. Alcohol amount in anolyte as moles over time in the separate electrolyte experiments for investigating possible alcohol oxidation at the anode at a current density of 200 mA/cm^2 in separate 250 mL of 1 M $KHCO_3$ electrolyte reservoirs.

Figure 38 shows that the added amounts of 0.75 mols of EtOH and 0.30 mols of PrOH stayed constant for 3 hours in chronopotentiometric experiments at 200 mA/cm^2. These results proved that EtOH and PrOH were not being consumed as a result of oxidation reactions at the anode under the employed experimental conditions.

A system with separate electrolyte reservoirs could only be run for a short time due to changing conductivities and pH values in the catholyte and anolyte without continuously refreshing the electrolytes. Therefore, the experiment duration was limited to 3 hours.

4.6.5. Calculating the Ohmic Resistance of the Electrolyte

The full electrochemical cell potential can be broken down into the following elements: the thermodynamic potential of the cell, ohmic overpotential, cathode kinetics overpotential, anode kinetics overpotential, and overpotential induced by mass transport effects.

Observing remarkably high cell potentials in the presence of the 100th day alcohol concentrations in the electrolyte was suggestive of the possibility of decreased electrolyte conductivity and a high ohmic resistance as a result. Therefore, the electrical conductivities of the electrolyte mixtures with alcohols were measured with an electrical conductivity meter (ProfiLine Cond 3310, WTW). Ohmic potentials resulting from the electrical conductivity of the electrolytes (V_{elec}) are calculated for each 1 M $KHCO_3$ solution with and without alcohol addition at I = 2 A following the Equation 19, where V is the resulting ohmic potential (volts), I is the applied total current (A), R is the ohmic resistance (ohm), L is the length of the conducting material (m), κ is the electrical conductivity of the electrolyte mixture (S m^{-1}) and A is the sectional area (m^2). Results are summarized in

Table 8.

$$V_{elec} = I \cdot R = I \cdot \frac{L}{\kappa \cdot A} \quad (19)$$

Table 8. Ohmic potentials at I = 2 A resulting from the electrical conductivity of the 1 M $KHCO_3$ electrolyte with and without alcohol addition.

Electrolyte	Measured cell potentials at t = 24 h in electrochemical measurements at I = 2 A (V)	Measured electrolyte conductivity (mS cm^{-1})	Calculated V_{elec} (V)
1 M $KHCO_3$	7.02 ± 0.92	78.0	1.28
1 M KHCO3 + 1.89 M PrOH	11.65 ± 2.03	53.2	1.88
1 M KHCO3 + 5.12 M PrOH	16.79 ± 3.01	41.3	2.42

The ohmic overpotential, which is the sum of the electron transport, ion transport, electrical contact, and membrane resistances, is measurable with the impedance spectroscopy method at high frequencies (>10^3 Hz) [182,183]. However, deconstructing how much each element contributes to the total ohmic overpotential is complicated [184]. For this very reason, the ohmic resistance of the electrolyte was not investigated via impedance spectroscopy.

4.6.6. Experimental Setup

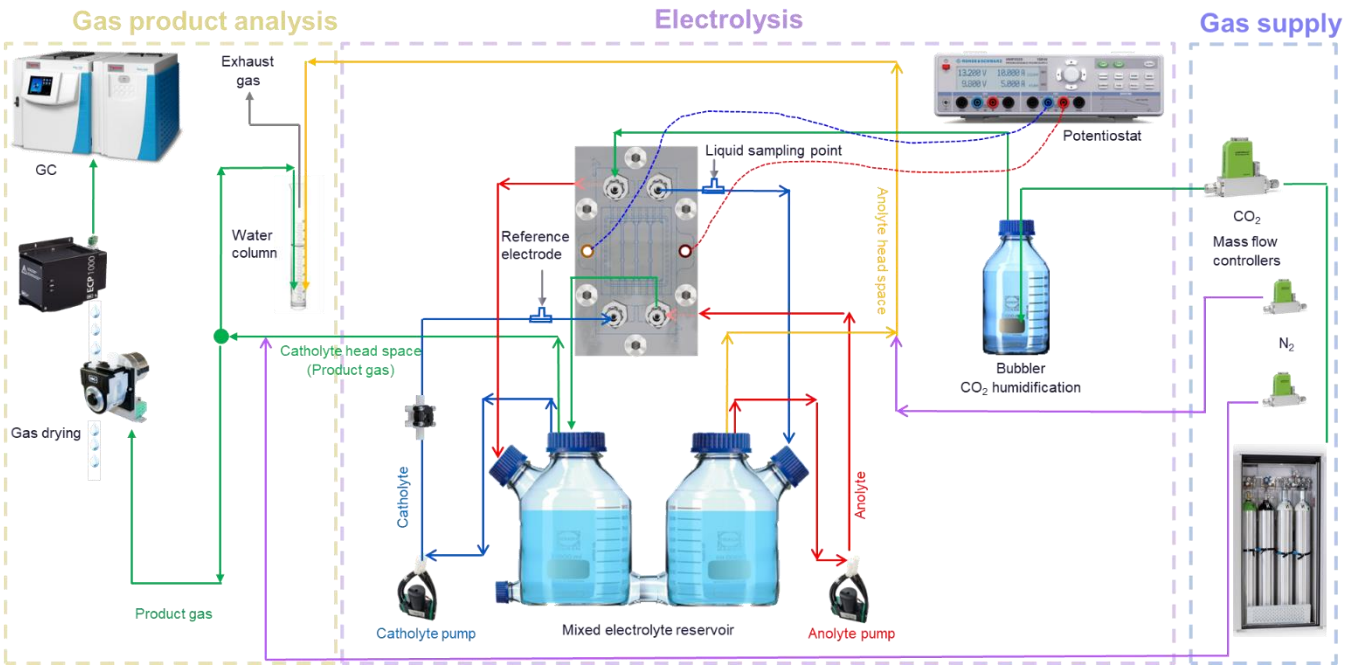

Figure 39. Detailed schematic illustration of the test stand. The only deviation from the **Figure 26** was not including a membrane valve to create back pressures.

4.6.7. Cell Potential Recordings of Experiments with and without Alcohol Addition

Figure 34A summarizes the recorded cell potentials in the 20-24 h window after the electrochemical reaction begin. **Figure 40** shows the online potentiostat measurement results of the cell potential from the reaction start until 24 h. As the 5.12 M EtOH and 1.89 M PrOH create harsh conditions for the membrane and the GDE, creating mechanical deformation for both, such effects resulted in higher variance in the repeated experiments of alcohol addition experiments. Nevertheless, there was a statistically significant difference between the alcohol-containing electrolyte experiments and the control experiments without alcohol addiction prior to the experiment's beginning. 5.12 M EtOH addition caused a further gradual increase of cell potential over time, possibly explained by membrane structural disfigurements as discussed in the main manuscript.

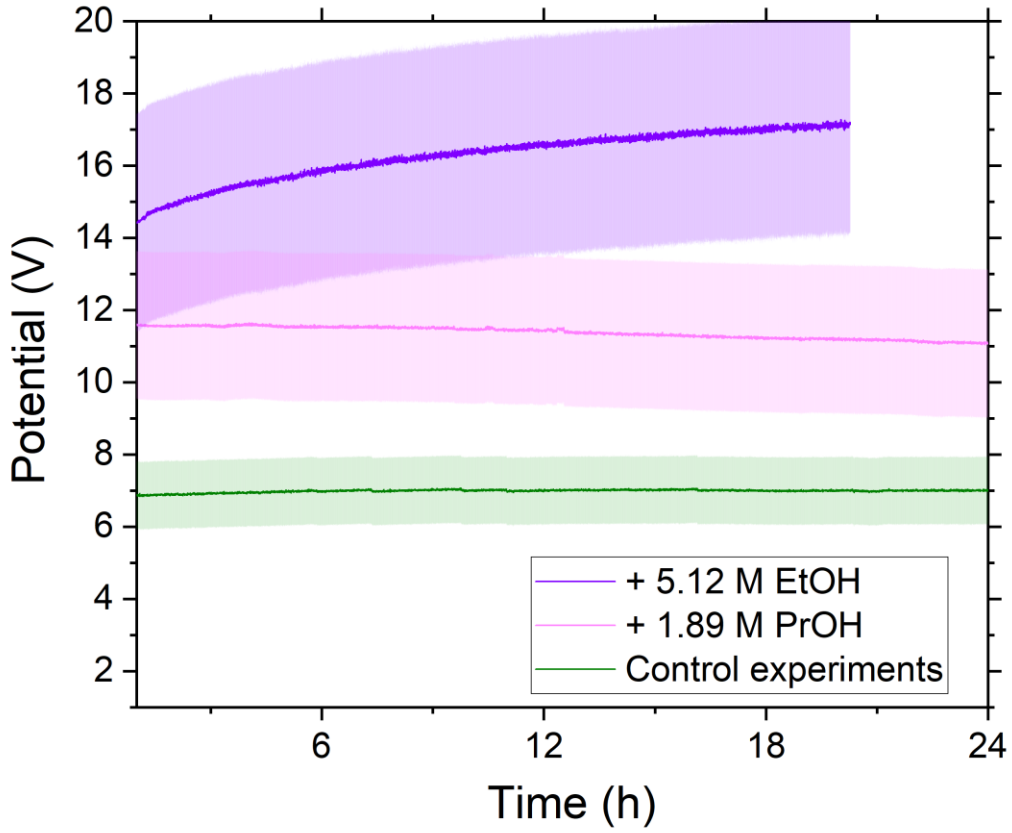

Figure 40. Potentiostat cell potential recordings of experiments containing 5.12 M EtOH, 1.89 M PrOH and no additional alcohol as control experiments. The experiments were repeated 2-3 times and the error ranges were included accordingly.

5. Fine-tuned Combination of Cell and Electrode Designs Unlocks Month-long Stable Low Temperature Cu-based CO_2 Electrolysis

Despite the urgency of implementing technologies that facilitate the defossilization of the chemical and mobility sectors, less attention has been devoted to readily upscalable CO_2 electrolyzer designs. To address this research gap, the study presented in this chapter focused on the fine-tuned combination of readily scalable cell and electrode designs, aiming to achieve high selectivity towards C_{2+} compounds, long-term stability, and low cell potentials in one cell and electrode design combination.

This study identified two readily scalable CO_2 electrolyzer cell architectures for industrial applications out of five options, based on experimental evidence of cell potential, CO_2 crossover, and technical maturity. The CEM-based zero-gap cell, with a 3.7 V cell potential, required electrode modifications due to acidic cathode conditions favoring HER. An innovative TiO_2-AEI layer overcame this hurdle allowing C_2H_4 formation with 14% faradaic efficiency. Nevertheless, focus shifted to the CEM-based one-gap cell, with a multilayered GDE showing superior selectivity results, down-selected for stability tests. Tests at 100-300 mA/cm^2 revealed degradation mechanisms, with 100 mA/cm^2 allowing month-long stable operations, while 300 mA/cm^2 showed shorter stabilities. SEM/EDX analyses indicated salt formation at 100 mA/cm^2 and catalyst agglomeration at 300 mA/cm^2 as main degradation mechanisms.

The results of this study emphasize that achieving stable, high-yield C_{2+} production in a readily scalable cell design is only possible, if the interdependencies between electrode design and cell architectures are considered and reflected in the design. Applying the know-how regarding operation conditions concomitantly with the fine-tuned combination of cell and electrode design enabled a breakthrough in this field, achieving a month-long stability.

This is based on the following publication:

Sahin, B., Kraehling, M., Facci Allegrini, V., Leung, J., Wiesner-Fleischer, K., Magori, E., Pastusiak, R., Tawil, A., Hodges, T., Brooke, E., Carbos, E., Fleischer, M., Simon, E., Hinrichsen, O (2023). Fine-tuned Combination of Cell and Electrode Designs Unlocks Month-long Stable Low Temperature Cu-based CO_2 Electrolysis. Accepted by Journal of CO_2 Utilization; 2024.

The contributions of the authors are summarized as follows:

- Baran Sahin: Conceptualization, methodology, experimental investigation, validation, data evaluation, manuscript preparation and visualization.
- Marc Kraehling: Experimental investigation, data evaluation and visualization.
- Vinicius F. Allegrini: Experimental investigation, data evaluation and visualization.
- Jane J. Leung: Experimental investigation and data evaluation.
- Kerstin Wiesner-Fleischer: Manuscript editing.
- Erhard Magori: Methodology.
- Remigiusz Pastusiak: Methodology.
- Angelika Tawil: Experimental investigation.
- Toby Hodges: Material resources and experimental investigation.
- Emily Brooke: Material resources and experimental investigation.
- Elena C. Corbos: Material resources and experimental investigation.
- Maximillian Fleischer: Funding acquisition and manuscript editing.
- Elfriede Simon: Supervision, funding acquisition and manuscript editing.
- Olaf Hinrichsen: Supervision and manuscript editing.

5.1. Abstract

The urgency of achieving green chemical production through Cu-based CO_2 electroreduction necessitates a rapid transition towards technical maturity and commercialization in the pursuit of addressing the global imperative of decarbonization. Surprisingly, limited emphasis has been placed on the exploration of readily scalable cell and electrode designs, which are pivotal in ushering in the era of stable and selective CO_2 electrolyzers, showcasing the innovative potential within this area. Herein, we report a breakthrough in achieving month-long stability in the production of C_2H_4, representing an unprecedented milestone in low-temperature CO_2 to C_{2+} electrolysis. Initial investigations involved the evaluation of five distinct cell architectures for Cu-based CO_2 electrolyzers, guided by considerations of cell potentials, scalability with current technology, and CO_2 crossover. An innovative multilayer Gas Diffusion Electrode (GDE) design, featuring an anion exchange ionomer and metal oxide layer, is introduced for CEM-based zero-gap cells, enabling C_2H_4 formation despite acidic CEM surroundings. However, selectivity towards C_2H_4 proved suboptimal for extended stability testing. Conversely, the tailored multilayer GDE for one-gap cell architecture achieves a commendable 54% faradaic efficiency (FE) towards C_{2+} products at 300 mA/cm^2. Remarkably, chronopotentiometric tests demonstrate 720 hours of stability ($FE_{C_2H_4}$ > 20%) at 100 mA/cm^2, highlighting the robustness of the one-gap cell configuration. At higher current densities (300 mA/cm^2), stability is reduced to 75 hours, with detailed analyses revealing distinct degradation mechanisms. At 100 mA/cm^2, salt formation predominates, while at 300 mA/cm^2, catalyst layer restructuring degrades catalytic activity towards C_2H_4. Our research underscores the potential for stable, high-yield C_{2+} product generation through innovative electrode design and scalable cell architectures, advancing sustainable CO_2 utilization.

5.2. Introduction

The rise in global warming will most likely exceed 1.5°C during the 21st century, and limiting the warming below 2°C as agreed in the 2018 Paris Agreement will fail unless global net zero emissions are achieved by rapid and sustained reductions in greenhouse gas emissions by 2050 [9]. One promising avenue in mitigating CO_2 emissions and transitioning towards a sustainable energy future is the development of CO_2 electrolyzers. The emerging technology of scalable low-temperature CO_2 electrolysis can replace fossil carbon with already emitted CO_2 to produce fuels and chemicals. This technology can reduce greenhouse gas emissions by up to 93% compared to traditional fossil methods, depending on the end product [160]. One potential commercial application for CO_2-to-C_2H_4 electrolyzers lies in the production chain for sustainable aviation fuel (SAF) derived from CO_2. This process integrates the electrolyzer with olefin oligomerization and hydrotreatment steps to directly convert CO_2 into the final product. Compared to alternative routes using methanol, ethanol, or Fischer-Tropsch synthesis, CO_2-to-C_2H_4 electrolysis offers a streamlined approach, potentially eliminating at least one process step.

Currently, only Cu-based catalyst systems can electrochemically reduce CO_2 to multicarbon products in significant amounts. However, they characteristically lack selectivity toward a single product and catalyze CO_2RR simultaneously to various C_{1-3} compounds, including carbon monoxide, formate, ethylene, ethanol, and *n*-propanol [20]. CO_2RR relies on CO_2 molecules binding to the Cu electrode's surface and undergoing adsorption and chemical activation. Nevertheless, CO_2 is remarkably inert, rendering the CO_2RR thermodynamically unfavorable. Only in the presence of a reducing electrical field on the Cu surface does the CO_2 binding mode with the Cu surface change from physisorption to chemisorption (via injection of metal electrons into the antibonding orbital of the adsorbate [37,38]). This electrochemical activation of CO_2 molecule is implied by higher adsorption energy, elongation of C-O bond and decrease in O-C-O angle [47].

The chemisorbed CO_2 dissociates to the CO* and O* species with concerted electron-proton transfer, forming the key intermediate of CO* for C_{2+} products [66,185,186]. The exact reduction pathway of the chemisorbed CO_2 to each CO_2RR product remains a vivid discussion in the field. Adsorbed reaction intermediates fundamentally define the inherent product distribution, being influenced by Cu oxidation state [187–189], applied local potentials [190–193], CO_2* and CO* coverages [74,95,194,195], surface structural effects [66,196–199] and local catalyst-electrolyte microenvironment [50,200–202]. However, unsteady state electrochemical phenomena occurring during the reaction may alter the inherent CO_2RR product distribution and may shift the selectivity toward the competing HER, often referred to as degradation.

So far, the longest stable operation without observed degradation was 150 h, reported by Dinh et al. [203] at 75-100 mA/cm^2. Two phenomena are consistently and repeatedly reported to cause the degradation of catalytic performance in Cu-based CO_2RR: catalyst surface restructuring and electrode flooding. The first is explained by Cu particles' weak cohesive energy and high surface mobility, resulting in atomic rearrangement driven by the thermodynamic demand for lowering electrode surface free energy [204]. In recent studies, the mechanisms of restructuring were suggested to be Cu particle dissolution followed by redeposition [205], reversible Cu clustering and irreversible Cu faceting due to CO_2 disassociation to CO* and O* [185], and potential-driven nanoclustering [141]. The morphology alteration and active site deterioration due to surface reconstruction can lead to a decline in catalytic performance [196,198,206]. Additionally, Weng et al. [197] reported accumulation of carbonaceous species deposited on Cu as a deactivation mechanism. The second degradation phenomena, flooding, does not interfere with the inherent catalyst activity but spoils the catalyst-electrolyte microenvironment, causing CO_2 depletion and subsequent selectivity swift toward the competing HER. This phenomenon is reported to be induced by electrowetting [162,207], salt permeation through the gas diffusion layer due to electroosmosis [124,208–211], pressure distribution in the GDE [155,212], polymerization of reaction

intermediates on the catalyst layer [158] and accumulation of alcohol products in the electrolyte [133], occurring dependently or independently of each other.

The scientific community has made significant progress in understanding the intricacies of electrochemical CO_2 reduction to C_{2+} products, developed efficient catalysts, and tested them in various cell architectures and reaction conditions. Considering the urgent need for defossilization, technologies such as enabling CO_2 electroreduction to green chemicals must reach technical maturity and commercialization as soon as possible. Nevertheless, insufficient effort has been devoted to researching readily scalable cell and electrode designs and achieving stable and selective CO_2 electrolyzers, despite their potential to advance the current state of the art. In this work, we will report that the fine-tuned combination of readily scalable cell and electrode designs enables month-long stable C_2H_4 formation, which is, in our knowledge the longest stability ever reached in the field of CO_2 to C_{2+} low-temperature electrolysis. Primarily, four different cell architectures were evaluated for Cu-based CO_2 electrolyzers considering cell potentials, scalability with the current state-of-the-art, and CO_2 crossover. CEM-based zero-gap cells (similar to PEM cells) and one-gap cells were down-selected for the electrode design investigation. A novel multilayer GDE electrode design consisting of an anion exchange ionomer / metal oxide layer was developed for CEM-based zero-gap cells that could reduce CO_2 to C_2H_4 in the cathode despite the acidic conditions dictated by the CEM vicinity. However, its selectivity towards C_2H_4 was unsatisfactory for the long-term stability tests. On the other hand, the multilayer GDE design tailored for one-gap cell architecture reached 54% faradaic efficiency towards C_{2+} products at 300 mA/cm^2, which qualified it for long-term stability investigations. 720 h stability ($FE_{C_2H_4}$ > 20%) was achieved in chronopotentiometric electrochemical measurements at 100 mA/cm^2. Higher current densities shrank the stability, reaching only 75 h at 300 mA/cm^2. FIB/SEM and FIB/EDX analyses verified that degradation was predominantly salt formation induced at 100 mA/cm^2 after the

month-long operation. Dissimilarly, the degradation root cause of the catalytic activity toward C_2H_4 at 300 mA/cm^2 was most likely the catalyst layer restructuring. **Table 9** includes a list of all relevant abbreviations and symbols for this study.

Table 9. List of abbreviations and symbols.

Abbreviations and symbols			
CO_2RR	CO_2 reduction reaction	λ	Lambda
HER	Hydrogen evolution reaction	$\dot{V}$	Gas flow rate
GDL	Gas diffusion layer	F	Faraday constant
GDE	Gas diffusion electrode	I	Applied current
AEM	Anion exchange membrane	j	Current density
CEM	Cation exchange membrane	t	Time
PEM	Proton exchange membrane	h	Hour
AEI	Anion exchange ionomer	z	Number of electrons
AEIL	Anion exchange ionomer layer	n	Number of mols
MO	Metal oxide	R	Ideal gas constant
CEI	Cation exchange ionomer	T	Temperature
CCM	Catalyst coated membrane	P	Gas pressure
PEEK	Polyether ether ketone	FE	Faradaic efficiency
BPM	Bipolar membrane	wt.%	Weight percentage
MEA	Membrane electrode assembly	*	Adsorbed species on surface
PTFE	Polytetrafluoroethylene		
PFSA	Perfluorinated sulfonic-acid		

5.3. Materials and Methods

5.3.1. Experimental Set-Up

A proprietary laminar flow cell constructed with PTFE and PEEK materials was used in one-gap and two-gap cell experiments. The two-gaps cell architecture consisted of three chambers where gas, catholyte and anolyte streams flowed. The electrolyte circulating in both anode and cathode chambers were mixed in an electrolyte chamber external to the cell and pumped continuously through the system with micro diaphragm liquid pumps (NFB 25 KPDCB-4A, KNF) operated at a constant flow of 100 mL min^{-1}. In the one-gap cell architecture, the anolyte flow chamber between the two electrodes was omitted and anode CCM was employed instead of separate anode and membrane parts. The gas chamber was fed with CO_2 (+99.998 %, Linde) via mass flow controllers (SFC5400 Sensirion). A custom-made water saturator at room temperature was used to humidify the CO_2 feed before entering the cell. The gas outlet from the cell was mixed with the catholyte head space. An IrOx-coated electrode with a 10 cm^2 active area (Electrocell) was used as the anode in two-gap cells. A preassembled Ir and cation exchange membrane-based anode CCM with 10 cm^2 active area (Siemens Energy) was built in as anode in the one-gap cells. CuO catalyst based GDEs were used in all experiments as the cathode. 250 mL of $KHCO_3$ (+99.7% in dry basis, Alfa Aesar) or KOH (99.98% purity, Thermo Scientific Chemicals) solution was used as the electrolyte in current density variation experiments. The volume of electrolyte was increased to 1 L for long-term stability experiments. The experimental set ups of two-gaps and one-gap cell experiments are shown in detail in Supporting Information. For zero-gap cell experiments, commercially available cells in zero-gap architecture from Dioxide Materials were used. CEM-based zero-gap cells were assembled with CuO catalyst based cathode GDEs

and anode CCM containing CEM (Siemens Energy). AEM-based zero-gap cell assembly consisted of CuO catalyst based GDEs, anion exchange membrane (Sustainion® 37 from Dioxide Materials) and Ti mesh coated with IrOx (DeNora). BPM-based zero-gap cells were assembled similarly to the AEM-based, only employing a bipolar membrane (FUMASEP® FBM-PK reinforced with PEEK) instead.

5.3.2. Electrode Preparation

Drop-casted electrodes: The catalyst ink suspension was prepared with CuO powder particles delivered by Johnson Matthey, the anion exchange ionomer (Sustanion® XA-9 anionic ionomer in EtOH solution from Dioxide Materials) at a certain ratio from 5 to 20 wt.% of the catalyst amount, and isopropanol (99.9%, Sigma Aldrich). The ink was sonicated in an ultrasonic water bath for 30 minutes and immediately drop-cast onto a 10 cm x 5.5 cm GDL, either the carbon-based GDL (Freudenberg H23C2) or the PTFE-based GDL (Sterlitech 0QL8222005). After one layer of catalyst ink was applied onto the carbon paper, it was placed in the drying oven at 40 °C for two minutes. This process was repeated until all the catalyst ink was used up. The catalyst loading was 1.0 mg/cm^2. PTFE-based GDLs required an additional top layer for electrical conductivity. An analogous procedure to the catalyst layer was repeated for the top layer, substituting CuO with carbon nanoparticles and anion exchange ionomer with three different binders (Fluoriniert^{TM} FC-40 from Sigma Life Science, Nafion perfluorinated resin solution 5 wt.% in mixture of lower aliphatic alcohols and 45% water from Aldrich Chemistry and Polytetrafluoroethylene 60 wt.% dispersion in H_2O from Sigma-Aldrich). Electrodes were dried overnight at room temperature under a N_2 atmosphere with a flow of 50 sccm. The dried electrode batch was cut into two pieces in the size of 48 mm x 44 mm. The active area that took part in the electrolysis was 10 cm^2. In the Dioxide Materials zero-gap cell experiments, the active area was 5 cm^2.

Drop-casted electrodes with AEIL: A metal oxide ink was prepared analogously to the catalyst layer ink preparation explained above. The metal oxide particles (TiO_2 in 5 µm and 100 nm particle sizes, ZrO_2 in 5 µm and 100 nm particle size, CeO_2 in 25 nm particle size, Y_2O_3 in 50 nm particle size and SiO_2 in 200 nm particle size from Sigma Aldrich) were mixed with Sustanion® XA-9 anionic ionomer in EtOH solution from Dioxide Materials to form the AEIL ink. The ink was sonicated in an ultrasonic water bath for 30 minutes and immediately drop-cast onto the anode CCM. The cathode electrode was pressed to the anode CCM with AEIL during cell assembly. The wet AEIL connected phsycially the cathode and anode side forming the MEA.

Dry-pressed electrodes with AEIL: The metal oxide and dry anion exchange ionomer (Sustainion® XA-9 Alkaline Ionomer Powder from Dioxide Materials) particles were mixed homogeneously using a laboratory-sized instrument for asymmetric centrifugation (SpeedMixer DAC 150 FVZ). Anode CCM was placed on a hot (80 °C) aluminum plate together with the 3 x 3 cm PTFE frame on top. The metal oxide – anion exchange ionomer powder mixture was distributed evenly filling the frame. The frame was removed and the pre-prepared cathode GDE, wetted with EtOH, placed on top of the powder mixture. The sandwich assemble was pressed between two aluminum plates at 80 °C with 2000 psi for 1 minute. The obtained MEA was dried overnight at room temperature under a N_2 atmosphere with a flow of 50 sccm.

5.3.3. Electrochemical Measurements

Chronopotentiometric electrochemical measurements were performed using a Bio-Logic VSP 3e potentiostat controlled by the EC-Lab® software. Ag/AgCl (3 M NaCl) reference electrode was placed at the catholyte inlet. A catalyst preconditioning with chronopotentiometry program of 25 mins at 50 mA/cm^2 was performed in all experiments. In stability experiments, the current densities were then set to 100, 200 or 300 mA/cm^2 for the complete experiment duration. In the current density variation experiments, the current density was varied each 45 minutes in an

increasing order. CO_2 feed flow rate was adjusted to be constant the total current based on the λ value (λ = 10.33), and the ratio of actual feed CO_2 flow rate to the CO_2 flow rate theoretically required for full utilization of electrons to ethylene formation, formulated in Equation 7**,** When the current density was varied, CO_2 flow rate was as well accordingly varied to satisfy λ = 10.33.

Stability experiments required electrolyte refurbishment to maintain the bulk pH. This was enabled by an external pumping system (micro diaphragm liquid pumps NFB 25 KPDCB-4A, KNF) that pumped out the electrolyte in the system and pumped in fresh electrolyte. The pumps were turned on every 48-72 hours. During this procedure, the experiment was uninterrupted and no further change in the system was necessary.

Electrochemical measurement results were expressed in terms of measured electrode potentials and faradaic efficiencies of each product.

5.3.4. Analytic Methods

GC: Gas product stream was analyzed with online measurements by gas chromatography (GC). A gas chromatograph instrument (Thermo Scientific Trace 1410) equipped with two thermal conductivity detector channels (TCD) for H_2, CO_2, O_2, N_2 and CO, and a flame ionization detector channel (FID) for CH_4 and C_2H_4 was connected to the test stand for online analysis. 5 Å mol-sieve columns (Restek) and micro packed GC columns (HayeSeP Q, Restek) were used to separate the gas mixture. Ar and He were the carrier gases. 1 mL of the gas product was automatically injected to the GC sampler every 8 minutes. The product stream was mixed with internal standard N_2 before being fed to the GC. Chromeleon™ software was used for the automated measurements and data evaluation. The quantification of gas products is elucidated in Supporting Information.

NMR: Liquid product analysis was performed with offline manual sampling of the electrolyte and following ^{1}H Nuclear magnetic resonance (NMR) spectroscopy measurements in which 500 MHz Bruker (Bruker Bio-Spin, Karlsruhe, Germany) instrument was used following the method described by Cuellar et al.[112]. Liquid product samples were collected from the catholyte outlet and prepared in an aliquot of the electrolyte containing liquid products (300 µL) mixed with 0.1 M sodium fumarate internal standard (50 µL) and D_2O (250 µL). The quantification of liquid products is elucidated in the Supporting Information.

FIB/SEM and FIB/EDX: The images of pristine and post-experiment GDE samples were captured by focused ion beam scanning electron microscopy (FIB/SEM) analysis with Zeiss Crossbeam 550 instrument equipped with a secondary electrons and secondary ions (SESI) detector. Electron high tension (EHT) of 2.00 kV and working distance of 5.1 mm were set in the measurements. For the milling, an accelerating voltage of 30 kV was used and probe currents of 65 nA, 30 nA (course mills) and 7nA (fine mill) were used. This was then followed by a 300 pA polishing mill. The images were captured at magnifications of 200000 and 50000. Energy-dispersive X-ray (EDX) spectroscopy was applied for compositional analysis at EHT of 15 kV and probe current of 2 nA.

XRD: Phase determination of the precipitated salt material was obtained via XRD analysis (Empyrean, Malvern Panalytical, UK). Cu-Kα radiation (λ = 1.54056 Å) and a monochromator were employed to scan the samples applying a step size of 0.007° and 70 steps/min from 2θ = 5 – 90°. Salt particles collected from the gas compartment of the cell and GDE were dried in 80 °C oven for 3 days prior to the XRD measurement. XRD measurement results are shown in the Supporting Information.

5.4. Results and Discussion

The results obtained in our research underlined the importance of a multi-factorial approach to enable selective and stable CO_2-to-C_2H_4 electrolyzers. Primarily, the potential cell architectures facilitating the electrochemical reaction were evaluated based on their performance by experimental evidence and their technical maturity for industrial applications. The two down-selected cell architectures were further studied with a focus on the electrode design. Subsequently, the fine-tuned cell and electrode design combination was tested for long-term stability in test stands tailored for such experiments.

5.4.1. Evaluation of Different Cell Architectures

Five cell architectures (named after the number of cell compartments between the electrodes and the employed membrane) were identified to facilitate CO_2 electrolysis. Three fundamental parameters were selected to evaluate the CO_2 electrolyzer architectures: Cell potential, scalability, and CO_2 crossover. The aspects such as faradaic efficiency towards desired C_2H_4 and long-term stability were deliberately not chosen for down-selection of the cell architecture, as these are predominantly determined by the electrode design and not necessarily by the cell architecture. Cell potential and CO_2 crossover aspects were assessed on the basis of electrochemical measurements. Cell potential directly affects the required energy input and hence the economic feasibility. CO_2 crossover is a fundamental hurdle that jeopardizes carbon efficiency by feed gas loss from cathode to anode and creates additional CO_2 separation costs for the downstream process. Scalability was reviewed based on the industrial examples of readily scaled up cell architectures and unsolved major technical challenges. Experiments presented in this section were conducted with identical experimental conditions (j = 200 mA/cm^2 and room temperature) using identical carbon-based gas diffusion electrodes. Further details can be found in the **Materials and Methods** section.

Two-gaps cell design showed the highest cell potential of 6.40 ± 0.51 V at 200 mA/cm^2. Unsurprisingly, CO_2 crossover was also the highest among the tested cell designs with an anodic CO_2/O_2 gas molar ratio of 2.57 ± 0.13 due to the employed mixed electrolyte operation mode. In two-gaps cells, catholyte and anolyte can be joined in a single vessel for ion and pH compensation, named as mixed electrolyte operation mode. Due to the nature of CO_2 electrolysis, cathode reactions continuously produce OH^- and drive the catholyte to an alkaline region over time. In contrast, an anode reaction produces H^+ and results in an acidic anolyte. Therefore, mixed electrolytes in a single vessel can compensate for the pH difference between two gaps over time. However, this method cannot be applied in the scaled-up cells, as CO_2 feed in the form of carbonates in the catholyte would mix with the anolyte and carbonates retransform to CO_2 near the anode due to local acidic conditions. This leads to CO_2/O_2 separation requirements from the anolyte gas. Another strategy to compensate for the inevitable ion migration between anolyte and catholyte through the ion exchange membrane is selecting the initial concentrations of anolyte and catholyte accordingly different to each other (molarities between 0.05 M until 10 M are reported in the literature [69,203]). However, this strategy necessitates constant replacement of catholyte and anolyte, which is not feasible for long-term operation. Two-gaps cell designs are already well established and scaled up to MW-range in commercial plants for other technologies such as alkaline water electrolyzers [213] and recently redox flow batteries as well [214].

One-gap CEM cell design achieved a reduced cell potential of 4.53 ± 0.44 V at 200 mA/cm^2. Employing a CEM-based CCM in the anode, therefore discarding the second gap between the anode and membrane, improved the cell potential compared to the two-gaps cell design by reduction of ohmic and diffusion overpotentials. An anodic CO_2/O_2 molar ratio of 0.05 ± 0.02 provided the lowest carbon crossover among the tested cell architectures. The thick CCMs (>90 µm) undoubtedly played a crucial role in low carbon crossover. This cell architecture was scaled up to the cell size of 5000 cm^2 for CO_2 electrolysis already [215]. Applicability of anode CCMs

from the industrial PEM electrolyzer products in the anode of the one-gap CEM-based cell architecture renders this design easily scalable for CO_2 electrolyzers.

Zero-gap CEM cell design enabled the lowest cell potential of 3.76 ± 0.27 V at 200 mA/cm^2 among the tested cell architectures. Carbon crossover to the anode was also low, with a CO_2/O_2 ratio of 0.19 ± 0.09 in the anodic gas. This cell design is already scaled up to the MW range in commercial plants by different companies for PEM water electrolysis [216–218]. Although zero-gap CEM cell satisfies the three design requirements of low cell potentials, low CO_2 crossover, and demonstrating the potential for scalability on an industrial level; electrode design must be significantly modified for adapting to CO_2 electrolyzers, which will be discussed in the next section.

Zero-gap AEM cell design also demonstrated low cell potential around 3.79 ± 0.36 V at 200 mA/cm^2. The carbon crossover levels in the same current density were, however, excessive. Carbonate ions were formed from CO_2 under alkaline conditions in the cathode and travelled through the AEM, following the well-described ion transport mechanism [219], and got released as CO_2 gas in the anode. The CO_2/O_2 molar ratio in the anode is a direct measure of feed gas crossover and implicates an inherently low carbon efficiency. GC measurements of the anolyte gas head space confirmed excessive CO_2/O_2 molar ratios of 1.55 ± 0.13. This ratio is theoretically determined by the negative charge carrier: HCO_3^-, CO_3^{-2}, and OH^- leading to volumetric CO_2/O_2 ratio of 4, 2, and 0, respectively (Details are explained in Supporting Information). Despite promising advancements in recent years in the scaling up of AEM water electrolysis technology [220,221], the alkaline decomposition problem of quaternary ammonium groups in AEMs via Hofmann elimination is not yet solved [222]. Moreover, the further unsolved challenges associated with lower charge mobility, slower transport mechanisms of carbonates and carbonate deposition [223–225], along with the AEM/AEI dissolution by alcohol byproducts [133,219], are unique to Cu-based CO_2 electrolyzers built with AEMs. These distinctive issues do not necessarily manifest in AEM water electrolysis systems and must be overcome before scaling up AEM-based CO_2 electrolyzers.

Zero-gap BPM cell design shows a high cell potential of 5.38 ± 0.55 V at 200 mA/cm^2 in the forward bias mode (AEL facing towards cathode). The high cell potentials, despite the zero-gap design, were associated with the intense salt formation in the AEL-CEL junction. The forward bias mode facilitates water association in the BPM in electrolysis from cathodically generated OH^- and anodically generated H^+. Under CO_2RR conditions operated with liquid electrolyte in anolyte, the cathodic ion transport occurs in the form of carbonates to the membrane junction, and the anodic ions being transported via CEL to the membrane junction are predominantly K^+ [226]. This leads to salt formation in the membrane junction depending on the current density. The strong salt formation was also observed in the cathode GDE, signalling K^+ permeance through AEL. The experiment duration was limited to 4 hours by the above-mentioned problems. The anodic CO_2/O_2 molar ratio of 0.44 ± 0.06 was significantly lower than the zero-gap AEM cell architecture, proving that the CEM layer is effective against carbonate crossover. BPMs reached a certain industrially relevant technical maturity for producing organic and inorganic acids and alkaline solutions from wastewater feed [227,228]. So far, there is no industrial BPM product developed for CO_2 reduction. Future design improvements in forward bias operated BPMs focusing on salt and water management in the membrane junction or future catalyst improvements in reverse bias operated BPMs for lowering the high potential losses to water dissociation are essential for BPM-based CO_2 electrolyzers.

From the cell potential aspect, only the AEM and CEM zero-gap cell architectures show arguably satisfactory performance (> 4 V at 25 °C) to candidate for industrial relevance considering the current state of the art for CO_2-to-C_2H_4 electrolyzers, whereas one-gap and BPM zero-gap cell architectures require additional development efforts for significant improvements in this regard. It must be noted that the commercial PEM electrolyzer stacks are not run at 25 °C, rather at 70-80 °C, which implies that cell potentials presented in **Figure 41** measured at 25 °C for each cell architecture will be much lower in their stacked and scaled up versions. The tested

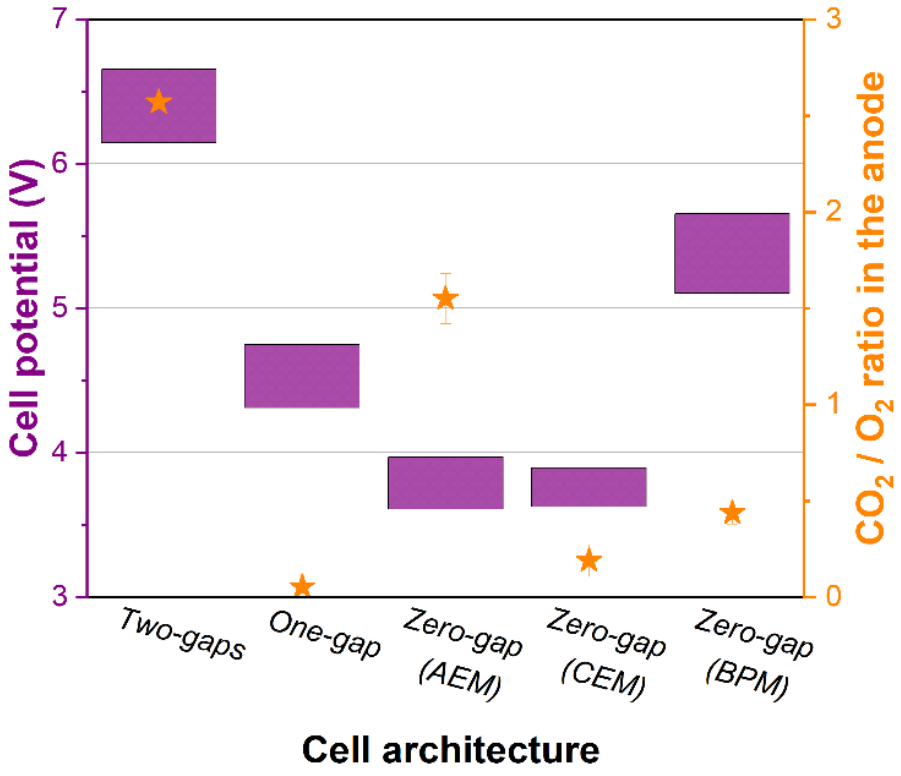

Figure 41. Cell potentials recorded during the electrochemical experiments at 200 mA/cm^2 between t = 1 - 24 h with different cell architectures (purple rectangulars assigned to left y-axis). Molar CO_2/O_2 ratio in the anode obseved in GC measurements of anode gas head space in different cell arcitectures between t = 1 – 24 h (orange stars assigned to right y-axis).

cells were not optimized for superior cell potential performance; therefore, the measured values should only serve as a guide for comparability between the cell architectures. From the scalability aspect, two-gaps, one-gap, and CEM zero-gap cell architectures were readily implemented in various industrial-scale applications. There have been promising advancements in the scaling up of AEM and BPM-based cell architectures; nevertheless, there are still specific technical challenges associated with their applications in Cu-based CO_2 electrolyzers. Additionally, the CO_2 crossover aspect depicts an acute issue for conversion efficiency, and the high rates of CO_2 crossover in AEM-based zero-gap and two-gaps cell architectures (CO_2/O_2 ratio in the anode > 1.5) would necessitate technology breakthroughs or innovative engineering solutions for these cell architectures' industrial relevance for CO_2 electrolyzers. These qualitative evaluations are

visualized in **Figure 42**. The overall evaluation led to the down-selection of one-gap and CEM-based zero-gap cell architectures for the successive phase of our research, directing our focus towards modifications to the cathode electrode.

5.4.2. Cathode Electrode Modifications

The cathode GDE is possibly the most critical component of Cu-based CO_2 electrolyzers, simply because the product selectivity and the stable formation of the products are fully determined by it. The rest of the components - Ir anode[229,230], cation exchange membrane[231,232] and stacking components[233,234] - had already been developed to be stable for thousands of hours as part of the PEM electrolyzer and PEM fuel cell development efforts dating back to 1970s.

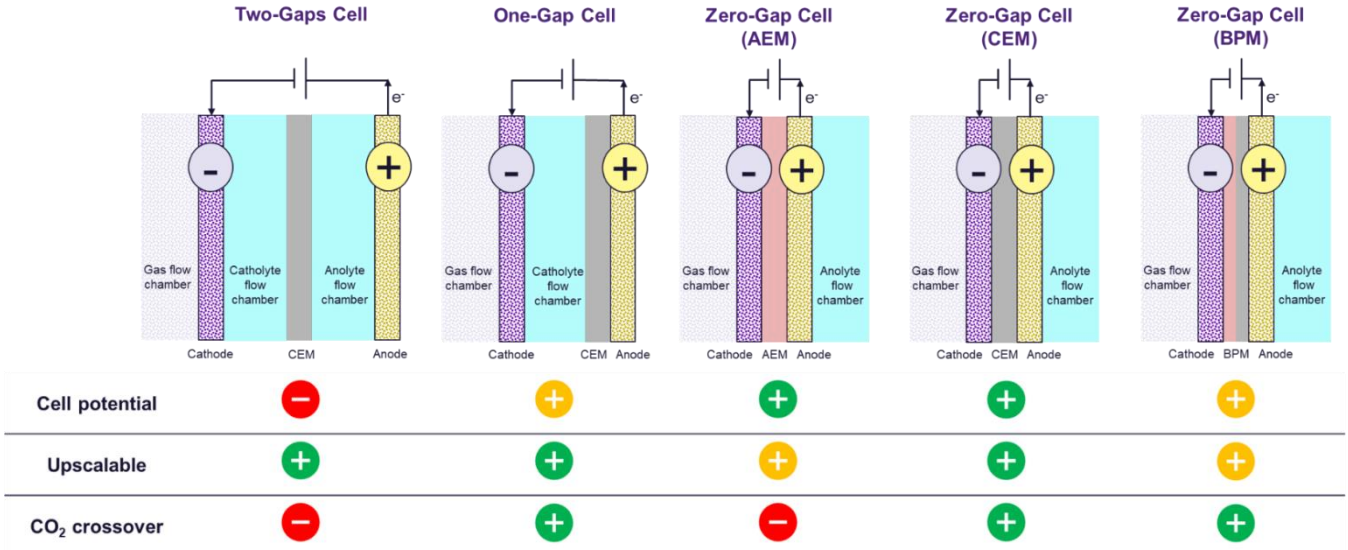

Figure 42. Qualitative evaluation of cell architectures for industrial CO_2RR applicability by the most relevant critical aspects based on the current state of the art. ⊕ denotes that the corresponding cell architecture is evaluated as applicable for industrial CO_2RR systems with respect to the corresponding aspect. ⊕ indicates to the further development requirement for the corresponding cell architecture to be applicable in industrial CO_2RR systems with respect to the corresponding aspect. ⊖ stands for currently non-applicable cell architecture in industrial CO_2RR systems with respect to the corresponding aspect. The overall evaluation leads to the down-selection of CEM zero-gap and one-gap cell architectures for electrode development.

Cathode GDE was modified in various ways to suit the two down-selected cell architectures separately, while keeping the used catalyst constant as CuO for comparability.

5.4.2.1. GDEs for CEM-based Zero-Gap Cell Architecture

CEM-based zero-gap cell architecture dictates an acidic environment throughout the MEA since the employed CEM, e.g., Nafion^{TM} 117, is conventionally perfluorosulfonic acid (PFSA) polymer membrane consisting of a polytetrafluoroethylene backbone with perfluoroether pendant side chains terminated by sulfonic acid groups. Water molecules form a hydrate shell around the sulfonate, enabling the dissociation of protons from the sulfonate group. The cations are transported along water channels in the PFSA by forming hydrogen bonds between the associated water molecules and cations or hydronium ions. The dissolved sulfonate side chains with the associated protons decrease the pH of alkaline aqueous solutions in their vicinity to less than 5 due to a pK_a of -5.6 [235]. Accordingly, a need exists to control the cathode microenvironment necessary for CO_2 reduction reactions and, in particular, to abrogate the acidic cathode microenvironment issue, as CO_2RR kinetics demand an alkaline microenvironment [71,143,236], independently of the bulk phase pH. Therefore, we have developed a porous anion exchange ionomer layer (AEIL) to be implemented between the anode CCM and cathode GDE. **Figure 43A** illustrates a cross-sectional area of a CEM-based zero-gap cell with the sandwiched MEA (2-3). The two core cell components, anode CCM (3) and cathode GDE (2), were assembled to form MEA. The anode CCM was preassembled and composed of the anodic catalyst layer (3b) and the CEM (3a). The cathode GDE consisted of three layers: GDL (2a), CuO catalyst layer (2b), and AEIL (2c), which contained AEI and metal oxides (MO). It was designed to limit H^+ concentration caused by the nature of CEMs in the catalyst vicinity, meanwhile being weakly permeative for K^+, therefore decoupling pathways for efficient anion transport via AEI particles towards the anode and weak cation transport via MO particles towards the cathode. Acting as filler particles for porous AEIL, MOs played a vital role which differentiates this unique design from BPM-based zero-gap cell architecture with two neighbouring continuous ion exchange layers.

The promising metal oxide candidate, TiO_2, possesses the remarkable electrochemical feature of being able to mobilize cations even at low temperatures (T<100°C), as discovered in the late 1990s and early 2000s [237,238]. Especially nanoparticles of TiO_2 show significant proton conductance capability through water absorption and cation transport on the surface and grain boundaries based on a hopping-based mechanism [239,240], which continues to catch significant attention in Li-ion battery research applications [241–243]. We believe TiO_2 is a promising candidate for this specific application in AEIL, as the solvated cation presence in the Helmholtz double layer increases the electrical field and strengthen the adsorption of dipolar CO_2RR intermediates [50,51]. As further candidates, we have chosen ZrO_2, SiO_2, CeO_2 and Y_2O_3 as MOs as filler particles for the common purpose of increasing the conductivity and porosity as well as bringing in rigidness to the otherwise pliable layer. AEIL was elaborately modified to enable CO_2RR in the cathode by varying the electrode preparation method, MO type in the AEIL and their particle sizes in micrometer and nanometer ranges, MO/AEI weight ratio and their total amounts.

Integration of AEIL into the MEAs was performed by drop casting or dry pressing (**Materials and Methods** refer to details of each technique). The first included the drop-casting of AEI + MO ink onto the anode CCM. As the AEIs are based on ethanolic solutions, ethanol presence near the CEM was unavoidable in this technique, resulting in surface dissolution of the CEM with locally formed cavities. The electrochemical measurements at 100 mA/cm^2 of MEAs prepared with drop casted AEIL were poorly reproducible, as shown in **Figure 43A**. We have discontinued using drop casting to synthesize MEAs as it was not possible to replicate electrodes.

On the other hand, the MEAs prepared with dry-pressed AEIL exhibited no such abnormalities. They were mechanically intact after synthesis. **Figure 43B** compares dry-pressed MEAs with varying AEIL loadings and MO particle sizes at constant 20 wt.% AEI/MO composition ratio tested at 100 mA/cm^2 with 1 M $KHCO_3$. ZrO_2-based AEILs could produce C_2H_4 only at low FEs (< 6%), regardless of particle size and loading. TiO_2-based AEILs with 55 mg/cm^2 TiO_2 loading

were active for CO_2RR at smaller size particles of 100 nm, allowing $FE_{C_2H_4}$ of 14.3 ± 2.7%. The half amount of loading, 27.5 mg/cm^2 of 100 nm TiO_2, enabled CO_2RR comparatively to a lesser extent at $FE_{C_2H_4}$ of 7.3% ± 1.9. Bigger size TiO_2 particles of 5 µm led to almost exclusive HER activity. The experiments with the other MOs (CeO_2, Y_2O_3 and SiO_2) did not yield to any CO_2RR activity, similar to the CEM-based zero-gap cell experiments without AEIL. These results proved that AEIL, with the right design, was able to counterbalance the H^+ dominance in the catalyst surface and yet still facilitate transport of CO_2RR essential K^+ to the catalyst vicinity. The further experiments were conducted to better understand the relationship between transport of cations to catalyst and its ability to reduce CO_2 to C_2H_4. For this purpose, AEIL loading, K^+ concentration in the anolyte, bulk anolyte pH and the composition ratio of AEI/MO were manipulated in the experiments, as the results summarized in **Figure 43B**. Doubling AEIL loading from 55 to 110 mg/cm^2 with constant 20 wt.% AEI ratio, and reducing $KHCO_3$ molarity from 1 to 0.1 M had similar outcomes and dropped $FE_{C_2H_4}$, whereas substituting 0.1 M KOH for 0.1 M $KHCO_3$ and doubling the AEI ratio from 20 wt.% to 40 wt.% at constant AEIL loading increased C_2H_4 selectivity. The findings affirmed the need of limiting the H^+ concentration and maintaining K^+ presence in the catalyst vicinity.

Even though CO_2RR was enabled by implementation and modification of the AEIL in zero-gap CEM-based cell architecture, no experiment in this configuration lasted longer than 3 – 4 hours due to excessive salt formation in the cell. This also did not allow to apply current densities higher than 100 mA/cm^2 due to even faster and more intense salt formation. The highest achieved

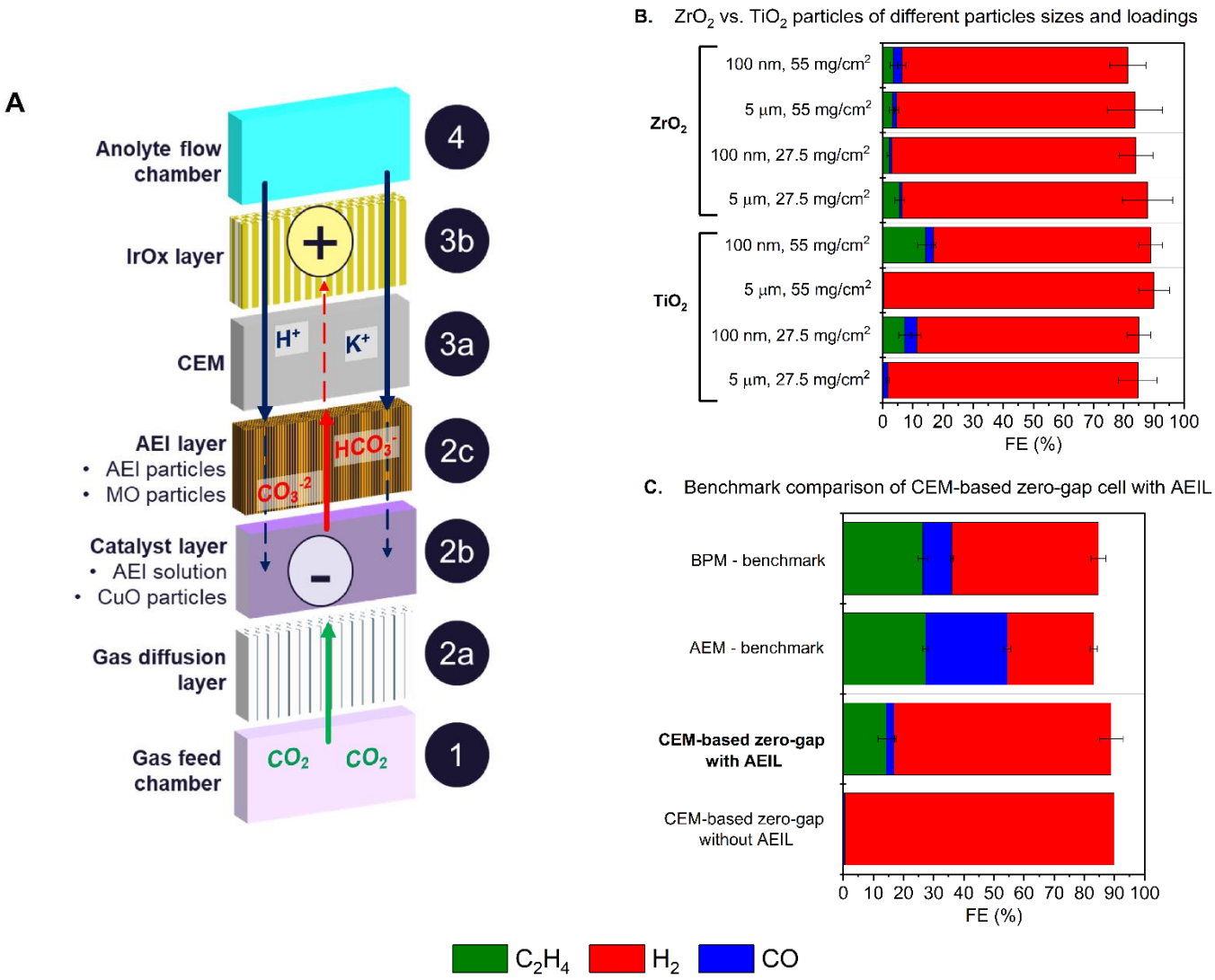

Figure 43. (**A**) Cross-sectional illustration of CEM-based zero-gap cell architecture with the novel MEA design. The arrows represent the following ion transport routes. Red straight arrow: Anion transport from cathode catalyst layer toward AEIL. Red dashed arrow: Depleted anion transport from AEIL toward anode catalyst layer. Blue straight arrow: Cation transport from anolyte toward AEIL. Blue dashed arrow: Depleted cation transport from AEI layer toward cathode catalyst layer. (**B**) Faradaic efficiencies of gas products obtained within the first 120 minutes of chronopotentiometric experiments (100 mA/cm^2) with AEIL-design MEAs prepared by dry pressing method with 100 nm and 5 µm sized particles comprising loadings of 27.5 and 55.0 mg/cm2 of TiO_2 and ZrO_2 at a constant MO:AEI ratio of 5:1. (**C**) Faradaic efficiencies of gas products obtained within the first 120 minutes of chronopotentiometric experiments (100 mA/cm^2) in zero-gap cell architectures consisting of AEM, BPM, CEM with and without AEIL implementation.

$FE_{C_2H_4}$ of 14.3% with AEIL design in CEM cell is lower than the benchmark results with AEM and BPM cells that were experimented with the identical catalyst and gas diffusion layers at 100 mA/cm^2, as compared in **Figure 43C.** As it is a novel step towards CEM-based zero-gap CO_2 electrolyzers with exciting initial results published in this work, we believe further research is

required to unlock the full potential of this design. Salt formation might be prevented with higher operation temperatures with corresponding alterations in the layers against flooding induced by higher humidity. The cation transport ability of TiO_2 can be enhanced by doping materials. The cation and anion transport paths can be decoupled completely by engineered channel networks within AEIL. Nevertheless, as this work focuses on readily scalable stable cell-electrode design combination, CEM-based zero-gap cell design with AEIL electrode modification could not be considered further for the long-term stability tests.

5.4.2.2. Electrode Modifications for One-Gap Cells

One-gap cell architecture with liquid catholyte adjacent to the cathode GDE alters the microenvironment requisites for C_2H_4 selective CO_2RR when compared to the zero-gap CEM-based cell architecture. As the alkaline electrolyte already creates a pH buffer zone between acidic CEM and GDE, an AEIL component in the GDE aiming for optimal H^+/K^+ presence is redundant in this configuration. Instead, the electrode modifications in the one-gap cell architecture focused on adjusting CO_2 availability and creating hydrophobic and hydrophilic domains since a common failure mode of the CO_2 reduction cathodes in a liquid electrolyte-containing configuration is flooding of the GDE pores. Hence, we investigated key parameters in the GDE design for optimal microenvironment for CO_2RR: AEI loadings in the catalyst layers, feed gas humidification, carbon and PTFE-based GDLs, and conductive overlayers for PTFE-based GDLs. **Figure 44A** illustrates a cross-sectional area of a one-gap cell with three core cell components, anode CCM (4) and cathode GDE (2), separated by the catholyte (3). Anode CCM was preassembled and composed of the anodic catalyst layer (3b) and the CEM (3a). Cathode GDEs consisted of three layers: GDL (2a), CuO catalyst layer (2b), and an optional electrically conductive layer composed of carbon-based particles (2c) for non-conductive GDLs.

Ionomers, used for binding the catalyst particles to the GDL, take part in defining hydrophobic and hydrophilic domains in the GDE. Extended gas diffusion and ion transport are

facilitated owing to hydrophobic and hydrated hydrophilic domains, respectively [107]. Imidazolium-based anion exchange ionomers are particularly interesting owing to the positively charged imidazole heterocycles as functional groups in the side chains that repel protons and accommodate hydroxide ions moving them along the side chains [244]. Its high OH^- mobility and CO_2 adsorption affinity [200] highlight AEI as a natural binder candidate for CO_2RR cathodes. **Figure 44B** presents the effects of AEI binder loading in the 1.0 mg/cm^2 CuO catalyst layer, where the given percentages account for the weight ratio of binder to catalyst. At all current densities, 10 wt.% AEI delivered the highest $FE_{C_2H_4}$ reaching up to 43.6 ± 0.5% at 400 mA/cm^2. Catalyst layers containing 5 and 10 wt.% AEI exhibited increasing $FE_{C_2H_4}$ from 100 to 400 mA/cm^2. Yet 500 mA/cm^2, the highest current density tested in this study, caused apparent mass transport limitations and cut down faradaic efficiency for CO_2RR in favor of HER. 20 wt.% AEI in the catalyst layer provoked the decline of CO_2RR and the increase of HER kinetics starting already at 400 mA/cm^2. Increasing AEI coverage in the catalyst layer may have limited the CO_2 availability at the catalyst surface by reducing the volume of free pores due to its swelling nature and by widening the CO_2 diffusion path through the wet layer on the catalyst surface. Increasing current densities require correspondingly increasing amounts of available CO_2 molecules in the catalyst vicinity to be converted into CO_2RR products. Limiting CO_2 availability by employing 20 wt.% AEI ratios in the catalyst layer resulted in the decline of $FE_{C_2H_4}$ at 400 mA/cm^2 instead of 500 mA/cm^2 compared to 5 and 10 wt.% AEI. This finding backs up the hypothesis of mass transport limitation as the reason for selectivity shift from CO_2RR to HER at high current densities (> 400 mA/cm^2) in short-term (< 24 h) experiments. A further important finding in the AEI loading study was the

relationship between FE_{CO} and the AEI ratio in the catalyst layer. 5 wt.% AEI containing catalyst

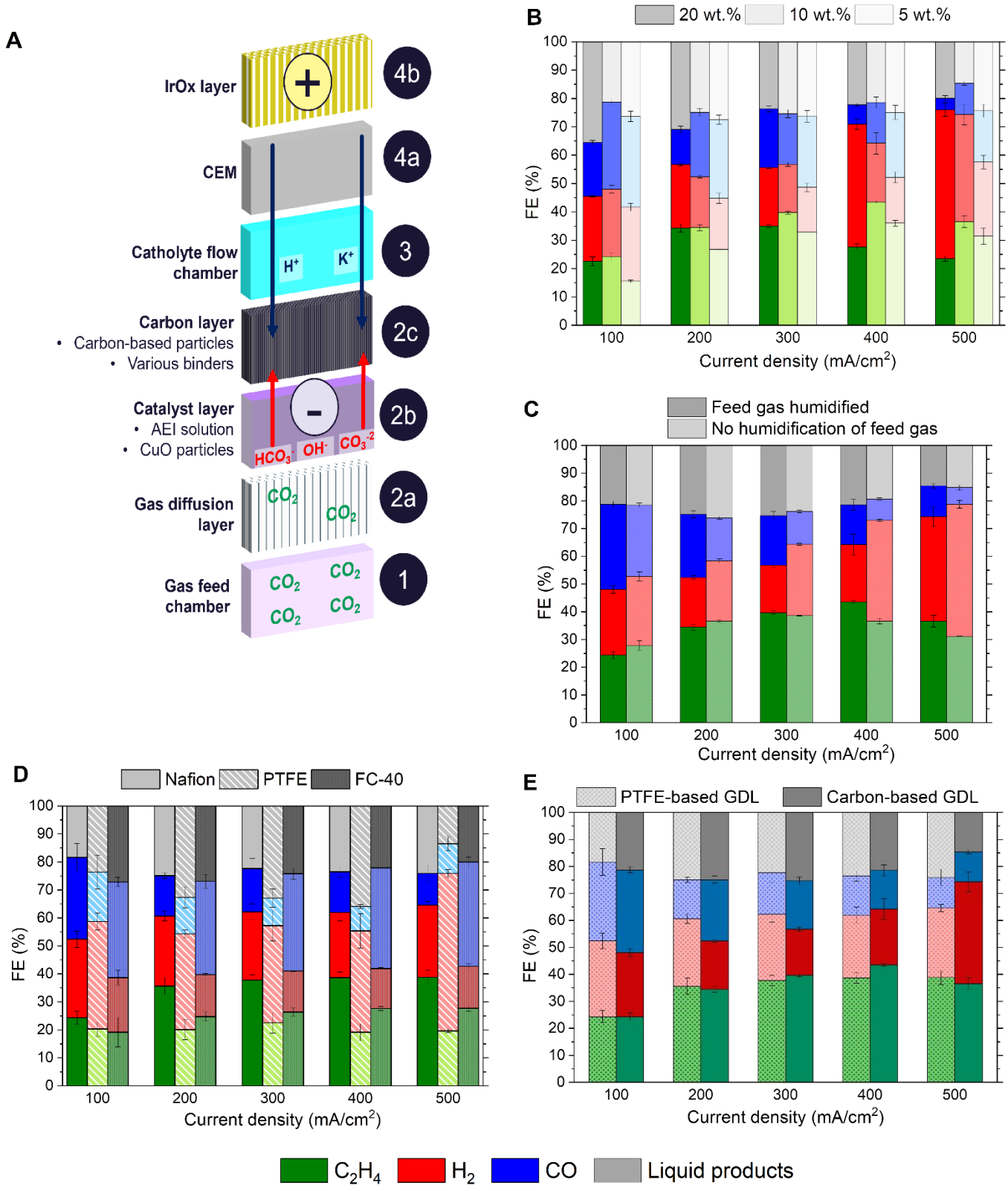

Figure 44. (**A**) Cross-sectional illustration of CEM-based one-gap cell architecture with multilayered GDE design. The arrows represent the following ion transport routes. Red straight arrow: anion transport from cathode catalyst layer toward electrolyte. Blue straight arrow: cation transport from CEM toward cathode. (**B**) Gas product distribution expressed in terms of faradaic efficiencies obtained at t = 24 h in the current density variation experiments with carbon-based GDEs containing different AEI loadings in the catalyst layer. (**C**) Gas product distribution expressed in terms of faradaic efficiencies obtained at t = 24 h in the current density variation experiments with carbon-based GDEs in the presence or absence of feed gas humidification. (**D**) Gas product distribution expressed in terms of faradaic efficiencies obtained at t = 24 h in the current density variation experiments with PTFE-based GDLs consisting of various binder types in the top carbon layer. (**E**) Gas product distribution expressed in terms of faradaic efficiencies obtained at t = 24 h in the current density variation experiments with carbon-based GDE containing 10 wt.%AEI in its catalyst layer and PTFE-based GDE containing 10 wt.% AEI in its catalyst layer combined with CEI containing top carbon layer.

100% total FE was assumed for assigning the total faradaic efficiency of the liquid products that were not quantified in this series of experiments.

layer produced significantly more CO at every current density. This may be a hint for AEIs determinative role in CO_2 adsorption behaviors (in parallel with other studies [245,246]), consequently defining CO_2 availability as well as CO_2/H coverage in the catalyst layer.

Product spectra obtained with the same type of electrode (10 wt.% AEI in the CuO layer and carbon-based gas diffusion layer) with and without feed gas humidification revealed the importance of water management in the catalyst layer, as shown in **Figure 44C**. Lack of humidification provided slightly better $FE_{C_2H_4}$ at 100 mA/cm^2 (27.8 ± 1.7 % versus 24.3 ± 1.4 %) and 200 mA/cm^2 (36.5 ± 0.4 % versus 34.4 ± 1.1%), where the mass transport of CO_2 is not critical. In contrast, humidification allowed increasing $FE_{C_2H_4}$ at higher current densities until 500 mA/cm^2, whereas the lack of humidification resulted in decreasing $FE_{C_2H_4}$ at j>300 mA/cm^2 at the cost of rising FE_{H_2}. Comparatively lower FE_{CO} was observed in the non-humidified feed gas experiments at all current densities. All these findings signal that CO_2 feed humidification facilitates the thin aqueous layer formation on the catalyst layer by swelling the AEI. The thin aqueous layer benefits CO_2 adsorption and CO_2RR selectivity in a similar manner to what Romiluyi et al. [247] proposed for Ag electrodes. Nonetheless, a thick aqueous layer can impose mass transport limitations by increasing the length of the CO_2 diffusion path, reaffirming our initial hypothesis regarding the findings of AEI loading effect. Despite the availability of carbon-based

GDLs developed for fuel cells and their easy handling owing to the good electrical conductivity, the degradation of carbon-based GDLs in long-term operation with high current density is inevitable as elaborated in recent works [150,210]. The salt formation in the conductive GDL due to cation drag and carbonate availability creates a solute concentration gradient between GDL (2a) and electrolyte (3), leading to osmatic pressure and water drag into the GDL. Flooded pores of carbon-GDL offer optimal conditions for HER: water, two HER catalysts (Cu and carbon), and non-competing CO_2RR due to CO_2 depletion.

To enable electrodes to function at high current densities without mass transport limitation, we discontinued employing carbon-based GDLs and substituted them with PTFE-based GDLs. PTFE-based GDLs cannot drag cations as they cannot create an electrical field due to their insulating nature. This omits the degradation mechanism observed in carbon-based GDL; nonetheless, a new challenge of incorporating a non-conducting layer in the electrode arises. Neither the insulative GDL layer (2a) nor the poorly conductive CuO-based catalyst layer (2b) enables in plane conduction to sustain the electron transfer. In this work, we solved the problem of non-conductivity in a similar manner to the already published works [161,203] with PTFE GDL by adding a well conductive third layer consisting of carbon-based particles (2c). The top carbon layer connects the catalyst layer to the electron source and ensures a uniform distribution of electrons over the catalytically active area.

Figure 44D shows the effect of the binder choice in the carbon layer on the product distribution. Two ionomers, AEI (Sustanion XA-9) and CEI (Nafion), as well as two hydrophobic fluorinated compounds, PTFE and a fluorocarbon oil including a tertiary amine group (Fluorinert™ FC-40) were investigated as binders for the top carbon layer. AEI binder in the carbon layer, combined with AEI binder in the catalyst layer, led to a high resistance against cation mobility towards the cathode and resulted in extremely high cell potential (> 20 V at 300 mA/cm^2). The other three compounds were tested successfully as the binder for the carbon layer on top of the catalyst layer

in similar loading ranges. CEI binder outperformed the other two hydrophobic binders without ion exchange abilities at every current density in terms of $FE_{C_2H_4}$. This result can be attributed to the anion trap provided by the outer CEI containing carbon layer which obstructed the transport of OH^- anions away from the catalyst layer. It created more alkaline local conditions promoting C-C coupling kinetics.

Figure 44E compares the product distribution obtained by carbon-based GDE with the catalyst layer containing 10 wt.% AEI and PTFE-based GDE with the containing catalyst layer 10 wt.% AEI and with top carbon layer containing CEI. PTFE-based GDEs did not exhibit the behavior of a mass transport limited electrode, which is typically revealed by shrinking $FE_{C_2H_4}$ / FE_{H_2} at high current densities as observed in carbon-based GDEs. With almost constant $FE_{C_2H_4}$ / FE_{H_2} ratio of approximately 1.5 at 200-500 mA/cm^2 current density range, PTFE-based GDEs provided steady selectivities even at high current densities, on the contrary decreasing $FE_{C_2H_4}$ / FE_{H_2} ratios of approximately 2.3 to 0.9 were observed for carbon-based GDEs at 300-500 mA/cm^2.

An electrically conductive layer (e.g., carbon-based GDL) behind the catalytically active layer in the cathode GDE causes an inherent problem of cation drag and salt formation induced flooding of GDEs in the salt electrolyte containing CO_2 electrolyzers. Stability experiments run with carbon-based GDLs at 100 mA/cm^2 confirmed that the selectivity shifted towards HER, the most stable being C_2H_4 selective for roughly 4 days, as provided in Supporting Information. As the future CO_2 electrolyzers will be feasible only with high current densities and must prove stable operation, PTFE-based GDEs were evaluated as the promising option for scaled up cells, even though carbon-based GDEs stay as a powerful tool for screening CO_2RR catalysts. Therefore, the most promising GDE candidate, the multilayered PTFE-based GDE consisting of 1.0 mg/cm^2

CuO catalyst layer with 10 wt.% AEI and top carbon layer with CEI was down-selected for the long-term stability investigation.

5.4.3. Long-Term Stability

Long-term stability experiments were performed with the fine-tuned combination of cell and electrode designs at 100, 200 and 300 mA/cm^2 current densities in a test rig specifically equipped with an external pumping system to allow electrolyte refurbishment without having to stop the experiment and sampling the electrolyte for liquid product quantification. Every 48-72 hours the used electrolyte was discarded and replaced with fresh 1 M $KHCO_3$ in the course of the reaction. A liquid sample was taken at t = 24 h for NMR analysis to calculate FEs for liquid products.

Figure 45 displays the faradaic efficiencies of gas products and the measured potentials in the long-term stability experiments. At 100 mA/cm^2, $FE_{C_2H_4}$ was above the 20% threshold for one month in an uninterrupted operation (**Figure 45A**). To our knowledge, this is the longest stable CO_2 electrochemical reduction to C_2H_4 ever reported in the literature. A rising FE_{H_2} (roughly after 600 h) followed by falling FE_{CO} (roughly after 700 h) coincided with the destabilization of working electrode potentials (around 600 h), while $FE_{C_2H_4}$ dropped under 20% after 720 h. At the end of the experiments after a month, GDEs lost their mechanical integrity. The catalyst and carbon layers were partially abraded leaving bare PTFE spots in the GDE surface, which could explain the destabilization of the potential. A rather more oscillating electrode potentials were observed at j = 200 mA/cm^2 (**Figure 45B**). $FE_{C_2H_4}$ was stable above 30% for 150 h and above 20% for 270 h. FE_{H_2} ascent was observable after 100 h, earlier than the start of $FE_{C_2H_4}$ descent – a trend similar to 100 mA/cm^2. At 300 mA/cm^2 (**Figure 45C**), electrode potentials were destabilized at an earlier time, resulting in abrupt end to the experiments due to potentiostat safety potential limits. A stable $FE_{C_2H_4}$ could be observed for 65 h followed by a declining trend from this time onwards.

The start of increase trend of FE_{H_2} around 30 h and a constant decrease of FE_{CO} from the experiment begin were detected. The amplification of the electrode potential destabilization with increasing current densities suggested that current density correlated phenomena such as salt formation or gas bubble build up might have contributed to the degradation. The full product distributions obtained by GC and NMR analyses at t = 24 h with 100-300 mA/cm^2 current densities are shown in **Figure 46A.** Expectedly, $FE_{C_{2+}}$ rose at more negative cathode potentials driven by higher current densities reaching 54% at 300 mA/cm^2, in parallel to the decline of FE_{C_1} from 41% at 100 mA/cm^2 to 22% at 300 mA/cm^2. In addition to the formate, ethanol and *n*-propanol as main liquid products, acetate, propionaldehyde and propionate grouped as other C_{2+} were detected in small amounts (each FE < 1%).

In order to gain a better understanding of stability experiment results, pristine and post-

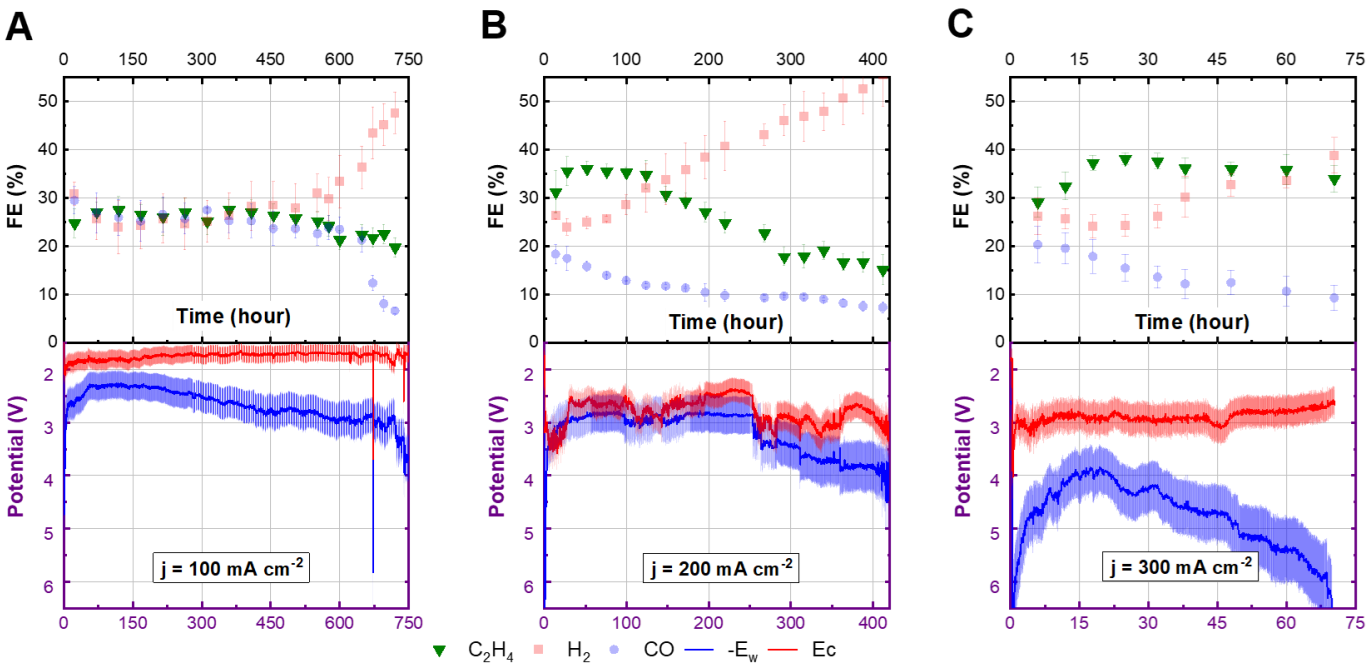

Figure 45. Faradaic efficiencies of the gas products and potentiostat recordings of working and counter electrode potentials obtained in the long-term stability chronopotentiometric tests of the multilayered PTFE-based GDEs consisting of 1.0 mg/cm^2 CuO catalyst layer with 10 wt.% AEI and top carbon layer with CEI at current densities of (**A**) 100 mA/cm^2, (**B**) 200 mA/cm^2, and (**C**) 300 mA/cm^2.

experiment electrodes were characterized with SEM/EDX. A cross-sectional FIB-SEM image of

the pristine multilayered GDE is presented in **Figure 46B:** 1) The bottom layer is PTFE GDL, 2) middle bright-coloured layer consists of flaky CuO particles, 3) top layer is carbon layer. An electrochemical experiment at 100 mA/cm^2 was interrupted purposedly at t = 48 h, when no downward trend for C_2H_4 or CO faradaic efficiencies and no upward trend for H_2 had yet begun. **Figure 46C** shows the post-experiment cross-sectional SEM image of that electrode, revealing partially blocked pores in the catalyst layer, which did not cause any observable degradation at t = 48 h. The deposition causing partial blockage of the pores were identified as salt deposition since EDX spectroscopy clearly detected K in the pores of catalyst and carbon layers (**Figure 56** in **Supporting Information**). The cross-sectional SEM image of the multilayered GDE tested uninterruptedly for 750 h at 100 mA/cm^2 is displayed in **Figure 46D**. By the experiment end, C_2H_4 and CO faradaic efficiencies had already begun declining and H_2 had risen steeply. This trend was evidently induced by extensive salt formation that fully packed the catalyst layer leaving no free pores, as confirmed with K detection in the catalyst layer by EDX spectroscopy (**Figure 57** in **Supporting Information**). The salt accumulation was observable even at a macroscopical scale. A sample was taken from the accumulated salt in the gas compartment, and XRD measurements confirmed it was $KHCO_3/K_2CO_3$, as presented in **Figure 48** in **Supporting Information**. It is widely understood that cations drawn to the cathode pull water molecules in their hydration shell and cause the accumulation of potassium, carbonate, and bicarbonate ions on the cathode over time. If the concentration of ions exceeds the solubility limit or water consumption becomes excessive, salt crystals will inevitably form on the cathode side. The experiments were repeated at elevated temperatures of electrolyte and gas humidifiers between 25 – 60°C to combat salt formation. Despite observing at the macroscopical scale that the formed salt clusters in the gas compartment diminished with temperature elevation, it led to the detriment of C_2H_4 selectivity and boosted H_2 selectivity (**Figure 59** in **Supporting Information**). Possible interpretations are the temperature-augmented wettability of system liquids and higher water-

uptake abilities of the employed ionomers at higher relative humidity levels, enabling water presence in all layers to a greater extent. Furthermore, a reduced liquid viscosity caused by higher temperatures may have potentially influenced the dynamics of gas bubble formation within the catalyst layer, which, in turn, could have had an impact on the local potentials within the cathode. Overall, this finding emphasizes the need to rethink electrode design suited for higher temperatures.

Interestingly, the post-experiment cross-sectional SEM image of the GDE tested at 300 mA/cm^2 for 75 hours indicated another degradation mechanism than salt formation: **Figure 46E** (and **Figure 46H** at elevated magnification) demonstrates a clear catalyst agglomeration and restructuring when compared to the pristine sample (**Figure 46F**). Furthermore, there was no indication of extensive K accumulation in the catalyst layer of that GDE as shown by EDX spectroscopy (**Figure 58** in **Supporting Information**). The flaky catalyst particle structure observed in the pristine GDE (**Figure 46F**) as well as after 48 hours of chronopotentiometric experiments at 100 mA/cm^2 (**Figure 46G**) differed substantially at 300 mA/cm^2. As revealed in **Figure 46H**, the dense flaky structure was turned into particle lumps of Cu, in some places partially agglomerated around salt particles. Higher local reaction rates may have expedited local dry-out and hotspots which may have potentially led to ionomer degradation. It is unclear from the SEM images whether ionomers initiated and/or contributed to the observed lump structures. These results reitarete that deconvoluting the reasons for potential morphological and reactive site transformations of the catalyst surface is crucial for understanding the degradation of CO_2 electroreduction, as pronounced by different researchers too [248,249].

Distinct degradation mechanisms at different current densities occurring at different time scales were identified in the long-term stability study. While salt formation was the primary identified degradation cause in the experiments run at 100 mA/cm^2 for one month, agglomeration in the catalyst layer and obvious catalyst restructuring could be recognized as the degradation

mechanism for the experiments run at 300 mA/cm^2 for three days. In general, the GDEs running for hundreds of hours showed decline in mechanical integrity at later stages which might stem

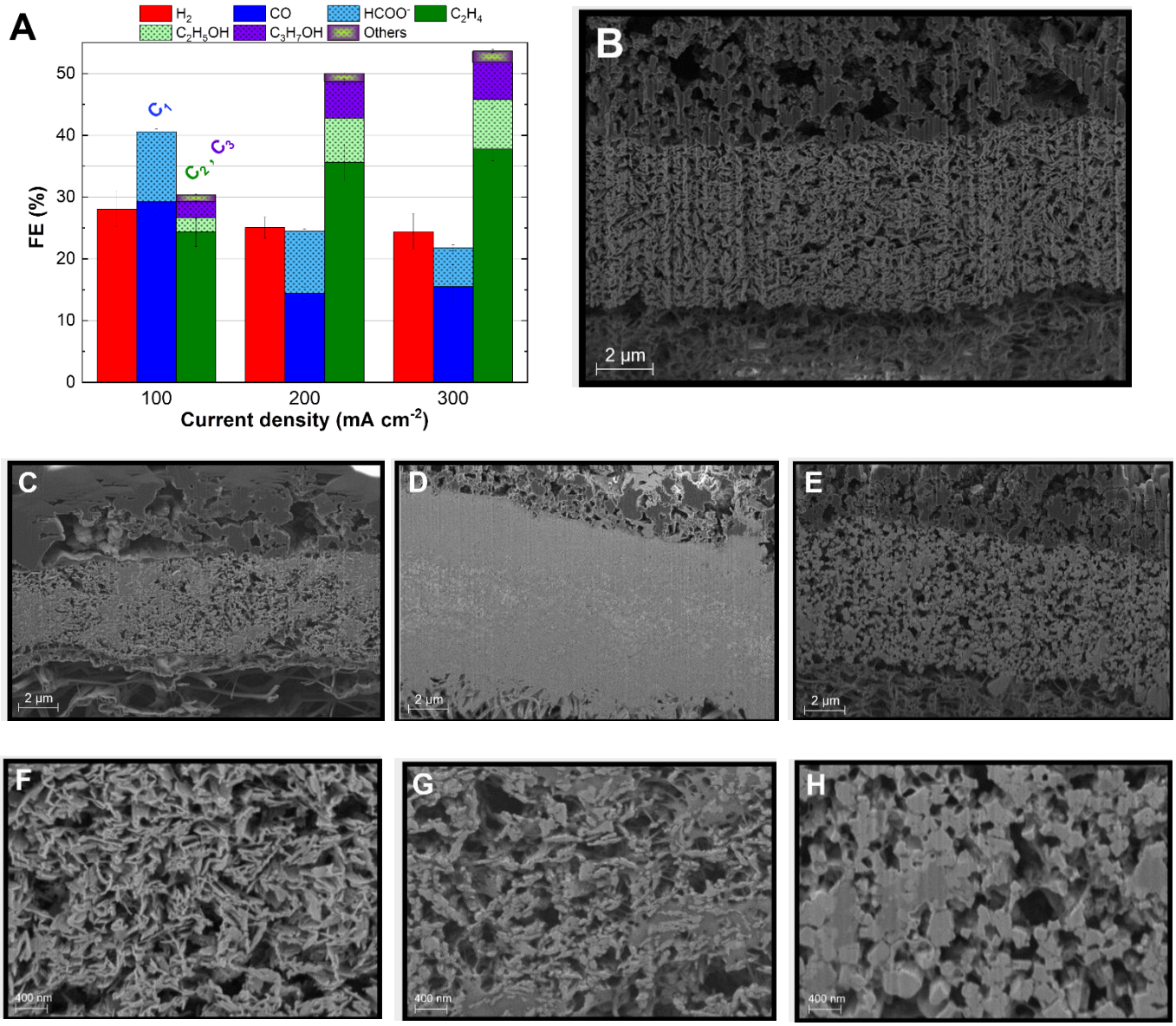

Figure 46. (**A**) Full product distribution expressed in terms of faradaic efficiencies obtained in the chronopotentiometric experiments (100-300 mA/cm^2) with the down selected GDE design at t = 24 h. Liquid products were displayed with dotted areas. (**B**) Cross-section SEM image of the pristine multilayered GDE consisting of the top carbon layer, middle CuO catalyst layer and the bottom PTFE GDL. Post-experiment cross-section SEM images GDEs tested at 100 mA/cm^2 for 48 h (**C**), at 100 mA/cm^2 for 750 h (**D**) and at 300 mA/cm^2 for 75 h (**E**). Cross section SEM images at elevated magnification: Pristine GDE (**F**), post-experiment GDEs tested at 100 mA/cm^2 for 48 h (**G**) and at 300 mA/cm^2 for 75 h (**H**).

from ionomer dissolution due to localized alcohol concentration or non-optimized drop-casting processes during electrode preparation.

5.5. Conclusions

In summary, we have identified two CO_2 electrolyzer cell architectures with apparent scalability to industrial sizes. This determination was grounded in experimental evidence, including cell potential and CO_2 crossover, as well as the technical maturity of their building blocks for industrial applications. Addressing significant challenges is essential for non-selected architectures before considering them as viable cell architecture options for future CO_2 electrolyzers.

The first candidate, the CEM-based zero-gap cell architecture, necessitated fundamental electrode design modifications to favor CO_2 electroreduction to C_2H_4 over the competing HER promoted by the acidic cathode conditions in CEM vicinity. For this purpose, we developed an innovative solution of integrating an additional metal oxide-based AEI layer which inhibited at the catalyst microenvironment H^+ to certain extend yet allowed K^+. The best AEIL candidate, 55 mg/cm^2 TiO_2-AEI with 20 wt.% AEI, enabled C_2H_4 formation in the CEM-based zero-gap cell architecture, yet at a low faradaic efficiency of 14%. Hence the electrode design modification efforts were focused on the CEM-based one-gap cell architecture. Important aspects of binder (AEI) to catalyst (CuO) ratio in the catalyst layer, feed gas humidification, gas diffusion layer type and binder types for carbon top layer required in non-conductive PTFE-based GDLs were investigated. It was confirmed that AEI ratio in the catalyst layer was a determinative factor for CO_2 availability and product selectivity. Feed gas humidification was proven to enhance C_2H_4 selectivity especially at high current densities (300 – 500 mA/cm^2) compared to no humidification case, likely by ensuring the thin aqueous layer formation on AEI coated CuO particles which contributes to CO_2 adsorption. The multilayered GDE consisting of PTFE-based GDL, CuO

catalyst layer with 10 wt.% AEI and a carbon top layer with CEI binder demonstrated superior results in the one-gap cell architecture. Those were $FE_{C_{2+}}$ of 54% at 300 mA/cm^2 leading to the down-selection of this variant for long-term stability experiments. Chronopotentiometric tests at 100-300 mA/cm^2 indicated a degradation mechanism dependent on current density. 100 mA/cm^2 tests allowed month-long (720 h) stable uninterrupted operations producing C_2H_4 at FE > 20%. In contrast, 300 mA/cm^2 showed shorter stabilities, not exceeding 75 h. SEM/EDX analyses of pristine and post-experiment GDEs revealed that extensive salt formation in the catalyst layer was the primary cause for degradation in 100 mA/cm^2 tests. Conversely, catalyst agglomeration and restructuring appeared as the initial degradation causes in 300 mA/cm^2 tests.

Further research should carry forward the achievements of AEIL implementation in CEM-based zero-gap CO_2 electrolyzers by investigating different cation transport enablers (e.g., with doping) and microengineering channels for decoupled anion and cation transport. Salt formation problem can be overcome in future at elevated operation temperatures, yet hydrophobicity of the electrode must be accordingly superior considering the water management in the layers. Mechanically more robust electrodes that sustain their layered structures beyond months should as well be considered in future. In-situ analyses can disentangle the agglomeration driven catalyst degradation.

High technological maturity is crucial for scaling this technology from lab to industrial applications. Near-term research should focus on the aforementioned areas, while long-term considerations encompass material development for all electrolyzer components to achieve tens of thousands of hours of operation and the exploration of fluorine-free membranes. Understanding the interplay between the electrolyzer and upstream (e.g., direct air capture) and downstream processes (e.g., olefin oligomerization) is crucial for their successful system-level integration, enabling CO_2-to-C_2H_4 electrolyzers to be directly integrated into the production process for SAF or polymers (e.g., polyethylene). Furthermore, the impact of scaling electrode area (up to 0.5 m^2

per stack) and the effects of stacking on CO_2 electrolyzer operation warrant investigation. Achieving industry-relevant lifetimes (>10,000 hours), which remains one of the biggest hurdles for commercialization, is critical to unlocking the potential of low-temperature CO_2-to-C_2H_4 electrolysis.

Acknowledgements

The research leading to these results has received funding from the European Union's Horizon 2020 research and innovation program under grant agreement no. 101006701, EcoFuel. Authors thank all EcoFuel partners for the valuable discussions. B.S. would like to express his gratitude to Tabea Gros from TU Munich for her support with XRD characterization and acknowledges support from the TUM Graduate School.

5.6. Supporting Information

5.6.1. Optimization of AEIL Integration into the CEM-based Zero-Gap Cells

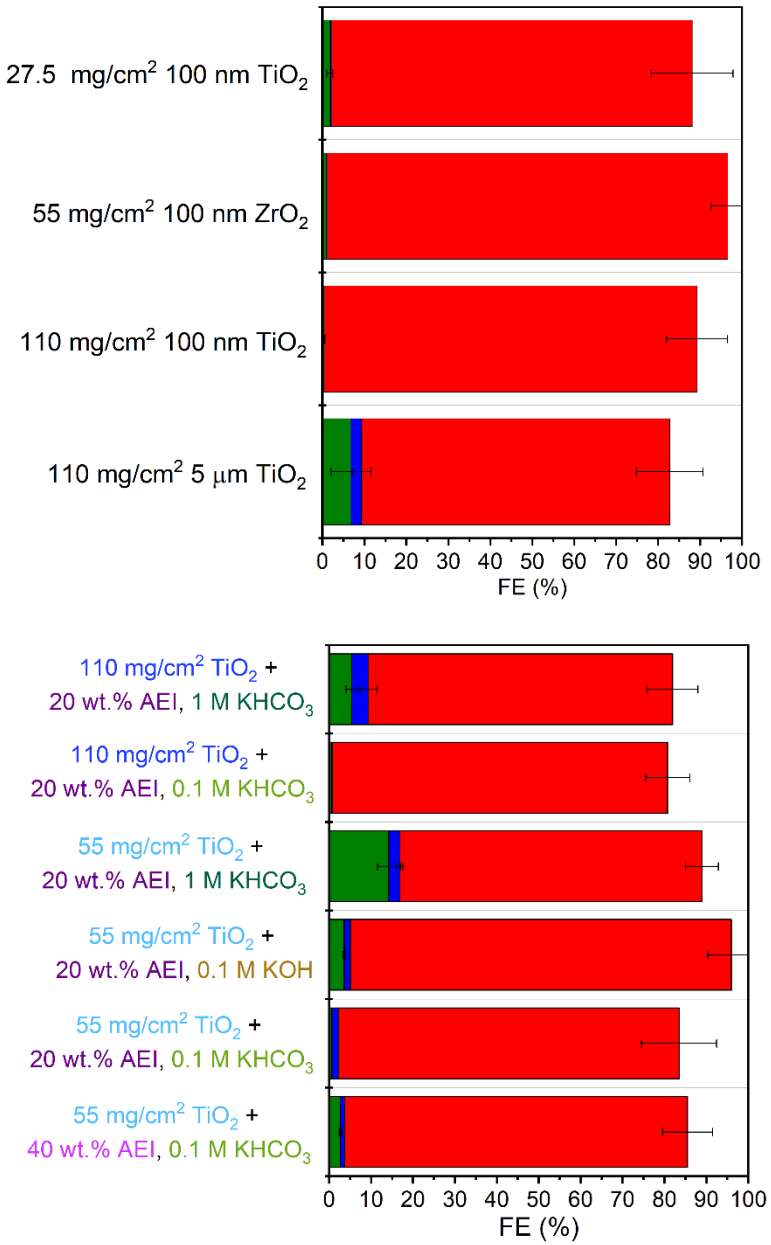

Figure 47. Faradaic efficiencies of gas products obtained within the first 120 minutes of chronopotentiometric experiments (100 mA/cm^2) with AEIL-design MEAs prepared by drop casting method with various TiO_2 and ZrO_2 particle sizes and loadings at a constant MO:AEI ratio of 5:1 (**A**). Faradaic efficiencies of gas products obtained within the first 120 minutes of chronopotentiometric experiments (100 mA/cm^2) with AEIL-design MEAs prepared by dry pressing method with 100 nm sized particles comprising loadings of 55.0 mg/cm^2 and 110.0 mg/cm^2 of TiO_2 at various AEI:MO ratios tested with various electrolytes (**B**).

The AEIL integration into MEAs involved two methods: drop casting and dry pressing (refer to the Materials and Methods section for details). Drop casting, which applied AEI + MO ink to the anode CCM, resulted in CEM dissolution due to ethanol from the AEIs. This led to inconsistent and inconclusive electrochemical measurements at 100 mA/cm^2, as shown in **Figure 47A**. Due to the inability to replicate electrodes, we discontinued using drop casting for MEA synthesis.

The findings presented in the main manuscript demonstrated that with proper design, AEIL could effectively offset the dominance of H^+ on the catalyst surface while still facilitating the transport of essential K^+ for CO_2RR. Subsequent experiments were carried out to deepen our understanding of the connection between cation transport to the catalyst and its capacity to convert CO_2 to C_2H_4. To explore this relationship, we manipulated AEIL loading, anolyte K^+ concentration, bulk anolyte pH, and the AEI/MO composition ratio, with summarized results presented in **Figure 47B**. Doubling the TiO_2 loading in the AEIL loading from 55 mg/cm^2 to 110 mg/cm^2 with constant 20 wt.% AEI ratio cut the obtained $FE_{C_2H_4}$ from 14.3% to 5.4%. Reducing the $KHCO_3$ molarity from 1 to 0.1 M caused $FE_{C_2H_4}$ to drop further from 5.4% to 0.6%. These findings confirmed the importance of limiting the H^+ concentration but assuring K^+ presence in the catalyst vicinity. To assess the bulk electrolyte pH effect in such complicated system, 0.1 M $KHCO_3$ (pH = 8.3) was replaced with 0.1 M KOH (pH = 13.0) for tests with the 55 mg/cm^2 TiO_2 containing AEILs. 0.1 M KOH yielded slightly more C_2H_4 , $FE_{C_2H_4}$ = 3.6% compared to 0.7% with 0.1 M $KHCO_3$. Overall, 0.1 M K^+ concentration in the anolyte diminished the CO_2RR activity in cathode significantly compared to 1 M K^+. The effect of the AEI amount in the 55 mg/cm^2 TiO_2 was investigated by doubling the AEI ratio from 20 wt.% to 40 wt.% in the 0.1 M $KHCO_3$ anolyte experiments. This resulted in a slight increase of $FE_{C_2H_4}$from 0.7% to 2.7%, aligning with the pH related finding: A higher AEI loading contributed to the depletion of H^+ concentration in catalyst vicinity, similar to KOH use instead of $KHCO_3$.

5.6.2. Ex-situ XRD Characterization of Crystallized Salt in Gas Inlet Gap

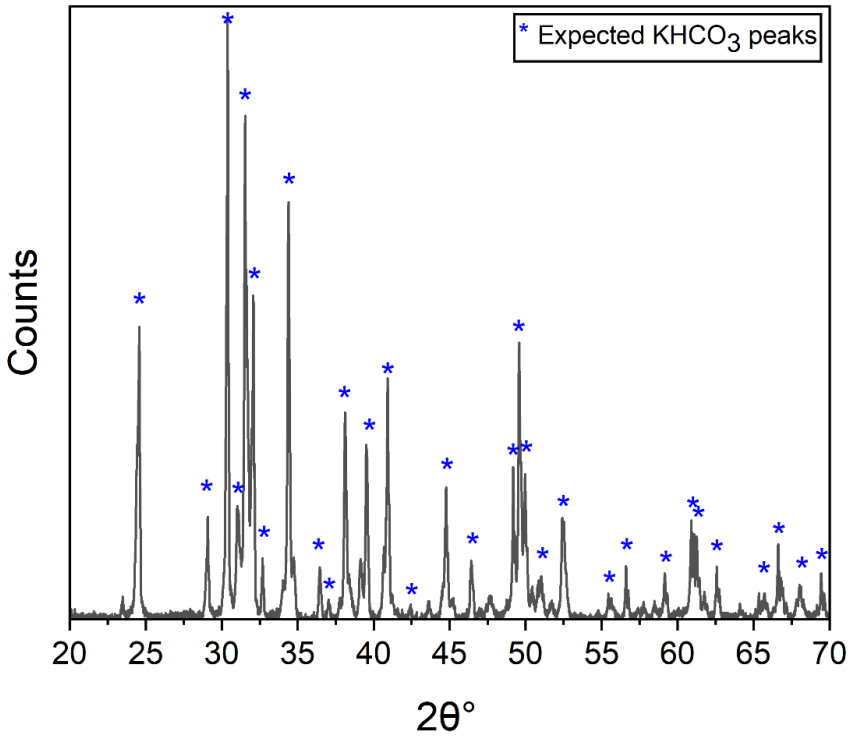

Figure 48. XRD patterns of the salt collected from the gas inlet gap after 750 h at 100 mA/cm^2. Blue stars indicate the expected $KHCO_3$ peaks.

XRD spectrum of the salt from the gas inlet clearly matched to the $KHCO_3$ salt crystalline[250], nevertheless the coexistence of K_2CO_3 salt cannot be excluded. The gas inlet gap was completely blocked with the salt after 750 h of electrochemical reaction.

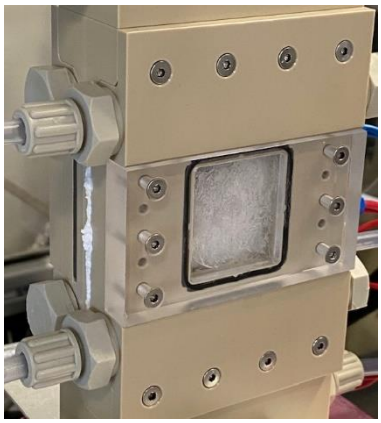

Figure 49. Front view of the 10 cm^2 Siemens Energy in-house cell after 750 h of reaction at 100 mA/cm^2. Extensive salt formation was observed in the gas inlet gap. Salt crystallites effused from the sides of the GDE.

5.6.3. Test Stand and Cell Architecture Details

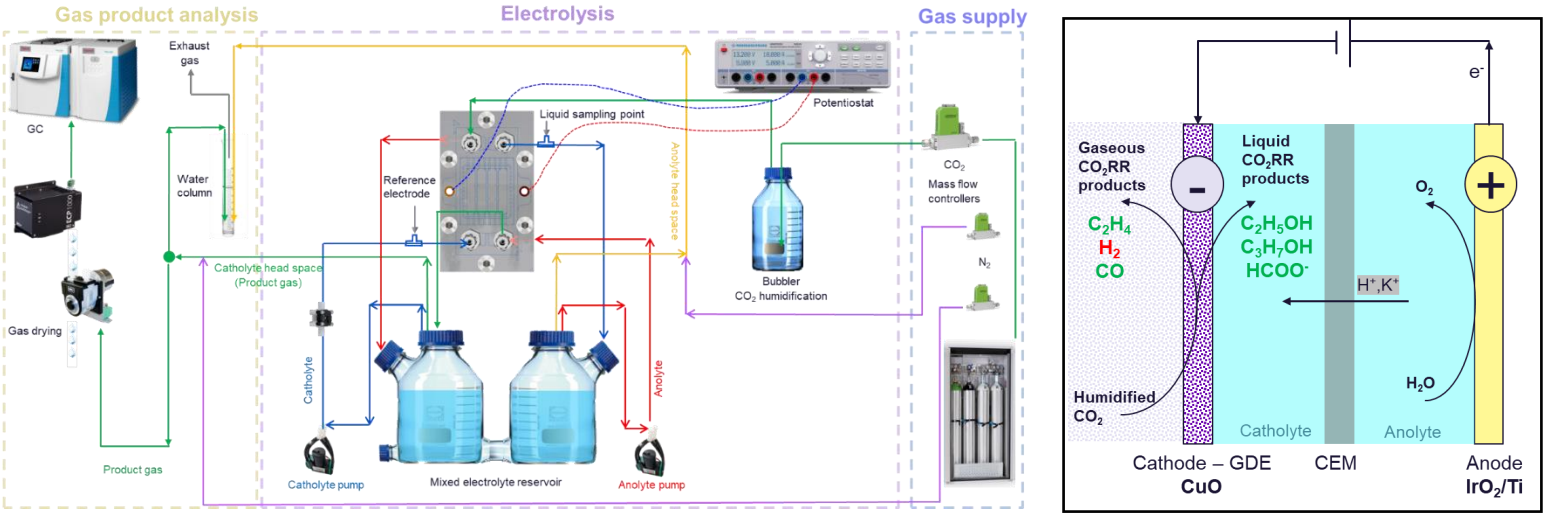

Figure 50. Detailed schematic illustration of the test stand for two-gaps cell experiments (**left**). Two-gap flow cell environment for CO_2 electrolysis to hydrocarbons on CuO-based electrode (**right**).

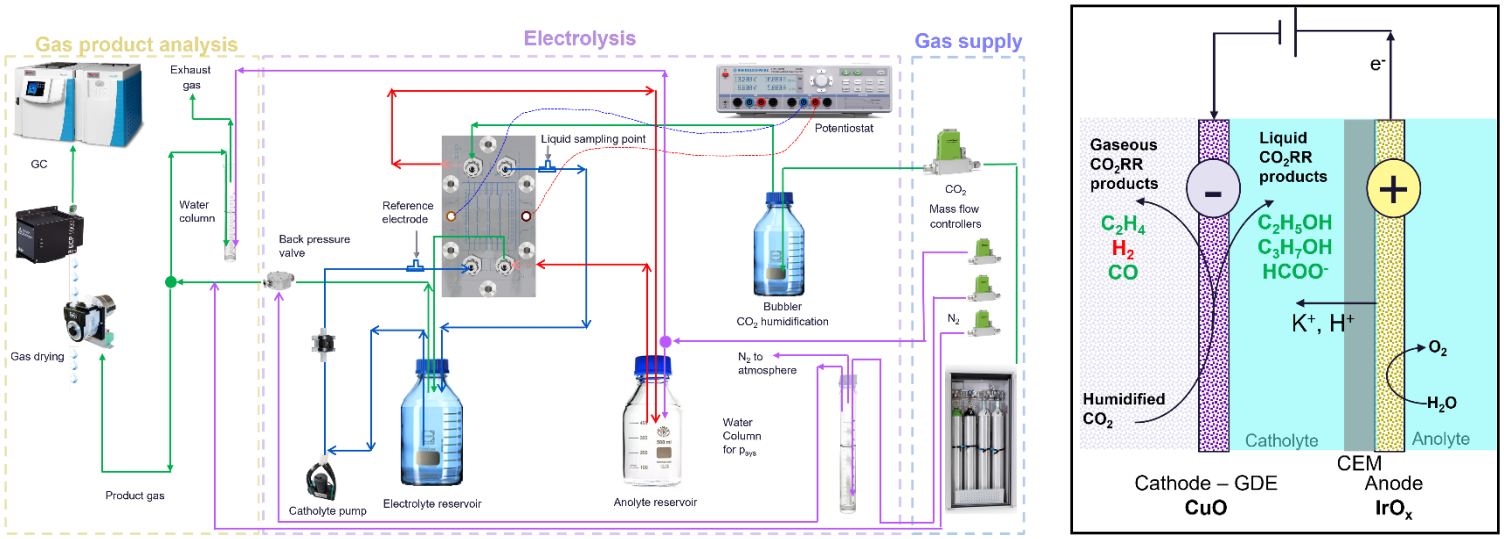

Figure 51. Detailed schematic illustration of the test stand for one-gap cell experiments (**left**). One-gap flow cell environment for CO_2 electrolysis to hydrocarbons on CuO-based electrode (**right**).

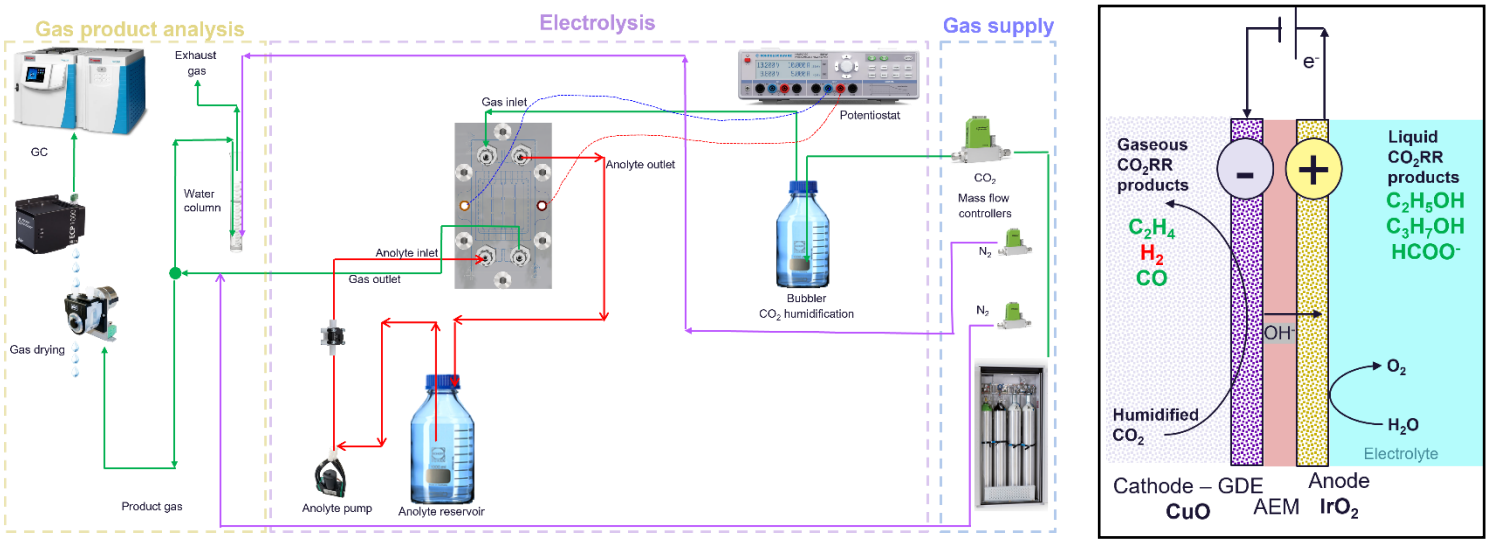

Figure 52. Detailed schematic illustration of the test stand for zero-gap cell experiments (**left**). Zero-gap flow cell environment for CO_2 electrolysis to hydrocarbons on CuO-based electrode. AEM component was simply replaced with CEM, CEM with AEIL and BPM for zero-gap cell experiments with such cell architectures (**right**).

5.6.4. CO_2 crossover to Anode with AEM separators

Considering that CO_2 reduction takes place in an alkaline microenvironment in the cathode, the reduction reaction (e.g., for C_2H_4 product) can be written as:

$$2CO_2 + H_2O + 12e^- \rightarrow C_2H_4 + 12OH^- \quad (20)$$

The OH^- produced can react with the constantly fed CO_2 forming bicarbonate in the cathode vicinity, which can also further react with OH^- forming carbonate.

$$CO_2 + OH^- \leftrightarrow HCO_3^- \quad (21)$$

$$HCO_3^- + OH^- \leftrightarrow CO_3^{-2} + H_2O \quad (22)$$

Meanwhile the anodic oxygen evolution reaction takes place in acidic conditions and can be written as:

$$H_2O \rightarrow 2H^+ + 0.5O_2 + 2e^- \quad (23)$$

In case of AEM usage as separator, the anions in the cathode migrate to the anode by electroosmosis. Assuming acidic conditions in the anode; the bicarbonate, carbonate and hydroxide anions are protonated in the anode vicinity following the below reactions:

$$HCO_3^- + H^+ \rightarrow CO_2 + H_2O \quad (24)$$

$$CO_3^{-2} + 2H^+ \rightarrow CO_2 + H_2O \quad (25)$$

$$OH^- + H^+ \rightarrow H_2O \quad (26)$$

Combining the protonation reactions (Equations 24 – 26) with OER (Equation 23) respectively yields the overall anodic reactions (Equations 27 – 29) representing the cases, if the charge carrier species were only HCO_3^- (Equation 27), CO_3^{-2} (Equation 28) or OH^- (Equation 29).

$$2HCO_3^- \rightarrow 2CO_2 + 0.5O_2 + H_2O + 2e^- \quad (27)$$

$$CO_3^{-2} \rightarrow CO_2 + 0.5O_2 + 2e^- \quad (28)$$

$$2OH^- + H^+ \rightarrow 0.5O_2 + H_2O + 2e^- \quad (29)$$

Based on the stoichiometric relations between CO_2 and O_2 in (Equations 27 – 29), it becomes evident that the anticipated anodic gas composition ratio of CO_2 to O_2 will vary depending on the type of ions transported through the AEM. If the transported ions through the AEM are HCO_3^-, CO_3^{-2} and OH^- then the expected CO_2 to O_2 ratios in the anode are 4, 2, and 0, respectively.

5.6.5. Stability Experiments with Carbon-based GDLs and Comparison to PTFE-based GDL

The drawback of employing carbon-based GDLs, in this work Freudenberg H23C2, is their tendency for flooding, particularly when operating at high current densities. Flooding occurs when the GDL becomes saturated with water, hindering the flow of reactant gases to the electrode surface, which ultimately compromises the electrolyzer efficiency and performance. Therefore, a low current density of 100 mA/cm^2 was chosen to assess the stability of C_2H_4 formation with various binder loadings. Not longer than 4 days of stability could be achieved with any of the carbon-based GDEs in this study as **Figure 53** illustrates. The lower achieved FEs and reduced operational lifespan observed in GDEs with 5 wt.% AEI might be attributed to issues related to the uneven distribution of binders and the non-uniform surface characteristics of the catalyst-ionomer interface. Because the concentration of binders directly influences the microenvironment within the catalyst layer, the reduced binder content may have resulted in a constrained ionomer

surface area available for CO_2 dissolution and ionic transport toward the electrolyte, in parallel to the findings of Romiluyi et al. [247].

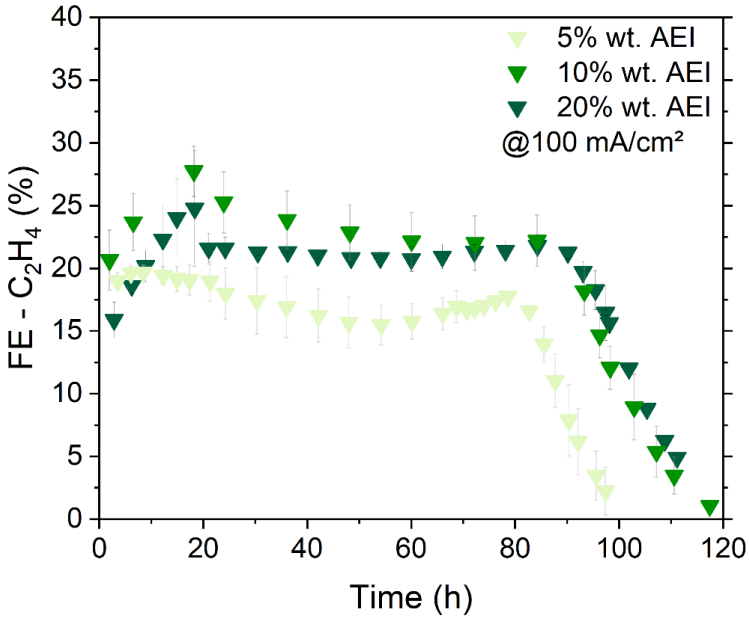

Figure 53. Stability experiments at 100 mA/cm^2 performed for carbon-based GDLs consisting of 1.0 mg/cm^2 CuO catalysis and 5, 10, 20 wt.% AEI.

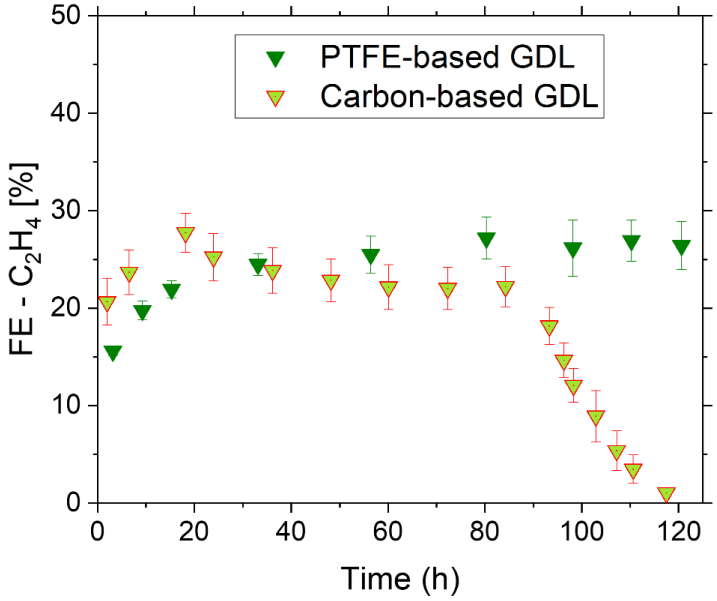

Figure 54. Comparison of stability experiments at 100 mA/cm^2 with carbon-based GDLs consisting of 1.0 mg/cm^2 CuO catalysis and 10 wt.% AEI and with PTFE-based GDLs consisting of the same catalyst layer.

5.6.6. FIB/SEM with EDX Analyses for GDE Cross-sections

Pristine GDE

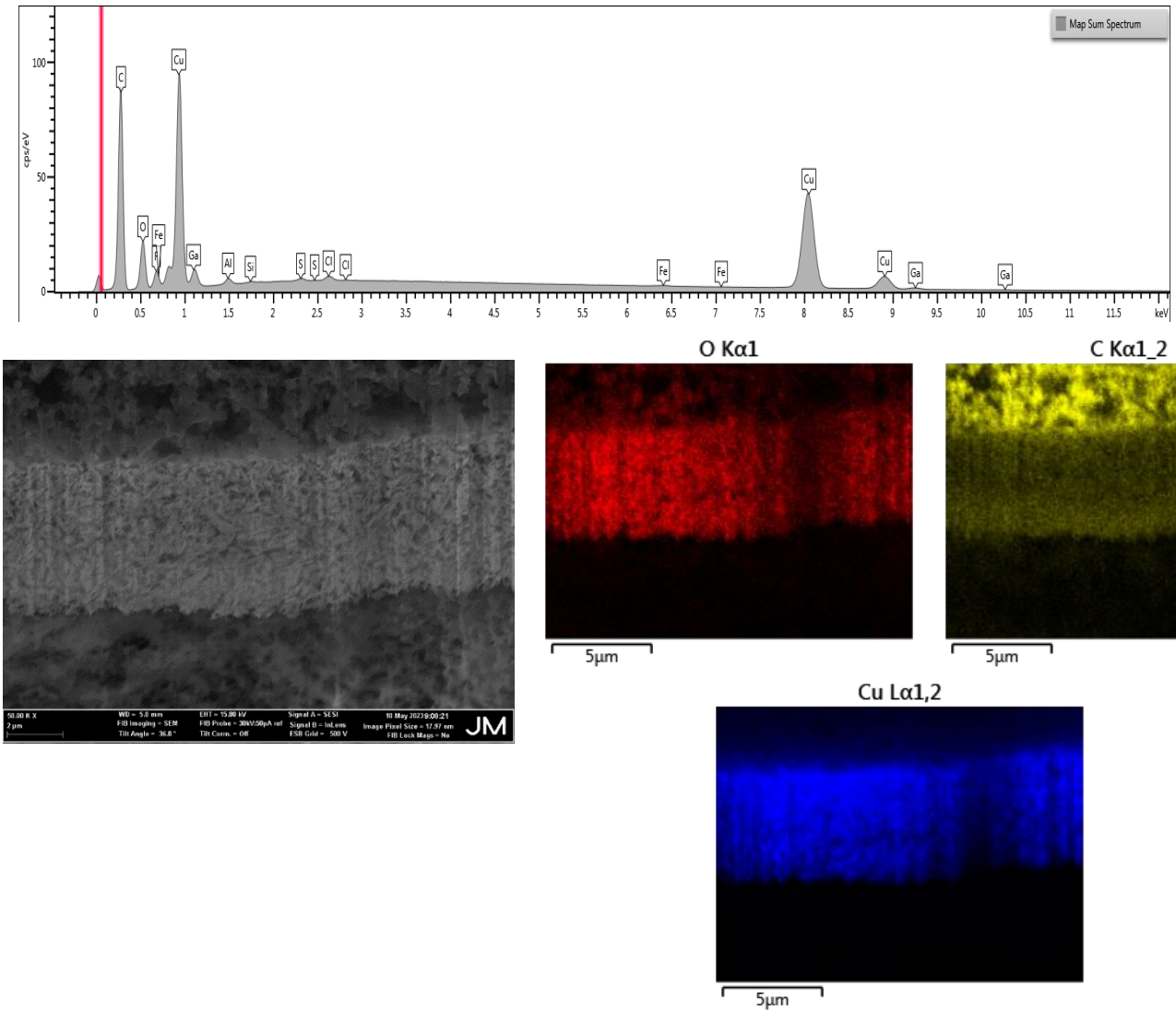

Figure 55. FIB/SEM with EDX analysis of pristine GDE cross-section with a focus on the catalyst layer. CuO catalyst layer was clearly identified in the images.

GDE tested at 100 mA/cm^2 for 48 h

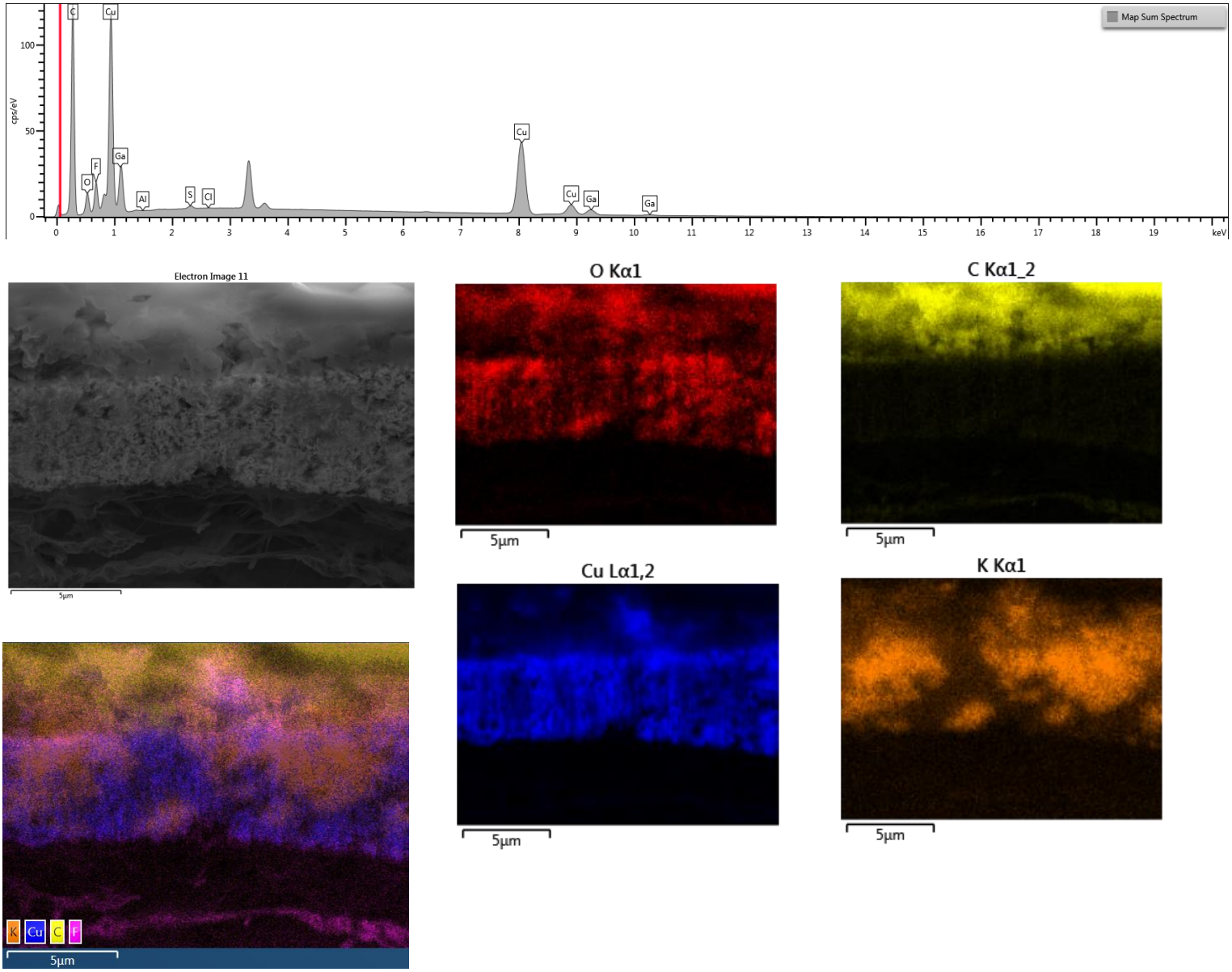

Figure 56. Post-mortem FIB/SEM with EDX analysis of GDE cross-section with a focus on the catalyst layer. The GDE was used in a stability experiment at 100 mA/cm^2 that was purposedly interrupted at t = 48 h, while the GDE could still produce C_2H_4 and no shift to HER had been observed. CuO catalyst layer was clearly identified in the images. Salt accumulation in the catalyst layer was proven with elementary analysis and imaging for K.

GDE tested at 100 mA/cm^2 for 750 h

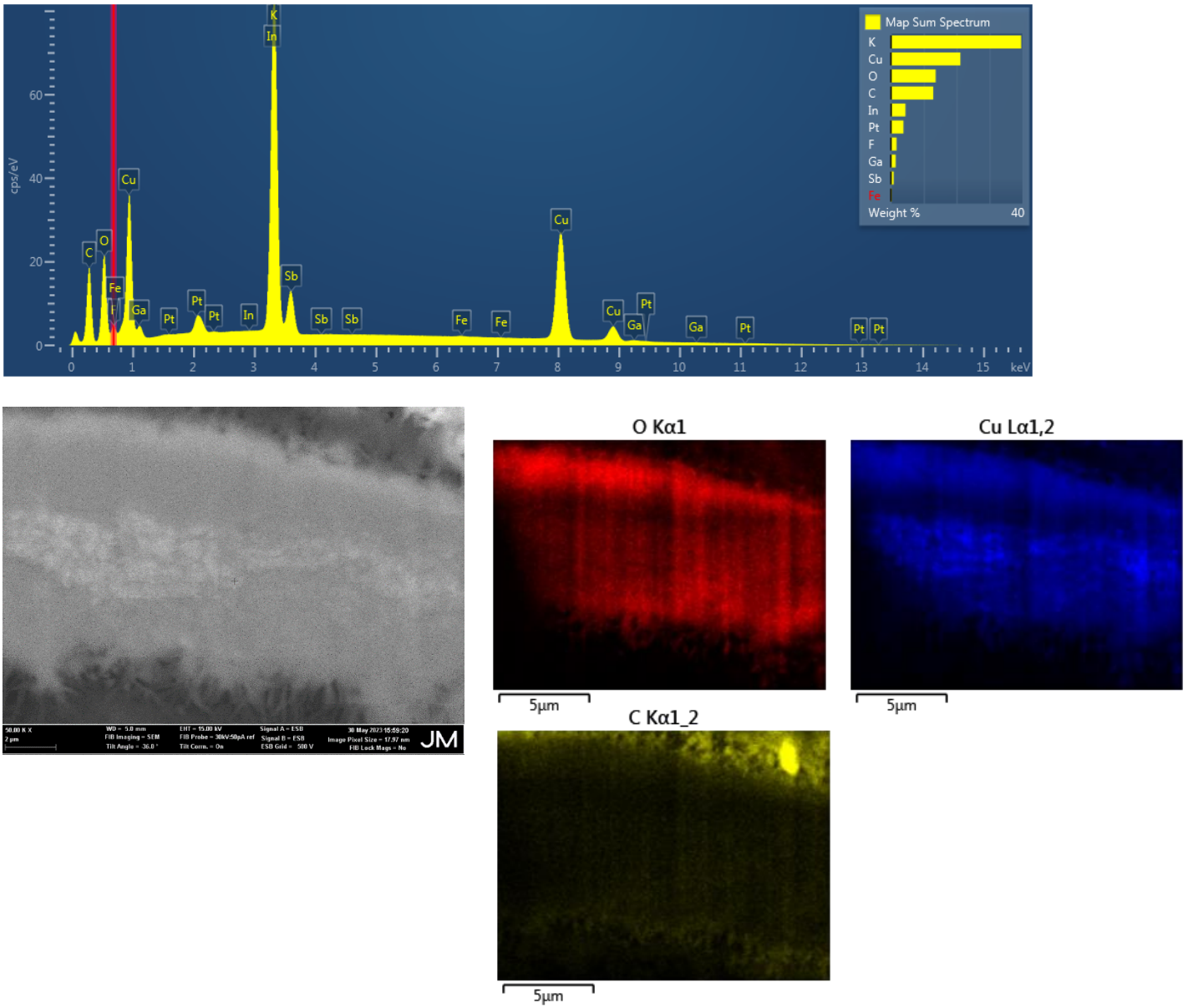

Figure 57. Post-mortem FIB/SEM with EDX analysis of GDE cross-section with a focus on the catalyst layer. The GDE was used in a stability experiment at 100 mA/cm^2 that was stopped at t = 750 h. Selectivity shift to H_2 had already been observed. CuO catalyst layer was clearly identified in the images. Intensive salt accumulation in the catalyst layer was proven with elementary analysis for K which demonstrated the biggest peak in the EDX spectrum.

GDE tested at 300 mA/cm^2 for 75 h

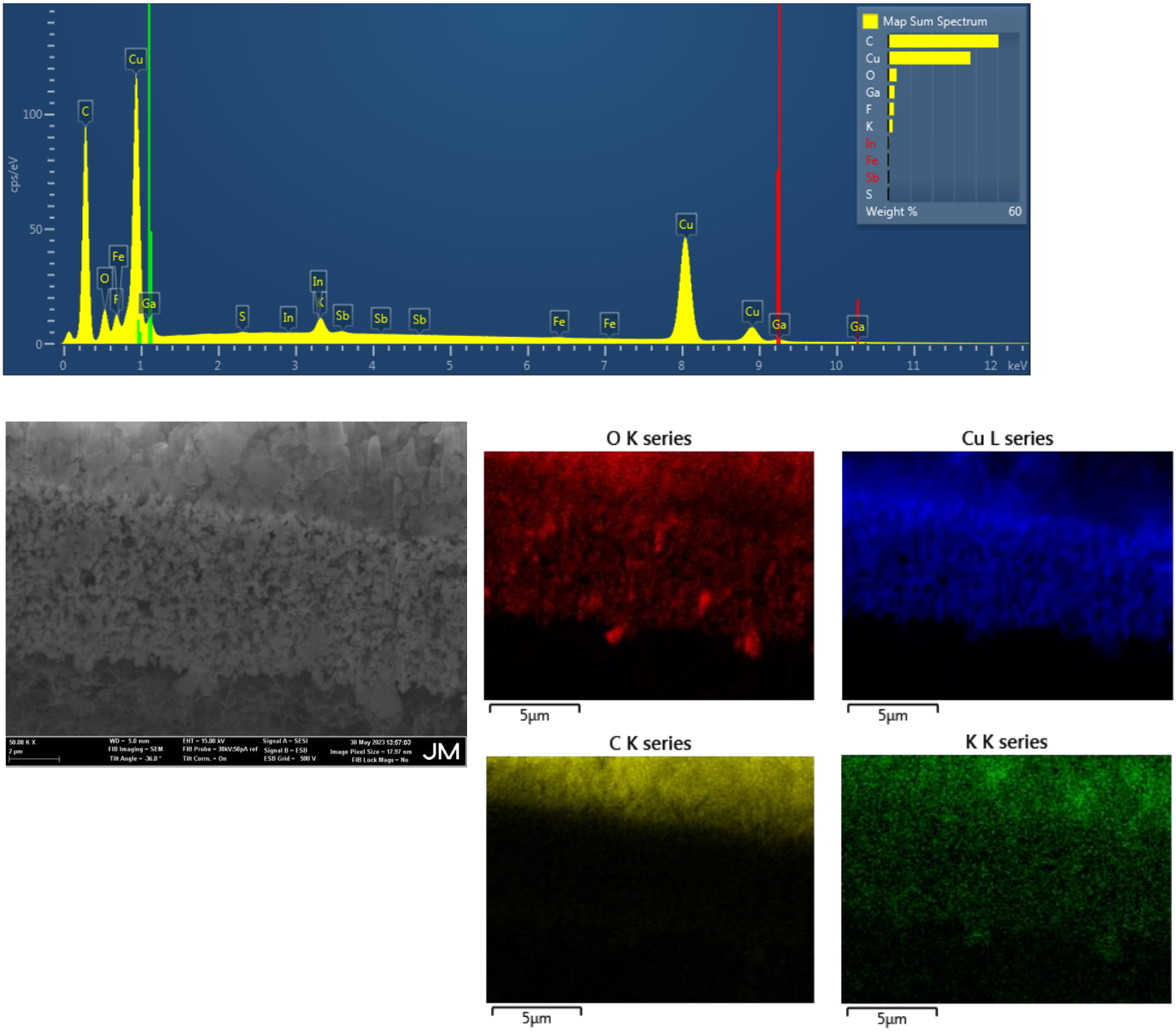

Figure 58. Post-mortem FIB/SEM with EDX analysis of GDE cross-section with a focus on the catalyst layer. The GDE was used in a stability experiment at 300 mA/cm^2 that was stopped at t = 75 h. Selectivity shift to H_2 had already been observed. CuO catalyst layer was clearly identified in the images. Minimal salt accumulation in the catalyst layer was observed with elementary analysis for K which demonstrated a very low peak in the EDX spectrum.

5.6.7. Cell Operation Temperature and Gas Humidification Temperature Effects

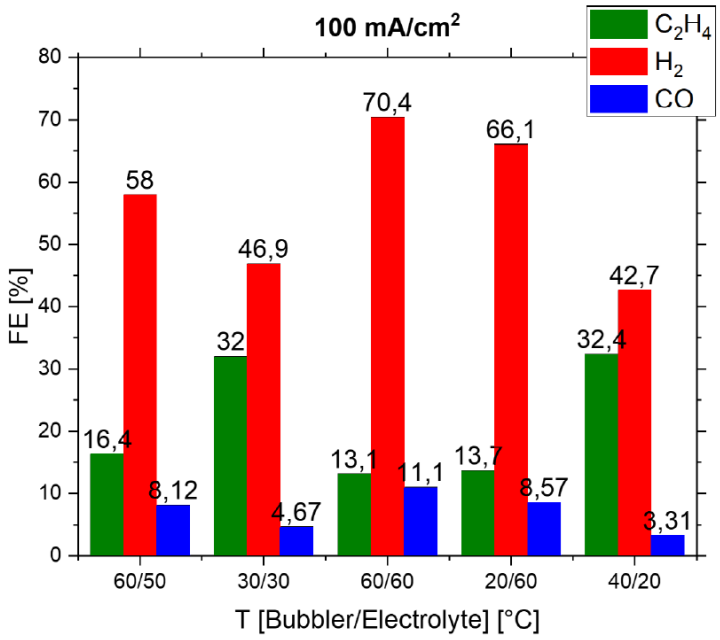

Figure 59. Faradaic efficiencies of gas products obtained at various bubbler and electrolyte temperatures maintained for 48 hours each. This investigation was conducted as part of stability experiments at 100 mA/cm² to confirm that no degradation occurred during temperature variation.

To mitigate salt precipitation and enhance operational stability, we conducted the experiment with external heating. Elevating the temperature improves the solubility of K_2CO_3 and $KHCO_3$, potentially delaying deactivation. Cell operation temperature was maintained by heating the electrolyte vessel. The plastic tubing carrying gas or liquids to and from the cell were thermally isolated. A temperature sensor was placed to the catholyte outlet to monitor cell temperature. Bubbler temperature was regulated by heating the bubbler vessel filled with water. A temperature sensor was placed to the bubbler water to monitor bubbler temperature. All other parameters were unchanged.

Elevated electrolyte temperatures (60 °C) had a detrimental effect on ethylene production, with $FE_{C_2H_4}$ of 13-14%, favoring FE_{H_2} of 66-70%. In contrast, low electrolyte temperatures led to

$FE_{C_2H_4}$ of 32% and FE_{H_2} of 43-47%. This can be attributed to the decreased CO_2 solubility in aqueous solutions at higher temperatures, resulting in a reduction in local CO_2 concentration, which limits the availability of reactant for the catalyst. Simultaneously, the swelling of binders may have obstructed active sites and led to the formation of thick diffusion layers for CO_2 gas particles, causing mass diffusion limitations. However, binder swelling is independent of the intrinsic water uptake at elevated temperatures as water uptake depends on the relative humidity rather than the applied temperature as suggested by Barique et al.[251]. Lower liquid viscosity at higher temperatures may have altered the gas bubble formation dynamics in the catalyst layer, which in turn could have affected the local reduction potentials in the cathode.

6. Summary and Outlook

The electrochemical reduction of CO_2 is gaining increased attention and significance as we strive towards a sustainable energy system. While it has shown considerable promise, there is substantial work yet to be undertaken before scaling up to industrial sıze can be achieved. This dissertation systematically investigates the electrochemical reduction of CO_2 to C_{2+} compounds under industrially relevant conditions, addressing critical challenges and proposing innovative solutions. The results presented in Chapter 3 and Chapter 4 quantify the effects of back pressure and accumulation of liquid byproducts in the electrolyte as two crucial operational conditions. They explore the potential of leveraging them to enhance selectivity, stability, and cell potential. Additionally, the findings of Chapter 5 demonstrate that a well-designed combination of electrode and cell design can enable month-long stability for CO_2 to C_{2+} electrolyzers. This chapter also introduces an innovative electrode design for zero-gap CEM-based cells. In summary, the selectivity, stability, and cell potentials of CO_2 to C_{2+} electrolysis have been improved under industrially relevant conditions.

Chapter 3 focuses on CO_2RR on CuO in a flow cell environment at an applied current density of 200 mA/cm^2, exploring various back pressures and feed flow rates. The application of 130 mbar back pressure demonstrates a significant extension of stable operation time to 72 hours, with increased selectivity for CO_2RR products, in particular the oxygenates. Abundant CO_2 coverage due to back pressure suppresses the competing hydrogen evolution reaction, enhancing stable formation of C_2H_4. Applying CO_2 partial pressure of 1.13 bar at ΔP = 130 mbar influences stability primarily through abundant CO_2 coverage on the catalyst surface. Back pressure not only reduces H_2 production but also facilitates higher faradaic efficiencies towards CO and oxygenates, adjusting the ratio of oxygenates to hydrocarbons. Although enhancing stability and oxygenate selectivity, back pressure leads to increased CO* desorption from the catalyst surface, resulting in increased CO production. To address this, a combination of back

pressure and low flow rates is employed, promoting a longer residence time for optimal CO_2 coverage for C_2H_4 formation. This strategy achieves a significant reduction in CO in favour of C_{2+} products, reaching to total faradaic efficiency towards C_{2+} (mainly ethylene, ethanol and *n*-propanol) of 60%. The study demonstrates that back pressure control could be implemented in upscaled cells to manipulate selectivity which could become an advantage in industrial settings.

Chapter 4 delves into the potential impacts of CO_2RR-induced liquid byproduct accumulation in the electrolyte on product selectivity, the stability of C_2H_4 formation, and cell potential. Electrochemical measurements at 200 mA/cm^2 with EtOH and PrOH-containing electrolyte media unveils those alcohols shifting faradic efficiency from CO_2RR products to H_2. High alcohol concentrations (5.12 M for EtOH and 1.89 M for PrOH) completely inhibits CO_2RR, while mild concentrations (1.54 M EtOH and 0.57 M PrOH) increase acetate and propionate formation. Stable C_2H_4 formation duration significantly decreases with high and mild alcohol concentrations. Contact angle measurements confirm the increase in the wettability of the alcohol containing electrolyte due to lower surface tension, supporting our hypothesis of alcohol-induced electrode flooding. Flooded electrodes favour H_2 selectivity, reducing stable C_2H_4 formation duration. Catalyst layers of the electrodes tested in high-alcohol media experience abrasion, likely due to ionomer binder dispersion. ATR-FTIR analysis of Nafion 117 membranes in 5.12 M EtOH-containing electrolyte reveals irreversible structural changes, suggesting mechanical deformation from swelling and plasticization. These effects, observed at 5.12 M EtOH and 1.89 M PrOH concentrations, implicate that PrOH is detrimental even at lower concentrations compared to EtOH, possibly due to higher sorption ability of PrOH. The structural changes in the membrane could disrupt ionic channel networks, leading to recorded high cell potentials above 10 V. Collectively, the findings of this study advocate for continuous alcohol removal from the electrolyte to prevent accumulation and minimize material failure risks associated with it.

Chapter 5 identifies two scalable CO_2 electrolyzer cell architectures for industrial applications out of five possible options, grounded in experimental evidence encompassing cell potential, CO_2 crossover, and technical maturity of their components. The CEM-based zero-gap cell architecture, the first candidate owing to the lowest recorded cell potential of 3.7 V at 200 mA/cm^2 among the tested designs, requires fundamental electrode design modifications. It is due to the acidic cathode conditions dictated by CEM vicinity which promotes the competing HER. An innovative solution is developed, integrating an additional metal oxide-based AEI layer that inhibits H^+ at the catalyst microenvironment to some extent while allowing K^+. The best AEIL candidate, 55 mg/cm^2 TiO_2-AEI with 20 wt.% AEI, enables C_2H_4 formation with a low faradaic efficiency of 14%. Consequently, electrode design modifications shift focus to the CEM-based one-gap cell architecture. The multilayered GDE, comprising PTFE-based GDL, CuO catalyst layer with 10 wt.% AEI, and a carbon top layer with CEI binder, exhibits superior results in the one-gap cell architecture, with a C_{2+} faradaic efficiency of 54% at 300 mA/cm^2, leading to its down-selection for long-term stability experiments. Chronopotentiometric tests at 100-300 mA/cm^2 indicate a degradation mechanism dependent on current density, with 100 mA/cm^2 tests allowing month-long stable operations, producing C_2H_4 at a faradaic efficiency exceeding 20%. Conversely, 300 mA/cm^2 shows shorter stabilities, not exceeding 75 h, with SEM/EDX analyses revealing extensive salt formation as the primary cause for degradation in 100 mA/cm^2 tests, while catalyst agglomeration and restructuring appear to be the initial degradation causes in 300 mA/cm^2 tests. This study emphasizes the potential of achieving stable and high-yield production of C_{2+} products through inventive electrode design coupled with readily scalable cell architectures, thereby promoting sustainable CO_2 utilization.

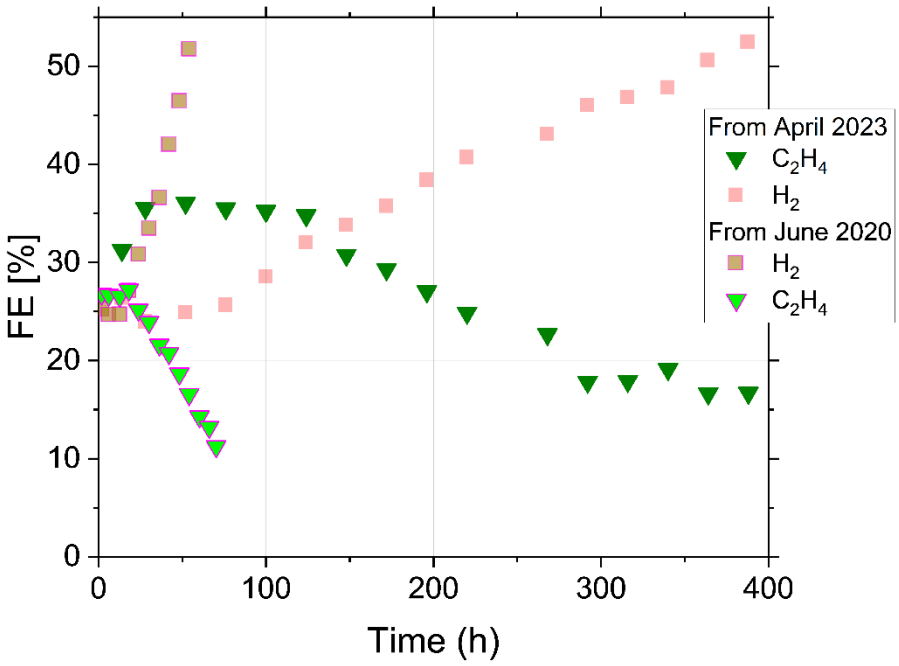

Figure 60. Comparison of two electrochemical experiments conducted in flow cells at 200 mA/cm^2 in terms of faradaic efficiencies over time indicating the achieved advancement during this dissertation. June 2020 experiment was conducted based on the state-of-the-art at the time. April 2023 experiment contains the improvements gained throughout this dissertation such as application of controlled back pressure on the electrode, removal of liquid products from the electrolyte medium and tailored gas diffusion electrode for the specific cell architecture.

With stability being the main hurdle for industrial application, future research should prioritize the elimination of identified degradation mechanisms to achieve stability exceeding 10000 hours, a prerequisite for industrialization. A comprehensive approach involving both detailed process simulation studies and experimental work is recommended, aiming to develop a separation unit capable of continuously removing alcohols and formate from the electrolyte before they reach critical concentrations, as indicated in this study. Simultaneously, the exploration of oleophobic surface coatings for electrodes is crucial to counteract the decreasing surface tension in the presence of alcohols. Moreover, alternative separators, such as ZrO_2 diaphragms, and ionomer binders, drawing inspiration from conductive polymers in Li-ion battery research, can be investigated for their resistance to long-term mechanical and chemical changes under alcohol

exposure. Building on the success of AEIL implementation in CEM-based zero-gap CO_2 electrolyzers, future investigations may explore various cation transport enablers, such as doping, and microengineering channels for decoupled anion and cation transport in zero-gap cells, as achieving a cell potential below 3 V seems most plausible in such a configuration. Addressing salt formation issues at elevated operation temperatures requires further material research, focusing on electrodes with superior hydrophobicity while considering water management in the layers and, secondly, on mechanically robust electrodes capable of sustaining layered structures beyond months. The catalyst-driven degradation due to restructuring can be better understood through an increased focus on in-situ analyses. The exploration of a two-step electrolyzer system, where CO_2 is initially converted to CO, presents an opportunity to leverage alkalinity in subsequent CO to hydrocarbons steps without encountering salt formation issues, providing a promising direction for future investigations. Further system optimizations regarding downstream gas product separation and recycling the unconverted CO_2 back to electrolyzer are crucial to obtain more realistic and precise overall system energy and conversion efficiencies. In addition to the identified future research directions, it is imperative to strategize for new material exploration in response to a potential ban on per- and polyfluoroalkyl substances (PFAS ban), particularly in the domains of membranes, ionomers, and gas diffusion layers.

7. References

1 S. Arrhenius, *The London, Edinburgh, and Dublin Philosophical Magazine and Journal of Science*, 1896, **41**, 237–276.

2 John Tyndall, *Proc. R. Soc. Lond.*, 1860, **10**, 37–39.

3 A. Witze, *Nature*, 2024, **625**, 637–639.

4 Hannah Ritchie, Pablo Rosado and Max Roser, 2023, https://ourworldindata.org/co2-and-greenhouse-gas-emissions.

5 B. Hönisch, A. Ridgwell, D. N. Schmidt, E. Thomas, S. J. Gibbs, A. Sluijs, R. Zeebe, L. Kump, R. C. Martindale, S. E. Greene, W. Kiessling, J. Ries, J. C. Zachos, D. L. Royer, S. Barker, T. M. Marchitto, R. Moyer, C. Pelejero, P. Ziveri, G. L. Foster and B. Williams, *Science (New York, N.Y.)*, 2012, **335**, 1058–1063.

6 J. D. Shakun, P. U. Clark, F. He, S. A. Marcott, A. C. Mix, Z. Liu, B. Otto-Bliesner, A. Schmittner and E. Bard, *Nature*, 2012, **484**, 49–54.

7 C. Le Quéré, R. M. Andrew, P. Friedlingstein, S. Sitch, J. Hauck, J. Pongratz, P. A. Pickers, J. I. Korsbakken, G. P. Peters, J. G. Canadell, A. Arneth, V. K. Arora, L. Barbero, A. Bastos, L. Bopp, F. Chevallier, L. P. Chini, P. Ciais, S. C. Doney, T. Gkritzalis, D. S. Goll, I. Harris, V. Haverd, F. M. Hoffman, M. Hoppema, R. A. Houghton, G. Hurtt, T. Ilyina, A. K. Jain, T. Johannessen, C. D. Jones, E. Kato, R. F. Keeling, K. K. Goldewijk, P. Landschützer, N. Lefèvre, S. Lienert, Z. Liu, D. Lombardozzi, N. Metzl, D. R. Munro, J. E. M. S. Nabel, S. Nakaoka, C. Neill, A. Olsen, T. Ono, P. Patra, A. Peregon, W. Peters, P. Peylin, B. Pfeil, D. Pierrot, B. Poulter, G. Rehder, L. Resplandy, E. Robertson, M. Rocher, C. Rödenbeck, U. Schuster, J. Schwinger, R. Séférian, I. Skjelvan, T. Steinhoff, A. Sutton, P. P. Tans, H. Tian, B. Tilbrook, F. N. Tubiello, I. T. van der Laan-Luijkx, G. R. van der Werf, N. Viovy, A. P. Walker, A. J. Wiltshire, R. Wright, S. Zaehle and B. Zheng, *Earth Syst. Sci. Data*, 2018, **10**, 2141–2194.

8 IEA Report, *CO2 Emissions in 2022,* available at: https://www.iea.org/reports/co2-emissions-in-2022, accessed 24 January 2024.

9 H. Lee, K. Calvin, D. Dasgupta, G. Krinner, A. Mukherji, P. W. Thorne, C. Trisos, J. Romero, P. Aldunce, K. Barrett, G. Blanco, W. W. Cheung, S. Connors, F. Denton, A. Diongue-Niang, D. Dodman, M. Garschagen, O. Geden, B. Hayward, C. Jones, F. Jotzo, T. Krug, R. Lasco, Y.-Y. Lee, V. Masson-Delmotte, M. Meinshausen, K. Mintenbeck, A. Mokssit, F. E. Otto, M. Pathak, A. Pirani, E. Poloczanska, H.-O. Pörtner, A. Revi, D. C. Roberts, J. Roy, A. C. Ruane, J. Skea, P. R. Shukla, R. Slade, A. Slangen, Y. Sokona, A. A. Sörensson, M. Tignor, D. van Vuuren, Y.-M. Wei, H. Winkler, P. Zhai, Z. Zommers, J.-C. Hourcade, F. X. Johnson, S. Pachauri, N. P. Simpson, C. Singh, A. Thomas, E. Totin, P. Arias, M. Bustamante, I. Elgizouli, G. Flato, M. Howden, C. Méndez-Vallejo, J. J. Pereira, R. Pichs-Madruga, S. K. Rose, Y. Saheb, R. Sánchez Rodríguez, D. Ürge-Vorsatz, C. Xiao, N. Yassaa, A. Alegría, K. Armour, B. Bednar-Friedl, K. Blok, G. Cissé, F. Dentener, S. Eriksen, E. Fischer, G. Garner, C. Guivarch, M. Haasnoot, G. Hansen, M. Hauser, E. Hawkins, T. Hermans, R. Kopp, N. Leprince-Ringuet, J. Lewis, D. Ley, C. Ludden, L. Niamir, Z. Nicholls, S. Some, S. Szopa, B. Trewin, K.-I. van der Wijst, G. Winter, M. Witting, A. Birt, M. Ha, J. Kim, E. F. Haites, Y. Jung, R. Stavins, D. J. A. Orendain, L. Ignon, S. Park, Y. Park, A. Reisinger, D. Cammaramo, A. Fischlin, J. S. Fuglestvedt, J. R. Matthews and C. Péan, *IPCC, 2023: Climate Change 2023: Synthesis Report. Contribution of Working Groups I, II and III to the Sixth Assessment Report of the Intergovernmental Panel on Climate Change [Core Writing Team, H. Lee and J. Romero (eds.)]. IPCC, Geneva, Switzerland*, 2023.

10 Smith, S. M., Geden, O., Nemet, G., Gidden, M., Lamb, W. F., Powis, C., Bellamy, R., Callaghan, M., Cowie, A., Cox, E., Fuss, S., Gasser, T., Grassi, G., Greene, J., Lück, S., Mohan, A., Müller-Hansen, F., Peters, G., Pratama, Y., Repke, T., Riahi, K., Schenuit, F., Steinhauser, J., Strefler, J., Valenzuela, J. M., and Minx, J. C., *The State of Carbon Dioxide Removal*, 2023.

11 W. Y. Hong, *Carbon Capture Science & Technology*, 2022, **3**, 100044.

12 A. Galadima and O. Muraza, *Renewable and Sustainable Energy Reviews*, 2019, **115**, 109333.

13 S. Kondaveeti, I. M. Abu-Reesh, G. Mohanakrishna, M. Bulut and D. Pant, *Front. Energy Res.*, 2020, **8**.

14 R. J. Detz, C. J. Ferchaud, A. J. Kalkman, J. Kemper, C. Sánchez-Martínez, M. Saric and M. V. Shinde, *Sustainable Energy Fuels*, 2023, **7**, 5445–5472.

15 V. Kumaravel, J. Bartlett and S. C. Pillai, *ACS Energy Lett.*, 2020, **5**, 486–519.

16 M. M. Ramirez-Corredores, G. Gadikota, E. E. Huang and A. M. Gaffney, *Front. Energy Res.*, 2020, **8**.

17 S. Overa, B. H. Ko, Y. Zhao and F. Jiao, *Accounts of Chemical Research*, 2022, **55**, 638–648.

18 R. G. Grim, D. Ravikumar, E. C. D. Tan, Z. Huang, J. R. Ferrell, M. Resch, Z. Li, C. Mevawala, S. D. Phillips, L. Snowden-Swan, L. Tao and J. A. Schaidle, *Energy Environ. Sci.*, 2022, **15**, 4798–4812.

19 K. Wiesner-Fleischer, M. Fleischer, J. Bachler, A. Makaruk, G. Kiss, A. Roth, C. Zalitis, N. Cros, P. Strasser and E. Tsang, *Proposal for RIA project to the European Comission. Renewable electricity-based, cyclic and economic production of fuel*, 2020.

20 S. Nitopi, E. Bertheussen, S. B. Scott, X. Liu, A. K. Engstfeld, S. Horch, B. Seger, I. E. L. Stephens, K. Chan, C. Hahn, J. K. Nørskov, T. F. Jaramillo and I. Chorkendorff, *Chemical reviews*, 2019, **119**, 7610–7672.

21 D. M. Kennes-Veiga, C. Fernández-Blanco, M. C. Veiga and C. Kennes, in *Advances in Synthesis Gas : Methods, Technologies and Applications*, Elsevier, 2023, pp. 147–171.

22 H. Park, H.-J. Chae, Y.-W. Suh, Y.-M. Chung and M.-J. Park, *ACS Sustain. Chem. Eng.*, 2022, **10**, 12016–12022.

23 S. van Bavel, S. Verma, E. Negro and M. Bracht, *ACS Energy Lett.*, 2020, **5**, 2597–2601.

24 K. Atsonios, J. Li and V. J. Inglezakis, *Energy*, 2023, **278**, 127868.

25 D. S. Marlin, E. Sarron and Ó. Sigurbjörnsson, *Frontiers in Chemistry*, 2018, **6**, 446.

26 L. Brübach, D. Hodonj, L. Biffar and P. Pfeifer, *Catalysts*, 2022, **12**, 630.

27 V. Dieterich, A. Buttler, A. Hanel, H. Spliethoff and S. Fendt, *Energy Environ. Sci.*, 2020, **13**, 3207–3252.

28 J. Sisler, S. Khan, A. H. Ip, M. W. Schreiber, S. A. Jaffer, E. R. Bobicki, C.-T. Dinh and E. H. Sargent, *ACS Energy Lett.*, 2021, **6**, 997–1002.

29 G. Inzelt, *ChemTexts*, 2015, **1**.

30 Peter Atkins, Julio de Paula, George Ratcliffe, and Mark Wormald, *Physical Chemistry for the Life Sciences*, OXFORD UNIV PRESS, [S.l.], 3rd edn., 2006.

31 Z. Sun, T. Ma, H. Tao, Q. Fan and B. Han, *Chem*, 2017, **3**, 560–587.

32 H.-Q. Liang, T. Beweries, R. Francke and M. Beller, *Angew. Chem., Int. Ed.*, 2022, **61**, e202200723.

33 D. E. Polyansky, in *Encyclopedia of Applied Electrochemistry*, ed. G. Kreysa, K. Ota and R. F. Savinell, Springer New York, New York, NY, 2014, pp. 431–437.

34 Y. Hori, K. Kikuchi and S. Suzuki, *Chem. Lett.*, 1985, **14**, 1695–1698.

35 Y. Hori, K. Kikuchi, A. Murata and S. Suzuki, *Chem. Lett.*, 1986, **15**, 897–898.

36 X. Li, Y. Chen, X. Zhan, Y. Xu, L. Hao, L. Xu, X. Li, M. Umer, X. Tan, B. Han, A. W. Robertson and Z. Sun, *TIMS*, 2023, **1**, 100014.

37 W. Jin, Y. Wang, T. Liu, C. Ding and H. Guo, *Appl. Surf. Sci.*, 2022, **599**, 154024.

38 S.-G. Wang, X.-Y. Liao, D.-B. Cao, C.-F. Huo, Y.-W. Li, J. Wang and H. Jiao, *J. Phys. Chem. C*, 2007, **111**, 16934–16940.

39 A. Bagger, W. Ju, A. S. Varela, P. Strasser and J. Rossmeisl, *ChemPhysChem*, 2017, **18**, 3266–3273.

40 H. A. Hansen, J. B. Varley, A. A. Peterson and J. K. Nørskov, *J. Phys. Chem. Lett.*, 2013, **4**, 388–392.

41 K. P. Kuhl, E. R. Cave, D. N. Abram and T. F. Jaramillo, *Energy Environ. Sci.*, 2012, **5**, 7050–7059.

42 S. Verma, S. Lu and P. J. A. Kenis, *Nat. Energy*, 2019, **4**, 466–474.

43 A. Seifitokaldani, C. M. Gabardo, T. Burdyny, C.-T. Dinh, J. P. Edwards, M. G. Kibria, O. S. Bushuyev, S. O. Kelley, D. Sinton and E. H. Sargent, *J. Am. Chem. Soc.*, 2018, **140**, 3833–3837.

44 T. Cheng, H. Xiao and W. A. Goddard, *J. Am. Chem. Soc.*, 2016, **138**, 13802–13805.

45 Y. Ye, H. Yang, J. Qian, H. Su, K.-J. Lee, T. Cheng, H. Xiao, J. Yano, W. A. Goddard and E. J. Crumlin, *Nat. Commun.* 2019, **10**, 1875.

46 M. Favaro, H. Xiao, T. Cheng, W. A. Goddard, J. Yano and E. J. Crumlin, *Proceedings of the National Academy of Sciences of the United States of America*, 2017, **114**, 6706–6711.

47 A. Jafarzadeh, K. M. Bal, A. Bogaerts and E. C. Neyts, *J. Phys. Chem. C*, 2020, **124**, 6747–6755.

48 Y. Hori, in *Modern Aspects of Electrochemistry*, ed. C. G. Vayenas, R. E. White and M. E. Gamboa-Aldeco, Springer New York, New York, NY, 2008, vol. 42, pp. 89–189.

49 W. Deng, P. Zhang, B. Seger and J. Gong, *Nat. Commun.*, 2022, **13**, 803.

50 B. Pan, Y. Wang and Y. Li, *Chem. Catal.*, 2022, **2**, 1267–1276.

51 G. Marcandalli, M. C. O. Monteiro, A. Goyal and M. T. M. Koper, *Acc. Chem. Res.*, 2022, **55**, 1900–1911.

52 J. S. Yoo, R. Christensen, T. Vegge, J. K. Nørskov and F. Studt, *ChemSusChem*, 2016, **9**, 358–363.

53 G. Jiang, D. Han, Z. Han, J. Gao, X. Wang, Z. Weng and Q.-H. Yang, *Trans. Tianjin Univ.*, 2022, **28**, 265–291.

54 S. A. Akhade, W. Luo, X. Nie, N. J. Bernstein, A. Asthagiri and M. J. Janik, *Phys. Chem. Chem. Phys.*, 2014, **16**, 20429–20435.

55 David W. DeWulf, Tuo Jin, and Allen J. Bard, *J. Electrochem. Soc.*, 1989, **136**, 1686–1691.

56 M. Rahaman, A. Dutta, A. Zanetti and P. Broekmann, *ACS Catal.*, 2017, **7**, 7946–7956.

57 A. A. Peterson and J. K. Nørskov, *J. Phys. Chem. Lett.*, 2012, **3**, 251–258.

58 K. J. P. Schouten, Y. Kwon, C. J. M. van der Ham, Z. Qin and M. T. M. Koper, *Chem. Sci.*, 2011, **2**, 1902.

59 R. Kortlever, J. Shen, K. J. P. Schouten, F. Calle-Vallejo and M. T. M. Koper, *J. Phys. Chem. Lett.*, 2015, **6**, 4073–4082.

60 L. Wang, S. A. Nitopi, E. Bertheussen, M. Orazov, C. G. Morales-Guio, X. Liu, D. C. Higgins, K. Chan, J. K. Nørskov, C. Hahn and T. F. Jaramillo, *ACS Catal.*, 2018, **8**, 7445–7454.

61 Andrew A. Peterson, Frank Abild-Pedersen, Felix Studt, Jan Rossmeisl and Jens K. Nørskov, *Energy Environ. Sci.*, 2010, **3**, 1311–1315.

62 Y. Lum and J. W. Ager, *Energy Environ. Sci.*, 2018, **11**, 2935–2944.

63 Y. Hori, R. Takahashi, Y. Yoshinami and A. Murata, *J. Phys. Chem. B*, 1997, **101**, 7075–7081.

64 Y. Hori, A. Murata and R. Takahashi, *J. Chem. Soc., Faraday Trans. 1*, 1989, **85**, 2309.

65 Y. Hori, A. Murata, R. Takahashi and S. Suzuki, *J. Am. Chem. Soc.*, 1987, **109**, 5022–5023.

66 D.-H. Nam, P. de Luna, A. Rosas-Hernández, A. Thevenon, F. Li, T. Agapie, J. C. Peters, O. Shekhah, M. Eddaoudi and E. H. Sargent, *Nat. Mater.*, 2020, **19**, 266–276.

67 S. Ma, M. Sadakiyo, R. Luo, M. Heima, M. Yamauchi and P. J. Kenis, *J. Power Sources*, 2016, **301**, 219–228.

68 K. P. Kuhl, T. Hatsukade, E. R. Cave, D. N. Abram, J. Kibsgaard and T. F. Jaramillo, *J. Am. Chem. Soc.*, 2014, **136**, 14107–14113.

69 Y. Wang, Z. Wang, C.-T. Dinh, J. Li, A. Ozden, M. Golam Kibria, A. Seifitokaldani, C.-S. Tan, C. M. Gabardo, M. Luo, H. Zhou, F. Li, Y. Lum, C. McCallum, Y. Xu, M. Liu, A. Proppe, A. Johnston, P. Todorovic, T.-T. Zhuang, D. Sinton, S. O. Kelley and E. H. Sargent, *Nat. Catal.*, 2020, **3**, 98–106.

70 X. Wang, J. F. de Araújo, W. Ju, A. Bagger, H. Schmies, S. Kühl, J. Rossmeisl and P. Strasser, *Nat. Nanotechnol.*, 2019, **14**, 1063–1070.

71 X. Liu, P. Schlexer, J. Xiao, Y. Ji, L. Wang, R. B. Sandberg, M. Tang, K. S. Brown, H. Peng, S. Ringe, C. Hahn, T. F. Jaramillo, J. K. Nørskov and K. Chan, *Nat. Commun.*, 2019, **10**, 32.

72 X. Nie, M. R. Esopi, M. J. Janik and A. Asthagiri, *Angew. Chem. Int. Ed.,* 2013, **52**, 2459–2462.

73 S. A. Akhade, W. Luo, X. Nie, A. Asthagiri and M. J. Janik, *Catal. Sci. Technol.*, 2016, **6**, 1042–1053.

74 J. Li, Z. Wang, C. McCallum, Y. Xu, F. Li, Y. Wang, C. M. Gabardo, C.-T. Dinh, T.-T. Zhuang, L. Wang, J. Y. Howe, Y. Ren, E. H. Sargent and D. Sinton, *Nat. Catal.*, 2019, **2**, 1124–1131.

75 M. Löffler, P. Khanipour, N. Kulyk, K. J. Mayrhofer and I. Katsounaros, *ACS Catal.*, 2020, **10**, 6735–6740.

76 T. Cheng, H. Xiao and W. A. Goddard, *Proceedings of the National Academy of Sciences of the United States of America*, 2017, **114**, 1795–1800.

77 J. D. Goodpaster, A. T. Bell and M. Head-Gordon, *J. Phys. Chem. Lett.*, 2016, **7**, 1471–1477.

78 E. Pérez-Gallent, M. C. Figueiredo, F. Calle-Vallejo and M. T. M. Koper, *Angew. Chem. Int. Ed.*, 2017, **56**, 3621–3624.

79 F. Calle-Vallejo and M. T. M. Koper, *Angew. Chem. Int. Ed.*, 2013, **52**, 7282–7285.

80 D. Cheng, Z.-J. Zhao, G. Zhang, P. Yang, L. Li, H. Gao, S. Liu, X. Chang, S. Chen, T. Wang, G. A. Ozin, Z. Liu and J. Gong, *Nat. Commun.*, 2021, **12**, 395.

81 Y. Lum, T. Cheng, W. A. Goddard and J. W. Ager, *J. Am. Chem. Soc.*, 2018, **140**, 9337–9340.

82 D. Ren, J. Fong and B. S. Yeo, *Nat. Commun.*, 2018, **9**, 925.

83 I. Ledezma-Yanez, E. P. Gallent, M. T. Koper and F. Calle-Vallejo, *Catalysis Today*, 2016, **262**, 90–94.

84 E. Bertheussen, A. Verdaguer-Casadevall, D. Ravasio, J. H. Montoya, D. B. Trimarco, C. Roy, S. Meier, J. Wendland, J. K. Nørskov, I. E. L. Stephens and I. Chorkendorff, *Angew. Chem. Int. Ed.*, 2016, **55**, 1450–1454.

85 E. L. Clark and A. T. Bell, *J. Am. Chem. Soc.*, 2018, **140**, 7012–7020.

86 Y. Y. Birdja and M. T. M. Koper, *J. Am. Chem. Soc.*, 2017, **139**, 2030–2034.

87 C. W. Li, J. Ciston and M. W. Kanan, *Nature*, 2014, **508**, 504–507.

88 D. Ren, N. T. Wong, A. D. Handoko, Y. Huang and B. S. Yeo, *J. Phys. Chem. Lett.*, 2016, **7**, 20–24.

89 X. Chang, A. Malkani, X. Yang and B. Xu, *J. Am. Chem. Soc.*, 2020, **142**, 2975–2983.

90 Y. Zheng, A. Vasileff, X. Zhou, Y. Jiao, M. Jaroniec and S.-Z. Qiao, *J. Am. Chem. Soc.*, 2019, **141**, 7646–7659.

91 D. M. Weekes, D. A. Salvatore, A. Reyes, A. Huang and C. P. Berlinguette, *Acc. Chem. Res.*, 2018, **51**, 910–918.

92 T. Jaster, A. Gawel, D. Siegmund, J. Holzmann, H. Lohmann, E. Klemm and U.-P. Apfel, *iScience*, 2022, **25**, 104010.

93 T. Burdyny and W. A. Smith, *Energy Environ. Sci.*, 2019, **12**, 1442–1453.

94 N. Martić, C. Reller, C. Macauley, M. Löffler, B. Schmid, D. Reinisch, E. Volkova, A. Maltenberger, A. Rucki, K. J. J. Mayrhofer and G. Schmid, *Adv. Energy Mater.*, 2019, **9**, 1901228.

95 B. Sahin, J. J. Leung, E. Magori, S. Laumen, A. Tawil, E. Simon and O. Hinrichsen, *Energy Technol.*, 2022, **10**.

96 N. Martić, C. Reller, C. Macauley, M. Löffler, A. M. Reichert, T. Reichbauer, K.-M. Vetter, B. Schmid, D. McLaughlin, P. Leidinger, D. Reinisch, C. Vogl, K. J. J. Mayrhofer, I. Katsounaros and G. Schmid, *Energy Environ. Sci.*, 2020, **13**, 2993–3006.

97 K. Jiang, R. B. Sandberg, A. J. Akey, X. Liu, D. C. Bell, J. K. Nørskov, K. Chan and H. Wang, *Nat. Catal.*, 2018, **1**, 111–119.

98 K. D. Yang, W. R. Ko, J. H. Lee, S. J. Kim, H. Lee, M. H. Lee and K. T. Nam, *Angew. Chem., Int. Ed.*, 2017, **56**, 796–800.

99 W. Tang, A. A. Peterson, A. S. Varela, Z. P. Jovanov, L. Bech, W. J. Durand, S. Dahl, J. K. Nørskov and I. Chorkendorff, *Phys. Chem. Chem. Phys.*, 2012, **14**, 76–81.

100 M. R. Gonçalves, A. Gomes, J. Condeço, T. Fernandes, T. Pardal, C. Sequeira and J. B. Branco, *Electrochim. Acta*, 2013, **102**, 388–392.

101 H. Mistry, A. S. Varela, C. S. Bonifacio, I. Zegkinoglou, I. Sinev, Y.-W. Choi, K. Kisslinger, E. A. Stach, J. C. Yang, P. Strasser and B. R. Cuenya, *Nat. Commun.*, 2016, **7**, 12123.

102 G. L. de Gregorio, T. Burdyny, A. Loiudice, P. Iyengar, W. A. Smith and R. Buonsanti, *ACS Catal.*, 2020, **10**, 4854–4862.

103 E. Bertheussen, T. V. Hogg, Y. Abghoui, A. K. Engstfeld, I. Chorkendorff and I. E. L. Stephens, *ACS Energy Lett.*, 2018, **3**, 634–640.

104 C. Chen, Y. Li, S. Yu, S. Louisia, J. Jin, M. Li, M. B. Ross and P. Yang, *Joule*, 2020, **4**, 1688–1699.

105 S. Lee, G. Park and J. Lee, *ACS Catal.*, 2017, **7**, 8594–8604.

106 Y. Zhou, F. Che, M. Liu, C. Zou, Z. Liang, P. de Luna, H. Yuan, J. Li, Z. Wang, H. Xie, H. Li, P. Chen, E. Bladt, R. Quintero-Bermudez, T.-K. Sham, S. Bals, J. Hofkens, D. Sinton, G. Chen and E. H. Sargent, *Nat. Chem.*, 2018, **10**, 974–980.

107 F. P. García de Arquer, C.-T. Dinh, A. Ozden, J. Wicks, C. McCallum, A. R. Kirmani, D.-H. Nam, C. Gabardo, A. Seifitokaldani, X. Wang, Y. C. Li, F. Li, J. Edwards, L. J. Richter, S. J. Thorpe, D. Sinton and E. H. Sargent, *Science (New York, N.Y.)*, 2020, **367**, 661–666.

108 E. W. Lees, B. A. W. Mowbray, D. A. Salvatore, G. L. Simpson, D. J. Dvorak, S. Ren, J. Chau, K. L. Milton and C. P. Berlinguette, *J. Mater. Chem. A*, 2020, **8**, 19493–19501.

109 S. Hernandez-Aldave and E. Andreoli, *Catalysts*, 2020, **10**, 713.

110 D. Higgins, C. Hahn, C. Xiang, T. F. Jaramillo and A. Z. Weber, *ACS Energy Lett.*, 2019, **4**, 317–324.

111 R. Kas, R. Kortlever, H. Yılmaz, M. T. M. Koper and G. Mul, *ChemElectroChem*, 2015, **2**, 354–358.

112 N. S. Romero Cuellar, K. Wiesner-Fleischer, M. Fleischer, A. Rucki and O. Hinrichsen, *Electrochim. Acta*, 2019, **307**, 164–175.

113 X. Feng, K. Jiang, S. Fan and M. W. Kanan, *ACS Cent. Sci.*, 2016, **2**, 169–174.

114 A. Verdaguer-Casadevall, C. W. Li, T. P. Johansson, S. B. Scott, J. T. McKeown, M. Kumar, I. E. L. Stephens, M. W. Kanan and I. Chorkendorff, *J. Am. Chem. Soc.*, 2015, **137**, 9808–9811.

115 C. Hahn, T. Hatsukade, Y.-G. Kim, A. Vailionis, J. H. Baricuatro, D. C. Higgins, S. A. Nitopi, M. P. Soriaga and T. F. Jaramillo, *Proceedings of the National Academy of Sciences of the United States of America*, 2017, **114**, 5918–5923.

116 Y.-G. Kim, A. Javier, J. H. Baricuatro and M. P. Soriaga, *Electrocatalysis*, 2016, **7**, 391–399.

117 Y. Hori, H. Konishi, T. Futamura, A. Murata, O. Koga, H. Sakurai and K. Oguma, *Electrochim. Acta*, 2005, **50**, 5354–5369.

118 J.-F. Xie, Y.-X. Huang, W.-W. Li, X.-N. Song, L. Xiong and H.-Q. Yu, *Electrochim. Acta*, 2014, **139**, 137–144.

119 J. Lee and Y. Tak, *Electrochim. Acta*, 2001, **46**, 3015–3022.

120 G. Kyriacou and A. Anagnostopoulos, *J. Electroanal. Chem.*, 1992, **322**, 233–246.

121 W. T. Osowiecki, J. J. Nussbaum, G. A. Kamat, G. Katsoukis, M. Ledendecker, H. Frei, A. T. Bell and A. P. Alivisatos, *ACS Appl. Energy Mater.,* 2019, **2**, 7744–7749.

122 L.-C. Weng, A. T. Bell and A. Z. Weber, *Phys. Chem. Chem. Phys.*, 2018, **20**, 16973–16984.

123 M. Leonard, M. Orella, N. Aiello, Y. Román-Leshkov, A. Forner-Cuenca and F. Brushett, *J. Electrochem. Soc.,* 2020, **167**, 124521.

124 M. E. Leonard, L. E. Clarke, A. Forner-Cuenca, S. M. Brown and F. R. Brushett, *ChemSusChem*, 2020, **13**, 400–411.

125 Y. C. Tan, K. B. Lee, H. Song and J. Oh, *Joule*, 2020, **4**, 1104–1120.

126 C. Kim, L.-C. Weng and A. T. Bell, *ACS Catal.*, 2020, **10**, 12403–12413.

127 C. Kim, J. C. Bui, X. Luo, J. K. Cooper, A. Kusoglu, A. Z. Weber and A. T. Bell, *Nat. Energy*, 2021, **6**, 1026–1034.

128 Y. Hori, A. Murata and Y. Yoshinami, *J. Chem. Soc. Faraday Trans.*, 1991, **87**, 125–128.

129 H. Ooka, M. C. Figueiredo and M. T. M. Koper, *Langmuir*, 2017, **33**, 9307–9313.

130 R. B. Sandberg, J. H. Montoya, K. Chan and J. K. Nørskov, *Surf. Sci.*, 2016, **654**, 56–62.

131 M. Moradzaman, C. S. Martínez and G. Mul, *Sustain. Energy Fuels.*, 2020, **4**, 5195–5202.

132 T. Chatterjee, E. Boutin and M. Robert, *Dalton Transactions (Cambridge, England : 2003)*, 2020, **49**, 4257–4265.

133 B. Sahin, S. Kimberly Raymond, F. Ntourmas, R. Pastusiak, K. Wiesner-Fleischer, M. Fleischer, E. Simon and O. Hinrichsen, *ACS Appl. Mater. Interfaces*, 2023.

134 Siemens Energy, *White paper: Power-to-X: The crucial business on the way to a carbon-free world*, 2021.

135 P. de Luna, C. Hahn, D. Higgins, S. A. Jaffer, T. F. Jaramillo and E. H. Sargent, *Science (New York, N.Y.)*, 2019, **364**.

136 S&P Global Commodity Insights, *Chemical Economics Handbook - Ethylene*, 2022.

137 S. Mu, H. Lu, Q. Wu, L. Li, R. Zhao, C. Long and C. Cui, *Nat. Commun.*, 2022, **13**, 3694.

138 S. H. Lee, J. C. Lin, M. Farmand, A. T. Landers, J. T. Feaster, J. E. Avilés Acosta, J. W. Beeman, Y. Ye, J. Yano, A. Mehta, R. C. Davis, T. F. Jaramillo, C. Hahn and W. S. Drisdell, *J. Am. Chem. Soc.*, 2021, **143**, 588–592.

139 C. Guo, Y. Guo, Y. Shi, X. Lan, Y. Wang, Y. Yu and B. Zhang, *Angew. Chem. Int. Ed.*, 2022, **61**, e202205909.

140 R. M. Arán-Ais, R. Rizo, P. Grosse, G. Algara-Siller, K. Dembélé, M. Plodinec, T. Lunkenbein, S. W. Chee and B. R. Cuenya, *Nat. Commun.*, 2020, **11**, 3489.

141 J. Huang, N. Hörmann, E. Oveisi, A. Loiudice, G. L. de Gregorio, O. Andreussi, N. Marzari and R. Buonsanti, *Nature communications*, 2018, **9**, 3117.

142 L. Zaza, K. Rossi and R. Buonsanti, *ACS Energy Lett.*, 2022, **7**, 1284–1291.

143 J. E. Huang, F. Li, A. Ozden, A. Sedighian Rasouli, F. P. García de Arquer, S. Liu, S. Zhang, M. Luo, X. Wang, Y. Lum, Y. Xu, K. Bertens, R. K. Miao, C.-T. Dinh, D. Sinton and E. H. Sargent, *Science (New York, N.Y.)*, 2021, **372**, 1074–1078.

144 M. Li, M. N. Idros, Y. Wu, T. Burdyny, S. Garg, X. S. Zhao, G. Wang and T. E. Rufford, *J. Mater. Chem. A*, 2021, **9**, 19369–19409.

145 P. Wilde, P. B. O'Mara, J. R. C. Junqueira, T. Tarnev, T. M. Benedetti, C. Andronescu, Y.-T. Chen, R. D. Tilley, W. Schuhmann and J. J. Gooding, *Chem. Sci. J.*, 2021, **12**, 4028–4033.

146 L. Fan, C.-Y. Liu, P. Zhu, C. Xia, X. Zhang, Z.-Y. Wu, Y. Lu, T. P. Senftle and H. Wang, *Joule*, 2022, **6**, 205–220.

147 J. Wicks, M. L. Jue, V. A. Beck, J. S. Oakdale, N. A. Dudukovic, A. L. Clemens, S. Liang, M. E. Ellis, G. Lee, S. E. Baker, E. B. Duoss and E. H. Sargent, *Adv. Mater.*, 2021, **33**, e2003855.

148 T. H. M. Pham, J. Zhang, M. Li, T.-H. Shen, Y. Ko, V. Tileli, W. Luo and A. Züttel, *Adv. Energy Mater.*, 2022, **12**, 2103663.

149 N. T. Nesbitt, T. Burdyny, H. Simonson, D. Salvatore, D. Bohra, R. Kas and W. A. Smith, *ACS Catal.*, 2020, **10**, 14093–14106.

150 K. Yang, R. Kas, W. A. Smith and T. Burdyny, *ACS Energy Lett.*, 2021, **6**, 33–40.

151 T. Burchardt, *J. Power Sources*, 2004, **135**, 192–197.

152 F. Bienen, J. Hildebrand, D. Kopljar, N. Wagner, E. Klemm and K. A. Friedrich, *Chem. Ing. Tech.* 2021, **93**, 1015–1019.

153 Y. Kong, H. Hu, M. Liu, Y. Hou, V. Kolivoška, S. Vesztergom and P. Broekmann, *J. Catal.*, 2022, **408**, 1–8.

154 S. Garg, M. Li, A. Z. Weber, L. Ge, L. Li, V. Rudolph, G. Wang and T. E. Rufford, *J. Mater. Chem. A*, 2020, **8**, 1511–1544.

155 B. de Mot, J. Hereijgers, M. Duarte and T. Breugelmans, *J. Chem. Eng.*, 2019, **378**, 122224.

156 B. Endrődi, E. Kecsenovity, A. Samu, F. Darvas, R. V. Jones, V. Török, A. Danyi and C. Janáky, *ACS Energy Lett.*, 2019, **4**, 1770–1777.

157 D. G. Wheeler, B. A. W. Mowbray, A. Reyes, F. Habibzadeh, J. He and C. P. Berlinguette, *Energy Environ. Sci.*, 2020, **13**, 5126–5134.

158 M. K. Kovalev, H. Ren, M. Zakir Muhamad, J. W. Ager and A. A. Lapkin, *ACS Energy Lett.*, 2022, **7**, 599–601.

159 E. R. Cofell, U. O. Nwabara, S. S. Bhargava, D. E. Henckel and P. J. A. Kenis, *ACS Appl. Mater. Interfaces.*, 2021, **13**, 15132–15142.

160 J. Wyndorps, H. Ostovari and N. von der Assen, *Sustain. Energy Fuels*, 2021, **5**, 5748–5761.

161 C. M. Gabardo, C. P. O'Brien, J. P. Edwards, C. McCallum, Y. Xu, C.-T. Dinh, J. Li, E. H. Sargent and D. Sinton, *Joule*, 2019, **3**, 2777–2791.

162 M. E. Leonard, M. J. Orella, N. Aiello, Y. Román-Leshkov, A. Forner-Cuenca and F. R. Brushett, *J. Electrochem. Soc.*, 2020, **167**, 124521.

163 S. Parvate, P. Dixit and S. Chattopadhyay, *J. Phys. Chem. B,* 2020, **124**, 1323–1360.

164 G. Vazquez, E. Alvarez and J. M. Navaza, *J. Chem. Eng. Data*, 1995, **40**, 611–614.

165 D. Ballal and W. G. Chapman, *J. Chem. Phys.,* 2013, **139**, 114706.

166 S. Khosharay, S. Tourang and F. Tajfar, *Fluid Phase Equilibria*, 2017, **454**, 99–110.

167 S. Overa, B. S. Crandall, B. Shrimant, D. Tian, B. H. Ko, H. Shin, C. Bae and F. Jiao, *Nat. Catal*, 2022, **5**, 738–745.

168 A. Katzenberg, A. Angulo, A. Kusoglu and M. A. Modestino, *Macromolecules*, 2021, **54**, 5187–5195.

169 O. Kwon and J. Park, *Polymers*, 2022, **14**.

170 T. D. Gierke, G. E. Munn and F. C. Wilson, *J. Polym. Sci. Polym. Phys. Ed.*, 1981, **19**, 1687–1704.

171 K. Kunimatsu, B. Bae, K. Miyatake, H. Uchida and M. Watanabe, *J. Phys. Chem. B*, 2011, **115**, 4315–4321.

172 R. Sigwadi, M. S. Dhlamini, T. Mokrani, F. Ṇemavhola, P. F. Nonjola and P. F. Msomi, *Heliyon*, 2019, **5**, e02240.

173 P. J. Larkin, *Infrared and Raman spectroscopy. Principles and spectral interpretation*, Elsevier, Amsterdam, op. 2011.

174 C. J. Pouchert, *The Aldrich library of infrared spectra*, Sigma Aldrich, Milwankee, 1981.

175 D. Rivin, C. E. Kendrick, P. W. Gibson and N. S. Schneider, *Polymer*, 2001, **42**, 623–635.

176 Y. D. Yi and Y. C. Bae, *Polymer*, 2017, **130**, 112–123.

177 S. A. Al-Tamreh, M. H. Ibrahim, M. H. El-Naas, J. Vaes, D. Pant, A. Benamor and A. Amhamed, *ChemElectroChem*, 2021, **8**, 3207–3220.

178 A. A. Peterson, F. Abild-Pedersen, F. Studt, J. Rossmeisl and J. K. Nørskov, *Energy Environ. Sci.*, 2010, **3**, 1311.

179 C. Oloman and H. Li, *ChemSusChem*, 2008, **1**, 385–391.

180 K. Xie, R. K. Miao, A. Ozden, S. Liu, Z. Chen, C.-T. Dinh, J. E. Huang, Q. Xu, C. M. Gabardo, G. Lee, J. P. Edwards, C. P. O'Brien, S. W. Boettcher, D. Sinton and E. H. Sargent, *Nat. Commun.*, 2022, **13**, 3609.

181 D. Raciti, M. Mao, J. H. Park and C. Wang, *J. Electrochem. Soc.*, 2018, **165**, F799-F804.

182 W. Vielstich and C. H. Hamann, *Elektrochemie*, Wiley-VCH, Weinheim, 4th edn., 2005.

183 K. U. Hansen, L. H. Cherniack and F. Jiao, *ACS Energy Lett.*, 2022, **7**, 4504–4511.

184 M. R. Gerhardt, L. M. Pant, J. C. Bui, A. R. Crothers, V. M. Ehlinger, J. C. Fornaciari, J. Liu and A. Z. Weber, *J. Electrochem. Soc.*, 2021, **168**, 74503.

185 J. Kim, Y. Yu, T. W. Go, J.-J. Gallet, F. Bournel, B. S. Mun and J. Y. Park, *Nat. Commun.*, 2023, **14**, 3273.

186 W. Quan, Y. Lin, Y. Luo and Y. Huang, *Advanced science (Weinheim, Baden-Wurttemberg, Germany)*, 2021, **8**, e2101597.

187 H. Xiao, W. A. Goddard, T. Cheng and Y. Liu, *Proceedings of the National Academy of Sciences of the United States of America*, 2017, **114**, 6685–6688.

188 C. Liu, M. Wang, J. Ye, L. Liu, L. Li, Y. Li and X. Huang, *Nano Lett.*, 2023, **23**, 1474–1480.

189 G. Iijima, T. Inomata, H. Yamaguchi, M. Ito and H. Masuda, *ACS Catal.*, 2019, **9**, 6305–6319.

190 F. Che, J. T. Gray, S. Ha, N. Kruse, S. L. Scott and J.-S. McEwen, *ACS Catal.*, 2018, **8**, 5153–5174.

191 H. Jiang, Z. Hou and Y. Luo, *Angew. Chem. Int. Ed.*, 2017, **56**, 15617–15621.

192 P. An, L. Wei, H. Li, B. Yang, K. Liu, J. Fu, H. Li, H. Liu, J. Hu, Y.-R. Lu, H. Pan, T.-S. Chan, N. Zhang and M. Liu, *J. Mater. Chem. A*, 2020, **8**, 15936–15941.

193 F. Greenwell, B. Siritanaratkul, P. K. Sharma, E. H. Yu and A. J. Cowan, *J. Am. Chem. Soc.*, 2023, **145**, 15078–15083.

194 C. Zhan, F. Dattila, C. Rettenmaier, A. Bergmann, S. Kühl, R. García-Muelas, N. López and B. R. Cuenya, *ACS Catal.*, 2021, **11**, 7694–7701.

195 X. Kong, J. Zhao, J. Ke, C. Wang, S. Li, R. Si, B. Liu, J. Zeng and Z. Geng, *Nano Lett.*, 2022, **22**, 3801–3808.

196 X. Wang, K. Klingan, M. Klingenhof, T. Möller, J. Ferreira de Araújo, I. Martens, A. Bagger, S. Jiang, J. Rossmeisl, H. Dau and P. Strasser, *Nat. Commun.*, 2021, **12**, 794.

197 Z. Weng, X. Zhang, Y. Wu, S. Huo, J. Jiang, W. Liu, G. He, Y. Liang and H. Wang, *Angew. Chem. Int. Ed.*, 2017, **56**, 13135–13139.

198 P. Grosse, D. Gao, F. Scholten, I. Sinev, H. Mistry and B. Roldan Cuenya, *Angew. Chem. Int. Ed.*, 2018, **57**, 6192–6197.

199 K. Jiang, Y. Huang, G. Zeng, F. M. Toma, W. A. Goddard and A. T. Bell, *ACS Energy Lett.*, 2020, **5**, 1206–1214.

200 J. C. Bui, C. Kim, A. J. King, O. Romiluyi, A. Kusoglu, A. Z. Weber and A. T. Bell, *Acc. Chem. Res.* 2022, **55**, 484–494.

201 D. A. Henckel, M. J. Counihan, H. E. Holmes, X. Chen, U. O. Nwabara, S. Verma, J. Rodríguez-López, P. J. A. Kenis and A. A. Gewirth, *ACS Catal.*, 2021, **11**, 255–263.

202 H. Zhang, J. Gao, D. Raciti and A. S. Hall, *Nat. Catal.*, 2023.

203 C.-T. Dinh, T. Burdyny, M. G. Kibria, A. Seifitokaldani, C. M. Gabardo, F. P. García de Arquer, A. Kiani, J. P. Edwards, P. de Luna, O. S. Bushuyev, C. Zou, R. Quintero-Bermudez, Y. Pang, D. Sinton and E. H. Sargent, *Science (New York, N.Y.)*, 2018, **360**, 783–787.

204 J. Chen and L. Wang, *Adv. Mater.*, 2022, **34**, e2103900.

205 J. Vavra, T.-H. Shen, D. Stoian, V. Tileli and R. Buonsanti, *Angew. Chem. Int. Ed.*, 2021, **60**, 1347–1354.

206 C.-J. Chang, S.-C. Lin, H.-C. Chen, J. Wang, K. J. Zheng, Y. Zhu and H. M. Chen, *J. Am. Chem. Soc.*, 2020, **142**, 12119–12132.

207 M. Li, M. N. Idros, Y. Wu, T. Burdyny, S. Garg, X. S. Zhao, G. Wang and T. E. Rufford, *J. Mater. Chem. A*, 2021, **9**, 19369–19409.

208 M. de Jesus Gálvez-Vázquez, P. Moreno-García, H. Xu, Y. Hou, H. Hu, I. Z. Montiel, A. V. Rudnev, S. Alinejad, V. Grozovski, B. J. Wiley, M. Arenz and P. Broekmann, *ACS Catal.*, 2020, **10**, 13096–13108.

209 A. Reyes, R. P. Jansonius, B. A. W. Mowbray, Y. Cao, D. G. Wheeler, J. Chau, D. J. Dvorak and C. P. Berlinguette, *ACS Energy Lett.*, 2020, **5**, 1612–1618.

210 J. Disch, L. Bohn, S. Koch, M. Schulz, Y. Han, A. Tengattini, L. Helfen, M. Breitwieser and S. Vierrath, *Nat. Commun.*, 2022, **13**, 6099.

211 S. Garg, Q. Xu, A. B. Moss, M. Mirolo, W. Deng, I. Chorkendorff, J. Drnec and B. Seger, *Energy Environ. Sci.*, 2023, **16**, 1631–1643.

212 L. M. Baumgartner, C. I. Koopman, A. Forner-Cuenca and D. A. Vermaas, *ACS Sustain. Chem. Eng.*, 2022, **10**, 4683–4693.

213 Sinopec Group, *Sinopec Launches the World's Largest Green Hydrogen-Coal Chemical Project in Inner Mongolia*, 2023, http://www.sinopecgroup.com/group/en/Sinopecnews/20230331/news_20230331_502557647316.shtml .

214 VRB Energy, *VRB Energy announces agreement for China's largest solar battery*, 2021, https://vrbenergy.com/vrb-energy-announces-agreement-for-chinas-largest-solar-battery-a-100mw-solar-storage-project-in-hubei-province/.

215 Kopernikus Project Consortium, *Verbundvorhaben P2X: Erforschung, Validierung und Implementierung von „Power-to-X"-Konzepten*, 2022, https://www.kopernikus-projekte.de/lw_resource/datapool/systemfiles/elements/files/EC511299093C1CE2E0537E695E866221/live/document/P2X-Flyer_Ergebnisse_Phase_II.pdf .

216 ITM Power, *World's largest Hydrogen Electrolysis in Shell's Rhineland Refinery*, 2021, https://itm-power.com/news/world-s-largest-hydrogen-electrolysis-in-shell-s-rhineland-refinery.

217 Air Liquide, *Air Liquide inaugurates the world's largest low-carbon hydrogen membrane-based production unit in Canada*, 2020, https://www.airliquide.com/group/press-releases-news/2021-01-26/air-liquide-inaugurates-worlds-largest-low-carbon-hydrogen-membrane-based-production-unit-canada.

218 Siemens Energy, *A lighthouse project at the southern tip of Chile: Production starts at the world's first industrial-scale facility for carbon-neutral fuel*, 2022, https://press.siemens-

energy.com/global/en/pressrelease/lighthouse-project-southern-tip-chile-production-starts-worlds-first-industrial-scale.

219 D. A. Salvatore, C. M. Gabardo, A. Reyes, C. P. O'Brien, S. Holdcroft, P. Pintauro, B. Bahar, M. Hickner, C. Bae, D. Sinton, E. H. Sargent and C. P. Berlinguette, *Nat. Energy*, 2021, **6**, 339–348.

220 Ionomr Innovations, *Ionomr Innovations' Pemion® hydrocarbon-based proton exchange membrane and polymer exceed industry durability targets*, 2023, https://ionomr.com/wp-content/uploads/2023/01/Pemion-Durability-Data_News-Release-and-Technical-Backgrounder_For-Release-Jan19.pdf.

221 Enapter AG, *Enapter simplifies green hydrogen production with new one-size-fits-all electrolyser*, 2022, https://www.enapter.com/newsroom/enapter-simplifies-green-hydrogen-production.

222 S. Willdorf-Cohen, A. Zhegur-Khais, J. Ponce-González, S. Bsoul-Haj, J. R. Varcoe, C. E. Diesendruck and D. R. Dekel, *ACS Appl. Energy Mater.*, 2023, **6**, 1085–1092.

223 L. N. Stanislaw, M. R. Gerhardt and A. Z. Weber, *ECS Trans.*, 2019, **92**, 767–779.

224 H. A. Miller, K. Bouzek, J. Hnat, S. Loos, C. I. Bernäcker, T. Weißgärber, L. Röntzsch and J. Meier-Haack, *Sustain. Energy Fuels*, 2020, **4**, 2114–2133.

225 N. Ziv, W. E. Mustain and D. R. Dekel, *ChemSusChem*, 2018, **11**, 1136–1150.

226 M. A. Blommaert, R. Sharifian, N. U. Shah, N. T. Nesbitt, W. A. Smith and D. A. Vermaas, *J. Mater. Chem. A*, 2021, **9**, 11179–11186.

227 M. Herrero-Gonzalez, J. López, G. Virruso, C. Cassaro, A. Tamburini, A. Cipollina, J. L. Cortina, R. Ibañez and G. Micale, *Membranes*, 2023, **13**.

228 L. Gazigil, E. Er, O. E. Kestioğlu and T. Yonar, *Membranes*, 2022, **12**.

229 J. Torrero, T. Morawietz, D. García Sanchez, D. Galyamin, M. Retuerto, V. Martin-Diaconescu, S. Rojas, J. A. Alonso, A. S. Gago and K. A. Friedrich, *Adv. Energy Mater.*, 2023, **13**.

230 L. Moriau, M. Smiljanić, A. Lončar and N. Hodnik, *ChemCatChem*, 2022, **14**, e202200586.

231 M. Dhimish, R. G. Vieira and G. Badran, *Int. J. Hydrog. Energy*, 2021, **46**, 37017–37028.

232 J. H. Russell, L. J. Nuttall, A. P. Fickett, *ACS Meeting, Division of Fuel Chemistry*, 1973, 24–33.

233 K. W. Ahmed, M. J. Jang, M. G. Park, Z. Chen and M. Fowler, *Electrochem*, 2022, **3**, 581–612.

234 A. S. Gago, S. A. Ansar, B. Saruhan, U. Schulz, P. Lettenmeier, N. A. Cañas, P. Gazdzicki, T. Morawietz, R. Hiesgen, J. Arnold and K. A. Friedrich, *J. Power Sources*, 2016, **307**, 815–825.

235 S. Singh, T. Taketsugu and R. K. Singh, *ACS Omega*, 2021, **6**, 32739–32748.

236 X. Li, P. Zhang, L. Zhang, G. Zhang, H. Gao, Z. Pang, J. Yu, C. Pei, T. Wang and J. Gong, *Chem. Sci.*, 2023, **14**, 5602–5607.

237 C. W. Lin, C. L. Hung, M. Venkateswarlu and B. J. Hwang, *J. Power Sources*, 2005, **146**, 397–401.

238 H. Lindström, S. Södergren, A. Solbrand, H. Rensmo, J. Hjelm, A. Hagfeldt and S.-E. Lindquist, *J. Phys. Chem. B*, 1997, **101**, 7717–7722.

239 J. Gao, Y. Meng, A. Benton, J. He, L. G. Jacobsohn, J. Tong and K. S. Brinkman, *ACS Appl. Mater. Interfaces*, 2020, **12**, 38012–38018.

240 X. Kang, A. Chatzitakis, T. Aarholt, X. Sun, C. Negri and T. Norby, *J. Mater. Chem. A,* 2021, **10**, 218–227.

241 P. Díaz-Carrasco, A. Duarte-Cárdenas, A. Kuhn and F. García-Alvarado, *J. Power Sources*, 2021, **515**, 230632.

242 D.-H. Lee, B.-H. Lee, A. K. Sinha, J.-H. Park, M.-S. Kim, J. Park, H. Shin, K.-S. Lee, Y.-E. Sung and T. Hyeon, *J. Am. Chem. Soc.*, 2018, **140**, 16676–16684.

243 H. Bi, S. Zhu, Y. Liang, H. Jiang, Z. Li, S. Wu, H. Wei, C. Chang and Z. Cui, *Chem. Eng. J.*, 2022, **442**, 136146.

244 R. B. Kutz, Q. Chen, H. Yang, S. D. Sajjad, Z. Liu and I. R. Masel, *Energy Technol.*, 2017, **5**, 929–936.

245 M. Esmaeilirad, Z. Jiang, A. M. Harzandi, A. Kondori, M. Tamadoni Saray, C. U. Segre, R. Shahbazian-Yassar, A. M. Rappe and M. Asadi, *Nat. Energy*, 2023, **8**, 891–900.

246 Y. Cheng, Y. Guo, H. He, W. Ding, Y. Diao and F. Huo, *Ind. Eng. Chem. Res.*, 2021, **60**, 6027–6037.

247 O. Romiluyi, N. Danilovic, A. T. Bell and A. Z. Weber, *Electrochem. Sci. Adv.*, 2023, **3**.

248 Lee, H.; Wu, X.; Wu, X.; Wang, X.; Ye, Q.; Sun, L., *Chemical Communications*, 2020, 56, 3797–3800.

249 Jeong, Y.; Kim, Y.; Kim, Y. J.; Park, J. Y., *Advanced Science*, 2023, 11.

250 K. Komatsu, H. Kagi, T. Nagai, T. Kuribayashi, J. B. Parise and Y. Kudoh, *American Mineralogist*, 2007, **92**, 1270–1275.

251 M. A. Barique, E. Tsuchida, A. Ohira and K. Tashiro, *ACS Omega*, 2018, **3**, 349–360.

List of Publications

Articles

- **B. Sahin**, M. Kraehling, V. Facci Allegrini, J. Leung, K. Wiesner-Fleischer, E. Magori, R. Pastusiak, A. Tawil, T. Hodges, E. Brooke, E. Corbos, M. Fleischer, E. Simon, O. Hinrichsen. *Fine-tuned Combination of Cell and Electrode Designs Unlocks Month-long Stable Low Temperature Cu-based CO_2 Electrolysis.* Accepted by Journal of CO_2 Utilization; 2024.
- **B. Sahin**, S. Kimberly Raymond, F. Ntourmas, R. Pastusiak, K. Wiesner-Fleischer, M. Fleischer, E. Simon, O. Hinrichsen. *Accumulation of Liquid Byproducts in an Electrolyte as a Critical Factor That Compromises Long-Term Functionality of CO_2-to-C_2H_4 Electrolysis.* ACS Applied Materials & Interfaces, vol. 15 (39); 2023. DOI: 10.1021/acsami.3c08454.
- **B. Sahin**, J. Leung, E. Magori, S. Laumen, A. Tawil, E. Simon, O. Hinrichsen. *Controlling Product Distribution of CO_2 Reduction on CuO-Based Gas Diffusion Electrodes by Manipulating Back Pressure*. Energy Technology, vol. 10 (12); 2022. DOU:10.1002/ente.202200972.

Conferences

- **B. Sahin**, V. Facci Allegrini, M. Kraehling, K. Wiesner-Fleischer, A. Tawil, R. Pastusiak, E. Magori, E. Simon, O. Hinrichsen. *Multi-Factor Approach on How to Enhance the System Stability of CO_2 Electrochemical Conversion to C_{2+} Products from Hours to a Month* (Lecture). 244th Electrochemical Society Meeting from The Electrochemical Society. October 8 - 12, 2023 in Gothenburg, Sweden.

- **B. Sahin**, S. Kimberly Raymond, E. Simon, O. Hinrichsen. *Investigations on the effects of liquid product accumulation in the electrolyte on CO_2 electrolysis with CuO-based electrodes* (Lecture). Electrochemistry Congress from Gesellschaft Deutscher Chemiker. September 27 - 30, 2022 in Berlin, Germany.
- S. Sarma, T. Hodges, G. Platt, C. Bosch, H. Chuma, E. Brooke, H. Marchbank, P. Jimenez, **B. Sahin**, E. Corbos. *Atomic to Microscale Tuning of CO_2 Electrolysis* (Poster). Gordon Research Conference – Electrochemistry. January 7 – 12. 2024 in California, United States.

Patents & Invention Disclosures

- E. Magori, R. Pastusiak, E. Simon, **B. Sahin**, A. Tawil, K. Wiesner-Fleischer. *Durchkontaktierung für Elektroden in Elektrolysezellen mit Gasdiffusionselektrode*. Filed on 14.12.2023. File reference: 23216528.2
- **B. Sahin**, E. Simon, K. Wiesner-Fleischer, E. Magori, R. Pastusiak, A. Tawil. *Novel membrane electrode assembly design for C_2H_4 selective PEM-type CO_2-electrolyzers*. Filed on 22.08.2023. File reference: EP23192695.7.
- **B. Sahin**, E. Simon, K. Wiesner-Fleischer, E. Magori, R. Pastusiak, A. Tawil. *Bipolar multilayer electrode design for stable electrochemical reduction of CO_2 to hydrocarbons*. Filed on 22.08.2023. File reference: EP23192687.4.
- **B. Sahin**, E. Simon, M. Fleischer, E. Magori. *Operation mode to optimize CO_2 electrolysis*. Published on 16.11.2023. File reference: 22172254.9.

Reprint Permissions

Wiley Article

Details

JOHN WILEY AND SONS LICENSE
TERMS AND CONDITIONS

Oct 14, 2023

This Agreement between Mr. Baran Sahin ("You") and John Wiley and Sons ("John Wiley and Sons") consists of your license details and the terms and conditions provided by John Wiley and Sons and Copyright Clearance Center.

License Number	5647880346997
License date	Oct 14, 2023
Licensed Content Publisher	John Wiley and Sons
Licensed Content Publication	ENERGY TECHNOLOGY (ELECTRONIC)
Licensed Content Title	Controlling Product Distribution of CO2 Reduction on CuO-Based Gas Diffusion Electrodes by Manipulating Back Pressure
Licensed Content Author	Olaf Hinrichsen, Elfriede Simon, Angelika Tawil, et al
Licensed Content Date	Oct 21, 2022
Licensed Content Volume	10
Licensed Content Issue	12
Licensed Content Pages	11
Type of use	Dissertation/Thesis
Requestor type	Author of this Wiley article

Format	Print and electronic
Portion	Full article
Will you be translating?	No
Title of new work	PhD Thesis of Baran Sahin
Institution name	Technical University of Munich
Expected presentation date	Jan 2024
Requestor Location	Mr. Baran Sahin Weilheimerstr. 21f Munich, 81373 Germany Attn: Mr. Baran Sahin
Publisher Tax ID	EU826007151
Total	0.00 EUR

Terms and Conditions

TERMS AND CONDITIONS

This copyrighted material is owned by or exclusively licensed to John Wiley & Sons, Inc. or one of its group companies (each a"Wiley Company") or handled on behalf of a society with which a Wiley Company has exclusive publishing rights in relation to a particular work (collectively "WILEY"). By clicking "accept" in connection with completing this licensing transaction, you agree that the following terms and conditions apply to this transaction (along with the billing and payment terms and conditions established by the Copyright Clearance Center Inc., ("CCC's Billing and Payment terms and conditions"), at the time that you opened your RightsLink account (these are available at any time at http://myaccount.copyright.com).

Terms and Conditions

- The materials you have requested permission to reproduce or reuse (the "Wiley Materials") are protected by copyright.

- You are hereby granted a personal, non-exclusive, non-sub licensable (on a stand-alone basis), non-transferable, worldwide, limited license to reproduce the Wiley Materials for the purpose specified in the licensing process. This license, **and any CONTENT (PDF or image file) purchased as part of your order,** is for a one-time use only and limited to any maximum distribution number specified in the license. The first instance of republication or reuse granted by this license must be completed within two years of the date of the grant of this license (although copies prepared before the end date may be distributed thereafter). The Wiley Materials shall not be used in any other manner or for any other purpose, beyond what is granted in the license. Permission is granted subject to an appropriate acknowledgement given to the author, title of the material/book/journal and the publisher. You shall also duplicate the copyright notice that appears in the Wiley publication in your use of the Wiley Material. Permission is also granted on the understanding that nowhere in the text is a previously published source acknowledged for all or part of this Wiley Material. Any third party content is expressly excluded from this permission.

- With respect to the Wiley Materials, all rights are reserved. Except as expressly granted by the terms of the license, no part of the Wiley Materials may be copied, modified, adapted (except for minor reformatting required by the new Publication), translated, reproduced, transferred or distributed, in any form or by any means, and no derivative works may be made based on the Wiley Materials without the prior permission of the respective copyright owner.**For STM Signatory Publishers clearing permission under the terms of the STM Permissions Guidelines only, the terms of the license are extended to include subsequent editions and for editions in other languages, provided such editions are for the work as a whole in situ and does not involve the separate exploitation of the permitted figures or extracts,** You may not alter, remove or suppress in any manner any copyright, trademark or other notices displayed by the Wiley Materials. You may not license, rent, sell, loan, lease, pledge, offer as security, transfer or assign the Wiley Materials on a stand-alone basis, or any of the rights granted to you hereunder to any other person.

- The Wiley Materials and all of the intellectual property rights therein shall at all times remain the exclusive property of John Wiley & Sons Inc, the Wiley Companies, or their respective licensors, and your interest therein is only that of having possession of and the right to reproduce the Wiley Materials pursuant to Section 2 herein during the continuance of this Agreement. You agree that you own no right, title or interest in or to the Wiley Materials or any of the intellectual property rights therein. You shall have no rights hereunder other than the license as provided for above in Section 2. No right, license or interest to any trademark, trade name, service mark or other branding ("Marks") of WILEY or its licensors is granted hereunder, and you agree that you shall not assert any such right, license or interest with respect thereto

- NEITHER WILEY NOR ITS LICENSORS MAKES ANY WARRANTY OR REPRESENTATION OF ANY KIND TO YOU OR ANY THIRD PARTY, EXPRESS, IMPLIED OR STATUTORY, WITH RESPECT TO THE MATERIALS OR THE ACCURACY OF ANY INFORMATION CONTAINED IN THE MATERIALS, INCLUDING, WITHOUT LIMITATION, ANY IMPLIED WARRANTY OF MERCHANTABILITY, ACCURACY, SATISFACTORY QUALITY, FITNESS FOR A PARTICULAR PURPOSE, USABILITY, INTEGRATION OR NON-INFRINGEMENT AND ALL SUCH WARRANTIES ARE HEREBY EXCLUDED BY WILEY AND ITS LICENSORS AND WAIVED BY YOU.

- WILEY shall have the right to terminate this Agreement immediately upon breach of this Agreement by you.

- You shall indemnify, defend and hold harmless WILEY, its Licensors and their respective directors, officers, agents and employees, from and against any actual or threatened claims, demands, causes of action or proceedings arising from any breach of this Agreement by you.

- IN NO EVENT SHALL WILEY OR ITS LICENSORS BE LIABLE TO YOU OR ANY OTHER PARTY OR ANY OTHER PERSON OR ENTITY FOR ANY SPECIAL, CONSEQUENTIAL, INCIDENTAL, INDIRECT, EXEMPLARY OR PUNITIVE DAMAGES, HOWEVER CAUSED, ARISING OUT OF OR IN CONNECTION WITH THE DOWNLOADING, PROVISIONING, VIEWING OR USE OF THE MATERIALS REGARDLESS OF THE FORM OF ACTION, WHETHER FOR BREACH OF CONTRACT, BREACH OF WARRANTY, TORT, NEGLIGENCE, INFRINGEMENT OR OTHERWISE (INCLUDING, WITHOUT LIMITATION, DAMAGES BASED ON LOSS OF PROFITS, DATA, FILES, USE, BUSINESS OPPORTUNITY OR CLAIMS OF THIRD PARTIES), AND WHETHER OR NOT THE PARTY HAS BEEN ADVISED OF THE POSSIBILITY OF SUCH DAMAGES. THIS LIMITATION SHALL APPLY NOTWITHSTANDING ANY FAILURE OF ESSENTIAL PURPOSE OF ANY LIMITED REMEDY PROVIDED HEREIN.

- Should any provision of this Agreement be held by a court of competent jurisdiction to be illegal, invalid, or unenforceable, that provision shall be deemed amended to achieve as nearly as possible the same economic effect as the original provision, and the legality, validity and enforceability of the remaining provisions of this Agreement shall not be affected or impaired thereby.

- The failure of either party to enforce any term or condition of this Agreement shall not constitute a waiver of either party's right to enforce each and every term and condition of this Agreement. No breach under this agreement shall be deemed waived or excused by either party unless such waiver or consent is in writing signed by the party granting such waiver or consent. The waiver by or consent of a party to a breach of any provision of this Agreement shall not operate or be construed as a waiver of or consent to any other or subsequent breach by such other party.

- This Agreement may not be assigned (including by operation of law or otherwise) by you without WILEY's prior written consent.

- Any fee required for this permission shall be non-refundable after thirty (30) days from receipt by the CCC.

- These terms and conditions together with CCC's Billing and Payment terms and conditions (which are incorporated herein) form the entire agreement between you and WILEY concerning this licensing transaction and (in the absence of fraud) supersedes all prior agreements and representations of the parties, oral or written. This Agreement may not be amended except in writing signed by both parties. This Agreement shall be binding upon and inure to the benefit of the parties' successors, legal representatives, and authorized assigns.

- In the event of any conflict between your obligations established by these terms and conditions and those established by CCC's Billing and Payment terms and conditions, these terms and conditions shall prevail.

- WILEY expressly reserves all rights not specifically granted in the combination of (i) the license details provided by you and accepted in the course of this licensing transaction, (ii) these terms and conditions and (iii) CCC's Billing and Payment terms and conditions.

- This Agreement will be void if the Type of Use, Format, Circulation, or Requestor Type was misrepresented during the licensing process.
- This Agreement shall be governed by and construed in accordance with the laws of the State of New York, USA, without regards to such state's conflict of law rules. Any legal action, suit or proceeding arising out of or relating to these Terms and Conditions or the breach thereof shall be instituted in a court of competent jurisdiction in New York County in the State of New York in the United States of America and each party hereby consents and submits to the personal jurisdiction of such court, waives any objection to venue in such court and consents to service of process by registered or certified mail, return receipt requested, at the last known address of such party.

WILEY OPEN ACCESS TERMS AND CONDITIONS

Wiley Publishes Open Access Articles in fully Open Access Journals and in Subscription journals offering Online Open. Although most of the fully Open Access journals publish open access articles under the terms of the Creative Commons Attribution (CC BY) License only, the subscription journals and a few of the Open Access Journals offer a choice of Creative Commons Licenses. The license type is clearly identified on the article.

The Creative Commons Attribution License

The Creative Commons Attribution License (CC-BY) allows users to copy, distribute and transmit an article, adapt the article and make commercial use of the article. The CC-BY license permits commercial and non-

Creative Commons Attribution Non-Commercial License

The Creative Commons Attribution Non-Commercial (CC-BY-NC)License permits use, distribution and reproduction in any medium, provided the original work is properly cited and is not used for commercial purposes.(see below)

Creative Commons Attribution-Non-Commercial-NoDerivs License

The Creative Commons Attribution Non-Commercial-NoDerivs License (CC-BY-NC-ND) permits use, distribution and reproduction in any medium, provided the original work is properly cited, is not used for commercial purposes and no modifications or adaptations are made. (see below)

Use by commercial "for-profit" organizations

Use of Wiley Open Access articles for commercial, promotional, or marketing purposes requires further explicit permission from Wiley and will be subject to a fee.

Further details can be found on Wiley Online Library
http://olabout.wiley.com/WileyCDA/Section/id-410895.html

Other Terms and Conditions:

v1.10 Last updated September 2015

American Chemical Society Article

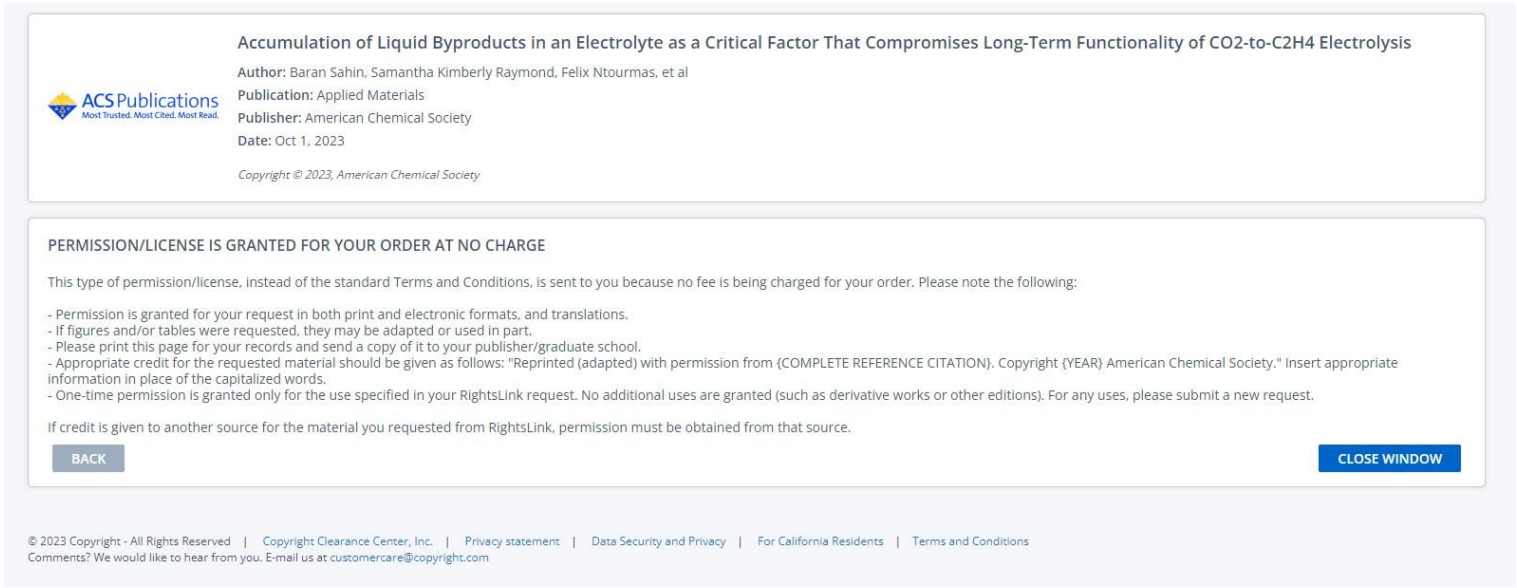

Accumulation of Liquid Byproducts in an Electrolyte as a Critical Factor That Compromises Long-Term Functionality of CO2-to-C2H4 Electrolysis

Author: Baran Sahin, Samantha Kimberly Raymond, Felix Ntourmas, et al
Publication: Applied Materials
Publisher: American Chemical Society
Date: Oct 1, 2023

Copyright © 2023, American Chemical Society

PERMISSION/LICENSE IS GRANTED FOR YOUR ORDER AT NO CHARGE

This type of permission/license, instead of the standard Terms and Conditions, is sent to you because no fee is being charged for your order. Please note the following:

- Permission is granted for your request in both print and electronic formats, and translations.
- If figures and/or tables were requested, they may be adapted or used in part.
- Please print this page for your records and send a copy of it to your publisher/graduate school.
- Appropriate credit for the requested material should be given as follows: "Reprinted (adapted) with permission from {COMPLETE REFERENCE CITATION}. Copyright {YEAR} American Chemical Society." Insert appropriate information in place of the capitalized words.
- One-time permission is granted only for the use specified in your RightsLink request. No additional uses are granted (such as derivative works or other editions). For any uses, please submit a new request.

If credit is given to another source for the material you requested from RightsLink, permission must be obtained from that source.

BACK CLOSE WINDOW

Declaration

The submitted thesis was supervised by Prof. Dr.-Ing. Kai-Olaf Hinrichsen and Dr. Elfriede Simon. Hereby, I affirm that I am the sole author of this thesis. To the best of my knowledge, I affirm that this thesis does not infringe upon anyone's copyright nor violate any proprietary rights. I affirm that any ideas, techniques, quotations, or any other material, are in accordance with standard referencing practices. Moreover, I affirm that, so far, the thesis has not been forwarded to a third party nor is it published. I obeyed all study regulations of the Technische Universität München.

Throughout the work, the internet was used for research and verification. Many of the keywords provided herein, references and other information can be verified on the internet. However, no sources are given, because all statements made in this work are fully covered by the cited literature sources.

Garching bei München, _____ _____

Baran Sahin